

FINAL TECHNICAL REPORT

AWARD NUMBER: G18AP00094

Evaluating Liquefaction Triggering Potential from Induced Seismicity

by

Tyler J. Quick, Russell A. Green, Ellen M. Rathje, James K. Mitchell

Period of Award:
8/15/2018 to 7/14/2020

Principal Investigator:

Russell A. Green (VT)
Virginia Polytechnic Institute and State University
Dept. of Civil and Environmental Engineering
750 Drillfield Drive
214 Patton Hall
Blacksburg, VA 24061
(540) 231-9826 (phone)
(540) 231-7532 (fax)
rugreen@vt.edu

Research supported by the U. S. Geological Survey (USGS), Department of Interior, under USGS award number G18AP00094. The views and conclusions contained in this document are those of the authors and should not be interpreted as necessarily representing the official policies, either expressed or implied, of the U. S. Government.

Abstract

Deep wastewater injection-induced seismicity has led to over a thousand moment magnitude (M_w) > 3 earthquakes and four M_w >5 earthquakes in Oklahoma over the last ten years. The 3 September 2016, M_w 5.8 Pawnee, Oklahoma, earthquake was the first induced seismic event worldwide, that the authors are aware of, where liquefaction was observed and documented, raising concerns regarding the liquefaction risk posed by future induced earthquakes. Although the stress-based “simplified” liquefaction evaluation procedure is the most widely used approach to evaluate liquefaction potential worldwide, the procedure is semi-empirical, with empirical aspects primarily derived from data from moderate-sized tectonic earthquakes in active shallow-crustal tectonic regimes (e.g., California, Japan, and New Zealand). Several studies have found that the ground motions from induced earthquakes have different characteristics than those from natural tectonic earthquakes. Additionally, the geologic/soil profiles in areas of the U.S. experiencing high rates of induced seismicity (e.g., Oklahoma) differ from profiles used to develop the most widely used variants of the simplified procedure. Accordingly, it is uncertain whether the depth-stress reduction factor (r_d) and Magnitude Scaling Factor (MSF) relationships used in existing simplified liquefaction evaluation procedures are suitable for use with induced earthquakes in Oklahoma and neighboring states. This is because both r_d , which accounts for the non-rigid response of the soil profiles to shaking, and MSF, which accounts for durational effects of shaking on liquefaction triggering, are affected by ground motion and soil profile characteristics.

This study addresses these issues by developing r_d and MSF relationships specific to wastewater injection-induced seismicity in Oklahoma, Texas, and Kansas. This approach, based on methods used in Green et al. (2017, 2020) to develop analogous liquefaction triggering models for evaluating liquefaction potential in the central and eastern United States and the Groningen region of the Netherlands, involved performing numerical site response analyses using induced ground motions and soil profiles from Oklahoma, Texas, and Kansas. The generated data were regressed to develop regional induced seismicity-specific r_d and MSF relationships that can be used to estimate normalized cyclic stress ratio (CSR^*) in the context of existing liquefaction evaluation procedures to estimate the liquefaction potential from induced earthquakes. To assess the efficacy of the new liquefaction triggering model, detailed site characterizations were performed at several sites that experienced intense shaking and liquefaction triggering during the 3 September 2016, M_w 5.8 Pawnee, OK, earthquake. Liquefaction potential was evaluated at these sites using the new liquefaction triggering model, as well as existing models developed for tectonic events. These predictions were then compared to field observations made following the Pawnee earthquake to evaluate the liquefaction evaluation models. At most locations evaluated, predictions from the new model were more consistent with the observed severity of liquefaction than were predictions from existing models, which

tended to over-predict the severity of liquefaction. This suggests that the new liquefaction hazard assessment model developed herein can provide more accurate assessments of the liquefaction hazard of induced earthquakes in Oklahoma, Texas, and Kansas than the widely used models developed from data from tectonic events.

Table of Contents

| | |
|---|----|
| Abstract..... | 2 |
| 1 Introduction and Objectives | 6 |
| 2 Background..... | 8 |
| 2.1 Induced Seismicity..... | 8 |
| 2.2 Differences Between Ground Motion Characteristics of Induced and Tectonic Earthquakes.... | 10 |
| 2.3 Existing Liquefaction Triggering Models and Their Applicability to Induced Seismicity..... | 15 |
| 2.3.1 Stress Reduction Factor, r_d | 18 |
| 2.3.2 Magnitude Scaling Factor, MSF | 21 |
| 3 Site Characterization of Sites Impacted by the 3 September 2016, M_w 5.8 Pawnee, OK, earthquake | 25 |
| 3.1 Site Selection and Preliminary Investigations..... | 26 |
| 3.2 Detailed Site Investigation..... | 32 |
| 3.3 Site Characterization Results | 35 |
| 4 Development of a New Liquefaction Triggering Model for Induced Seismicity in Oklahoma, Texas, and Kansas | 55 |
| 4.1 Induced Ground Motion Database | 55 |
| 4.2 Representative Soil Profiles | 58 |
| 4.3 Equivalent-Linear Site Response Analysis | 60 |
| 4.4 Proposed r_d Relationship..... | 60 |
| 4.5 Proposed n_{eq} and MSF Relationships | 73 |
| 4.6 Correlation of r_d across Depth and Correlation between Oklahoma r_d and $\ln(n_{eq})$ Relationships | 82 |
| 4.7 MSF and r_d Summary and Comparison with Relationships from Prior Studies | 83 |
| 4.8 Implementation of r_{d-OK} and MSF_{OK} for Assessing Liquefaction Hazard for Induced Ground Motions in Oklahoma, Texas, and Kansas..... | 86 |
| 5 Validation of the Induced Seismicity Liquefaction Triggering Model | 87 |
| 5.1 Ground Motion Characteristics and Other Inputs for Liquefaction Hazard Assessment..... | 88 |
| 5.2 Assessment of Liquefaction Potential at the Pawnee Earthquake Test Sites | 93 |

| | | |
|-----|--|-----|
| 5.3 | Liquefaction Hazard Analysis and Model Validation Results – FS_{liq} and LPI_{ish} | 96 |
| 6 | Summary and Conclusion | 129 |
| 7 | Acknowledgements..... | 131 |
| | References..... | 132 |

1 Introduction and Objectives

Deep wastewater disposal into injection wells has led to a significant increase in seismicity in areas where oil and gas production are prevalent such as Oklahoma, Kansas, and Texas. Although recent regulations enacted to limit wastewater injection volumes in Oklahoma have led to reductions in regional seismicity, over 60 earthquakes with moment magnitudes (M_w) of three or greater occurred in 2019, which is still 60 times the natural tectonic rate of about one $M_w \geq 3$ earthquake per year in the state (Langenbruch and Zoback 2016; U.S. Geologic Survey 2020a). Additionally, although the number of $M_w \geq 3$ earthquakes has been decreasing since 2015 when wastewater injection was scaled back, some of the largest events, including the 2016 M_w 5.8 Pawnee, OK earthquake, have occurred since that time. This is consistent with observations made in other regions impacted by induced seismicity, where elevated levels of seismic activity have persisted for years after the conclusion of the inducing activities and where some of the largest induced events have occurred after operations have ceased (Ellsworth 2013). This dramatic increase in seismicity is of particular concern because it is occurring primarily in historically aseismic areas where building codes and construction methods have not traditionally accounted for higher levels of seismicity. This means that infrastructure in these areas may be more susceptible to damage caused by ground shaking. Although most earthquakes induced by deep wastewater injection in Oklahoma have been small, larger events have resulted in structural damage and, of particular interest to this study, liquefaction (Clayton et al. 2016; Kolawole et al. 2017). In addition to damages caused by induced earthquakes in Oklahoma, potentially-induced events worldwide such as the 2017 M_w 5.5 Pohang, South Korea, earthquake and the 25 February 2019 M_L 4.9 Sichuan, China earthquake have led to injuries, extensive liquefaction, and significant economic losses (Choi et al. 2019; Yang et al. 2020). Observations of liquefaction during the 2016 Pawnee, OK earthquake and other induced events highlight the need to develop a suitable framework for accurately assessing the liquefaction risk associated with induced seismicity.

Although the stress-based “simplified” liquefaction evaluation procedure (Whitman 1971; Seed and Idriss 1971) is the most widely used approach for evaluating liquefaction potential worldwide, the procedure is semi-empirical, with the empirical aspects of it derived from data from moderate-sized tectonic earthquakes in active shallow-crustal tectonic regimes (e.g., California, Japan, and New Zealand). As a result, the suitability of this procedure to evaluate the liquefaction hazard due to induced seismicity in stable continental tectonic regimes is uncertain. Several studies have shown that ground motions from induced earthquakes may have different characteristics than those from natural tectonic earthquakes (e.g., Bommer et al. 2016; Hough 2014; Novakovic et al. 2018; Zalachoris and Rathje 2019). Additionally, the geologic profiles and soil deposits in areas in the US experiencing the highest rate of induced seismicity (e.g., Oklahoma) differ from those used to develop the empirical aspects of the most widely used variants of the

simplified procedure. This, in combination with the generally smaller magnitudes of induced earthquakes, raises questions about whether the depth-stress reduction factor (r_d) and Magnitude Scaling Factor (MSF) relationships used in existing simplified liquefaction evaluation procedures for estimating normalized Cyclic Stress Ratio (CSR^*) are suitable for use with induced earthquakes. This is because both r_d , which accounts for the non-rigid response of the soil profiles to shaking, and MSF, which accounts for shaking duration on liquefaction triggering, are affected by ground motion and soil profile characteristics.

The objective of this study is to develop and test a new liquefaction triggering model for evaluating liquefaction potential of soils subjected to ground motions from induced earthquakes in Oklahoma, Texas, and Kansas. The approach used to develop this model was based upon the methods used in Green et al. (2017, 2020) to develop analogous liquefaction triggering models for evaluating the liquefaction potential due to tectonic earthquakes in the central and eastern United States (CEUS) and due to induced earthquakes resulting from natural gas extraction in the Groningen region of the Netherlands. This approach involved developing new regional induced seismicity-specific r_d and MSF relationships for calculating CSR^* within the context of existing liquefaction evaluation procedures. The new r_d and MSF relationships were developed using induced ground motion recordings from the Oklahoma region and representative soil profiles from liquefaction-susceptible sites in the region. The motions and profiles were used in numerical site response analyses, performed using the program ShakeVT2 (Lasley et al. 2014; Thum et al. 2019), to generate profiles of r_d and number of equivalent cycles (n_{eq}) for each motion/profile combination. Statistical analysis of the generated data was then used to regress the new r_d and MSF relationships for use with wastewater injection-induced seismic ground motions in Oklahoma, Texas, and Kansas.

To assess the efficacy of the modified relationships, sites that experienced intense shaking during the 3 September 2016, M_w 5.8 Pawnee, OK, earthquake were evaluated using the new liquefaction triggering models as well as existing models developed for tectonic events. Predictions were then compared to field observations of liquefaction response made following the Pawnee event to validate the new model and evaluate the utility of existing models for predicting the liquefaction triggering during induced earthquakes. Towards this end, detailed geotechnical site characterizations were performed at sites where evidence of liquefaction was and was not observed during the Pawnee event. The field testing included seismic Cone Penetration Tests (sCPT), Multichannel Spectral Analysis of Surface Waves (MASW) tests, and Horizontal-to-Vertical Spectral Ratio (HVSr) tests.

This report will first present additional background on induced seismicity, differences between induced and tectonic ground motions, and the applicability of existing liquefaction triggering models to evaluate the liquefaction hazard from induced earthquakes. Results of the site characterization for the Pawnee earthquake will then be presented. Next, the procedures used to develop the new liquefaction triggering

model for induced seismicity will be described, and the proposed model will be presented. Finally, the results of the model validation and conclusions drawn from this study will be discussed.

2 Background

2.1 Induced Seismicity

Induced seismicity refers to seismic events caused by human activity. Human activities that may induce earthquakes include fracking, oil and gas extraction, wastewater injection, carbon capture and storage, and reservoir filling. These activities cause changes in pore pressures and stresses on existing faults, which can lead to fault rupture (Ellsworth 2013; Foulger et al. 2018). Wastewater injection affects pore pressures and stresses in several ways including (Rubinstein and Mahani 2015):

1. Injection pressure raises pore pressure within a fault.
2. Injection of fluids fills and compresses fluids within pore spaces causing deformation.
3. Injection of fluid colder than the rock causes thermo-elastic deformation.
4. Injected fluid adds mass to the formation in which the fluid is injected.

Several studies have indicated that most faults in the earth's crust are nearly critically stressed (e.g., Foulger et al. 2018; Zoback and Zoback 1980). This suggests that even minor changes to pore pressures, confining stress, or shear stresses resulting from human activity can lead to fault rupture (Foulger et al. 2018).

Ruptures triggered by anthropogenic activities can lead to the release of both induced stresses and pre-existing tectonic stresses. Thus, the seismic energy released during induced events can be significantly larger than that due to the induced stress changes themselves (McGarr et al. 2002). This led Mitchell and Green (2017) to distinguish between “triggered” anthropogenic earthquakes, which primarily release pre-existing tectonic stresses, and “induced” anthropogenic earthquakes, which primarily release induced stresses. In practice, it is difficult to distinguish between the two, and both are generally referred to as “induced” earthquakes (Foulger et al. 2018). This is the convention used herein.

The use of fracking for shale gas development has grown extensively over the last couple of decades. Fracking consists of drilling a hole vertically to up to a few thousand meters deep and then horizontally for a distance up to 3000 m. A mixture of water, chemicals and sand is then pumped under high pressure to hydraulic fracture points successively in stages. Some of the sand, referred to as “proppant,” is retained in the fractured shale joints and cracks to keep them open to facilitate the escape of gas into the well for removal. Several million gallons of water may be required to complete the process for any single well, and

comparable amounts of return wastewater are collected at the well-head and either treated or stored in tanks for reinjection into wastewater disposal wells.

The volume of wastewater injected into a single disposal well is typically many times greater than the volume of water used in a fracking well. Large volumes of wastewater produced by fracking, as well as wastewater from other oil and gas production processes, mining, and industrial operations are injected into the subsurface through disposal wells. The US currently has approximately 150,000 Class II disposal wells (i.e., disposal wells for wastewater from oil and gas production). The rates of fluid injection range from about 100 barrels to more than 100 million barrels per month. Increasing numbers of felt induced seismic events are being reported as either caused by or likely related to these wells.

Although fracking itself generally results in small earthquakes, wastewater injection has led to over nine $M \geq 4.8$ events in Oklahoma including the $M_w 5.8$ 2016 Pawnee, OK earthquake, which was the strongest recorded earthquake in Oklahoma history and is one of the largest recorded earthquakes in the CEUS in the last 70 years (Tiwari and Rathje 2018). Wastewater injection in Oklahoma and surrounding areas has led to a dramatic increase in seismicity over the last decade. This is illustrated in Figure 1, which shows a cumulative count of $M3+$ earthquakes in the CEUS since 1973. While the rate of $M3+$ earthquakes was fairly constant between 1973 and 2009, the rate of $M3+$ earthquakes dramatically spiked after 2009, particularly in areas where wastewater injection is most prevalent. As noted above, regulations enacted to limit wastewater injection volumes in Oklahoma have led to reductions in regional seismicity, but the rate of $M3+$ earthquakes in Oklahoma is still roughly 60 times the natural tectonic rate. Additionally, although the number of $M3+$ earthquakes has been decreasing since 2015, some of the largest events, including the 2016 $M_w 5.8$ Pawnee, OK earthquake, have occurred since that time.

While wastewater injection-induced events are generally centered near injection sites, elevated pore pressures induced by wastewater injection migrate through the subsurface and can trigger events at substantial distances from the injection point. Induced events have been observed up to 90 km from the actual injection site (Peterie et al. 2018). Additionally, as the pressure front migrates away from injection sites, the potential for large earthquakes may increase with time due to greater number of faults affected by the pressure front (Keranen et al. 2014). This can even lead to the reactivation of historically dormant faults (McNamara et al. 2015). Even though injection operations in a given well may cease, elevated pore pressures in the subsurface may remain for years following the end of operations and some of the largest induced events have occurred after operations have ceased (Ellsworth 2013; Johann and Shapiro 2020; Peterie et al. 2018; Pollyea et al. 2019).

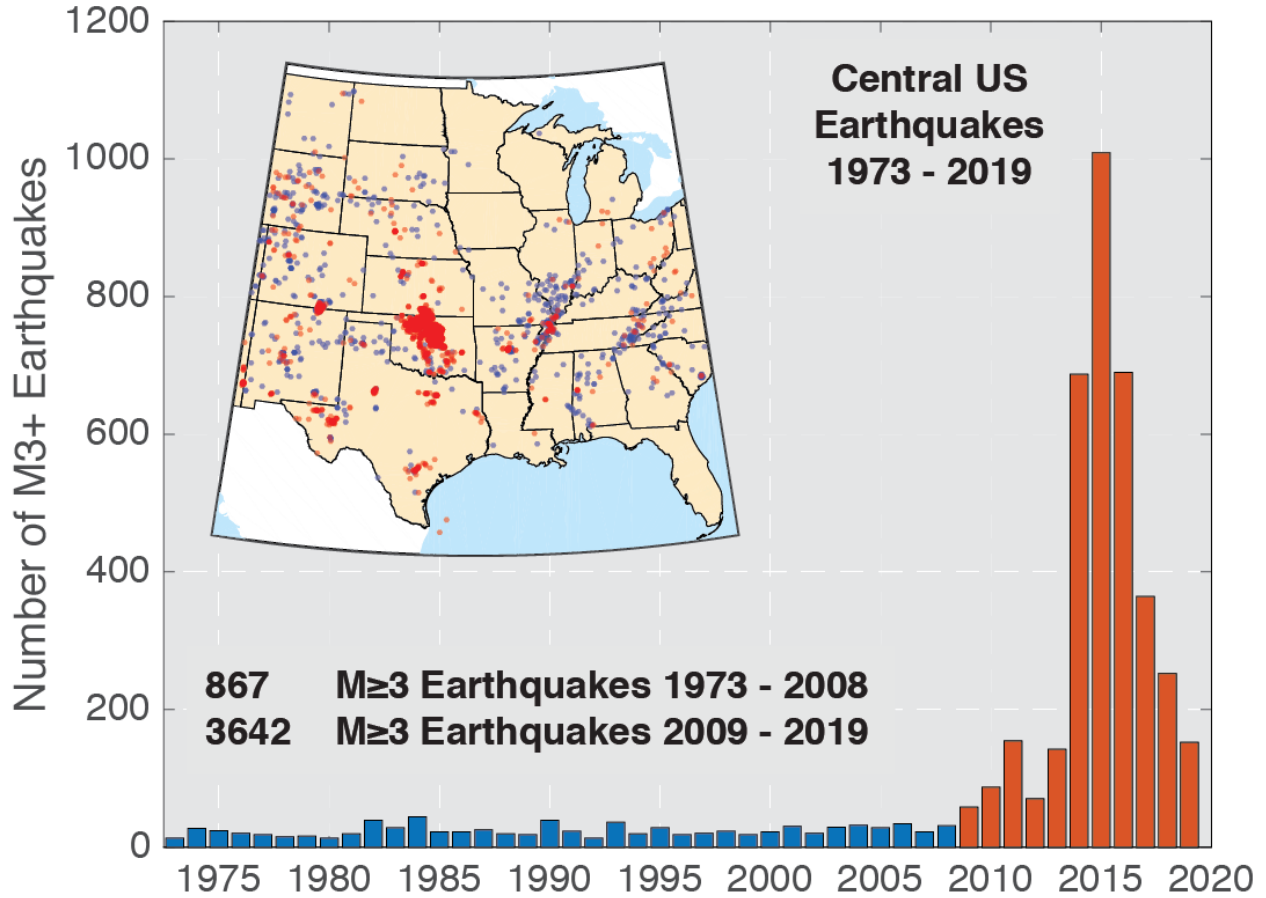


Figure 1. Annual number of earthquakes with a magnitude of 3.0 or larger in the central and eastern United States, 1970–2019. (U.S. Geologic Survey 2020b)

2.2 Differences Between the Ground Motion Characteristics of Induced and Tectonic Earthquakes

Several studies have noted differences between the ground motion characteristics of tectonic and induced earthquakes (e.g., Bommer et al. 2016; Hough 2014; Novakovic et al. 2018; Zalachoris and Rathje 2019). However, although various studies have noted these differences, there is some debate over what causes these differences. Several studies have suggested that the stress drops associated with induced events are lower than those of similarly-sized tectonic earthquakes (e.g., Boyd et al. 2017; Hough 2014; Sumy et al. 2017). Other studies have found that there is no significant difference in the observed stress drops for induced versus tectonic events once rupture depth, faulting mechanism, and other factors are taken into account (e.g., Cramer 2017; Huang et al. 2017; Kaski and Atkinson 2017; Wu et al. 2018; Yenier et al. 2017; Zhang et al. 2016). As an example, Huang et al. (2017) found that stress drops for induced earthquakes tend to be lower than the average stress drops for tectonic events in the CEUS. However, they

also found that the stress drops of induced-earthquakes in OK, which are predominantly strike-slip, are, in fact, comparable to the stress drops of tectonic earthquakes occurring in the central US that have similar rupture mechanisms and focal depths. These stress drops are approximately 3 to 6 times less than the stress drops of earthquakes in the eastern US, which predominantly occur on reverse faults. Based on this, Huang et al. (2017) concluded that stress drops of induced and tectonic events are similar if focal depth and faulting mechanism are properly considered. Stress drops of events in Oklahoma, as with CEUS events in general, tend to be higher than for events in the western United States (WUS) (Atkinson 2020; Cramer 2017). However, some studies have noted that for shallow earthquakes (focal depths of ~ 5 km or less), stress drops for CEUS earthquakes are similar to those in the WUS (Atkinson and Assatourians 2017; Cramer 2017). Although stress drops may be similar for induced and tectonic earthquakes with the same focal depth and focal mechanism, induced earthquakes in Oklahoma generally have shallower focal depths than tectonic earthquakes in the CEUS (e.g., Huang et al. 2017; Zalachoris and Rathje 2019). As a result, induced events in Oklahoma tend to have lower stress drops, on average, than tectonic events. Smaller stress drops are generally associated with smaller spectral accelerations (Jeong et al. 2020). However, several studies (e.g., Novakovic et al. 2018; Zalachoris and Rathje 2019) have noted that, for some magnitudes, hypocentral distances (R_{hyp}), and frequencies, induced events in Oklahoma can result in larger spectral accelerations than would be expected for similarly-sized tectonic earthquakes.

Zalachoris and Rathje (2019) and Novakovic et al. (2018) both developed ground motion prediction equations (GMPEs) specific to induced seismicity in Oklahoma, Texas, and Kansas. Novakovic et al. (2018) found that for small events ($M_w \approx 4$) and high frequencies (> 3 Hz), response spectral acceleration (5% damped pseudo-spectral acceleration, PSA) amplitudes for induced events in Oklahoma were similar to those predicted by the Yenier and Atkinson (2015) GMPE for tectonic events in the central and eastern North America (CENA). However, for low frequencies, induced events were found to have higher PSA amplitudes for these smaller events. This was attributed to amplification effects associated with regional geology. Novakovic et al. (2018) found that for higher magnitude events ($M_w \geq 5$), PSA of induced ground motions was larger than predicted for tectonic ground motions, especially at high frequencies. They attribute this to differences in magnitude and depth dependence of the stress parameter. Zalachoris and Rathje (2019) found that for large magnitudes and oscillator periods ($T < 1.0$ s), their model for induced earthquakes tended to predict smaller ground motions than their reference GMPE for the CENA (Hassani and Atkinson 2015). This is consistent with the smaller stress drops of induced earthquakes. However, Zalachoris and Rathje (2019) note that for $R_{\text{hyp}} < 20$ km, spectral accelerations predicted for induced ground motions were larger than those predicted by the CENA model. This was observed at all periods with the largest differences observed for $T \leq 0.1$ s. Zalachoris and Rathje (2019) attribute this to the close proximity of these events to the ground surface. The close proximity of the rupture plane to the ground surface tends

to offset the lower stress drops, resulting in more intense shaking in the epicentral region but more rapid attenuation with lateral distance than shaking from tectonic events or deeper induced events (Atkinson 2020; Zalachoris and Rathje 2019).

Zalachoris and Rathje (2019) also found that ground motion amplification for time-averaged small-strain shear wave velocity of the upper 30 m (V_{s30}) values less than 600 m/s is lower in Oklahoma than predicted by the Hassani and Atkinson (2015) GMPE. They attribute this weaker scaling with V_{s30} to the generally moderate soil depths at sites in Texas, Oklahoma, and Kansas (Zalachoris et al. 2017), which leads to weaker V_{s30} scaling, even at sites with small V_{s30} . Similarly, Novakovic et al. (2018) observed that average site amplification relative to National Earthquake Hazards Reduction Program (NEHRP) B/C site conditions ($V_{s30} = 760$ m/s) (American Society of Civil Engineers 2010) was close to zero for the sites used in their study. However, they found that individual sites still exhibited peak amplifications greater than a factor of 2 at certain frequencies, particularly in the 2-8 Hz frequency range.

Several of the differences noted above are illustrated in Figure 2. This figure shows 5% damped PSA for the Zalachoris and Rathje (2019) and Novakovic et al. (2018) GMPEs for induced earthquakes in Oklahoma, the Hassani and Atkinson (2015) GMPE for tectonic events in the CEUS, and the Boore et al. (2014) GMPE for tectonic events in the WUS. Spectra are shown for M_w 4, 5, and 5.8, R_{hyp} of 5 and 30 km, and $V_{s30} = 760$ m/s. The Novakovic et al. (2018) GMPE was implemented using the depth-dependent stress drop model based on the median focal depth of induced earthquakes in Oklahoma (~5 km). Updated model coefficients were used as presented in the paper erratum (Novakovic et al. 2020). As shown in Figure 2, for small R_{hyp} and M_w 4.5 and M_w 5, spectral accelerations are higher for induced earthquakes than for tectonic earthquakes across all periods. This difference is much smaller for M_w 5.8, with the Zalachoris and Rathje (2019) GMPE actually predicting slightly smaller ground motions than the Hassani and Atkinson (2015) GMPE for $T < 0.1$ s. For $R_{hyp} = 30$ km, induced earthquake ground motions tend to exhibit similar or smaller spectral accelerations than tectonic earthquakes in the CEUS at all magnitudes and periods. This effect is more pronounced for the Zalachoris and Rathje (2019) GMPE. Although it predicts lower spectral accelerations for $M_w > 5$ and $T < 0.1$ s, the Novakovic et al. (2018) GMPE still predicts slightly higher spectral accelerations than the Hassani and Atkinson (2015) GMPE for $T > 0.1$ s. For both $R_{hyp} = 10$ km and $R_{hyp} = 30$ km, spectral accelerations for both induced and tectonic ground motions in the CEUS tend to exceed WUS values predicted by the Boore et al. (2014) GMPE. This difference is particularly pronounced for small R_{hyp} , smaller magnitudes, and shorter periods ($T \lesssim 0.2$ s).

Figure 3 provides a comparison of site amplification scaling with V_{s30} for the Zalachoris and Rathje (2019) and Hassani and Atkinson (2015) GMPEs. As noted by Zalachoris and Rathje (2019), spectral accelerations for induced events in Oklahoma do not scale as strongly with V_{s30} as predicted for CENA tectonic events

by Hassani and Atkinson (2015). As shown in Figure 3, spectral accelerations for induced ground motions tend to be similar for $V_{s30} = 200$ m/s and 760 m/s, while spectral accelerations for tectonic ground motions increased with decreasing V_{s30} . These trends are generally consistent for all periods and magnitudes shown. However, some stronger scaling was observed for $M_w = 5.8$ and $T = 0.05$ to 0.5 s with smaller spectral accelerations observed for $V_{s30} = 200$ m/s.

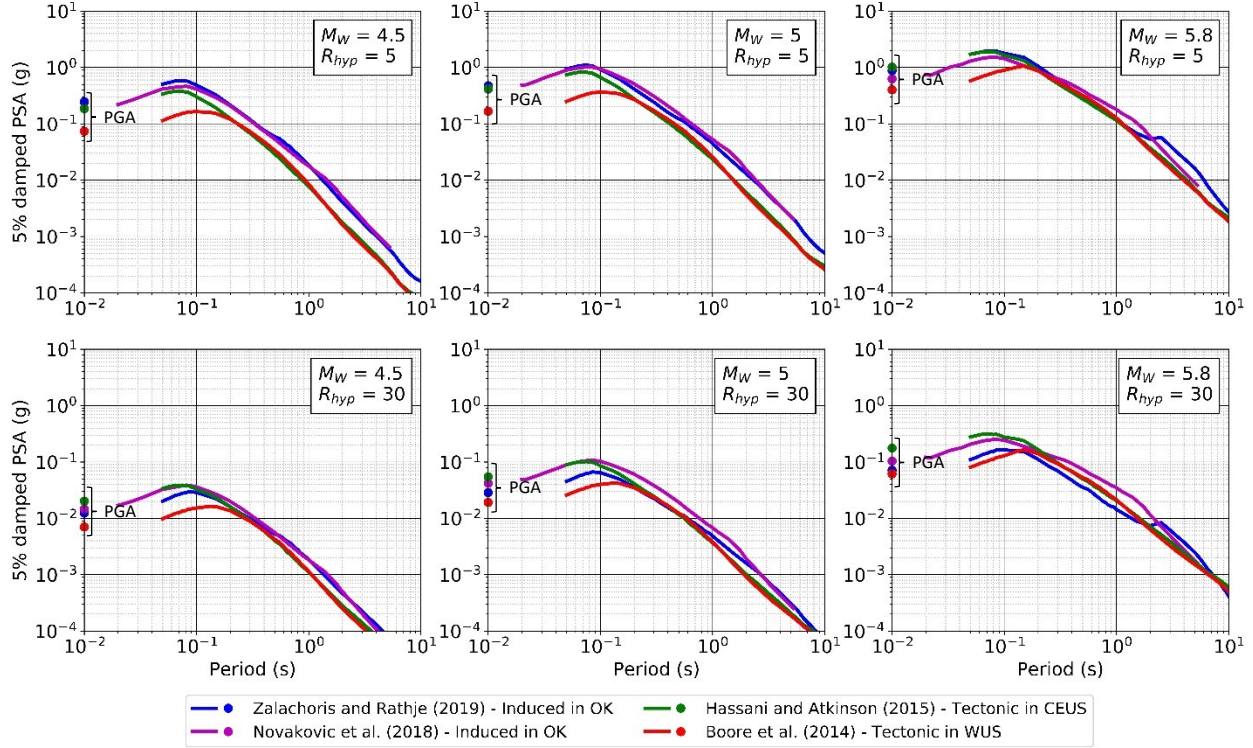


Figure 2. 5% damped PSA for M_w 4, 5, and 5.8, R_{hyp} of 5 and 30 km, and $V_{s30} = 760$ m/s based on the Zalachoris and Rathje (2019) and Novakovic et al. (2018) GMPEs for induced earthquakes in Oklahoma, the Hassani and Atkinson (2015) GMPE for tectonic events in the CEUS, and the Boore et al. (2014) GMPE for tectonic events in the WUS.

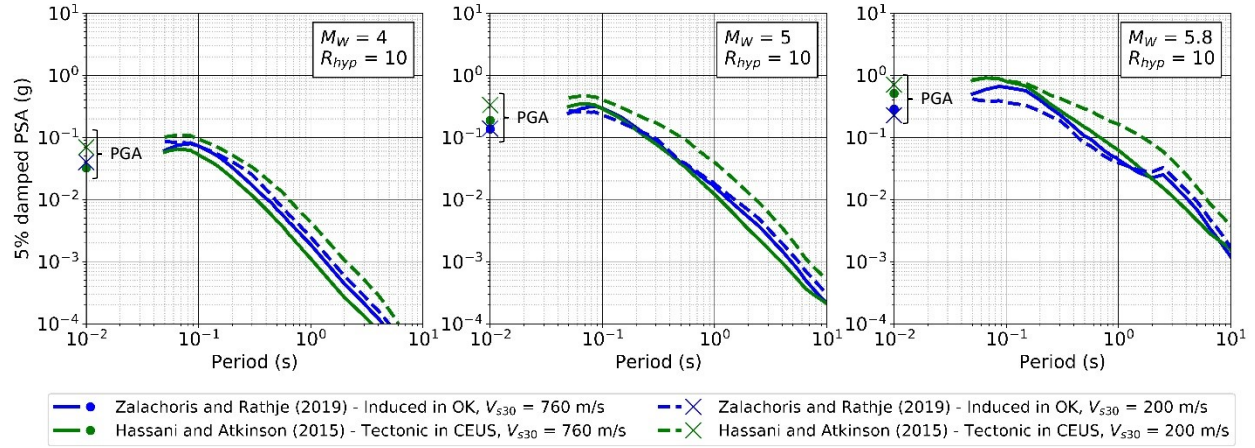


Figure 3. Comparison of V_{s30} scaling for Zalachoris and Rathje (2019) GMPE for induced earthquakes in OK and Hassani and Atkinson (2015) GMPE for tectonic events in the CEUS for M_w 4, 5, and 5.8, R_{hyp} of 10 km, and V_{s30} of 200 m/s and 760 m/s.

In addition to differences in spectral accelerations, there may be differences in the duration of shaking of induced versus tectonic events which may impact liquefaction triggering. Oklahoma and the CEUS generally are considered stable continental tectonic regimes while the WUS is considered an active crustal regime. As noted previously, most liquefaction evaluation methods (e.g., Boulanger and Idriss 2014) were developed primarily for active shallow-crustal earthquakes. Boore and Thompson (2015) found that ground motion duration increases with distance at a much faster rate in stable continental regions than in active crustal regions. This is illustrated by Figure 4, which presents path duration models for western North America (WNA) (Boore and Thompson 2014) and eastern North America (ENA) (Boore and Thompson 2015). In the Boore and Thompson (2014, 2015) ground motion duration models, 5 to 95% significant duration (t_{5-95}) is computed by adding path duration, determined from the relationships plotted Figure 4, to source duration, which is a function of corner frequency. Although there are differences in source duration between ENA and WNA, for the small magnitude events relevant to induced events in Oklahoma, the path duration term is much longer than the source duration term (Boore and Thompson 2015). As a result, the trends shown in Figure 4 likely reflect the overall trends between t_{5-95} and source distance for events in the ENA and WNA.

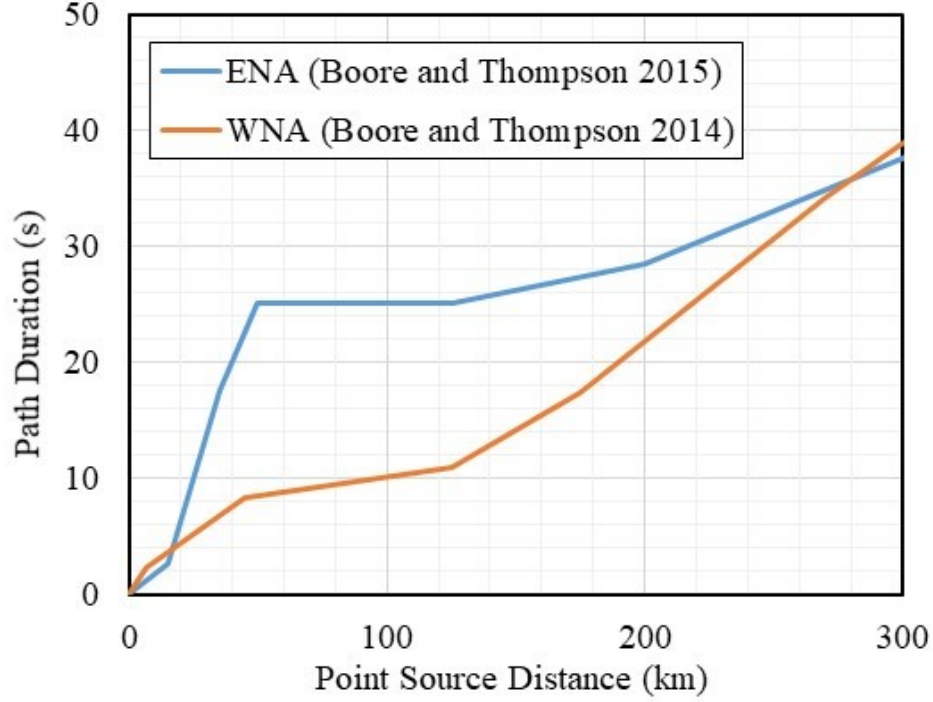


Figure 4. Path duration vs. point source distance for ENA (Boore and Thompson 2015) and WNA (Boore and Thompson 2014) ground motions.

Because of differences in spectral amplitude and ground motion duration between induced events in Oklahoma and tectonic events in the CEUS and WUS, it is likely that the damage potential of these events will differ. As a result, liquefaction evaluation procedures developed for tectonic earthquakes, particularly tectonic earthquakes in active crustal regions, may not be suitable for evaluating the liquefaction triggering potential from induced earthquakes.

2.3 Existing Liquefaction Triggering Models and Their Applicability to Induced Seismicity

Several methods exist for evaluating liquefaction triggering in soils due to tectonic ground motions. The most commonly used approach is the stress-based “simplified” liquefaction evaluation procedure (Whitman 1971; Seed and Idriss 1971). This method evaluates liquefaction triggering in a soil by comparing the imposed seismic demand in terms of the cyclic stress ratio (CSR) to the liquefaction resistance of the soil to cyclic stresses in terms of the cyclic resistance ratio (CRR). The CSR is the average cyclic shear stress imposed on the soil at a given depth normalized by the initial vertical effective stress at that depth. The CSR at a given depth is calculated as:

$$CSR = \frac{\tau_{avg}}{\sigma'_{v0}} = 0.65 \frac{a_{max}}{g} \frac{\sigma_v}{\sigma'_{v0}} r_d \quad (1)$$

where τ_{avg} is average shear stress at a given depth in a soil profile, σ_v and σ'_{v0} are the total and initial vertical effective stresses at a given depth in a soil profile, a_{max} is the peak ground acceleration at the ground surface, g is the acceleration of gravity in the same units as a_{max} , and r_d is a dimensionless stress reduction factor that accounts for the non-rigid response of the soil column. The value 0.65 is an arbitrary value defining the ratio of τ_{avg} to τ_{max} , the maximum shear stress imposed by the cyclic loading, (i.e., $\tau_{avg} = 0.65 \cdot \tau_{max}$). To account for the effects of shaking duration, initial effective overburden stress, and initial static shear stresses, additional factors are applied to calculate CSR^* , which is the CSR normalized to the motion duration of a $M_w 7.5$ event, 1 atm initial effective overburden stress, and level ground surface conditions. CSR^* is calculated as:

$$CSR^* = \frac{CSR}{MSF \cdot K_\sigma \cdot K_\alpha} = 0.65 \frac{a_{max}}{g} \frac{\sigma_v}{\sigma'_{v0}} r_d \frac{1}{MSF \cdot K_\sigma \cdot K_\alpha} \quad (2)$$

where MSF is a magnitude scaling factor that adjusts CSR for shaking duration based on a reference $M_w 7.5$ event, K_σ is a correction factor for initial vertical effective overburden stress using a reference initial effective overburden stress is 1 atm, and K_α is a correction factor for initial horizontal static shear stress using a reference initial static shear stress of zero (e.g., level ground conditions).

To develop curves for the cyclic resistance of soil, case histories were compiled from post-earthquake investigations and categorized as either “liquefaction” or “no liquefaction” based on whether evidence of liquefaction was observed. CSR^* for each case history was plotted as a function of the corresponding normalized in-situ test metric, e.g.: normalized blow count ($N_{1,60cs}$) from standard penetration tests (SPTs); normalized tip resistance (q_{c1Ncs}) from cone penetration tests (CPTs); or normalized small-strain shear wave velocity (V_{s1}) from shear wave velocity (V_s) tests. Once plotted, the “liquefaction” and “no liquefaction” case histories tend to lie in two different regions of the graph. The approximate boundary separating these regions is referred to as the normalized cyclic resistance ratio ($CRR_{M7.5}$). This represents the resistance of the soil to liquefaction triggering during an $M_w 7.5$ event under level ground surface conditions and an initial vertical effective stress of 1 atm. This boundary is represented as a function of the selected normalized in-situ test metric as depicted in Figure 5. As shown in this figure, liquefaction is predicted to trigger when CSR^* exceeds the $CRR_{M7.5}$ for a given value of normalized in-situ test metric.

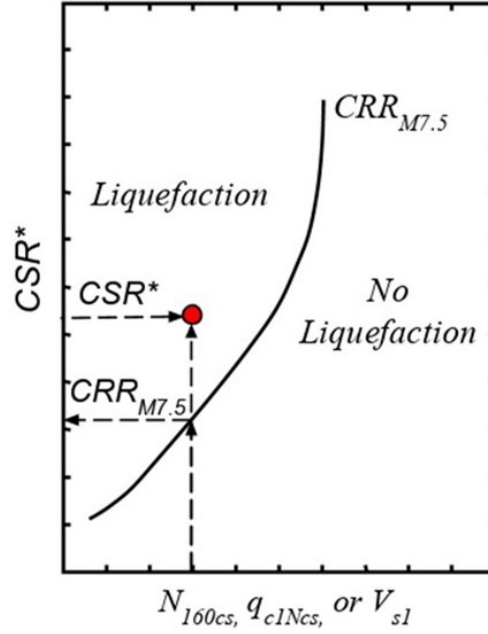


Figure 5. Illustration of normalized Cyclic Resistance Ratio ($CRR_{M7.5}$) curve

Once $CRR_{M7.5}$ and CSR^* have been determined for a given soil profile and ground motion, the factor of safety against liquefaction (FS_{liq}) can be computed as:

$$FS_{liq} = \frac{CRR_{M7.5}}{CSR^*} \quad (3)$$

Within the framework of the simplified procedure, $CRR_{M7.5}$ is assumed to be an inherent property of the soil and state, and independent of shaking characteristics, while CSR^* is a function of ground motion characteristics. For this reason, $CRR_{M7.5}$ curves developed using case histories from tectonic earthquakes are suitable for use when estimating FS_{liq} for induced events. However, due to differences in ground motion characteristics, relationships used to calculate CSR^* for tectonic ground motions, specifically r_d and MSF , may not be suitable for use with induced earthquake ground motions (Green et al. 2019, 2020). Several of these differences were discussed in the previous section, although others may exist. Induced earthquakes also tend to have smaller magnitudes than the typical range of magnitudes considered during liquefaction evaluations for tectonic earthquakes. As a result, using existing liquefaction evaluation methods to evaluate liquefaction potential for induced earthquakes typically requires extrapolation to smaller magnitudes which introduces additional uncertainties. Although CSR^* represents seismic demand, some factors used to compute CSR^* , including r_d and MSF , are influenced by site profile characteristics and profile's response to shaking. For this reason, relationships for these factors developed in other regions, such as California,

may not be applicable to the regions primarily affected by induced seismicity, such as Oklahoma. Primarily, site profiles in Oklahoma (and in the CEUS in general) typically have higher bedrock shear wave velocities and larger impedance contrasts between bedrock and the overlying soil profiles than profiles in the WUS, both of which influence site response. Lasley et al. (2016, 2017) note that impedance contrast has a significant influence on both r_d and MSF. Accordingly, the r_d and MSF relationships developed for use in existing simplified liquefaction triggering models may not be suitable for estimating CSR* for induced earthquakes. The following sections provide additional discussion about existing r_d and MSF relationships and their applicability for evaluating the liquefaction hazard of induced earthquakes.

2.3.1 Stress Reduction Factor, r_d

The stress reduction factor, r_d , is an empirical factor that accounts for the non-rigid response of the soil profile to seismic shaking. The factor, r_d , is defined as the ratio between the peak shear stress at the base of a flexible soil column subjected to a seismic shaking and the peak shear stress at the base of a rigid soil column having the same length subjected to the same shaking. The value of r_d generally ranges from 0 to 1 (typically assumed to be 1 at the ground surface), with $r_d = 1$ at all depths corresponding to rigid profile response. This factor allows for computation of induced shear stresses at any point in a soil column without needing to perform a full numerical site response analysis. Instead, shear stress at a given depth is calculated using Newton's second law assuming a rigid soil column, and then the resulting shear stress is multiplied by r_d to estimate the actual shear stress imposed at that depth (i.e., Equation 1).

Several relationships for estimating r_d are commonly used in practice, including Liao and Whitman (1986), where r_d is solely a function of depth, and Idriss (1999), where r_d is a function of both earthquake magnitude and depth. Cetin (2000) proposed two additional variants using ground motions and site profiles from the WUS, in which r_d is a function of M_w , a_{max} , depth, and the time-weighted average small-strain shear wave velocity of the upper 12 m of the soil profile (V_{s12}), when available. Lasley et al. (2016) developed updated r_d relationships for the WUS using the site profiles compiled by Cetin (2000) and a larger set of recorded ground motions. Lasley et al. (2016) also developed representative site profiles for the CEUS by modifying the Cetin (2000) WUS site profiles to account for the higher bedrock shear wave velocities in the CEUS. Using these profiles and CEUS ground motions compiled by McGuire et al. (2001), Lasley et al. (2016) developed a second set of r_d relationships for the CEUS. Lasley et al. (2016) developed r_d relationships for both active (e.g., the WUS) and stable continental (e.g., the CEUS) shallow crustal tectonic regimes to account for differences between the two regions in both ground motion characteristics and geologic profiles, both of which affect r_d . They found that r_d values, although similar between the two regions, tended to be lower in the CEUS than the WUS. Lasley et al. (2016) developed two forms of the r_d relationship for each

regime, one that could be used if shear wave velocity information is available and one that could be used if this information is not available. In each case, the equation for r_d takes the functional form:

$$r_d = (1 - \alpha) \exp\left(\frac{-z}{\beta}\right) + \alpha \quad (4)$$

where α is the limiting value of r_d at large depths and can range from 0 to 1, β controls the curvature of the function at shallow depths, and z is depth in meters. The term $(1 - \alpha)$ scales the exponential so that r_d is 1 at the ground surface. Both α and β are functions of magnitude and V_{s12} , when available.

Green et al. (2020) used the approach presented in Lasley et al. (2016) to develop an r_d relationship specific to induced seismic events in the Groningen region of the Netherlands. They used a functional form based upon a sigmoidal shape with the primary variable being logarithmic depth as given by the following equation:

$$r_{d-Gron} = 1 - \frac{A_{rd}}{1 + \exp\left[-\frac{\ln(z) - (\beta_2 + \beta_6 \cdot M_w)}{(\beta_3 + \beta_7 \cdot M_w)}\right]}; \quad 0 \leq r_d \leq 1 \quad (5)$$

where β_i are regression coefficients and A_{rd} represents the asymptotic level of r_{d-Gron} at depth. A_{rd} is a function of M_w , a_{max} , and V_{s12} .

For each relationship cited above, r_d tends to increase with magnitude, leading to more rigid response of the soil profile. This is because soil profiles tend to exhibit more rigid response if the characteristic wavelength of the earthquake loading is significantly longer than the height of the profile (Green et al. 2020). As a result, for larger magnitude events which tend to have longer characteristic periods and, hence, longer wavelengths (e.g., Green et al. 2011), the soil column acts more rigidly. For this reason, magnitude, and the associated frequency content of the ground motions, has a strong influence on r_d . Green et al. (2020) note that, for this reason, the Idriss (1999) r_d relationship, which was developed for moderate to major tectonic events with $5 < M_w < 8$ may be inappropriate for use with evaluating the liquefaction potential for induced earthquakes, which tend to have much smaller magnitudes (e.g., $M_w \leq 5.8$ in Oklahoma).

As an example of how the available r_d relationships vary, Figure 6 shows r_d curves based on the Idriss (1999), Lasley et al. (2016) CEUS, and Green et al. (2020) r_d relationships for magnitudes of 4.0, 5.5, and 7 and V_{s12} values of 135 m/s and 200 m/s. As shown in this figure, r_d estimates are similar for these relationships for large magnitude events, but they diverge significantly for small-to-moderate magnitude events. Although the discrepancies are somewhat smaller for stiffer soils (e.g., V_{s12} of 200 m/s), there are still significant differences in the r_d values estimated by these methods, particularly for smaller magnitudes. These differences highlight the effect that ground motion characteristics and regional geology can have on

r_d because the relationships shown were developed for the WUS (Idriss 1999; Lasley et al. 2016), CEUS (Lasley et al. 2016), and Groningen, Netherlands (Green et al. (2020)). For this reason, it is doubtful whether available r_d relationships developed for tectonic earthquakes or for different geologic settings are suitable for evaluating liquefaction potential due to induced earthquakes in Oklahoma, Texas, and Kansas. To address these issues, a new induced seismicity-specific r_d relationship is regressed as part of this study.

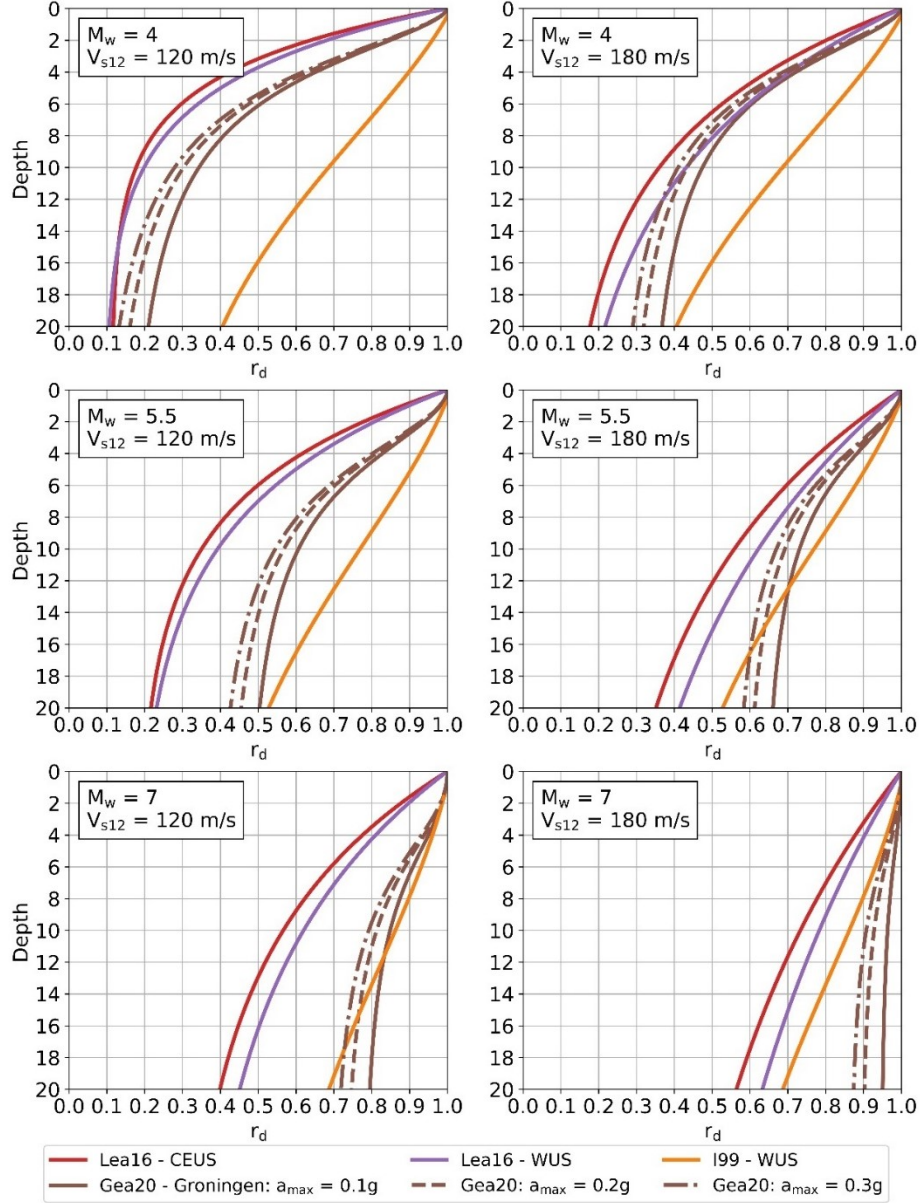


Figure 6. Comparison of r_d relationships proposed by Idriss (1999) (I99), Lasley et al. (2016) (Lea16), and Green et al. (2020) (Gea20). Relationships are shown for $M_w = 4, 5.5$, and 7.0 and for $V_{s12} = 135$ and 200 m/s. Additionally, because Gea20 is a function of a_{max} , curves for $a_{max} = 0.1, 0.2$, and 0.3 g are shown.

2.3.2 Magnitude Scaling Factor, MSF

Magnitude scaling factors are used to adjust CSR for the influence of shaking duration on liquefaction triggering. In general, as ground motion duration increases, the seismic demand on the soil increases and liquefaction is more likely to occur. This effect is modeled in the simplified procedure using MSF, which is inversely related to ground motion duration. For historical reasons, CSR is normalized to a magnitude of 7.5 and MSF is calculated as:

$$MSF = \left(\frac{n_{eq\ M7.5}}{n_{eq\ M}} \right)^b \quad (6)$$

where $n_{eq\ M7.5}$ is number of equivalent stress cycles (n_{eq}) for an $M_w 7.5$ event, $n_{eq\ M}$ is the value of n_{eq} for an event of magnitude, M_w , and b is the negative slope of the CSR vs. number of cycles to trigger liquefaction (N_{liq}) curve, both in log scale. The equivalent cycles concept converts a given earthquake loading to an equivalently damaging number of uniform cycles (e.g., Lasley et al. 2017). For liquefaction evaluations, the most commonly used method for computing n_{eq} is the Seed et al. (1975) variant of the Palmgren-Miner (P-M) fatigue theory (Miner 1945; Palmgren 1924). In this method, a normalized CSR vs. N_{liq} curve is developed from laboratory testing. The curve is used to relate the “damage” induced in a soil sample from a pulse having one amplitude to that having a different amplitude. Using this normalized CSR vs. N_{liq} curve as a weighting function, n_{eq} is computed as the weighted average of the individual peaks within a given acceleration time history. In this method, peaks with amplitude less than $0.3 \cdot a_{max}$ are excluded because their contribution to liquefaction triggering is considered negligible. Both Lasley et al. (2017) and (Green et al. 2019) point out shortcomings of this approach to calculating n_{eq} . These include issues related to assuming that the both n_{eq} and its uncertainty are constant with depth, use of a relative amplitude criterion to exclude pulses in the acceleration time history, handling of multi-directional shaking, and failure to account for the negative correlation between amplitude and duration of earthquake ground motions (e.g., Bradley 2011).

To address these issues, Lasley et al. (2017) developed new n_{eq} correlations based on the alternative implementation of the P-M theory proposed by Green and Terri (2005), which uses dissipated energy as the damage metric in order to better account for nonlinear response of the soil and to account for multidirectional shaking. Dissipated energy is used because it has been shown to correlate well with excess pore pressure generation in saturated cohesionless soil samples subjected to undrained cyclic loading (Green et al. 2000). In the approach proposed by Green and Terri (2005), stress and strain time histories are obtained at various depths in a soil profile using a numerical site response analysis. Cumulative dissipated energy per unit volume is computed by integrating the variation in shear stress over shear strain, and the

value of n_{eq} is then calculated by dividing the cumulative dissipative energy for the entire motion by the energy dissipated in one equivalent cycle. Multidirectional shaking is accounted for by performing separate site response analyses for each horizontal component of the input ground motion, adding the energy dissipated at the respective depths for each component of motion, and setting the amplitude of the equivalent cycle as 0.65 times the geometric mean of the maximum shear stresses experienced at a given depth. This method for handling multidirectional shaking is referred to in Lasley et al. (2017) as Approach 2. Lasley et al. (2017) also regressed n_{eq} relationships using individual horizontal components of motion. This is referred to in their paper as Approach 1 and is used in this study, as discussed in Section 4.5. Lasley et al. (2017) developed the following n_{eq} relationship:

$$\ln(n_{eq}) = a_1 + a_2 \ln\left(\frac{a_{max}}{g}\right) + a_3 M_w + \delta_{event} + \delta_{profile} + \delta_0 \quad (7)$$

where a_1 - a_3 are regression coefficients, δ_{event} and $\delta_{profile}$ are random effects terms corresponding to the average event residual and the average profile residual, respectively, and δ_0 is a residual term. Lasley et al. (2017) used the same motions and site profiles to develop their n_{eq} relationships for both the WUS and CEUS that were used by Lasley et al. (2016) to develop their r_d relationship. Lasley et al. (2017) point out that the n_{eq} relationship developed for the WUS is likely applicable for use in active shallow crustal tectonic regimes worldwide because the site profiles used were selected to be representative of profiles in the liquefaction database, which are taken from around the world. In contrast, Lasley et al. (2017) note that the n_{eq} relationship for the CEUS is likely restricted to stable continental tectonic regimes with impedance contrasts between bedrock and soil similar to the profiles used in their regression.

Green et al. (2020) followed Approach 1 from Lasley et al. (2017) to develop an n_{eq} relationship for induced events in the Groningen gas field ($n_{eqM-Gron}$). Green et al. (2020) used a slightly modified form of the Lasley et al. (2017) relationship that accounts for V_{s12} and a break in scaling above an a_{max} of 0.3g. The resulting relationship is:

$$\ln[n_{eqM-Gron}(M, a_{max}, V_{s12})] = a_1 + a_2 \cdot \ln(a_{max}) + a_4 \cdot M + a_5 \cdot V_{s12}; \text{ for } a_{max} \leq 0.3 \text{ g} \quad (8a)$$

$$= a_1 + a_2 \cdot \ln(a_{max}) + a_3 \cdot \ln\left(\frac{a_{max}}{0.3}\right) + a_4 \cdot M + a_5 \cdot V_{s12}; \text{ for } a_{max} > 0.3 \text{ g} \quad (8b)$$

where a_{max} is in units of g, V_{s12} is in units of m/s, and α_i are regression coefficients.

Idriss and Boulanger (2008) and Boulanger and Idriss (2014) are two commonly used liquefaction evaluation procedures which use the Seed et al. (1975) approach to determine n_{eq} and then estimate MSF using b -values derived from laboratory testing. Idriss and Boulanger (2008) use a constant b -value of 0.34 for clean sands, while Boulanger and Idriss (2014) use a b -value that is a function of soil state, represented

by q_{c1Ncs} or $N_{1,60cs}$. Ulmer et al. (2018) point out that the b -values used in Boulanger and Idriss (2014) were derived from several different laboratory studies performed on various soils, and it is uncertain whether a consistent definition of liquefaction was used in interpreting the test data. As a result, they state that the b -values used by Boulanger and Idriss (2014) entail a considerable amount of uncertainty. To address this and other potential issues, Green et al. (2017) developed new MSF relationships for the WUS and CEUS based on the Lasley et al. (2017) n_{eq} models. As an alternative to the approaches used by Idriss and Boulanger (2008) and Boulanger and Idriss (2014) and to be consistent with the shear modulus and damping degradation curves used in the equivalent-linear site response analysis to develop the associated r_d and n_{eq} relationships, Green et al. (2017) computed b -values for a range of confining stress-soil density combinations using the Darendeli and Stokoe (2001) shear modulus reduction and damping degradation (MRD) curves, with the resulting b -values ranging from 0.33 to 0.35. In the majority of cases, $b = 0.34$, so Green et al. (2017) used this value to compute MSF.

As mentioned previously, $n_{eq M7.5}$ is the value of n_{eq} for an $M_w 7.5$ earthquake. Green et al. (2017) computed an average value for $n_{eq M7.5}$ using Equation (7 for $M_w = 7.5$ and $a_{max7.5} = 0.35g$, where $a_{max7.5}$ was the average a_{max} value for the 116 case histories used in their study that fell within the range of $M_w 7.4$ and $M_w 7.6$. Using these values, $n_{eq M7.5}$ was computed to be ~ 14 . Based on $n_{eq M7.5} = 14$ and $b = 0.34$, the final MSF relationship proposed by Green et al. (2017) is:

$$MSF = \left(\frac{14}{n_{eq}(M_w, a_{max})} \right)^{0.34} \leq 2.02 \quad (9)$$

where $n_{eq}(M, a_{max})$ is the n_{eq} for a given magnitude and a_{max} , determined from Equation (7). The upper limit on MSF corresponds to a scenario where the earthquake motion consists of a single shear stress pulse in one of the horizontal components of motion. Green et al. (2020) used a similar approach to develop an MSF relationship for the induced seismicity in the Groningen gas field based on $n_{eqM-Gron}$. However, because single component motions generated using a seismic source model were used in developing the Green et al. (2020) $n_{eqM-Gron}$ relationship, $n_{eq M7.5} = 7.25$ was used as opposed to $n_{eq M7.5} = 14$, which was developed by Green et al. (2017) using both horizontal components of motions. Note, $n_{eq M7.5} = 7.25$ is n_{eq} for an $M_w 7.5$ event and $a_{max} = 0.35g$ computed using the Lasley et al. (2017) n_{eq} relationship for individual components of motion (i.e., Approach 1) in active shallow-crustal tectonic regimes. The resulting Green et al. (2020) MSF relationship for the Groningen gas field is:

$$MSF_{Gron} = \left(\frac{7.25}{n_{eqM-Gron}(M_w, a_{max})} \right)^{0.34} \leq 2.04 \quad (10)$$

Figure 7 shows several existing MSF relationships including the Boulanger and Idriss (2014), Green et al. (2017), and Green et al. (2020) relationships discussed above. Green et al. (2017) MSF curves are shown for both the Lasley et al. (2017) CEUS and Lasley et al. (2017) WUS n_{eq} relationships. As shown in this figure, MSF values estimated by these relationships are fairly similar for a magnitude range of 6.5 to 7.75, the range in which most events in the liquefaction case history database lie. However, MSF predictions diverge widely below magnitude 6, which is the range of most interest for induced seismicity in Oklahoma where the largest recorded event was the M_w 5.8 2016 Pawnee, OK earthquake. For magnitudes less than 6, estimated MSF values based on the relationships shown vary by up to a factor of 3, which can have a significant impact when estimating CSR*.

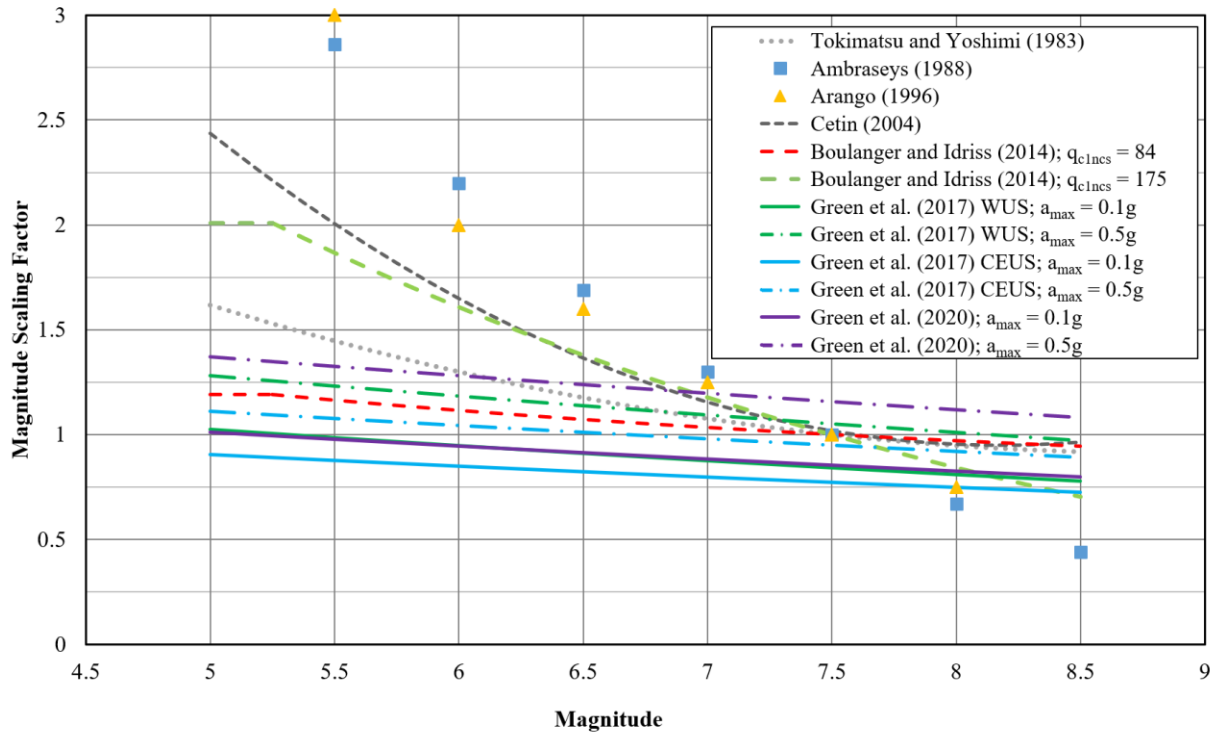


Figure 7. MSF relationships proposed by various studies.

Much of the variation in MSF at smaller magnitudes is likely the result of the motions used to develop the n_{eq} relations only representing a limited range of magnitudes. Because these relationships were developed primarily from motions from earthquakes with magnitudes greater than 6, the MSF are extrapolated to smaller magnitude events. This can lead to large uncertainties. The relationships proposed by Green et al. (2017) were developed using a larger set of input motions than was used in previous studies and included motions from earthquakes with magnitudes ranging from 4.5 to 7.6. As a result, the Green et al. (2017)

relationship is likely more suitable for use with small-to-moderate magnitude events. Differences noted between the Green et al. (2017) CEUS, Green et al. (2017) WUS, and Green et al. (2020) relationships highlight the influence that regional geology and ground motion characteristics can have on MSF. Although all three relationships were developed using similar approaches, the relationships were developed using regional soil profiles and ground motions, leading to differences in the final regressed MSF relationships. Because regional geology and tectonic setting can have a significant impact on MSF, as with r_d , it is questionable whether available MSF relationships developed for tectonic ground motions or for different geologic settings are suitable for use in evaluating liquefaction potential due to wastewater injection-induced earthquakes in Oklahoma, Texas, and Kansas. This is particularly the case due to large variation in MSF estimates for small-to-moderate magnitudes typical of wastewater injection-induced earthquakes. To address these issues, a new induced seismicity-specific MSF relationship is regressed as part of this study.

3 Site Characterization of Sites Impacted by the 3 September 2016, M_w 5.8 Pawnee, OK, earthquake

The epicenter of the 3 September 2016, M_w 5.8 Pawnee, Oklahoma, earthquake, was located about 15 km northwest of Pawnee, OK. This event was the strongest recorded earthquake in Oklahoma history and is one of the largest recorded earthquakes in the CEUS in the last 70 years (Tiwari and Rathje 2018). The U.S. Geological Survey (USGS) ShakeMap of a_{max} for the Pawnee event is shown in Figure 8 (U.S. Geologic Survey 2016a). Inferred a_{max} values were as high as 0.36g within 5 km of the earthquake epicenter, decreasing to less than 0.06g at a distance of approximately 40 km. In order to provide additional site profiles for use in developing an induced seismicity-specific liquefaction triggering model, detailed site characterizations were performed at several sites that experienced significant shaking during the Pawnee event. Site characterization results were also used as liquefaction and non-liquefaction case histories for validating the new model. The following sections discuss the site selection process, describe the tests performed as part of the site investigations, and present results from the site characterization program.

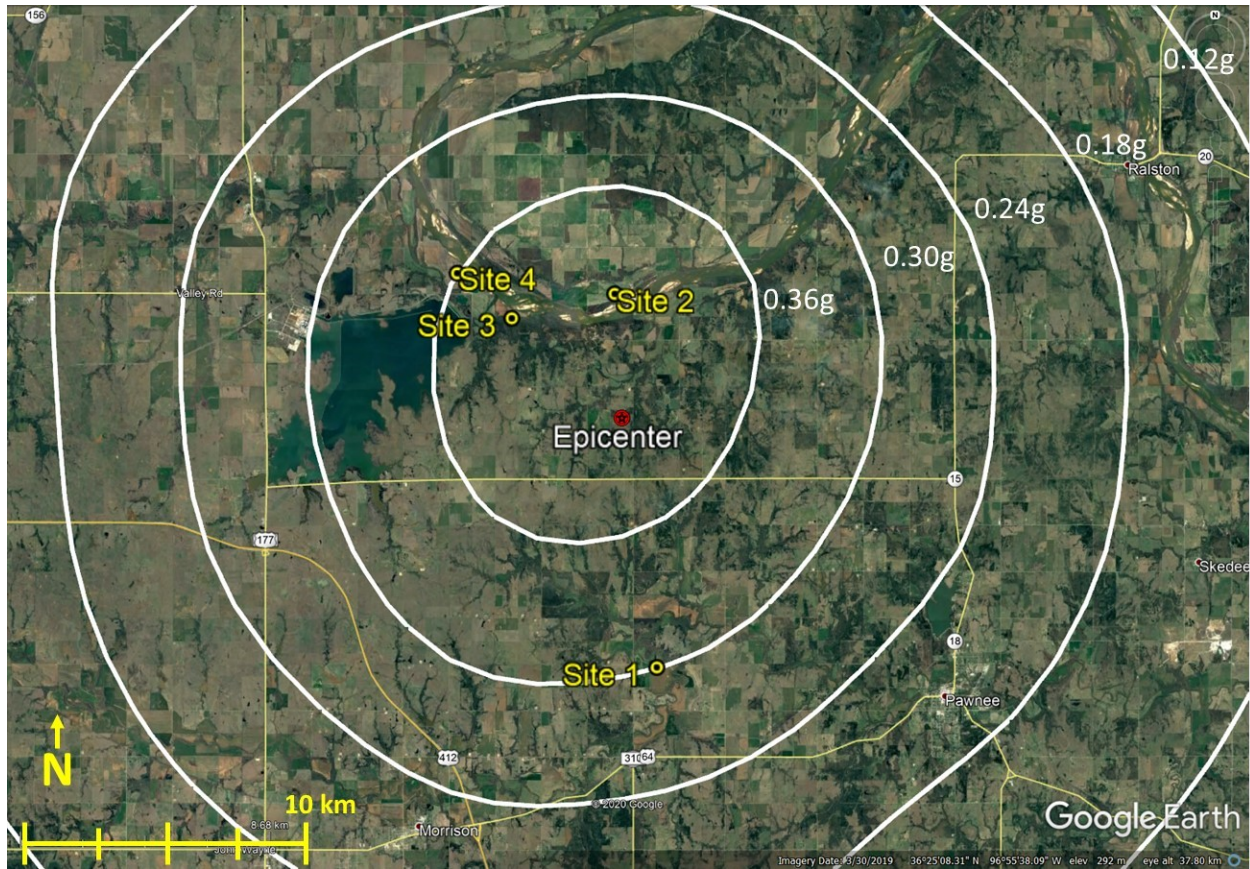


Figure 8. USGS ShakeMap for 2016 M_w 5.8 Pawnee, OK earthquake showing contours of inferred peak ground acceleration. Liquefaction Sites 1, 2, 3, and 4, identified by Clayton et al. (2016) and Kolawole et al. (2017), are also indicated. Aerial imagery source: Google Earth, imagery date 3/30/2019, date accessed 10/7/2020.

3.1 Site Selection and Preliminary Investigations

Post-earthquake reconnaissance performed by Clayton et al. (2016) and Kolawole et al. (2017) following the 2016 Pawnee, Oklahoma earthquake identified four sites where potential liquefaction manifestations were observed and documented. These sites are labeled in Figure 8 as Sites 1 through 4. Site 1 lies along Black Bear Creek, a tributary of the Arkansas River, while Sites 2 through 4 are located within the floodway of the Arkansas River. Examples of the liquefaction manifestations observed at each site are shown in Figure 9 through Figure 12. Liquefaction features at Site 1 included sand boils ranging from a few inches to a few feet in diameter at several locations on the property. Sand boils in the eastern part of the property were aligned and oriented NNE (Clayton et al. 2016). Site 2 included cracks approximately 2 to 5 m long with small amounts of ejecta. Deep cracks extending meters deep near the river at this and the adjacent property were also observed (Jefferson Chang, Personal Communication, 13 July 2018). Manifestations at

Site 3 included cracking and ejecta. Cracks were reported with lengths ranging from 4 to 42 m and widths ranging from 0.5 to 8 cm. Sand ejecta associated with two of the largest cracks covered approximately 145 and 56 m², respectively (Kolawole et al. 2017). Large fractures measuring 0.5-34 cm wide were also observed along the riverbank, possibly associated with lateral spreading (Kolawole et al. 2017). Site 4 was described as potential lateral spreading due to large cracks subparallel to the riverbank. However, Clayton et al. (2016) noted that it could not be confirmed from post-earthquake communication with the property owner whether the cracking and sliding of the riverbank was associated with lateral spreading or a simple slump failure of the riverbank. Conversations with landowners near the selected sites indicated that there were additional locations where liquefaction was observed but not documented. This included the property directly to the west of Site 2, which experienced cracking near the riverbank and sand boils about 1000 m from the riverbank. While these additional sites were not included in the present study, they are evidence that liquefaction was more widespread than suggested by initial post-earthquake reconnaissance.



Figure 9. Photos of liquefaction manifestations at Test Site 1. (Photos courtesy of Dan Ripley)



Figure 10. Photos of liquefaction manifestations at Test Site 2. (Photos courtesy of Rick Rice)

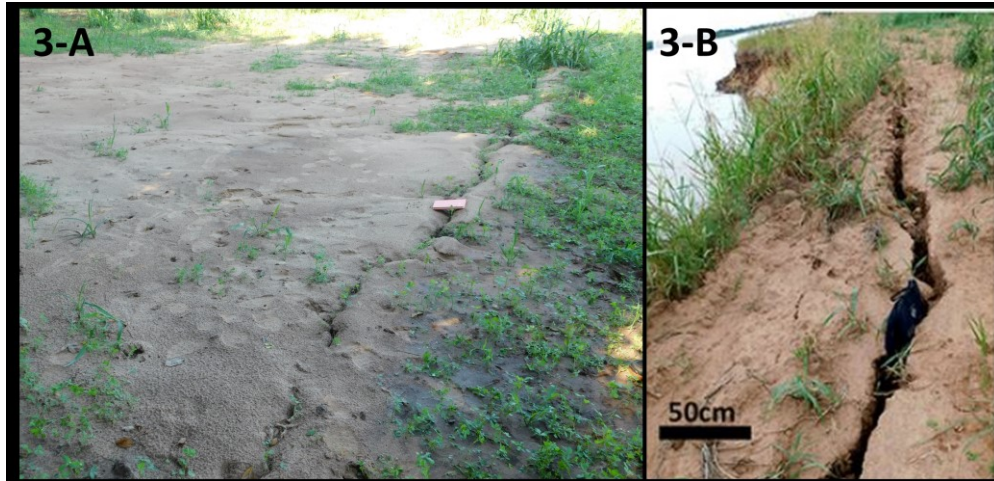


Figure 11. Photos of liquefaction manifestations at Test Site 3. (Kolawole et al. 2017)

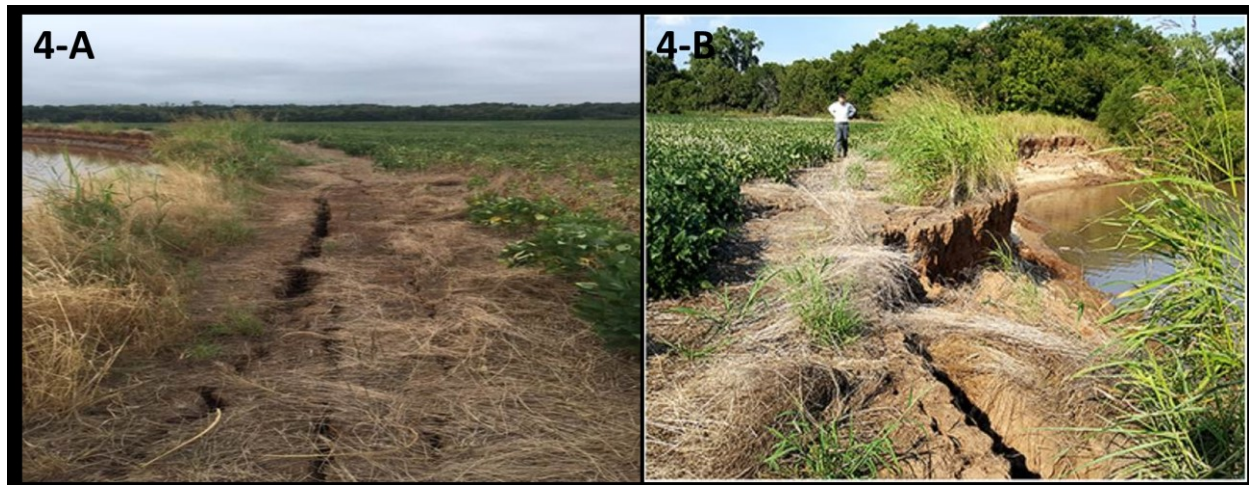


Figure 12. Photos of cracking at Test Site 4. (Photos courtesy of Martin Williams)

Preliminary site investigations were performed at the identified sites in January 2019. The primary purpose of these investigations was to gather existing information and accurately determine areas at each site where liquefaction features were and were not observed. USGS geologic maps for the four Pawnee liquefaction sites are shown in Figure 13 (Stanley and Chang 2016). All four sites are located in alluvial zones, which the USGS describes as consisting of sand, silt, clay, and gravel with maximum thicknesses along major streams ranging from 9 to 24 m and along minor streams ranging from 0 to 18 m (U.S. Geologic Survey 2019). These descriptions are consistent with the results from the site investigations, as discussed in the Section 3.3. Groundwater depth during the January 2019 site investigation was visually estimated as 1 m at Site 1, 2 m at Sites 2 and 4, and 1 to 2 m at Site 3 based on river/stream levels adjacent to the sites.

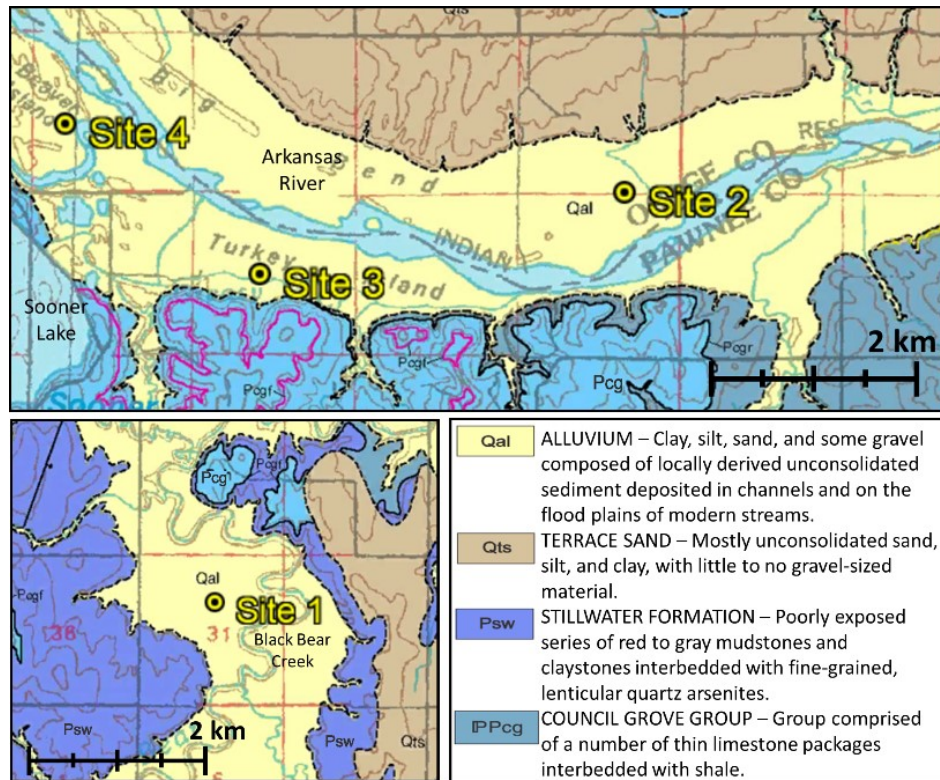


Figure 13. Geologic maps of the Pawnee earthquake liquefaction sites. (Stanley and Chang 2016)

Findings from Clayton et al. (2016) and Kolawole et al. (2017) in conjunction with GPS-tagged photos and anecdotal evidence provided during interviews with the property owners were used to estimate the extent of areas where liquefaction was and was not observed at each site. Based on this information, test locations were selected at each site. Test locations were selected both in areas where liquefaction manifestations were observed and in areas where liquefaction manifestations were not observed. No-liquefaction sites were selected so as to be near to the observed liquefaction sites and in areas where conditions are favorable for liquefaction to occur (e.g., profiles with liquefiable materials, locations inside river bends, areas of low elevation, etc.) while remaining in areas where it was determined that no liquefaction manifestations were reported.

Based on field observations from site visits in January 2019 and further discussion with the owner and others that visited the site following the earthquake, it was determined that the cracking reported at Site 4 was likely related to a seismic slope failure and not the result of liquefaction as initially reported. As such, Site 4 was excluded from further site investigation. It should also be noted that, while Kolawole et al. (2017) provided detailed mapping of cracking and ejecta in some areas at Site 3, at Sites 1, 2, and 4 as well as in some areas of Site 3, only approximate locations were available for liquefaction features. As a result, the

identified zones of liquefaction may not represent the complete extent of liquefaction manifestations that occurred at each site, and liquefaction manifestations may have occurred outside these areas. Difficulties in observing the full extent of liquefaction features following the earthquake due to crops, plowed fields, and other vegetation may also have led to underreporting and underestimations of the extent of liquefaction at these sites. However, test locations were selected using the best available information, so as to select liquefaction test locations in areas of confirmed liquefaction and no-liquefaction test locations outside of these areas. The estimated liquefaction extents and proposed test locations are shown in Figure 14. The locations of the photos of liquefaction manifestations shown in Figure 9 through Figure 12 are also indicated.

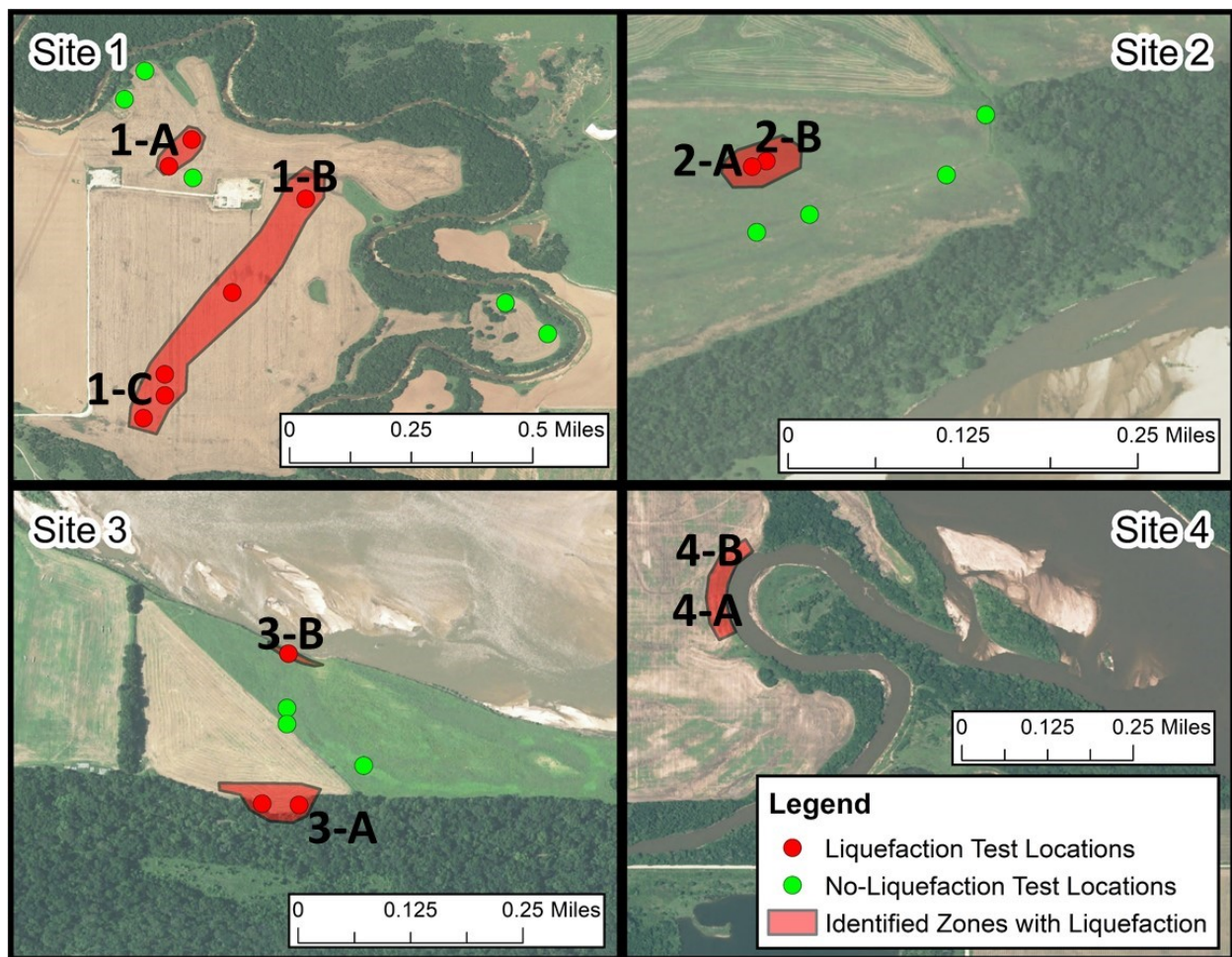


Figure 14. Identified liquefaction areas at the Pawnee sites and potential CPT test locations.
Locations of the photos presented in Figure 9 through Figure 12 are also indicated.

HVSR tests were also performed at each site as part of the preliminary site investigations. HVSR tests were performed following the guidelines provided by the SESAME project (Bard 2004) using ambient vibrations recorded using a three-component broadband seismometer. HVSR test results were used to constrain the V_s models determined from MASW tests (Yust et al. 2018) performed as part of the subsequent full site characterization, as described in the following sections. The results of the HVSR tests are presented in Section 3.3 in context of the other tests performed during the full site investigation.

Initial estimates of the liquefaction hazard at the test sites based on ground motions from the Pawnee earthquake were made as part of the preliminary investigations using the method presented by Baise and Rashidian (2008). This method estimates probability of liquefaction and liquefaction spatial extent (LSE), the percent of a given area covered by surface manifestations of liquefaction. Estimates were made based on peak ground velocity (PGV), V_{s30} , mean annual precipitation, closest distance to water, and water table depth. PGV was estimated based on the USGS ShakeMap (U.S. Geologic Survey 2016a), and precipitation data were taken from National Oceanic and Atmospheric Administration (NOAA) Station USC00346940 (NOAA 2019). Shear wave velocity information was not available for any of the sites during the preliminary investigation, but V_{s30} values reported by Zalachoris et al. (2017) for regional alluvial sites ranged from 362 m/s to 580 m/s. As a result, a V_{s30} of 360 m/s was used as a conservative estimate in the preliminary analysis. Inputs and results for each site are shown in Table 1.

Table 1. Liquefaction Hazard Estimates for the Pawnee Earthquake Test Sites based on Baise and Rashidian (2008).

| Site | Peak Ground Velocity (cm/s) | V_{s30} (m/s) | Mean Annual Precipitation (mm) | Closest Distance to Water (km) | Water Table Depth (m) | Probability of Liquefaction | Liquefaction Spatial Extent (%) |
|------|-----------------------------|-----------------|--------------------------------|--------------------------------|-----------------------|-----------------------------|---------------------------------|
| 1 | 20 | 360 | 1021 | 0.15 | 2 | 0.262 | 2.11 |
| 2 | 25 | 360 | 1021 | 0.3 | 2.5 | 0.268 | 2.28 |
| 3 | 20 | 360 | 1021 | 0.11 | 1.5 | 0.267 | 2.26 |
| 4 | 20 | 360 | 1021 | 0 | 2.5 | 0.265 | 2.20 |

For this preliminary estimate, the predicted probability of liquefaction at the four sites based on geologic proxies was ~26%, corresponding to an LSE of ~2%. Given the fairly small areal extent of liquefaction reported at Sites 1 and 2, a 2% LSE was a reasonable estimate. However, LSE of ~2% appeared low for Site 3 where liquefaction was more extensive. This analysis was updated with V_{s30} values for Sites 1 through 3 determined during the full site characterization. Based on the new V_{s30} values (270.2 m/s, 273.6 m/s, and 285.7 m/s at Sites 1, 2, and 3, respectively), probability of liquefaction at Sites 1 through 3 was estimated

at ~38% with an estimated LSE of 8-10%. These estimates for LSE appear high for Sites 1 and 2 but may be reasonable for Site 3 based on the observed extent of liquefaction at the site.

The Baise and Rashidian (2008) approach was developed for tectonic earthquakes and may not be entirely suitable for use with induced earthquakes. However, this analysis does provide some insight as to what the risk of liquefaction was in the area due to ground motions from the Pawnee event. Comparable estimates of probability of liquefaction and LSE would be expected for similar, nearby sites along the Arkansas River and Black Bear Creek depending on site-specific soil conditions. This suggests liquefaction likely was more widespread than officially reported. This agrees with observations made by local landowners that liquefaction occurred at other sites in the area, in addition to those formally documented in Clayton et al. (2016) and Kolawole et al. (2017).

3.2 Detailed Site Investigation

Detailed investigations of the selected sites including CPT and MASW tests were performed in November 2019 and March 2020. CPT soundings were performed at both liquefaction and no-liquefaction test locations identified at Sites 1, 2, and 3. sCPT tests were performed at two liquefaction locations and two no-liquefaction locations at Site 2 and at all test locations at Site 3. CPT soundings extended to refusal. Table 2 provides a summary of the CPT tests performed at each site.

Table 2. Summary of CPT Soundings at Pawnee, OK Test Sites.

| Sounding | Site | Max Depth of Sounding (m) | Seismic CPT Test | Liquefaction Reported |
|-----------------|-------------|----------------------------------|-------------------------|------------------------------|
| CPT-01 | 1 | 17 | N | N |
| CPT-02 | 1 | 16 | N | Y |
| CPT-03 | 1 | 15 | N | Y |
| CPT-04 | 2 | 14 | Y | Y |
| CPT-05 | 2 | 14 | Y | Y |
| CPT-06 | 2 | 13 | N | N |
| CPT-07 | 2 | 14 | N | N |
| CPT-08 | 2 | 13 | Y | N |
| CPT-09 | 2 | 13 | Y | N |
| CPT-10 | 3 | 15 | Y | Y |
| CPT-11 | 3 | 14 | Y | Y |
| CPT-12 | 3 | 16 | Y | Y |
| CPT-13 | 3 | 15 | Y | N |
| CPT-14 | 3 | 15 | Y | N |
| CPT-15 | 3 | 15 | Y | N |

MASW tests were also performed at Sites 1 through 3. MASW tests at each site were performed in identified areas of liquefaction. Two MASW tests were performed at Site 1 using perpendicular geophone arrays. One MASW test was performed at Sites 2 and 3. MASW tests were performed using a 2-m geophone spacing and source offsets of 5, 10, 20, and 40 m. A sledge hammer that impacted a Plexiglas strike-plate was used as the active source for the MASW testing. Locations for CPT and MASW tests are shown in Figure 15 through Figure 17. Hand auger samples were taken near CPT-03 at Site 1 and CPT-05 at Site 2 as indicated in Figure 15 through Figure 17. Sampling depth was limited to 4.5 m at CPT-03 due to unsafe weather conditions and 4 m at CPT-05 due to borehole collapse. As noted, HVSR tests were also performed at all sites during the preliminary investigation. The HVSR test locations are also included in Figure 15 through Figure 17. As discussed previously, no additional testing (CPT or MASW) was performed at Site 4 because the manifestations noted at this site following the Pawnee event were likely a seismic slope stability issue and unrelated to liquefaction.

Several test locations had to be adjusted due to site conditions at the time of testing. In particular, at Site 1, testing was limited to the northwest portion of the site due to wet ground conditions and ponding in other areas of the site. CPT-02 was relocated farther from the center of the identified liquefaction area due to soft ground conditions that made the original test location inaccessible to the CPT rig. Flooding of the Arkansas River in May 2019 eroded a large portion of Site 3, including one area of potential liquefaction, which resulted in the relocation of CPT-15. The riverbank alignment at the time of CPT testing in March 2020 is shown in Figure 17. CPT-13 at Site 3 was also moved from its planned location due to ponding at the site during testing.

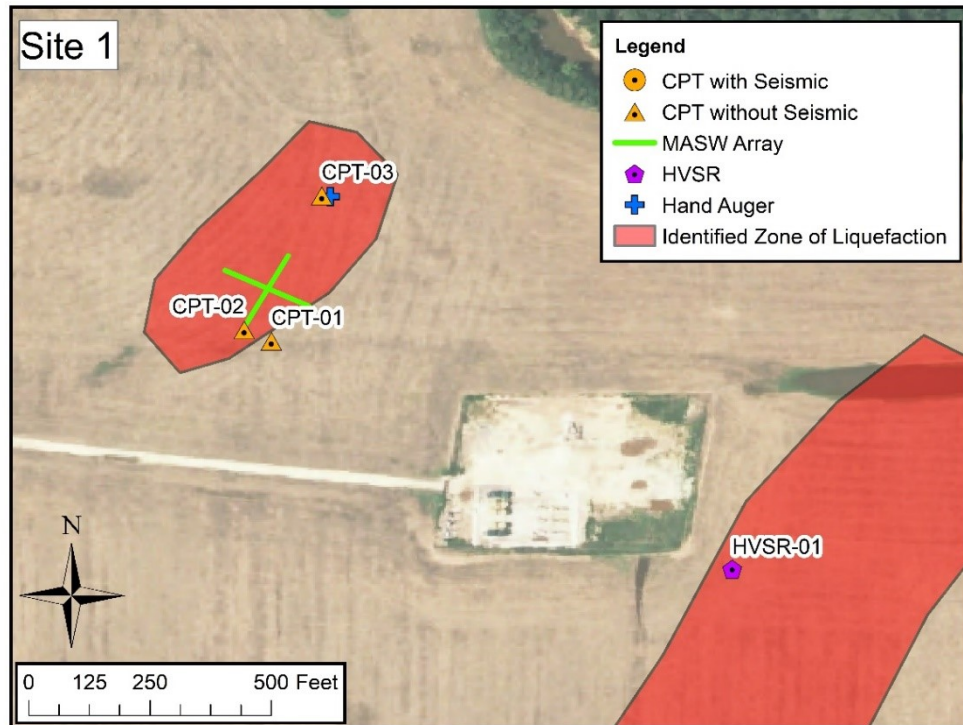


Figure 15. CPT, MASW, HVSR, and Hand Auger test locations at Site 1.

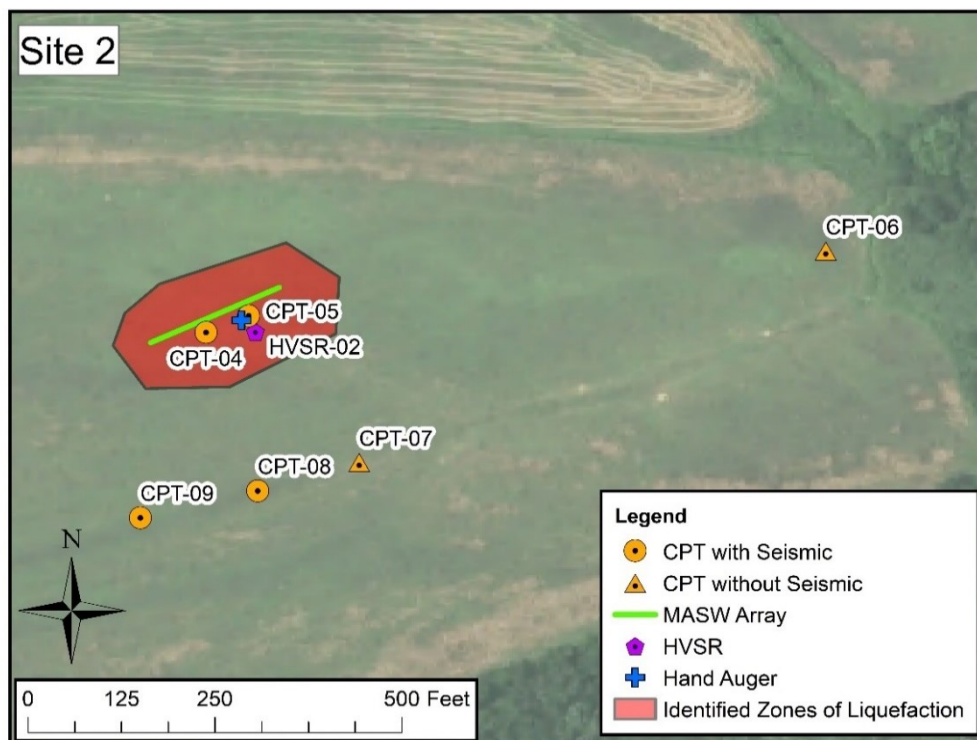


Figure 16. CPT, MASW, HVSR, and Hand Auger test locations at Site 2.

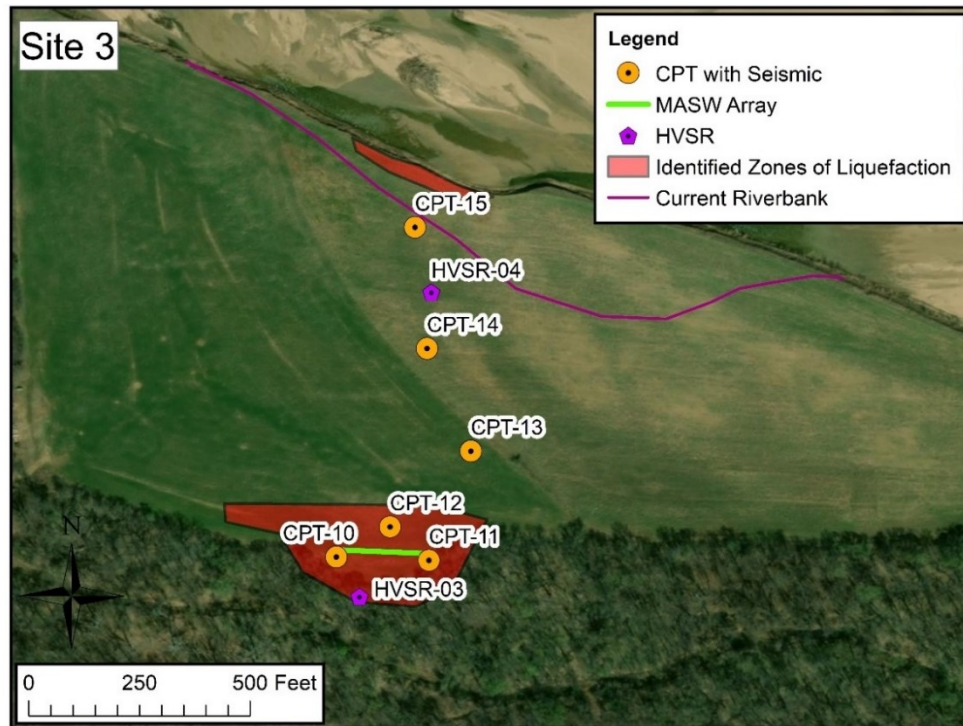


Figure 17. CPT, MASW, and HVSR test locations at Site 3.

3.3 Site Characterization Results

Profiles of CPT tip resistance (q_t), friction ratio (F_r), and soil behavior type index (I_c) for the soundings performed at Sites 1 through 3 are presented in Figure 18 through Figure 32. As noted previously, CPT soundings extended to refusal. The figure titles indicate whether liquefaction manifestations were or were not reported at a given test location following the Pawnee event. CPT data were processed based on recommendations in Robertson and Cabal (2015). I_c values and the listed soil behavior types are based off the normalized CPT soil behavior type (SBT_n) chart developed by Robertson (2010) as presented in Robertson and Cabal (2015). Ground water depth at the time of CPT testing is also indicated as estimated from CPT pore pressure measurements.

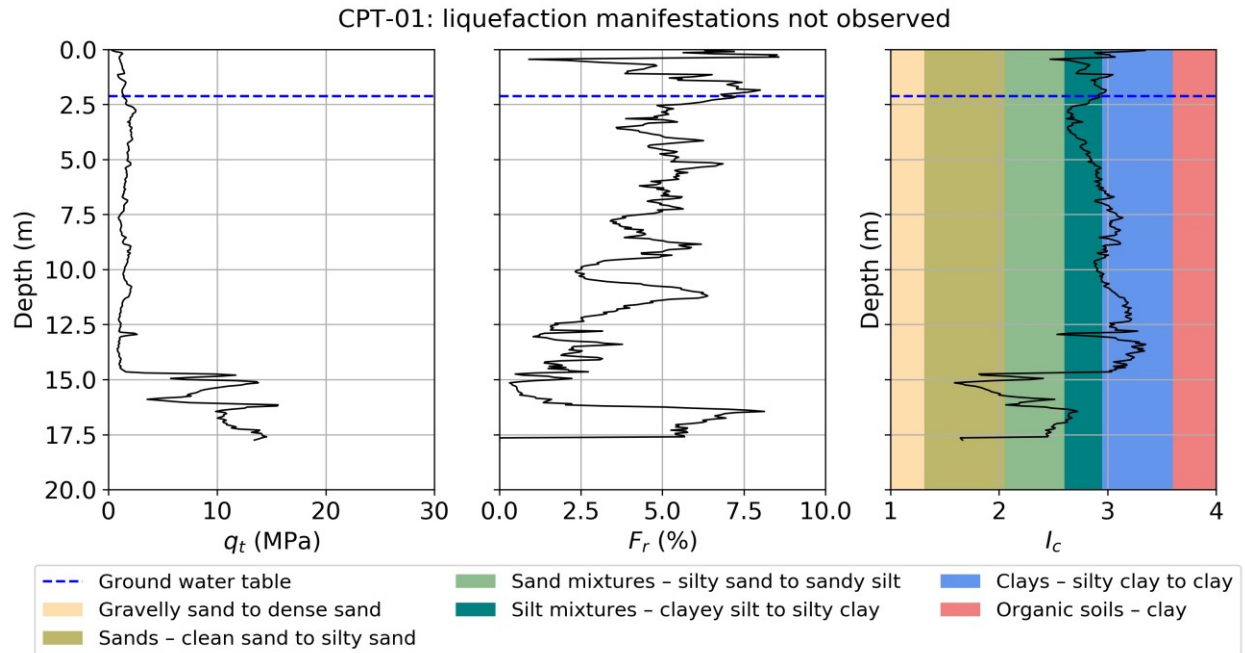


Figure 18. CPT test results for CPT-01, Site 1.

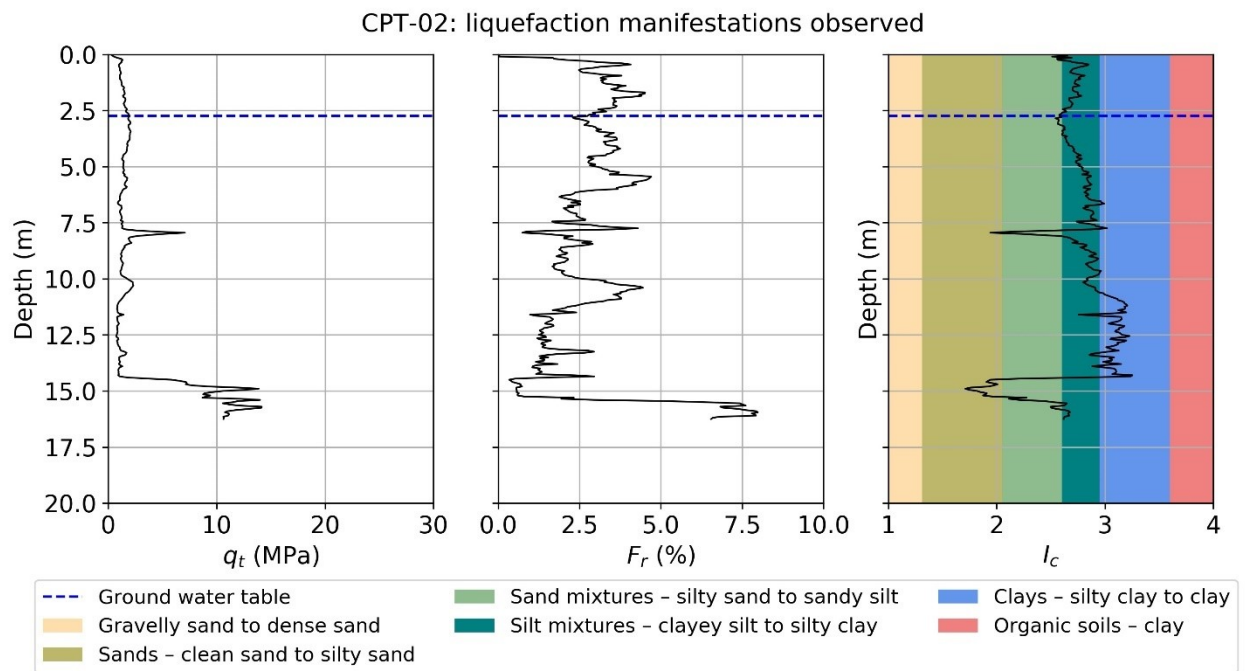


Figure 19. CPT test results for CPT-02, Site 1.

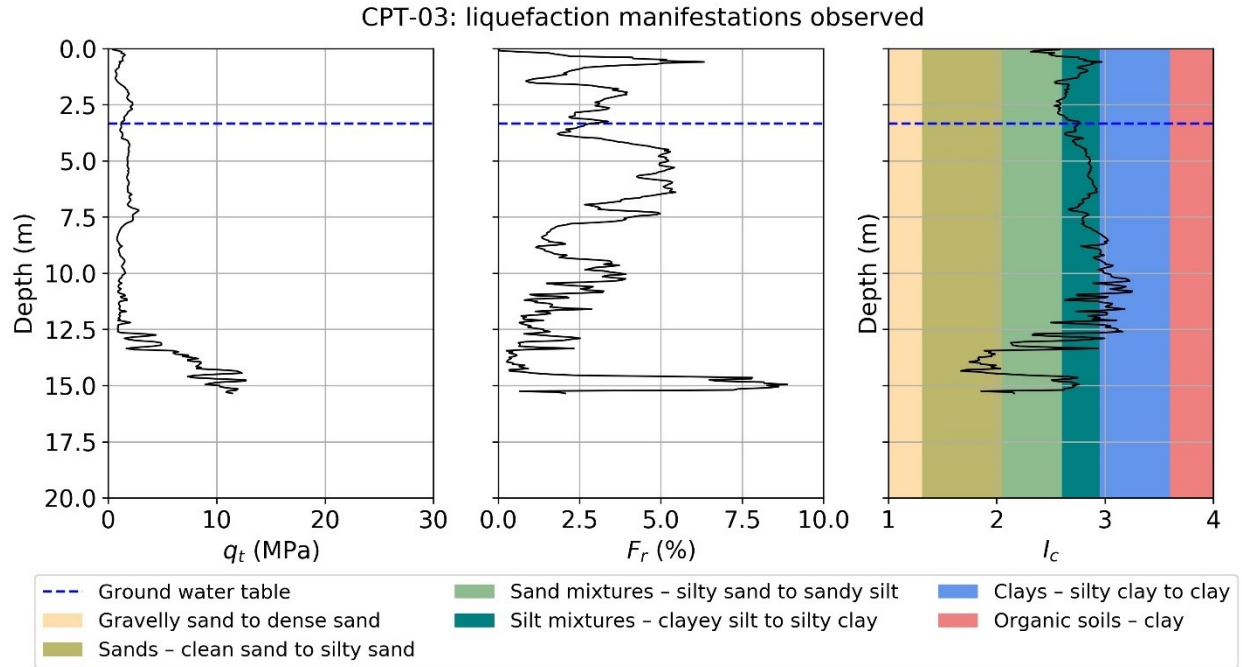


Figure 20. CPT test results for CPT-03, Site 1.

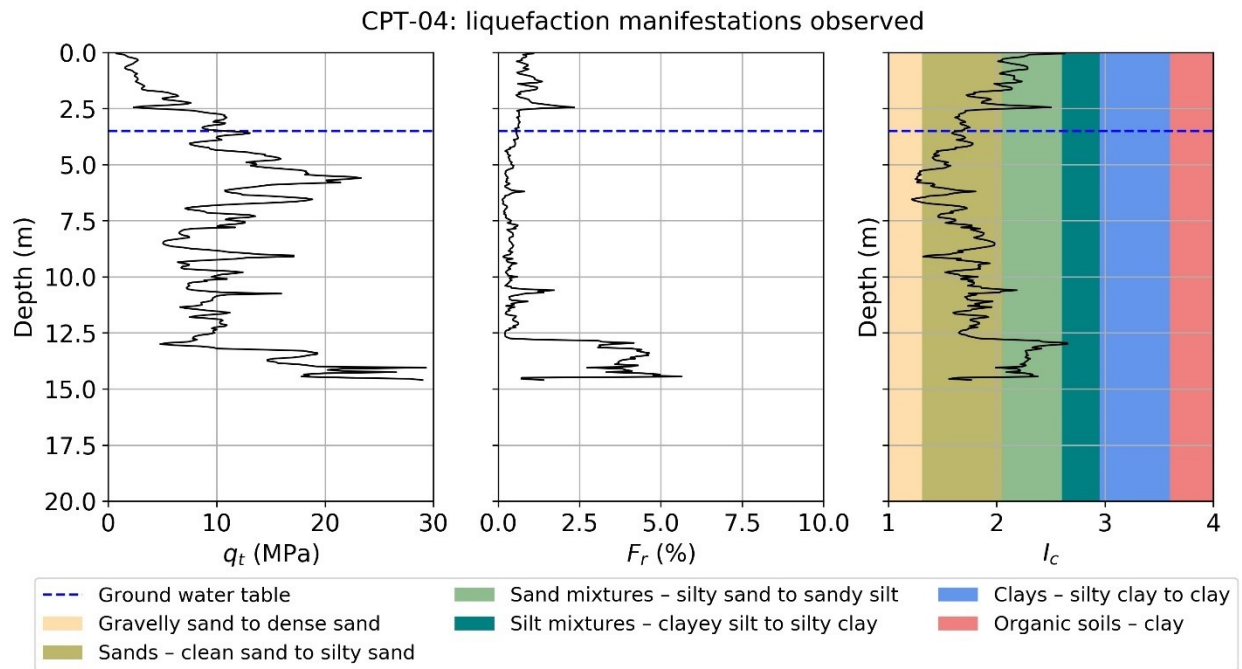


Figure 21. CPT test results for CPT-04, Site 2.

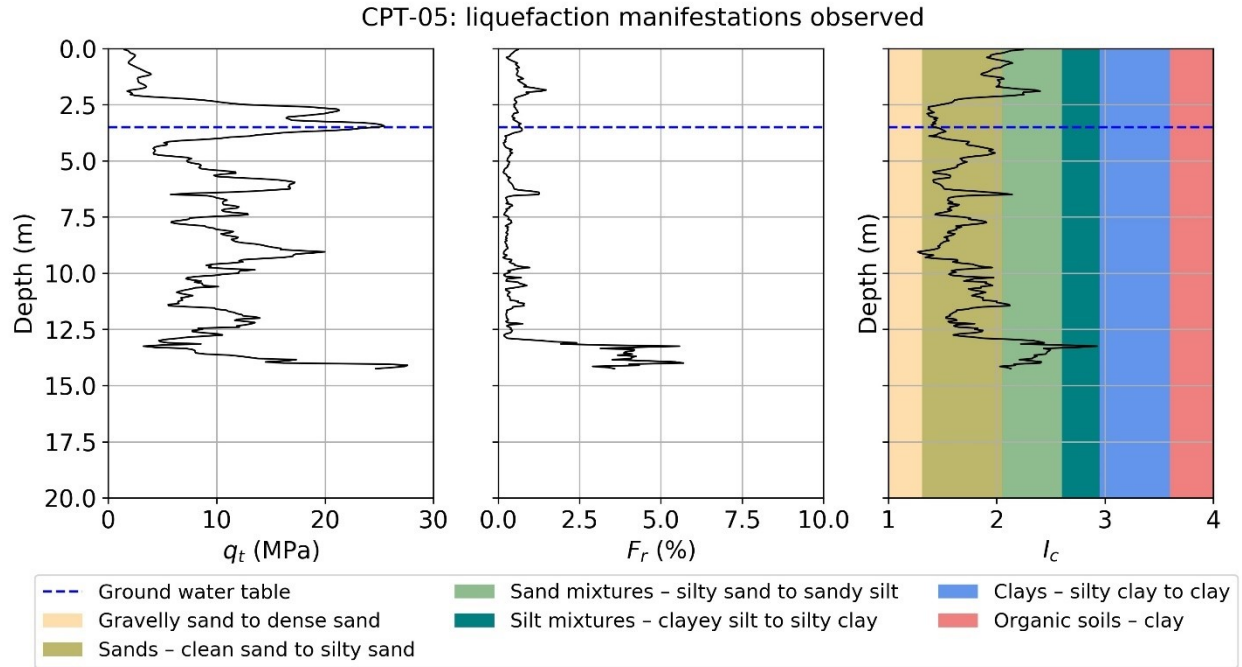


Figure 22. CPT test results for CPT-05, Site 2.

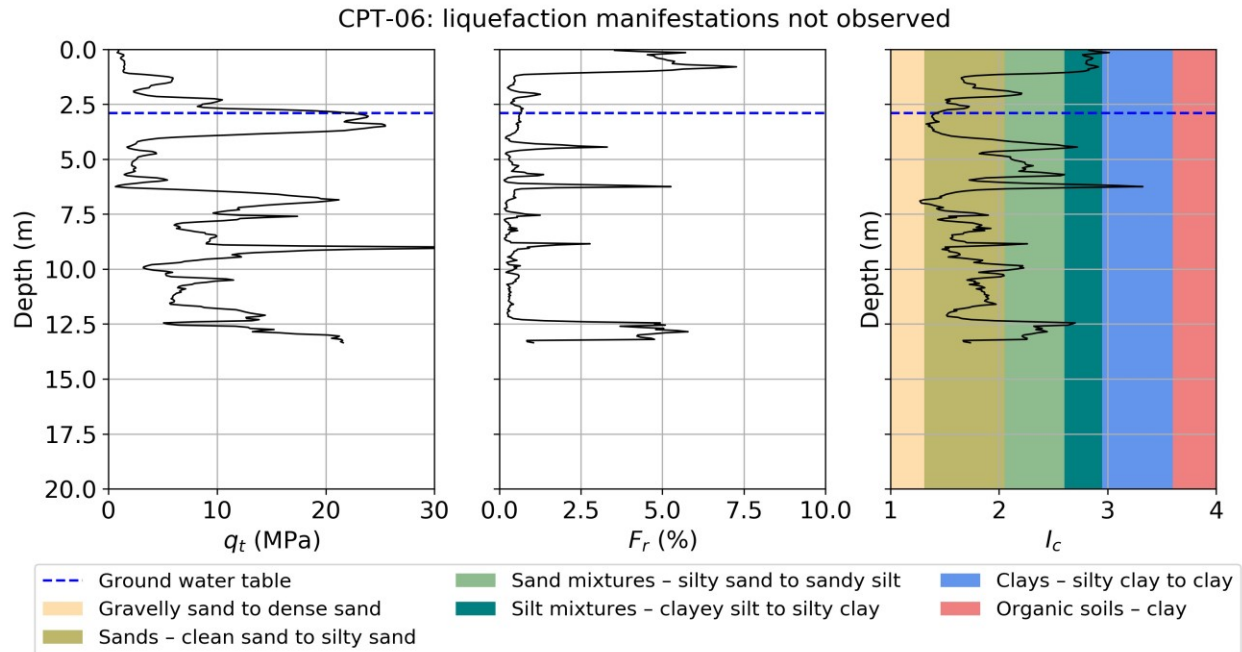


Figure 23. CPT test results for CPT-06, Site 2.

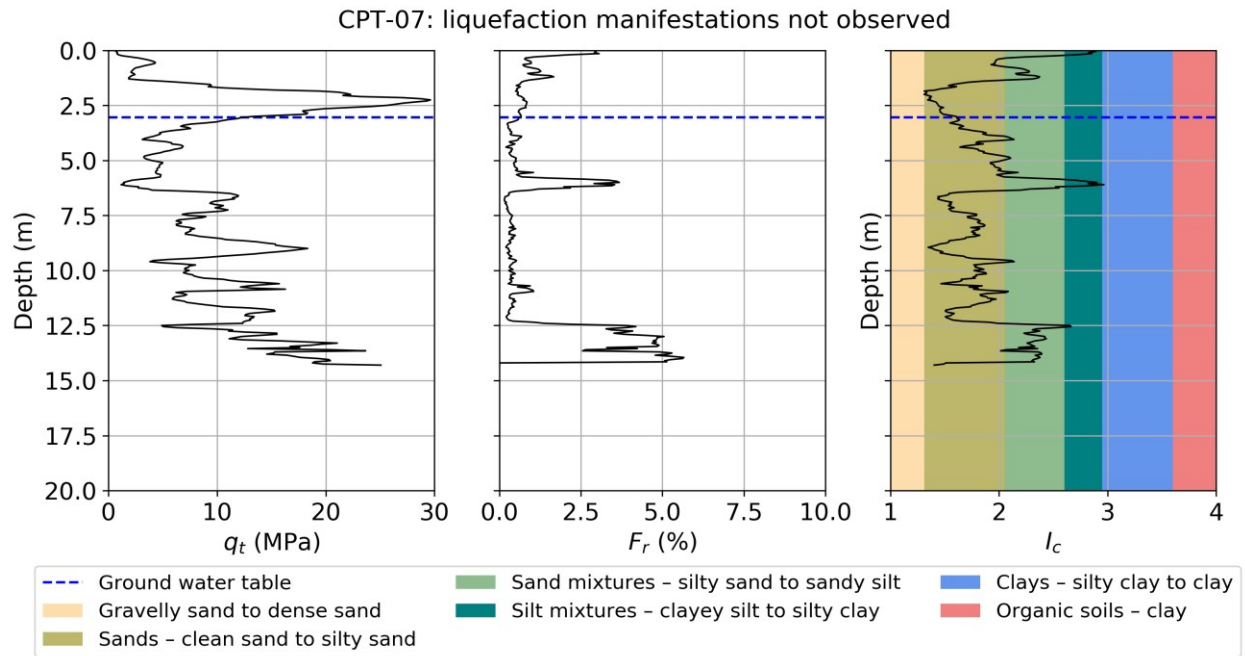


Figure 24. CPT test results for CPT-07, Site 2.

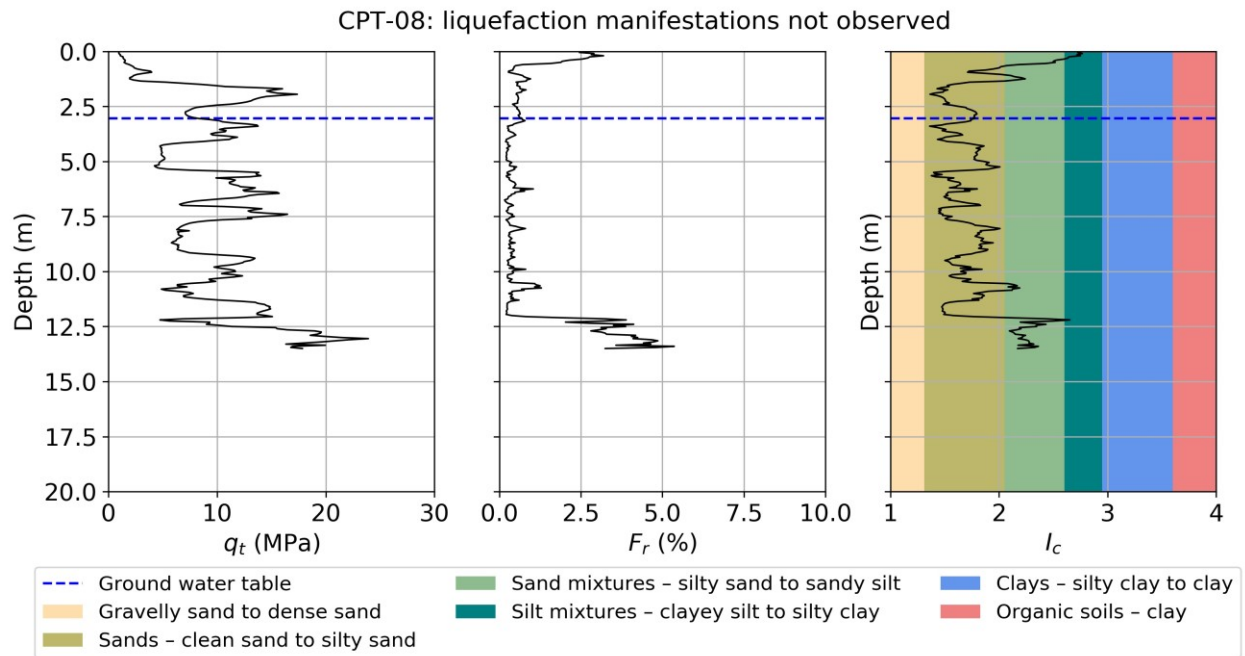


Figure 25. CPT test results for CPT-08, Site 2.

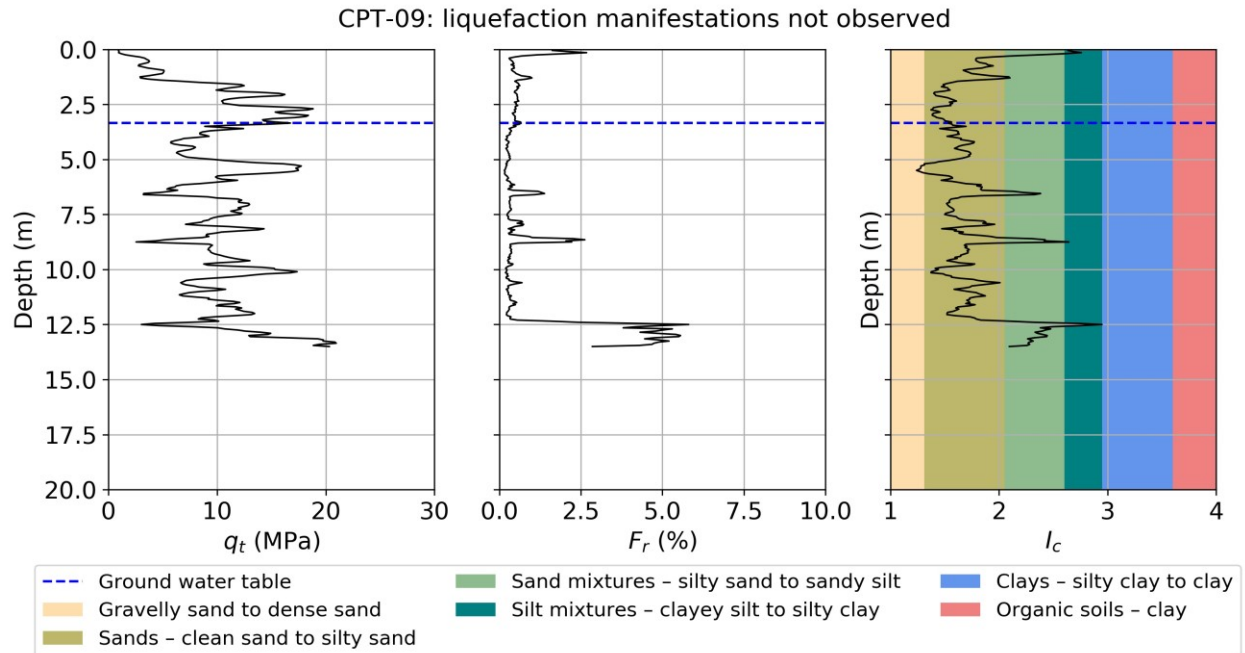


Figure 26. CPT test results for CPT-09, Site 2.

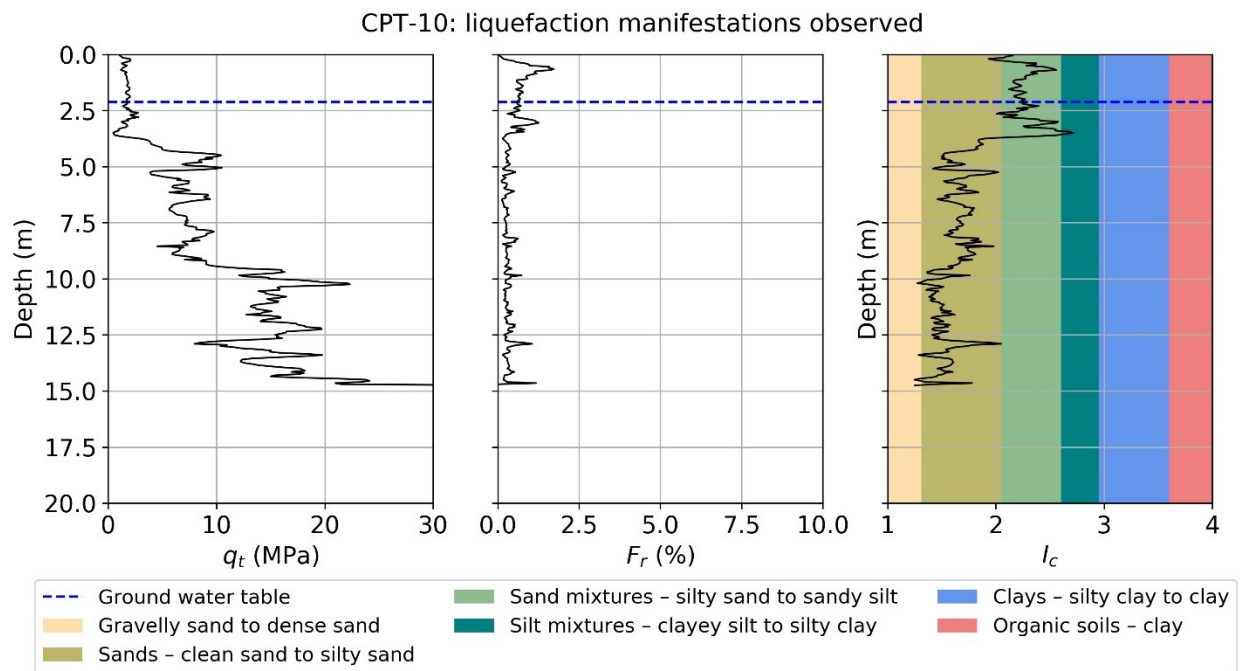


Figure 27. CPT test results for CPT-10, Site 3.

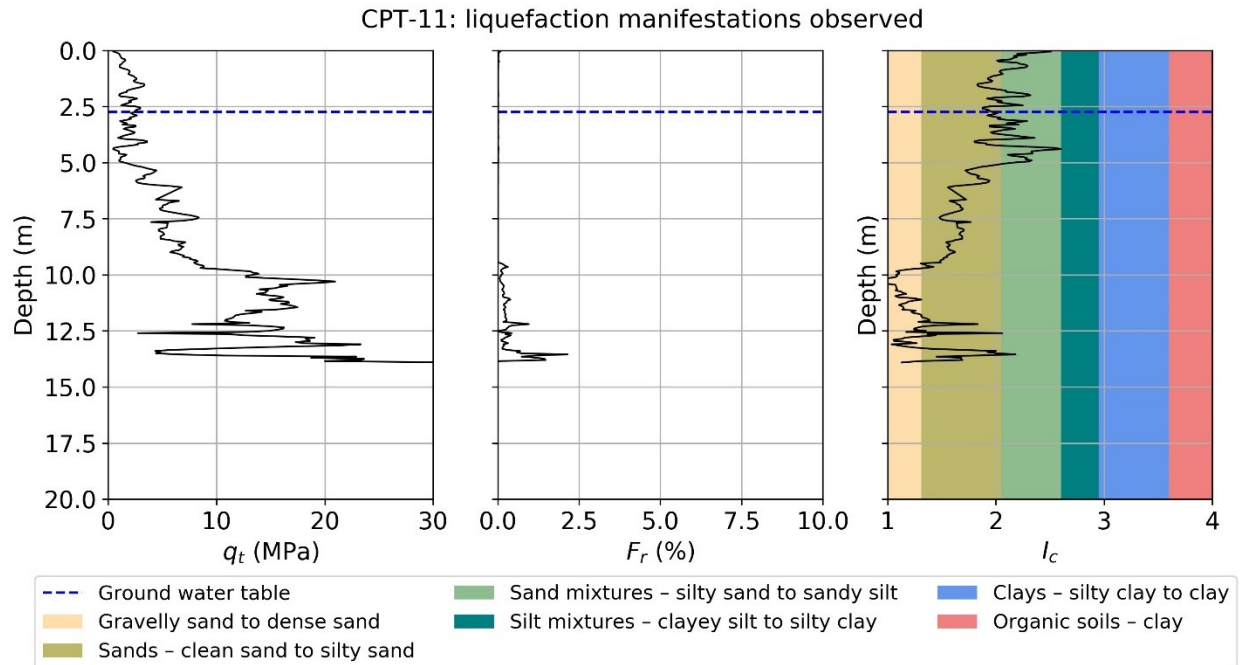


Figure 28. CPT test results for CPT-11, Site 3.

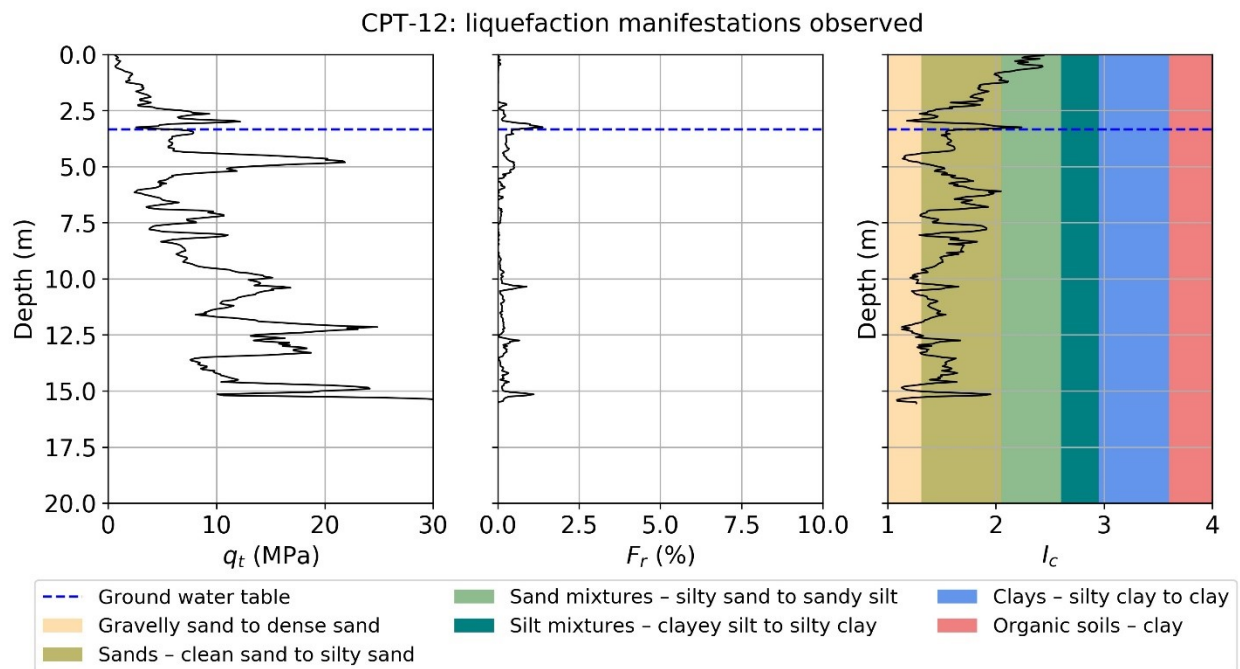


Figure 29. CPT test results for CPT-12, Site 3.

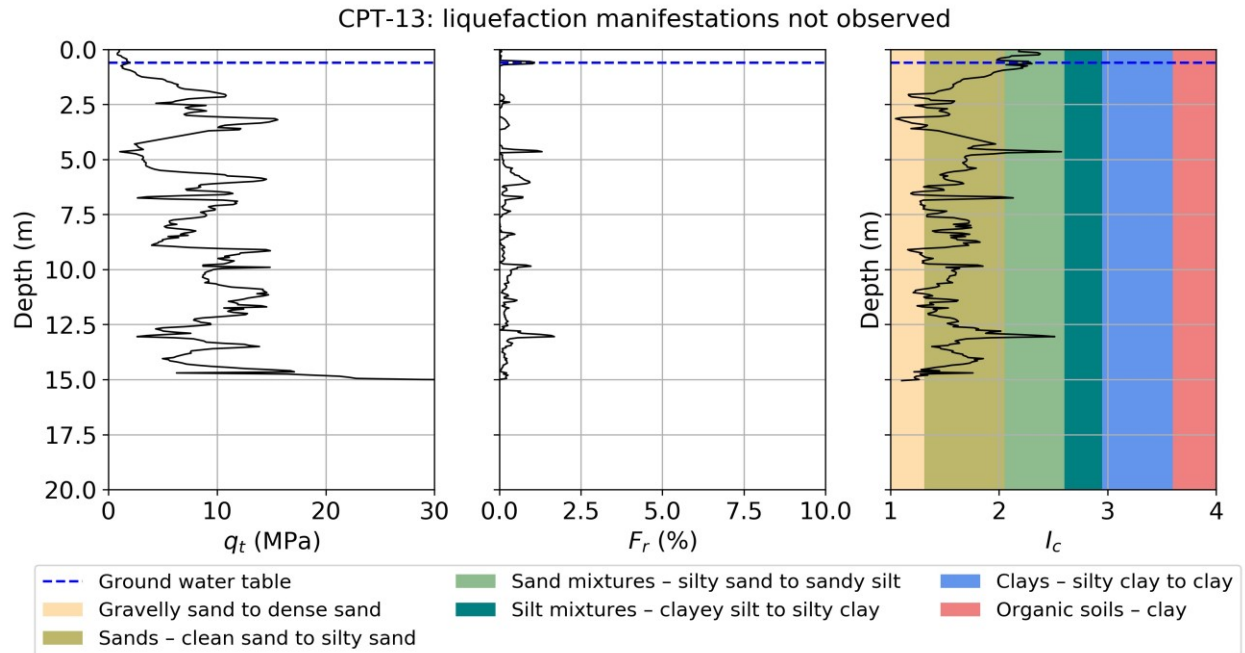


Figure 30. CPT test results for CPT-13, Site 3.

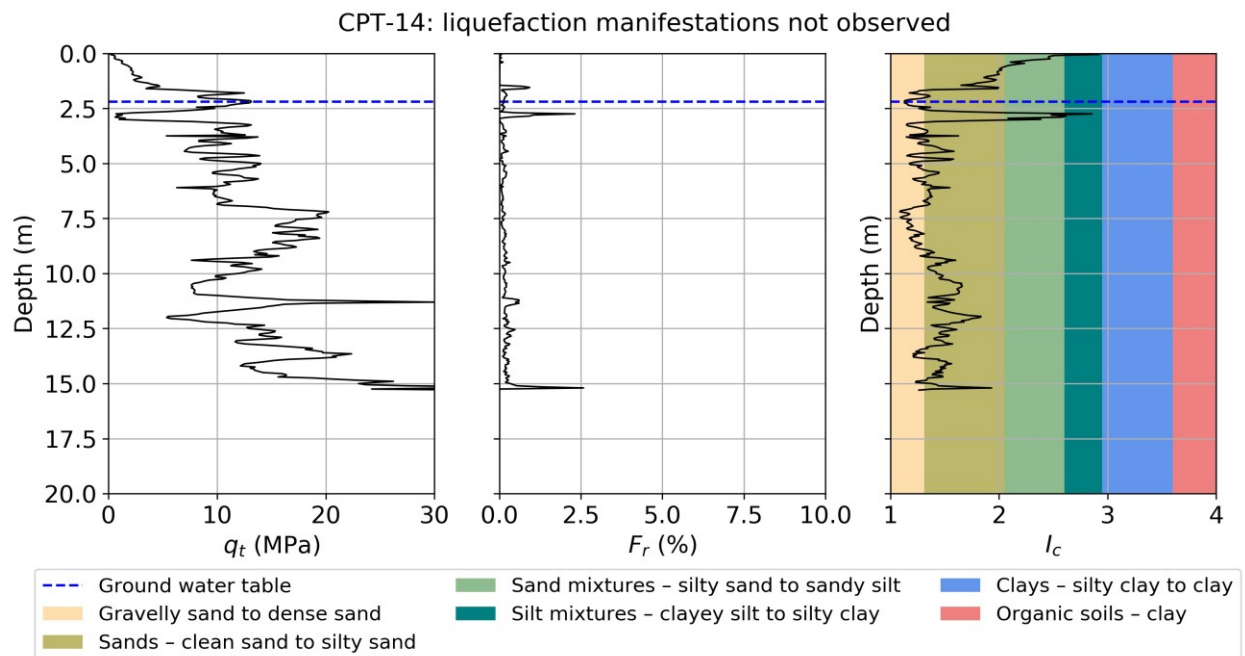


Figure 31. CPT test results for CPT-14, Site 3.

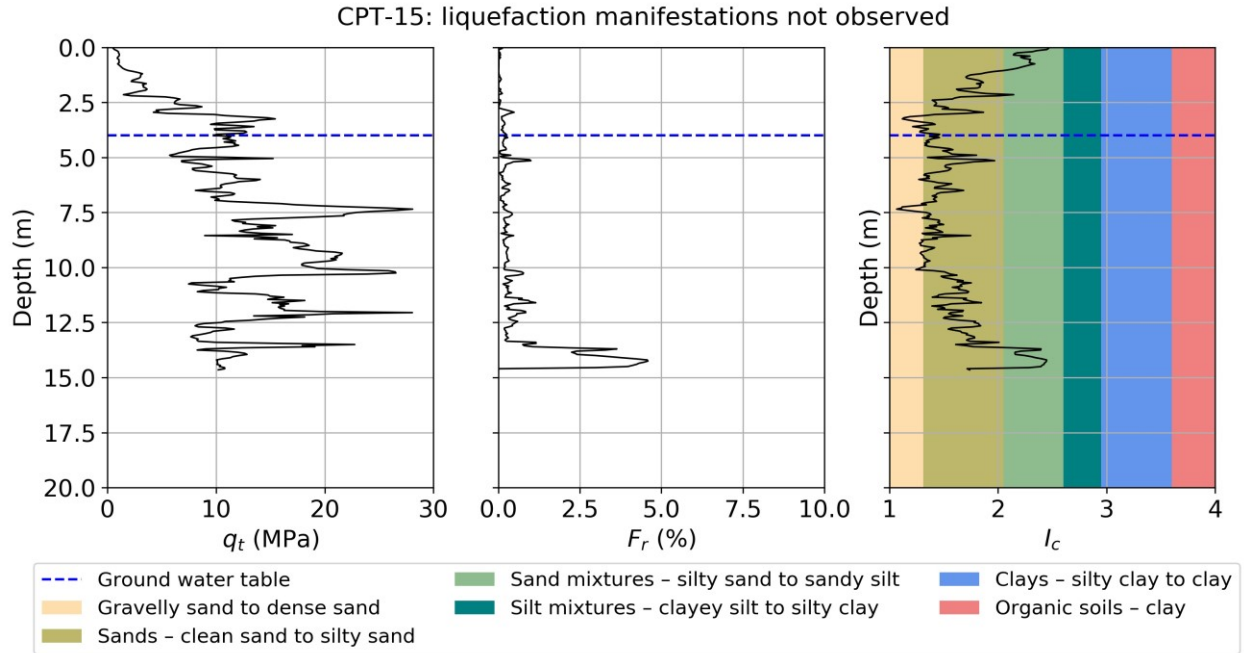


Figure 32. CPT test results for CPT-15, Site 3.

An I_c value of 2.6, the boundary between “sandy silt” and “clayey silt mixtures” based on SBT_n , is often used to screen out clay-like soils from liquefaction analyses (Robertson and Wride 1998) because they are likely not susceptible to liquefaction. However, Boulanger and Idriss (2014) note that other cutoff values as high as 2.8 or as low as 2.4 may be justified based on site-specific sampling and testing. For this reason, lab tests, including particle-size analysis and Atterberg limit tests, were performed on hand auger samples taken near CPT-03 at Site 1 and CPT-05 at Site 2. Samples were taken at depths where I_c values were close to 2.6 to better assess the properties of these soils.

Samples taken from depths of approximately 1, 2, 3, and 4 m near CPT-03 at Site 1 were classified as lean clay (CL) with fines contents (FC) of 96-99%, a liquid limit (LL) of approximately 30, and a plasticity index (PI) of approximately 9. These soils would not be considered liquefiable. These samples have $I_c > \sim 2.6$, which supports the use of $I_c = 2.6$ as a threshold for liquefaction susceptibility at Site 1.

Samples taken from depths of approximately 1, 2, 3, and 4 m near CPT-05 at Site 2 were also tested. Fines content varied across the depths tested with FC of 41% at 1 m depth, 91% at 2 m depth, 2% at 3 m depth, and 4% at 4 m depth. Soils at 1 m were classified as silty sand (SM) with non-plastic fines. Soils at 2 m depth were classified as lean clay (CL) with LL of approximately 45 and PI of approximately 28. Soils at depths of 3 and 4 m were classified as fine, poorly graded sand (SP). Lab tests are reflective of the I_c profiles at CPT-04 and CPT-05, which indicate silty sand or sandy silt at depths less than approximately 1.5 m with

higher I_c values between depths 2 and 2.5 m, indicating more clay-like behavior. I_c values below a depth of 2.5 m indicate sand-like behavior. Based on the lab test results, the soils sampled at a depth of 2 m would likely not be susceptible to liquefaction while the soils sampled at depths of 1, 3, and 4 m would likely be susceptible to liquefaction. $I_c \approx 2.4$ for the non-susceptible soils at a depth of 2 m while I_c was as high as 2.3 for the liquefaction susceptible soils above this depth. These results suggest that a cutoff for liquefaction of $I_c = 2.4$ may be justified at Site 2. A sensitivity analysis was performed during liquefaction hazard assessment (Section 5.3) to test the effect of I_c cutoff on estimated liquefaction potential. This analysis found that, due to the scarcity of soil having $2.4 \leq I_c < 2.6$, the choice of I_c threshold between 2.4 to 2.6 had negligible impact on estimated risk of liquefaction at Site 2. As such, an I_c cutoff of 2.6 was used to be consistent with typical implementation of the selected liquefaction triggering models.

Although lab tests were not performed on soils from Site 3, a sensitivity analysis was completed for Site 3 using I_c thresholds ranging from 2.4 to 2.6. As with Site 2, selection of the I_c liquefaction susceptibility threshold within this range had negligible impact on the estimated risk of liquefaction at Site 3. An I_c threshold for liquefaction susceptibility of 2.6 was also used at Site 3.

HVSR analysis was performed using the Geopsy software package. Ground motion recordings from each site were divided up into smaller time windows, and Fourier spectra were computed for each time window for each of the recorded components of motion (N-S, E-W, Vertical). A cosine taper was applied and the spectra were smoothed using a Konno-Ohmachi (Konno and Ohmachi 1998) smoothing filter, with the parameter b set to 20. The ratio of the vertical spectrum to geometric mean of the two horizontal spectra was plotted for each window and the mean horizontal-to-vertical (H/V) curve was calculated. H/V curves for the individual time windows, as well as the mean H/V curve, were plotted for each site. Once plotted, the frequency corresponding to the maximum point of the mean H/V curve is identified. This peak frequency corresponds to the fundamental frequency of the given site. Figure 33 shows the HVSR results for the Sites 1 through 3. Individual H/V curves for each individual time window are plotted. Mean H/V curves, mean \pm one standard deviation, and the corresponding frequency \pm one standard deviation are also indicated. The fundamental frequencies at the three sites along the Arkansas River (i.e., Sites 2, 3, and 4) were approximately 3 Hz, while it was 0.86 Hz at Site 1, located along Black Bear Creek. This may be an indication of differences in alluvium thickness along the Arkansas River versus that along Black Bear Creek, where less alluvium would lead to a stiffer site and higher fundamental frequency and vice-versa.

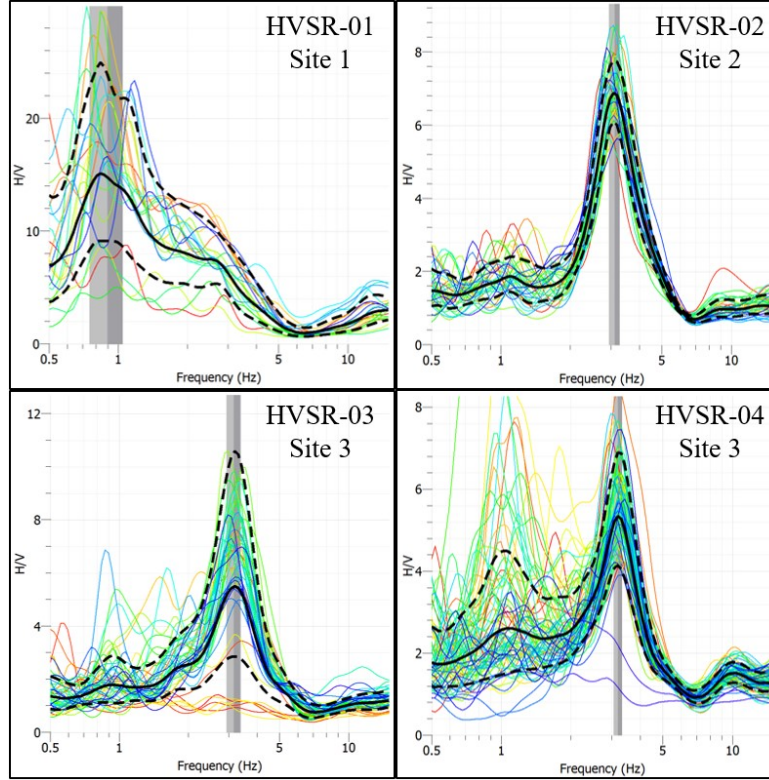


Figure 33. HVSR results for the Sites 1 through 3. H/V vs frequency curves are shown for individual time windows from the recorded ambient ground motions. Average H/V curves +/- standard deviation and the corresponding frequency +/- one standard deviation are also indicated.

V_s profiles were developed at each CPT sounding location using a combination of CPT, sCPT, and MASW data. V_s profiles based on sCPT data were developed using the interval and slope methods as presented by Hallal and Cox (2019). V_s profiles from MASW data were developed using the program Dinver following the Layering Ratio method proposed by Cox and Teague (2016). HVSR data were used to constrain bedrock depth during V_s profile inversion (Yust et al. 2018). However, due to limitations of the source used during MASW testing, the V_s values below a depth of approximately 30 m could not reliably be resolved. As such, the developed V_s profiles do not extend below this depth. Correlations with CPT data were also used to develop V_s profiles. Correlations used include the Robertson and Cabal (2015) correlation for general soils and the Ulmer et al. (2020) correlation for liquefiable soils. Combined correlation-based V_s profiles were also developed by using the Robertson and Cabal (2015) correlation to estimate V_s for non-liquefiable soils and the Ulmer et al. (2020) correlation to estimate V_s for liquefiable soils. The resulting V_s profiles are plotted in Figure 34 through Figure 48.

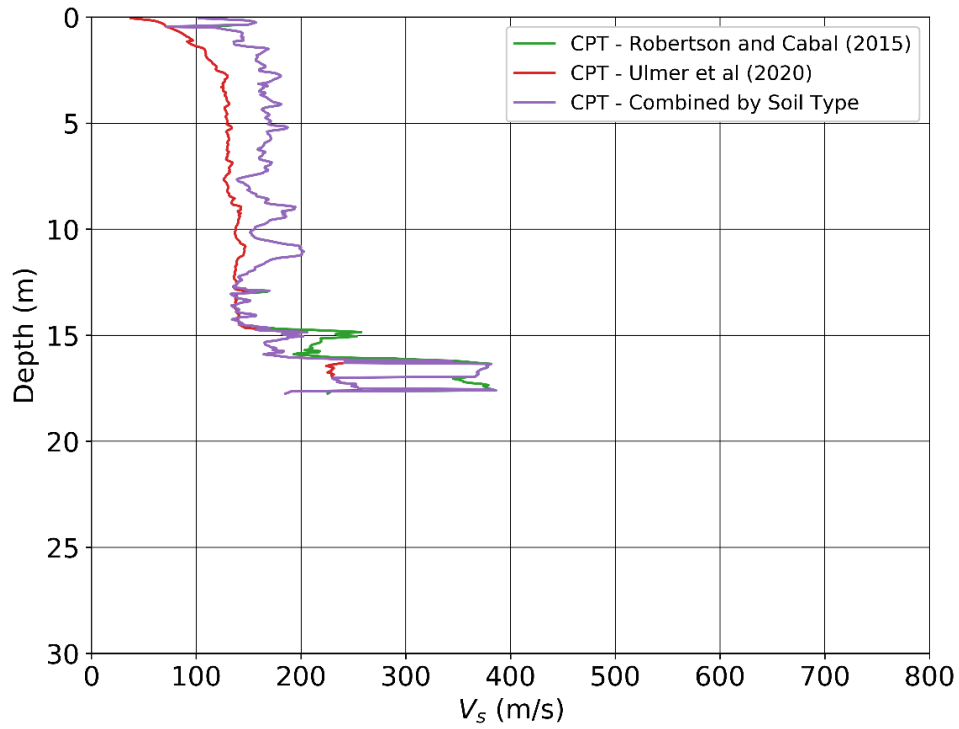


Figure 34. V_s profiles for CPT-01, Site 1, developed using CPT correlations.

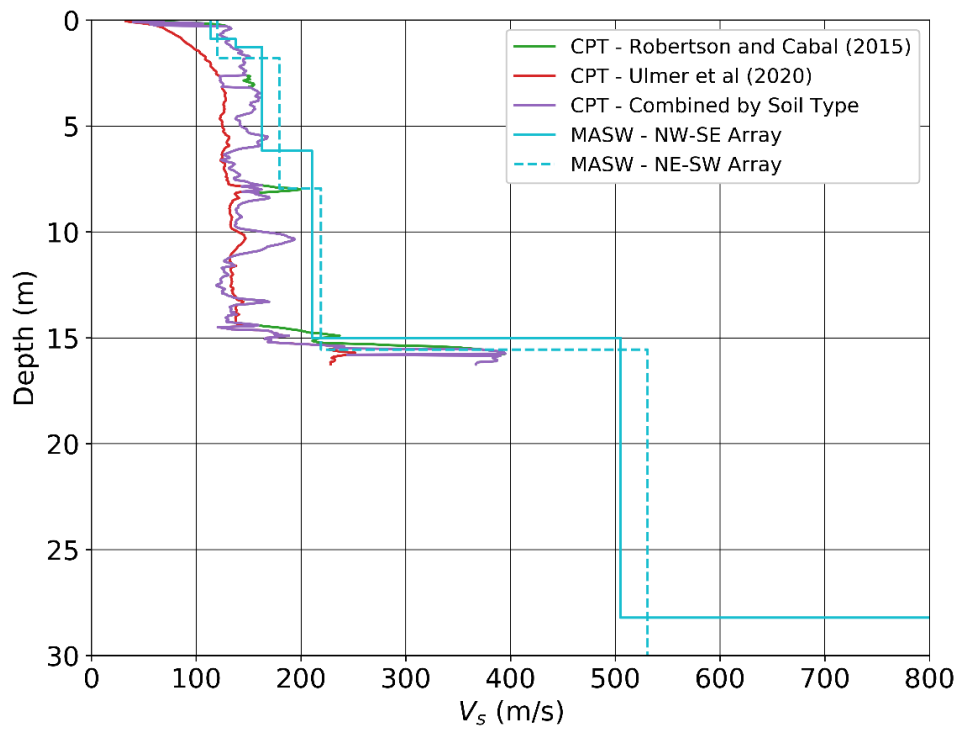


Figure 35. V_s profiles for CPT-02, Site 1, developed using CPT correlations and MASW tests.

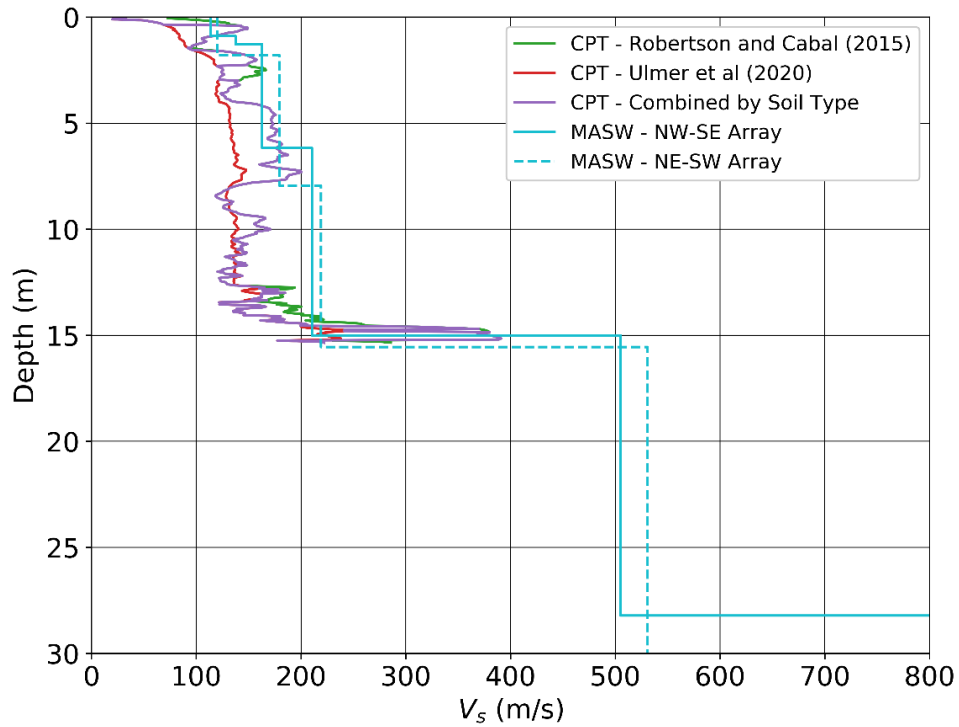


Figure 36. V_s profiles for CPT-03, Site 1, developed using CPT correlations and MASW tests. MASW results for both MASW geophone array layouts are shown.

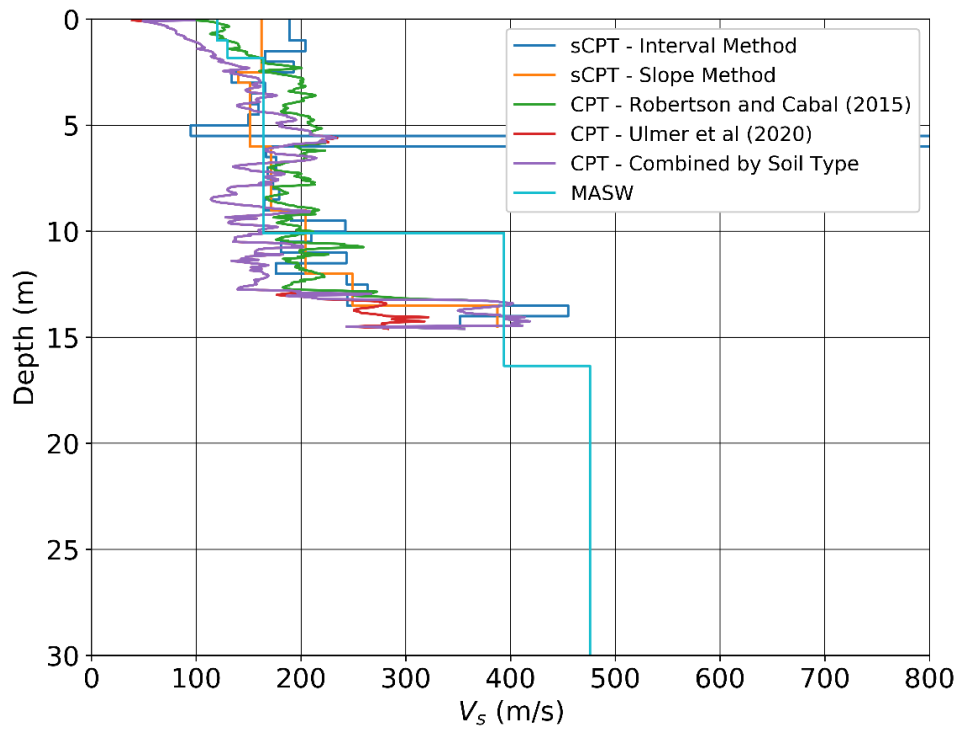


Figure 37. V_s profiles for CPT-04, Site 2, developed using CPT correlations, sCPT tests, and MASW tests.

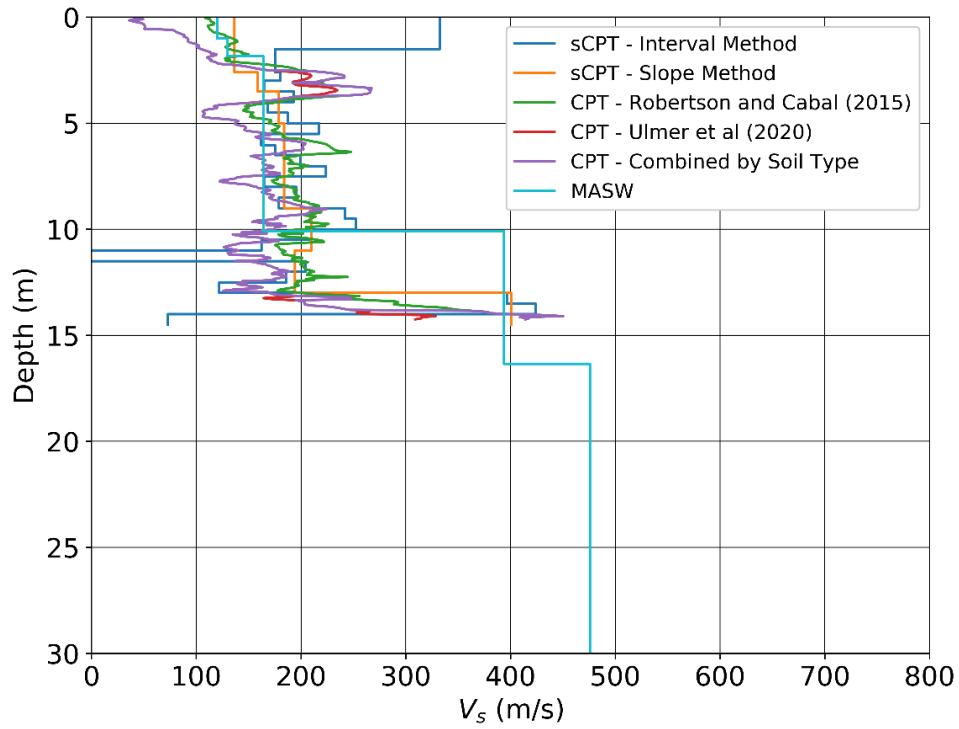


Figure 38. V_s profiles for CPT-05, Site 2, developed using CPT correlations, sCPT tests, and MASW tests.

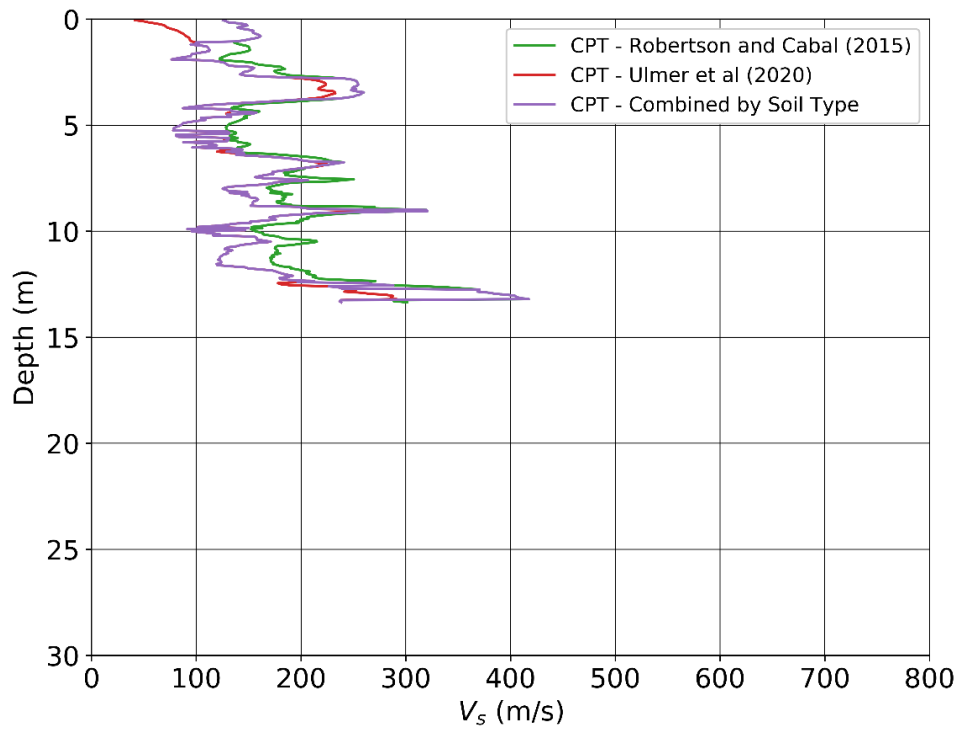


Figure 39. V_s profiles for CPT-06, Site 2, developed using CPT correlations.

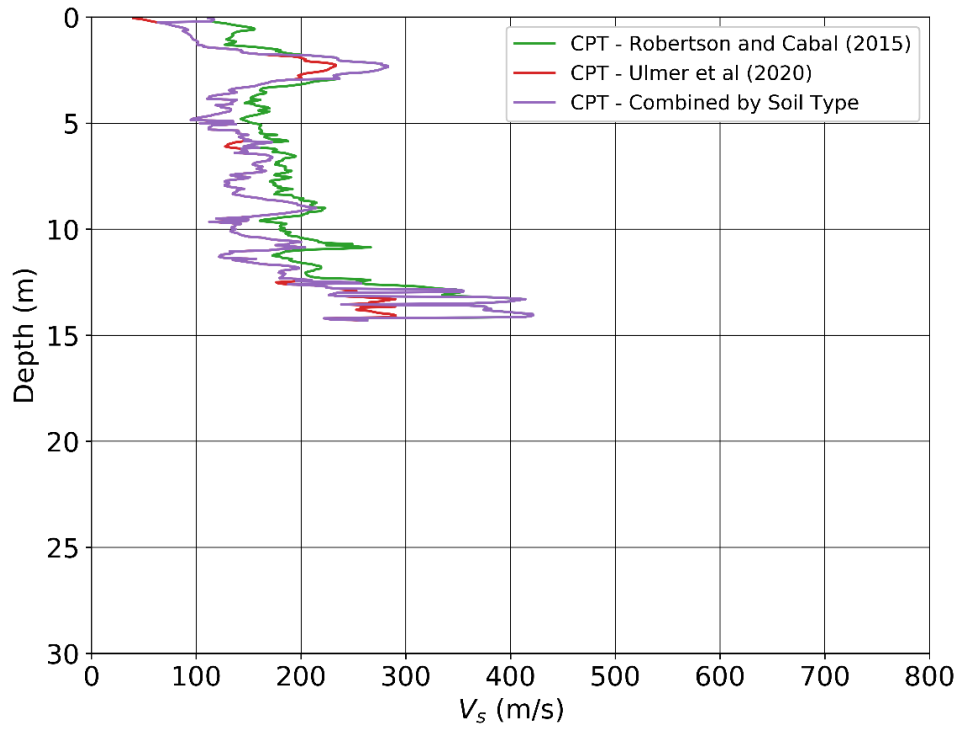


Figure 40. V_s profiles for CPT-07, Site 2, developed using CPT correlations.

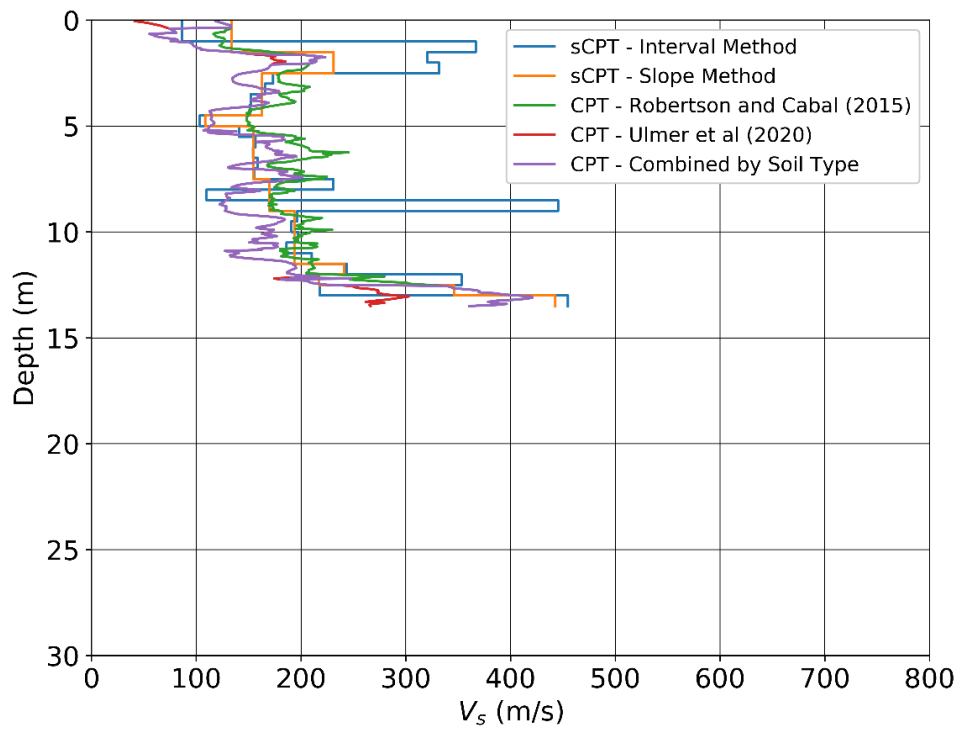


Figure 41. V_s profiles for CPT-08, Site 2, developed using CPT correlations and sCPT tests.

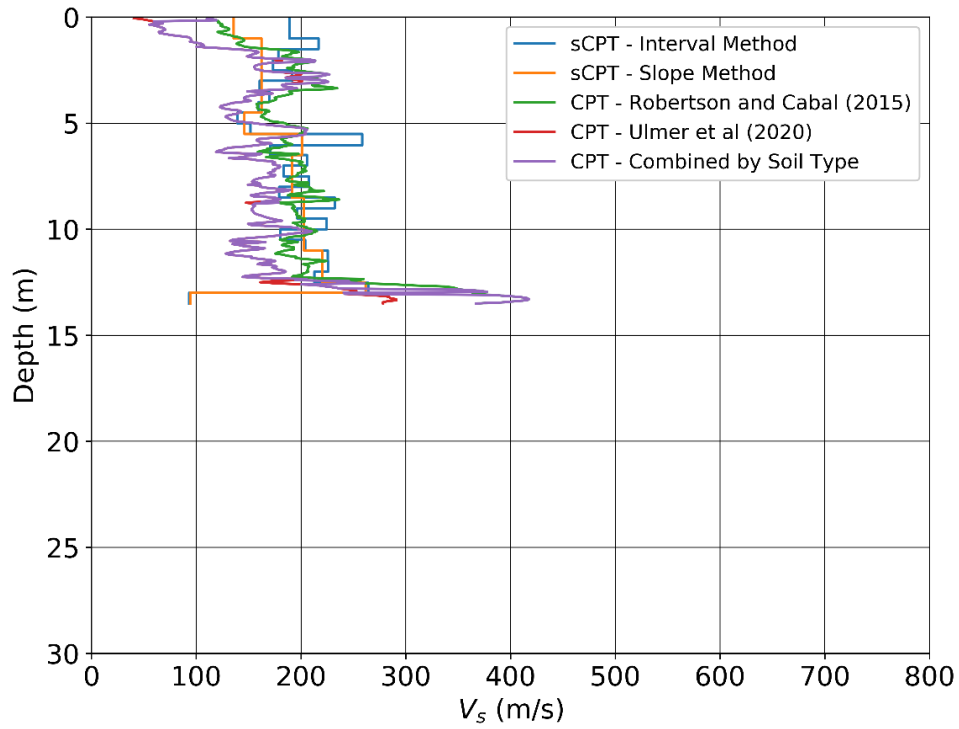


Figure 42. V_s profiles for CPT-09, Site 2, developed using CPT correlations and sCPT tests.

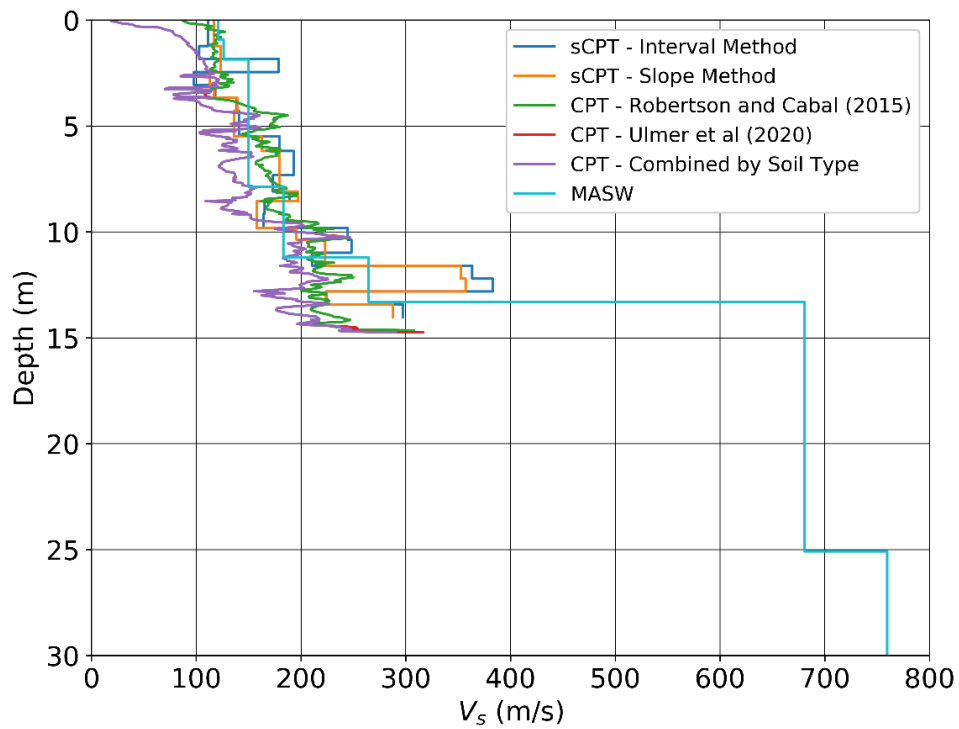


Figure 43. V_s profiles for CPT-10, Site 3, developed using CPT correlations, sCPT tests, and MASW tests.

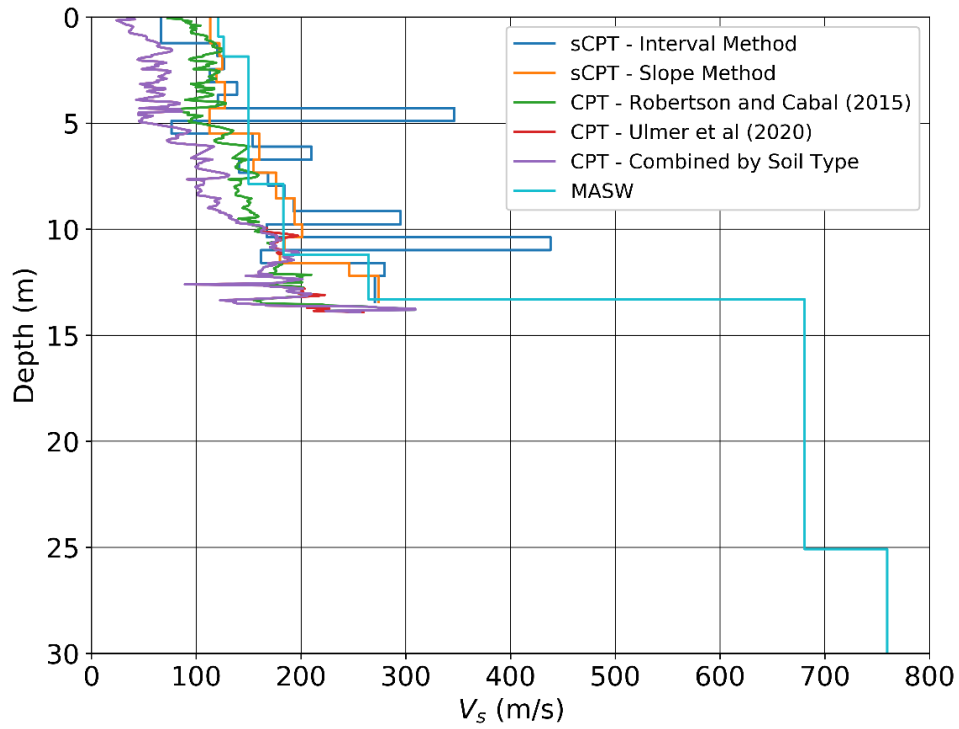


Figure 44. V_s profiles for CPT-11, Site 3, developed using CPT correlations, sCPT tests, and MASW tests.

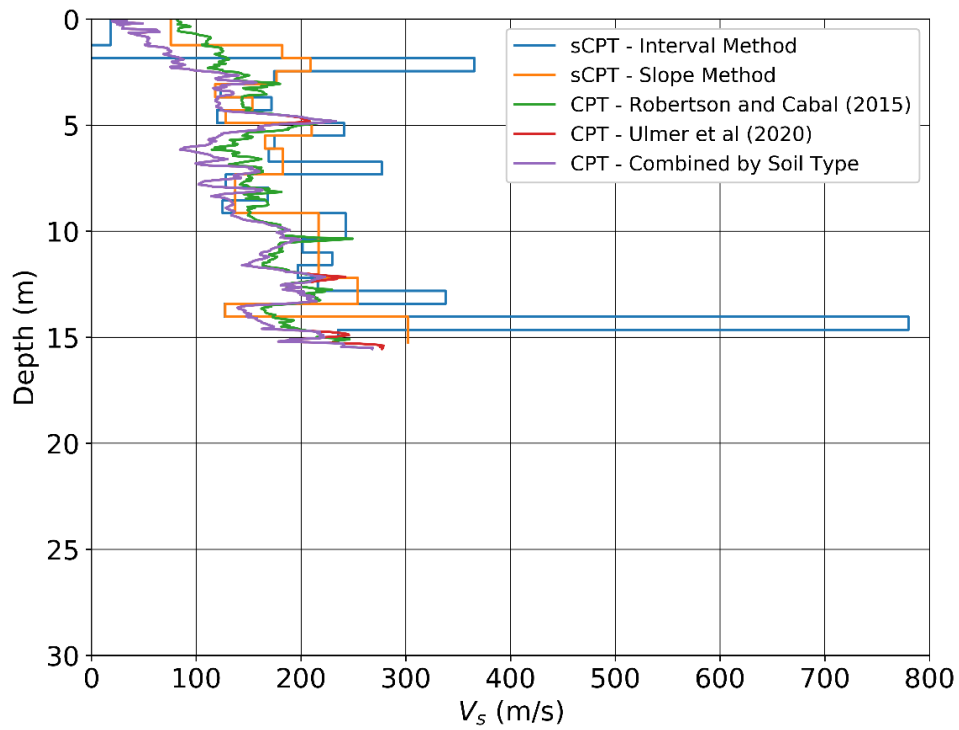


Figure 45. V_s profiles for CPT-12, Site 3, developed using CPT correlations and sCPT tests.

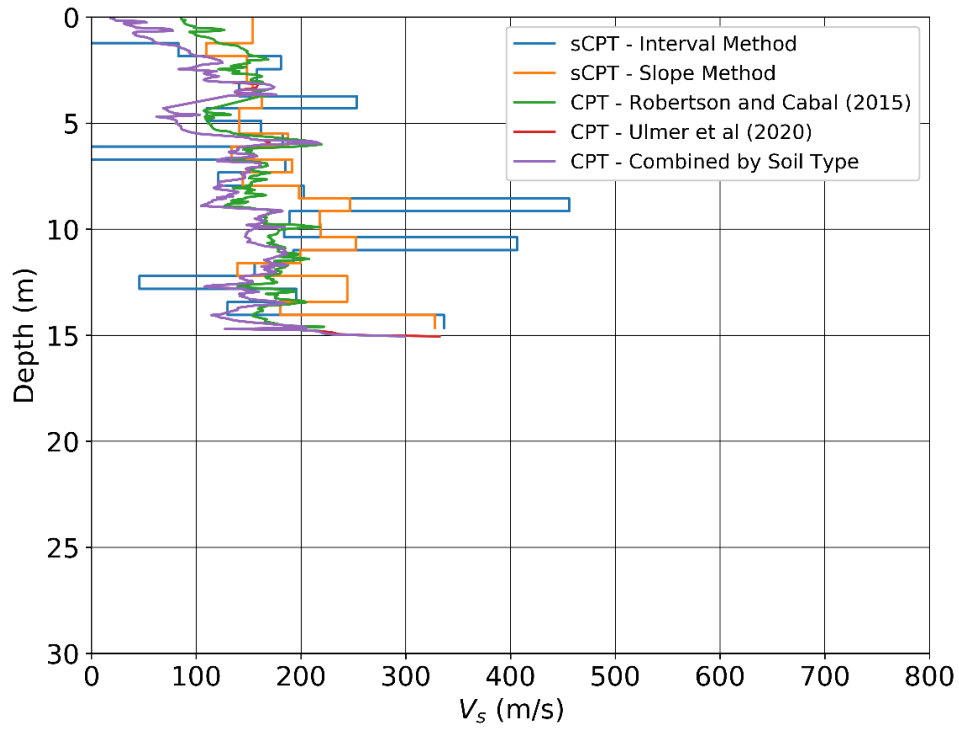


Figure 46. V_s profiles for CPT-13, Site 3, developed using CPT correlations and sCPT tests.

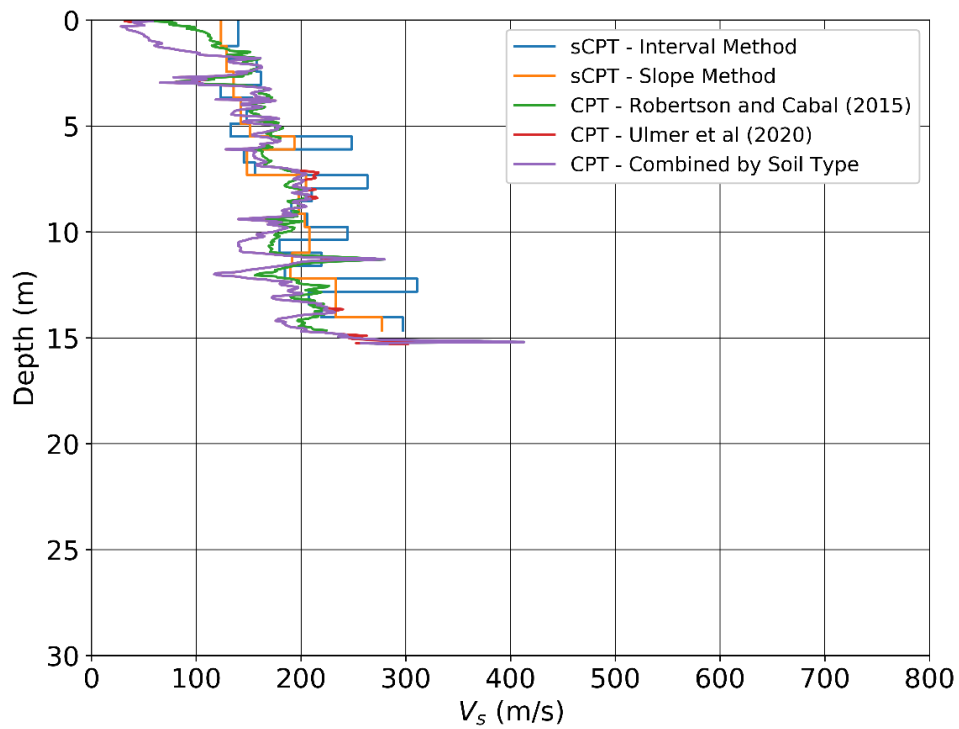


Figure 47. V_s profiles for CPT-14, Site 3, developed using CPT correlations and sCPT tests.

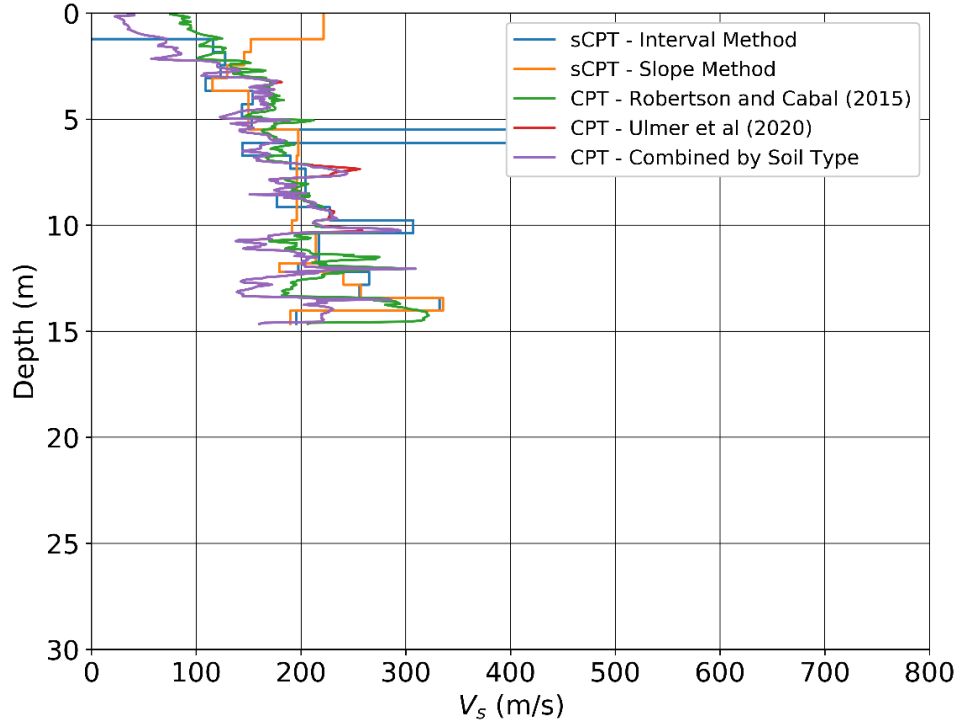


Figure 48. V_s profiles for CPT-15, Site 3, developed using CPT correlations and sCPT tests

There is fairly good agreement among the V_s profiles developed based on the different test methods, although the sCPT interval method leads to more erratic profiles with larger swings in V_s than other methods. This agrees with the observations of Hallal and Cox (2019) that the sCPT slope method provides more reliable velocities than the interval method. V_{s12} at each sounding location was estimated based on tests performed at the given location. These results are provided in Table 3. MASW geophone arrays were laid out between two liquefaction test locations at each site (between CPT-02 and CPT-03, CPT-04 and CPT-05, and CPT-10 and CPT-11 at Sites 1, 2, and 3, respectively). As a result, the same V_{s12} from the MASW tests is presented for both sounding locations. V_{s30} was also estimated at these locations based on MASW results. While there is likely variation in V_{s30} across the sites, V_{s30} for these locations were used as best estimates of V_{s30} for a given site. V_{s30} was estimated at 270.2 m/s, 273.6 m/s, and 285.7 m/s at Sites 1, 2, and 3, respectively. Estimated V_{s12} values were used during model validation to estimate r_d and n_{eq} based on the Lasley et al. (2016), Lasley et al. (2017), and new relationships presented herein. Where available, V_{s12} measurements from sCPT tests were used in liquefaction analysis. MASW results were used if sCPT data were not available, and CPT correlation-based V_{s12} results were used if sCPT and MASW data were not available. Estimated V_{s30} values were used in estimating PGA at the Pawnee test sites based on the Zalachoris and Rathje (2019) GMPE for comparison with PGA values from the USGS ShakeMap (U.S.

Geologic Survey 2016a). Due to source limitations, estimated V_s values from MASW testing for depths greater than 20-25 m entail a large amount of uncertainty. As a result, the estimated V_{s30} values are only approximations. However, the V_{s30} estimates were considered acceptable for the purpose of comparing PGA between the USGS ShakeMap and Zalachoris and Rathje (2019) GMPE. Ground motions used for liquefaction assessment (Section 5.3) were based on the USGS ShakeMap and did not require more accurate estimates of V_{s30} .

Table 3. Estimated V_{s12} (m/s) at CPT Sounding Locations Based on sCPT, CPT, and MASW Tests.

| Sounding | Site | V_{s12} (m/s) | | | | | |
|----------|------|------------------------|---------------------|----------------------------------|---------------------------|-----------------------------|-----------------|
| | | sCPT - Interval Method | sCPT - Slope Method | CPT - Robertson and Cabal (2014) | CPT - Ulmer et al. (2020) | CPT - Combined by Soil Type | MASW |
| CPT-01 | 1 | - | - | 162.65 | 119.95 | 162.65 | - |
| CPT-02 | 1 | - | - | 143.73 | 117.13 | 140.28 | 175.51 177.07 |
| CPT-03 | 1 | - | - | 144.72 | 118.13 | 135.68 | 175.51 177.07 |
| CPT-04 | 2 | 177.40 | 169.02 | 181.30 | 139.05 | 141.58 | 171.60 |
| CPT-05 | 2 | 204.21 | 172.04 | 177.83 | 133.56 | 134.67 | 171.60 |
| CPT-06 | 2 | - | - | 171.91 | 127.51 | 140.19 | - |
| CPT-07 | 2 | - | - | 177.61 | 134.94 | 140.98 | - |
| CPT-08 | 2 | 161.26 | 158.96 | 177.39 | 133.95 | 141.12 | - |
| CPT-09 | 2 | 195.87 | 173.28 | 182.05 | 138.98 | 143.97 | - |
| CPT-10 | 3 | 157.54 | 148.28 | 152.34 | 117.25 | 116.67 | 157.80 |
| CPT-11 | 3 | 147.96 | 142.91 | 126.29 | 77.92 | 77.89 | 157.80 |
| CPT-12 | 3 | 78.31 | 150.18 | 144.98 | 101.96 | 102.04 | - |
| CPT-13 | 3 | 179.41 | 156.54 | 144.39 | 99.41 | 99.71 | - |
| CPT-14 | 3 | 165.65 | 156.89 | 157.34 | 124.37 | 125.99 | - |
| CPT-15 | 3 | 274.14 | 174.91 | 162.27 | 113.79 | 113.77 | - |

CPT test results and V_s profiles were used to create site profiles that could be used in site response analyses as part of the r_d and MSF model development phase of this project. Additionally, the results of the site investigation, in conjunction with field observations of liquefaction, were used to validate the liquefaction triggering model for induced seismicity presented herein. These validation efforts are discussed in Section 5.

4 Development of a New Liquefaction Triggering Model for Induced Seismicity in Oklahoma, Texas, and Kansas

As noted previously, because of differences between the ground motion characteristics of induced earthquakes and tectonic earthquakes as well as regional differences in geologic/soil profiles, it is uncertain whether existing liquefaction hazard evaluation procedures developed for tectonic earthquakes, primarily in active shallow-crustal regions of the WUS, are suitable for use with induced earthquakes in Oklahoma, Texas, and Kansas. Specifically, it is uncertain whether the r_d and MSF relationships used in existing simplified liquefaction evaluation procedures for estimating CSR* are suitable for use with induced earthquakes because both r_d and MSF are affected by ground motion and soil profile characteristics. To address this issue, a new model for evaluating liquefaction potential of soils subjected to ground motions from induced earthquakes in Oklahoma, Texas, and Kansas is developed.

The approach used to develop this liquefaction triggering model was based upon the methods used by Green et al. (2017, 2020) in developing analogous models for evaluating the liquefaction potential from tectonic earthquakes in the CEUS and from induced earthquakes in the Groningen region of the Netherlands. Following this approach, equivalent-linear site response analyses were performed to develop new empirically derived r_d and MSF relationships for induced seismicity in Oklahoma, Texas, and Kansas. The site response analyses were performed using induced ground motion recordings and representative regional soil profiles from the Oklahoma region. The output r_d and n_{eq} profiles from the site response analyses were then used to regress the new r_d and MSF relationships. These new relationships are used to calculate CSR*, which can be used in conjunction with the Green et al. (2019) $CRR_{M7.5}$ curve to evaluate the liquefaction potential of induced earthquakes in Oklahoma, Texas, and Kansas.

In the following sections, brief descriptions of the ground motion database and soil profiles used in model development are provided. Next, the proposed r_d and MSF relationships are presented and comparisons are made with commonly used relationships for tectonic earthquakes. Implementation of the new r_d and MSF models for liquefaction analysis is then discussed. Finally, results of validation tests on the new liquefaction triggering model are presented.

4.1 Induced Ground Motion Database

Motions were selected from the induced ground motion database compiled and processed by the Center for Integrated Seismic Research (CISR) at the University of Texas at Austin (Zalachoris et al. 2020). Ground motions included recordings from Oklahoma, Texas, and Kansas. All motions in the database were consistently processed as described in Zalachoris and Rathje (2019). The recordings were instrument corrected and the mean was removed, and the records were examined for obvious irregularities (i.e.,

clipping, distortion, apparent high noise) on an individual basis. A 5% cosine taper, acausal Butterworth filter, and baseline correction were then applied. The high-pass and low-pass filter frequencies were determined based on a Signal-to-Noise Ratio (SNR) threshold of 3. Any records with SNR values consistently less than 3 within the examined bandwidth were rejected. Overall, the ground motion database compiled by Zalachoris and Rathje (2019) consists of 4,815 3-component ground motion records from 223 seismic stations.

For the purpose of this research, motions were selected that had $M_w > 3.5$ and $R_{hyp} < 70$ km. Although the range of magnitudes of interest to liquefaction hazard evaluations is generally higher than $M_w 4.5$ (Green and Bommer 2019), lower magnitude events were included to constrain the lower end of the regressed r_d and MSF relationships. Induced earthquakes are generally small magnitude events with shallow focal depths. For this reason, induced ground motions often have large amplitudes near the source but attenuate quickly with distance (Atkinson 2020; Zalachoris and Rathje 2019). For this reason, the hypocentral distance of the selected motions was limited to 70 km because induced motions at greater distances do not generate damaging ground motions. Only ground motion recordings from sites with $V_{s30} \geq 600$ m/s were used in site response analysis.

Due to the scarcity of motions having $M_w > 5.1$ and $R_{hyp} < 50$ at sites with $V_{s30} \geq 600$, additional ground motions from softer sites ($500 \leq V_{s30} \leq 600$) were spectrally matched to reference rock site conditions using the approach developed by Al Atik and Abrahamson (2010) and implemented by the program RSPMatch09. Recorded ground motions were matched to spectra developed using the Zalachoris and Rathje (2019) and Novakovic et al. (2018) GMPEs. The Zalachoris and Rathje (2019) GMPE predicts spectra based on rotation-angle independent geometric average of horizontal ground-motion amplitudes (RotD50) (Boore 2010), while the Novakovic et al. (2018) GMPE predicts spectra for the geometric mean of the horizontal components of motion. RotD50 amplitudes are typically very similar to geometric mean amplitudes (Novakovic et al. 2018), which allows a direct comparison of the two GMPEs.

The spectral matching process scales ground motions based on amplitude while maintaining duration characteristics such as t_{5to95} (Al Atik and Abrahamson 2010). As a result, scaling ground motions for an event of a given magnitude to the response spectrum of an event of a larger magnitude will reflect the increased amplitude but not necessarily the increased duration expected for a larger magnitude event. This can lead to errors when trying to model the relationship between M_w , a_{max} , and n_{eq} because n_{eq} is directly related to ground motion duration. Similar issues occur when spectrally matching ground motions with a given R_{hyp} to a spectrum developed using a different R_{hyp} , because the influence of R_{hyp} on duration and n_{eq} may not be properly maintained during the spectral matching process. To avoid these errors and to preserve the relationships among M_w , a_{max} , R_{hyp} , duration, and n_{eq} , ground motions were only spectrally matched to

spectra for events having the same M_w and R_{hyp} . This essentially allowed for ground motions from softer sites ($500 \leq V_{s30} \leq 600$) to be scaled to stiffer site conditions for use in site response analyses while maintaining M_w and R_{hyp} . These constraints limited the available motions for use in site responses analyses, but did provide several additional ground motions with $M_w \geq 4.7$ and $R_{hyp} < 50$, while avoiding any issues in modelling n_{eq} . Ground motions were scaled to spectra for site conditions at the NEHRP B/C site class boundary ($V_{s30} = 760$ m/s) (American Society of Civil Engineers 2010), which is the default output for the Novakovic et al. (2018) GMPE. A sensitivity analysis on the effect of the target V_{s30} on site response was performed, and it was found that site response results were fairly insensitive to the selected target V_{s30} for $760 \text{ m/s} \leq V_{s30} \leq 1100 \text{ m/s}$. This corresponds to the range of V_{s30} values for the majority of recording stations used as sources for this study.

Al Atik and Abrahamson (2010) note that while site condition (e.g., V_{s30}) is an important factor in ground motion scaling, it is not as important in spectral scaling methods such as theirs. This is true as long as extreme conditions such as very soft soil sites are excluded because the spectral matching process is able to correct for differences in frequency content between the rock and soil sites. Furthermore, Bahrampouri et al. (2020) found no significant trends between duration and V_{s30} for $V_{s30} \geq 500$ m/s. As a result, scaling ground motions with $V_{s30} \geq 500$ m/s to $V_{s30} = 760$ m/s is not expected to significantly affect ground motion duration or alter observed trends among M_w , a_{max} , R_{hyp} , and n_{eq} .

The resulting distribution of the ground motions used in the site response analyses is shown in Figure 49. To account for potential differences in the spectra generated using the Zalachoris and Rathje (2019) and Novakovic et al. (2018) GMPEs, two ground motion databases were developed: the first is comprised of the recorded ground motions and motions matched to spectra developed using the Zalachoris and Rathje (2019) GMPE and the second is comprised of the recorded ground motions and motions matched to spectra developed using the Novakovic et al. (2018) GMPE. Site response and regression analyses were then carried out using both databases and the results compared.

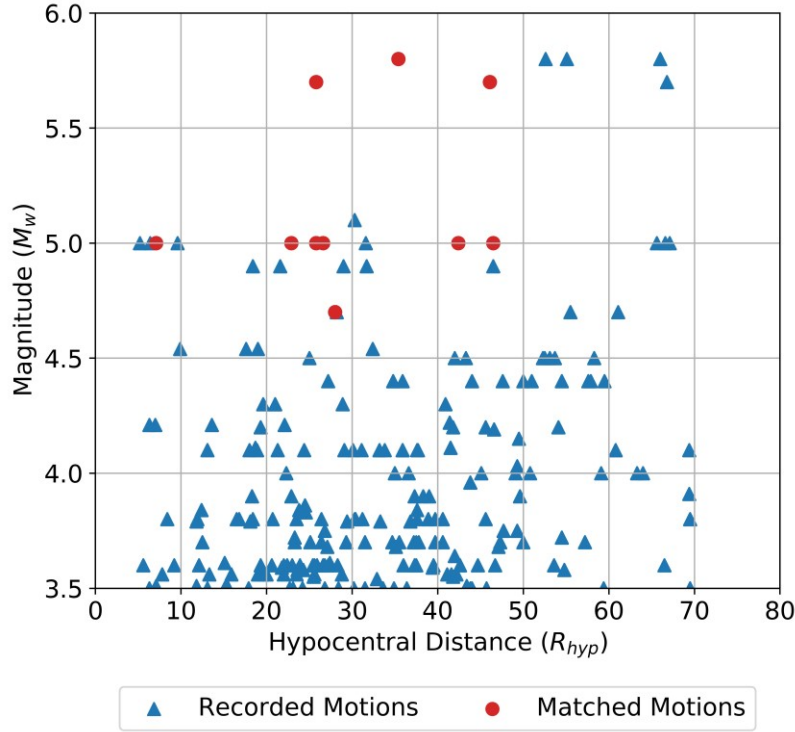


Figure 49. Magnitude versus distance distribution of the ground motion database used in this study.

4.2 Representative Soil Profiles

Representative soil profiles for the region were developed for use in site response analyses. In addition to the profiles developed based on the site investigation discussed in Section 3, soil profiles were also developed based on soil profile information from several other sites across Oklahoma. A map of these additional sites is provided in Figure 50.

Soil profile data at these sites were provided by contractors and government agencies and included a mix of CPT, SPT, and lab test data. Soil parameters required for site response analysis include V_s , total unit weight of the soil, and depth to groundwater table. Additional soil parameters used during site response analyses include PI, over-consolidation ratio, and strength parameters such as friction angle, $(N_1)_{60}$, and undrained shear strength. V_s values for these additional sites were estimated using correlations with CPT (Robertson and Cabal 2015; Ulmer et al. 2020) and SPT (Ulmer et al. 2020; Wair et al. 2012) results. Other soil parameters were obtained from lab test data when available. At sites where lab test information was not available, soil parameters were estimated using CPT correlations (Robertson and Cabal 2015) or randomly assigned using soil type-specific distributions developed using the lab test data from the other sites.



Figure 50. Source locations for site profile data.

Although the data provided for these sites allowed for reasonable characterization of the soil profiles at these sites, information about the bedrock layers (e.g., V_s , weathered rock thickness) was generally not available. To address this issue, bedrock V_s data from Stephenson et al. (n.d.) was used to estimate bedrock layering and V_s values at each site. Stephenson et al. (n.d.) developed V_s profiles at 28 seismograph stations located in central and northern Oklahoma near the epicenters of the 2011 Fairview, 2016 Pawnee, and 2016 Cushing, Oklahoma earthquakes. The developed V_s profiles consisted of 3-4 layers generally intended to reflect a soil/weathered rock/rock profile. Weathered rock and bedrock information from these profiles was used to develop statistical distributions for V_s of the bedrock (V_{sbed}) and the thickness of weathered rock zone between the soil and bedrock layers for use in the current study. These distributions were used to randomly assign V_{sbed} and weathered rock thickness for the developed site profiles. V_{sbed} for the Stephenson et al. (n.d.) ranged from 800 to 2700 m/s and roughly followed a log-normal distribution with a mean ($\mu_{\ln(V_{sbed})}$) of 7.26 (1508.5 m/s) and standard deviation ($\sigma_{\ln(V_{sbed})}$) of 0.32. This range is consistent with V_{sbed} values for CEUS site profiles used by Lasley et al. (2016, 2017) in developing r_d and n_{eq} relationships for the CEUS.

The thickness of the weathered rock transition zone between the soil profile and bedrock layers ranged from 0 to 28 m and approximately exhibited a normal distribution with mean of 16 m and standard deviation of

7.5 m. This weathered rock transition was also added to the developed profiles using a randomly assigned thickness based on the Stephenson et al. (n.d.) distribution. For the purposes of the developed profiles, the transition zone was divided into four sublayers with V_s values linearly increasing from the V_s at the base of the soil profile to V_{sbed} . This approach, as well as this range of weathered rock thicknesses, is consistent with weathered rock transitions observed in the Lasley et al. (2016, 2017) CEUS profiles.

In order to account for the effect of the random distributions used to develop the site profiles, three iterations of each profile were created using different realizations of each randomly assigned soil or rock parameter. Site response analysis results for all iterations were included in the regression database.

4.3 *Equivalent-Linear Site Response Analysis*

Equivalent-linear site response analyses were performed using ShakeVT2 (Lasley et al. 2014; Thum et al. 2019), a rewrite of SHAKE and SHAKE91 (Idriss and Sun 1992; Schnabel et al. 1972). Separate analyses were performed using both the Darendeli and Stokoe (2001) and Ishibashi and Zhang (1993) MRD curves. These curves are used to model the nonlinear response of the soil. The results from analyses using the two different MRD curves were compared to see the effects of the curves on the resulting r_d and n_{eq} relationships. Site response analyses were used to output r_d and n_{eq} data for each liquefiable soil layer as a function of depth for ground motion/site profile combination. This was repeated for both ground motion databases, resulting in four sets of site response analysis results developed using: (1) the Zalachoris and Rathje (2019) ground motion database with Ishibashi and Zhang (1993) MRD curves (hereafter referred to as the ZR19_IZ dataset), (2) the Zalachoris and Rathje (2019) ground motion database with Darendeli and Stokoe (2001) MRD curves (ZR19_DS dataset), (3) the Novakovic et al. (2018) ground motion database with Ishibashi and Zhang (1993) MRD curves (Nea18_IZ dataset), and (4) the Novakovic et al. (2018) ground motion database with Darendeli and Stokoe (2001) MRD curves (Nea18_DS dataset). Separate r_d , n_{eq} , and MSF relationships were developed for each dataset to account for the effects of MRD and GMPE selection on the regressed relationships.

4.4 *Proposed r_d Relationship*

Figure 51 presents the output r_d from site response analyses as a function of the predictor variables used in the Green et al. (2020) model. These included depth, M_w , $\ln(a_{max})$, and V_{s12} . For clarity, plots for M_w , $\ln(a_{max})$, and V_{s12} were shown for data for depths from 5 to 10 m, although similar trends were observed at other depths. Other variables were considered for inclusion in the model, but none were shown to be significant predictors of r_d . Plots are shown for the ZR19_IZ dataset, but the observed trends are similar for all datasets. The trend of r_d with depth follows a sigmoidal shape, similar to the trend observed by Green et al. (2020), with r_d decreasing with increasing depth. Positive correlations are observed between r_d and both

M_w and V_{s12} while a negative correlation is observed between r_d and a_{max} . The observed trend between M_w and r_d is consistent with previous studies and the expectation that larger magnitude events with longer wavelengths will lead to more rigid profile response (higher r_d). The observed positive trend between V_{s12} and r_d is also consistent with Green et al. (2020) and Lasley et al. (2016). Stiffer soil profiles (higher V_{s12}) would be expected to behave more rigidly as demonstrated by the data shown in Figure 51. The negative correlation between a_{max} and r_d is consistent with the findings of Green et al. (2020) and Cetin (2000). Lasley et al. (2016) also noted that a strong correlation between r_d and shaking intensity as measured by a_{max} would be expected, but they did not find significant correlation between a_{max} and r_d for their dataset. Based on the observed trends in the r_d datasets, as well as observations from previous studies, it was decided that M_w , a_{max} , and V_{s12} would be included in the r_d regression.

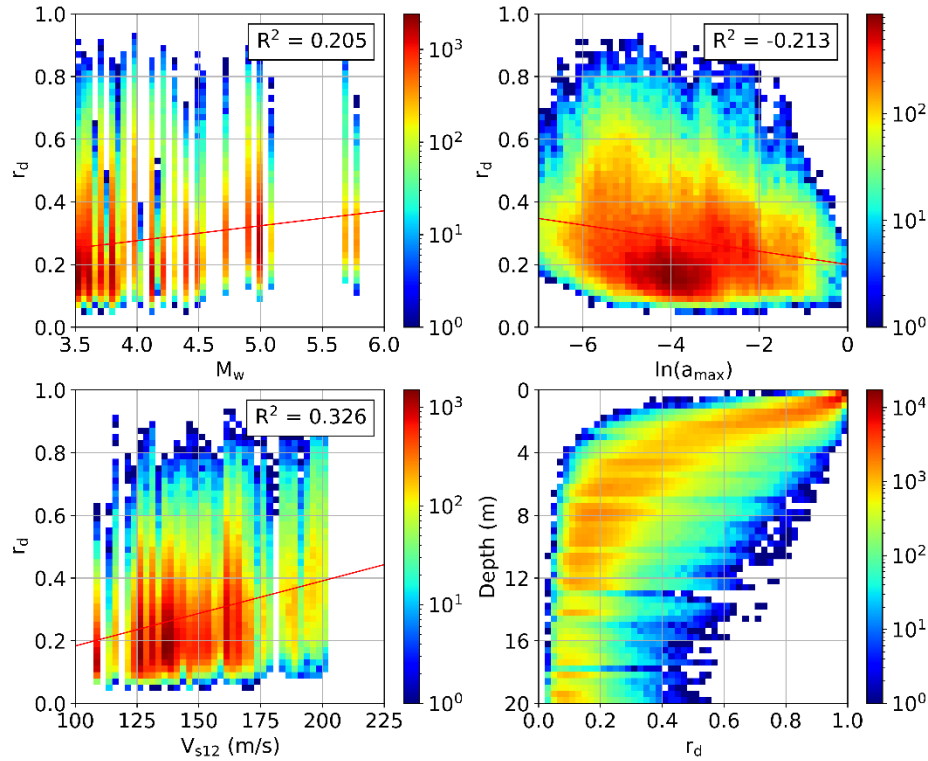


Figure 51. Heat map of r_d versus potential predictor variables: M_w , $\ln(a_{max})$, V_{s12} , and depth. Plots for M_w , $\ln(a_{max})$, and V_{s12} are for depths of 5 to 10 m. Values shown are for the ZR19_IZ dataset.

Statistical regressions for this project were performed using the program *R* (R Core Team 2018) with the *lme4* package (Bates et al. 2015). The *lme4* package implements mixed effects regressions, which were used to avoid potential biases from earthquakes or profiles that have a relatively large number of data points. Random effects terms were included during both the r_d and n_{eq} regressions. These included an earthquake

event term and a soil profile term as shown in the r_d and n_{eq} relationships presented in this and the following section.

Several functional forms for r_d were considered, including the Lasley et al. (2016) and Green et al. (2020) functional forms presented in Section 2.3.1. The final function form was a slightly modified version of the r_d functional form from Green et al. (2020), which is based on a sigmoid shape with a main variable of logarithmic depth, and location and scale parameters that are functions of M_w , a_{max} , and V_{s12} . This proposed r_d relationship is

$$r_{d-ok} = 1 - \frac{A_{rd}}{1 + \exp\left[-\frac{\ln(z) - B_{rd}}{C_{rd}}\right]} + \beta_{15} + \delta_{event_rd} + \delta_{profile_rd} + \delta_{0_rd}; 0 \leq r_d \leq 1 \quad (11)$$

where z is depth in m, A_{rd} , B_{rd} , and C_{rd} are functions of M_w , a_{max} , and V_{s12} ; β_{15} is a regression coefficient; δ_{event_rd} and $\delta_{profile_rd}$ are random effect terms for the earthquake events and soil profiles; and δ_{0_rd} is the residual. The random effect terms and residual terms are assumed to be zero-mean normally distributed random variables with standard deviations of τ_{event_rd} , $\tau_{profile_rd}$, σ_{0_rd} for the event, profile, and residual terms, respectively. As with the Green et al. (2020) study, an apparent scaling break for relatively large values of a_{max} ($> 0.25g$ for this study) was observed and included in the regression. Functional forms with the random effect terms included in the A_{rd} term, providing for depth-dependent random effects, were considered. However, analysis of the residuals of a mixed effect regression that did not include the profile random effect showed no significant trends in depth-dependence as a function of profile. Similarly, an analysis of the residuals of a mixed effect regression that did not include the event random effect showed no significant trends in depth-dependence as a function of earthquake event. As a result, depth-independent random effect terms were used as shown in Equation (11).

Two sets of relationships were developed for A_{rd} , B_{rd} , and C_{rd} , one with V_{s12} and one without V_{s12} , to allow for this model to be used for varying levels of site characterization. The first set of expressions for A_{rd} , B_{rd} , and C_{rd} when V_{s12} is available is:

$$A_{rd} = \beta_1 + \beta_4 \cdot M_w + \beta_5 \cdot \ln(a_{max}) + \beta_9 \cdot V_{s12}; \text{ for } a_{max} \leq 0.25g \quad (12a)$$

$$= \beta_1 + \beta_4 \cdot M_w + \beta_5 \cdot \ln(a_{max}) + \beta_8 \cdot \ln\left(\frac{a_{max}}{0.25}\right) + \beta_9 \cdot V_{s12}; \text{ for } a_{max} > 0.25g \quad (12b)$$

$$B_{rd} = \beta_2 + \beta_6 \cdot M_w + \beta_{10} \cdot \ln(a_{max}) + \beta_{14} \cdot V_{s12}; \text{ for } a_{max} \leq 0.25g \quad (13a)$$

$$= \beta_2 + \beta_6 \cdot M_w + \beta_{10} \cdot \ln(a_{max}) + \beta_{12} \cdot \ln\left(\frac{a_{max}}{0.25}\right) + \beta_{14} \cdot V_{s12}; \text{ for } a_{max} > 0.25g \quad (13b)$$

$$C_{rd} = \beta_3 + \beta_7 \cdot M_w + \beta_{11} \cdot \ln(a_{max}); \text{ for } a_{max} \leq 0.25g \quad (14a)$$

$$= \beta_3 + \beta_7 \cdot M_w + \beta_{11} \cdot \ln(a_{max}) + \beta_{13} \cdot \ln\left(\frac{a_{max}}{0.25}\right); \text{ for } a_{max} > 0.25g \quad (14b)$$

and the second set when V_{s12} is not available is:

$$A_{rd} = \beta_1 + \beta_4 \cdot M_w + \beta_5 \cdot \ln(a_{max}); \text{ for } a_{max} \leq 0.25g \quad (15a)$$

$$= \beta_1 + \beta_4 \cdot M_w + \beta_5 \cdot \ln(a_{max}) + \beta_8 \cdot \ln\left(\frac{a_{max}}{0.25}\right); \text{ for } a_{max} > 0.25g \quad (15b)$$

$$B_{rd} = \beta_2 + \beta_6 \cdot M_w + \beta_{10} \cdot \ln(a_{max}); \text{ for } a_{max} \leq 0.25g \quad (16a)$$

$$= \beta_2 + \beta_6 \cdot M_w + \beta_{10} \cdot \ln(a_{max}) + \beta_{12} \cdot \ln\left(\frac{a_{max}}{0.25}\right); \text{ for } a_{max} > 0.25g \quad (16b)$$

$$C_{rd} = \beta_3 + \beta_7 \cdot M_w + \beta_{11} \cdot \ln(a_{max}); \text{ for } a_{max} \leq 0.25g \quad (17a)$$

$$= \beta_3 + \beta_7 \cdot M_w + \beta_{11} \cdot \ln(a_{max}) + \beta_{13} \cdot \ln\left(\frac{a_{max}}{0.25}\right); \text{ for } a_{max} > 0.25g \quad (17b)$$

where β_i are regression coefficients, a_{max} is in units of g, and V_{s12} is in units of m/s. The two sets of expressions will hereafter be referred to as r_d Model 1 (with V_{s12}) and r_d Model 2 (without V_{s12}) in this report. Regressions were performed using all four datasets. A bootstrapping technique (Efron and Tibshirani 1994) was used during regression to obtain mean and standard deviations for all regression coefficients. The bootstrapping technique consisted of the following steps:

1. 30,000 data points were randomly selected (without replacement) from the dataset.
2. Regression coefficients were obtained for the sampled 30,000 data points and the functional form of interest.
3. Steps 1 and 2 were repeated 1,000 times and the regression coefficients for each iteration were recorded.
4. The mean and standard deviation of the distribution of each regression coefficient were calculated.

The mean values and standard deviations of the regression coefficients for the r_d models are presented in Table 4. Standard deviation can be used as a measure of whether the coefficients are well-constrained by the data. Based on the low observed standard deviations relative to the mean values, M_w , a_{max} , and V_{s12} appear well-constrained by the data. Standard deviations were somewhat higher for terms in A_{rd} than for terms in B_{rd} and C_{rd} . This appears to reflect the relatively small variation in r_d at larger depths, which is governed in the model by A_{rd} . The A_{rd} terms were kept because model residuals at depth increased for

models where these terms were removed. Regressed values of τ_{event_rd} and $\tau_{profile_rd}$, are presented in Table 4.

Table 4. Regression coefficients for r_d Models 1 and 2.

| | Model 1: $r_d = f(z, M_w, a_{max}, V_{s12})$ | | | | Model 2: $r_d = f(z, M_w, a_{max})$ | | | |
|-----------------------|--|-------------------------|-------------------------|-------------------------|---|-----------------|----------------|-----------------|
| Dataset: | ZR19_DS | Nea18_DS | ZR19_IZ | Nea18_IZ | ZR19_DS | Nea18_DS | ZR19_IZ | Nea18_IZ |
| β_1 | 0.9504 | 0.9843 | 0.9514 | 0.9693 | 0.9147 | 0.9545 | 0.8939 | 0.9172 |
| σ_{β_1} | 0.02106 | 0.02286 | 0.02085 | 0.02281 | 0.01842 | 0.02133 | 0.01842 | 0.01989 |
| β_2 | -1.1204 | -1.2094 | -0.9855 | -1.0643 | -0.4313 | -0.5251 | -0.3243 | -0.4058 |
| σ_{β_2} | 0.05544 | 0.05976 | 0.05682 | 0.05977 | 0.04749 | 0.04971 | 0.04541 | 0.04927 |
| β_3 | 0.05063 | 0.00191 | 0.03472 | -0.03643 | 0.04963 | 0.00539 | 0.02729 | -0.03972 |
| σ_{β_3} | 0.03463 | 0.03781 | 0.03344 | 0.03706 | 0.03562 | 0.03883 | 0.03341 | 0.03740 |
| β_4 | -0.01387 | -0.02252 | -0.00614 | -0.01079 | -0.01573 | -0.02466 | -0.00802 | -0.01321 |
| σ_{β_4} | 0.003986 | 0.004450 | 0.003882 | 0.004339 | 0.004114 | 0.004746 | 0.004148 | 0.004545 |
| β_5 | -0.01211 | -0.01133 | -0.00957 | -0.00911 | -0.01027 | -0.00944 | -0.00838 | -0.00806 |
| σ_{β_5} | 0.0014337 | 0.0014482 | 0.0013634 | 0.0013855 | 0.001406 | 0.001452 | 0.001364 | 0.001320 |
| β_6 | 0.2283 | 0.2536 | 0.2261 | 0.2480 | 0.2242 | 0.2502 | 0.2240 | 0.2462 |
| σ_{β_6} | 0.008446 | 0.009438 | 0.008375 | 0.009193 | 0.008863 | 0.009666 | 0.008755 | 0.009936 |
| β_7 | 0.09263 | 0.1090 | 0.09936 | 0.1210 | 0.09009 | 0.1052 | 0.09814 | 0.1185 |
| σ_{β_7} | 0.00718 | 0.00788 | 0.00694 | 0.00789 | 0.00736 | 0.00816 | 0.00702 | 0.00796 |
| β_8 | 0.1148 | 0.1365 | 0.0672 | 0.0981 | 0.1507 | 0.1757 | 0.0853 | 0.1148 |
| σ_{β_8} | 0.02984 | 0.03208 | 0.01700 | 0.01862 | 0.03222 | 0.03564 | 0.01713 | 0.01837 |
| β_9 | -2.179×10^{-4} | -1.848×10^{-4} | -3.672×10^{-4} | -3.404×10^{-4} | - | - | - | - |
| σ_{β_9} | 8.383×10^{-6} | 8.515×10^{-6} | 8.361×10^{-6} | 8.582×10^{-6} | - | - | - | - |
| β_{10} | -0.1470 | -0.1452 | -0.1237 | -0.1228 | -0.1435 | -0.1421 | -0.1218 | -0.1210 |
| $\sigma_{\beta_{10}}$ | 0.004163 | 0.004199 | 0.003993 | 0.004088 | 0.004378 | 0.004236 | 0.004075 | 0.003851 |
| β_{11} | -0.050288 | -0.04787 | -0.047108 | -0.04516 | -0.04905 | -0.04675 | -0.04671 | -0.04499 |
| $\sigma_{\beta_{11}}$ | 0.002943 | 0.002915 | 0.002723 | 0.002719 | 0.002899 | 0.003002 | 0.002757 | 0.002778 |
| β_{12} | -1.0824 | -1.1500 | -0.5747 | -0.5665 | -1.0219 | -1.0755 | -0.5377 | -0.5309 |
| $\sigma_{\beta_{12}}$ | 0.09958 | 0.09958 | 0.05256 | 0.05083 | 0.10696 | 0.10234 | 0.05543 | 0.05019 |
| β_{13} | 0.7333 | 0.7687 | 0.3977 | 0.4480 | 0.7772 | 0.8222 | 0.4162 | 0.4628 |
| $\sigma_{\beta_{13}}$ | 0.1298 | 0.1314 | 0.0574 | 0.0625 | 0.1385 | 0.1446 | 0.0605 | 0.0610 |
| β_{14} | 0.004663 | 0.004664 | 0.004568 | 0.004556 | - | - | - | - |
| $\sigma_{\beta_{14}}$ | 0.0002191 | 0.0002247 | 0.0002289 | 0.0002346 | - | - | - | - |
| β_{15} | 0.01109 | 0.01421 | 0.00990 | 0.01367 | 0.00856 | 0.01145 | 0.00855 | 0.01209 |
| $\sigma_{\beta_{15}}$ | 0.002086 | 0.002215 | 0.001998 | 0.002105 | 0.002188 | 0.002227 | 0.002181 | 0.002203 |
| τ_{event_rd} | 0.0547 | 0.0570 | 0.0550 | 0.0574 | 0.0548 | 0.0570 | 0.0551 | 0.0574 |
| $\tau_{profile_rd}$ | 0.0380 | 0.0379 | 0.0360 | 0.0355 | 0.0456 | 0.0449 | 0.0445 | 0.0437 |

Plots of residuals as a function of predictor variables for r_d Models 1 and 2 for the ZR19_IZ dataset are shown in Figure 52 and Figure 53, respectively. This includes M_w , a_{max} , V_{s12} , and depth. Both loess and linear fits to the residuals are presented to show overall trends in the residual. Error bars showing σ_{0_rd} of the binned residuals are also presented. Although there is some variation, binned residuals tend to be mean-zero and normally distributed for both models. This suggests that both models provide acceptable fits to the r_d data for the range of M_w , a_{max} , V_{s12} , and depth considered. Although both models provide acceptable fits to the data, the inclusion of V_{s12} in Model 1 significantly reduced $\tau_{profile}$, indicating a better fit. Model 1 also provided better fits for larger values of a_{max} , which is significant for liquefaction hazard analyses.

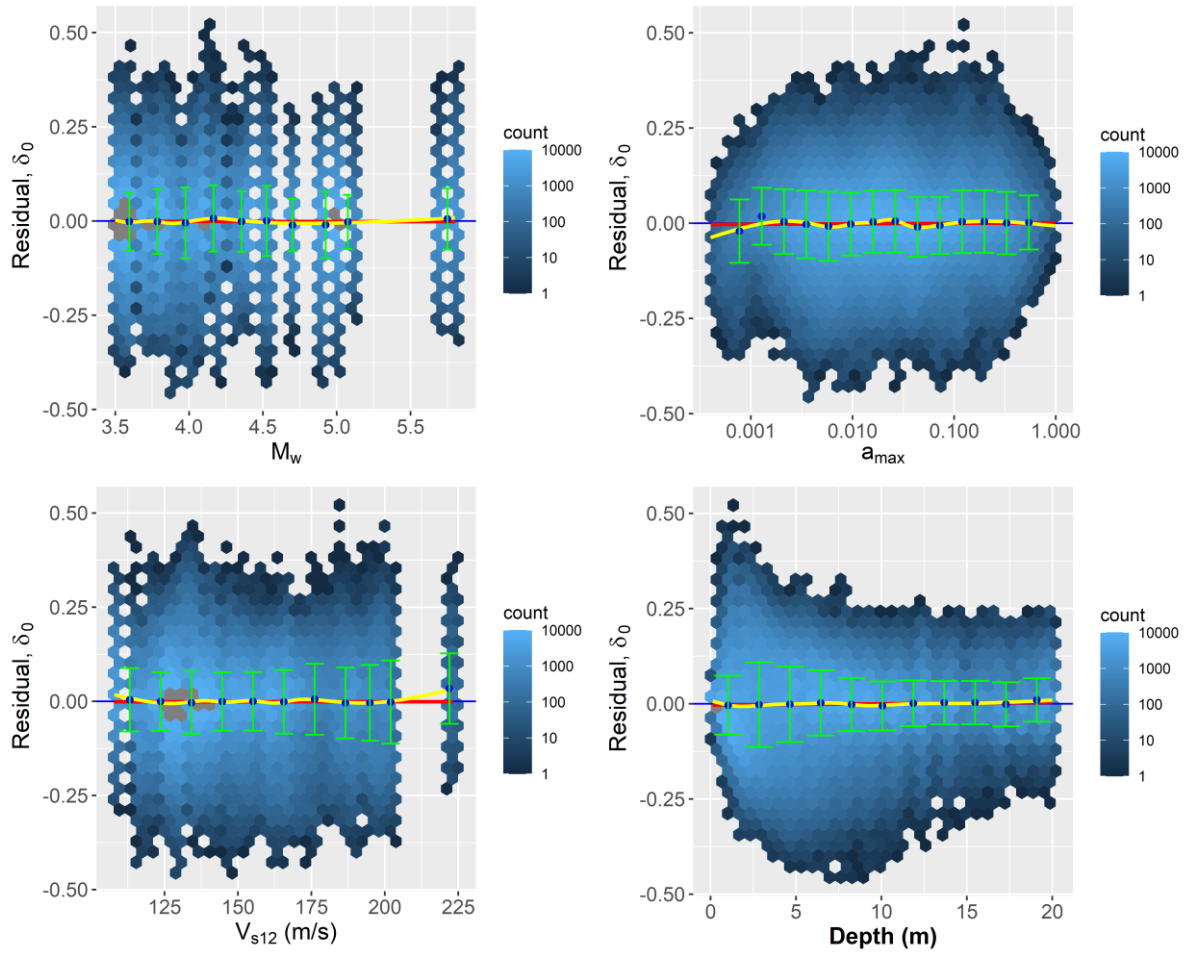


Figure 52. Heat map of r_d Model 1 residuals versus predictor variables (Equations (11) - (14). Yellow lines show loess fits to the residuals, red lines show linear trends fitted to the residuals, and the green error bars show the means and standard deviations of the binned residuals. Results shown for ZR19_IZ dataset.

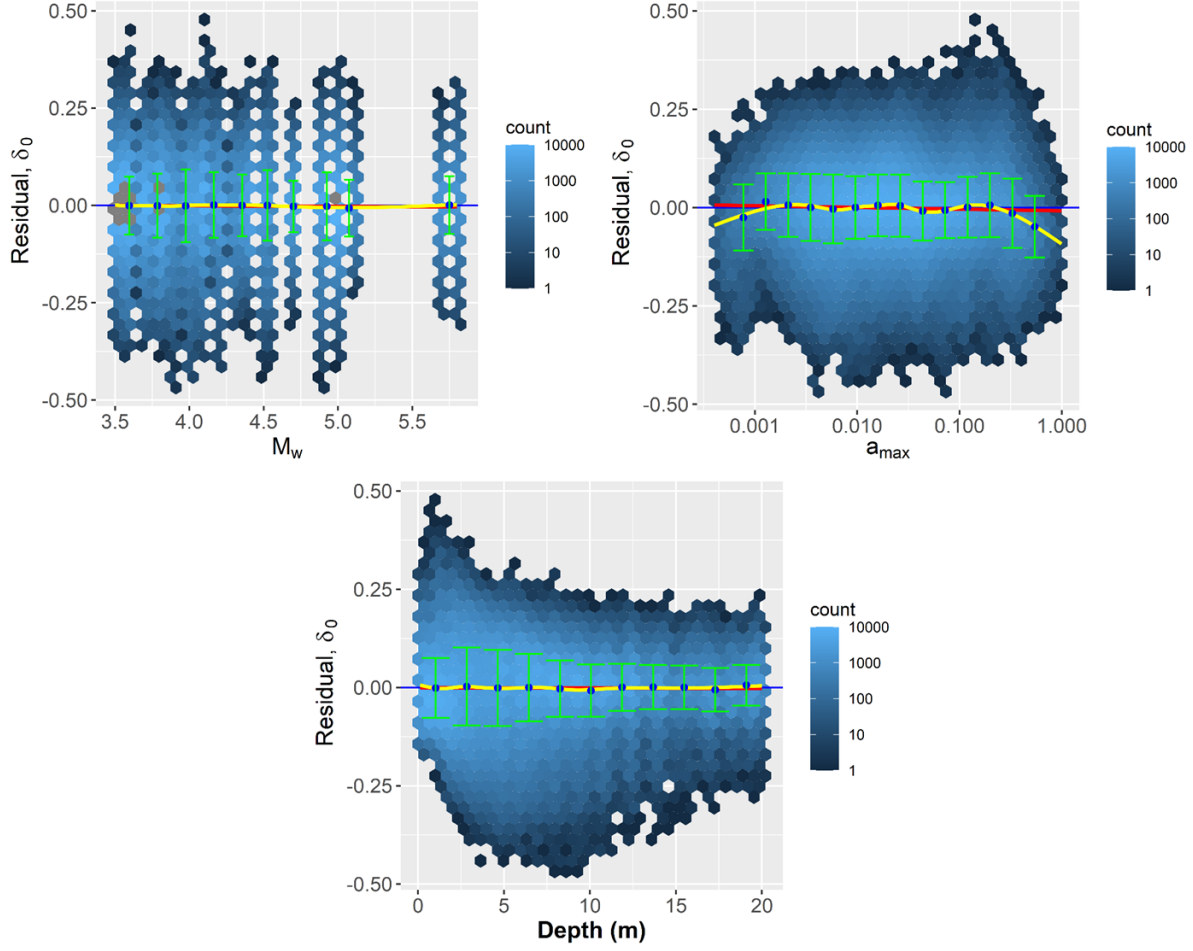


Figure 53. Heat map of r_d Model 2 residuals versus predictor variables (Equations (11), (15 - (17)). Yellow lines show loess fits to the residuals, red lines show linear trends fitted to the residuals, and the green error bars show the means and standard deviations of the binned residuals. Results shown for ZR19_IZ dataset.

Assuming model random effect terms are uncorrelated, the total standard deviation (σ_{total_rd}) can be estimated as:

$$\sigma_{Total_rd} = \sqrt{\tau_{event_rd}^2 + \tau_{profile_rd}^2 + \sigma_{0_rd}^2} \quad (18)$$

As shown in Figure 52 and Figure 53, δ_{0_rd} was found to have a heteroscedastic standard deviation (σ_{0_rd}) that increases with depth for $z \leq 3.5$ m and decreases with depth for $z > 3.5$ m. This behavior was modeled as:

$$\sigma_{0_{rd}}(z) = \frac{\beta_{20}}{\{1+\exp[-\beta_{22}(\ln(z)-\beta_{21})]\}} \cdot \left[\frac{\beta_{18}}{\{1+\exp[-\beta_{19}(3.5-\beta_{17})]\}} + \beta_{16} \right]; \quad (19a)$$

for $z \leq 3.5$ m

$$= \frac{\beta_{18}}{\{1+\exp[-\beta_{19}(z-\beta_{17})]\}} + \beta_{16}; \text{ for } z > 3.5 \text{ m} \quad (19b)$$

A logistic scaling term, the first term in Equation 19a, was used for depths less than 3.5 m because it provided a good fit to the data and ensured σ_0 would be zero at the ground surface. This constraint on σ_0 was used to maintain the constraint of $r_d \leq 1$ near the ground surface. Regression coefficients for Equation 19 were determined through non-linear least squares regression. The regressed coefficients are presented for the $\sigma_{0_{rd}}$ are shown in Table 5. An example of the resulting curve fit for $\sigma_{0_{rd}}$ is provided in Figure 54 for r_d Model 1.

Table 5. Regression coefficients for the $\sigma_{0_{rd}}$ model.

| Model | Dataset | β_{16} | β_{17} | β_{18} | β_{19} | β_{20} | β_{21} | β_{22} |
|-------|----------|--------------|--------------|--------------|--------------|--------------|--------------|--------------|
| 1 | ZR19_DS | 0.0537 | 6.0516 | 0.0647 | -0.3607 | 1.0243 | -0.9984 | 1.6515 |
| 1 | Nea18_DS | 0.0528 | 5.8068 | 0.0682 | -0.3412 | 1.0225 | -0.9988 | 1.6857 |
| 1 | ZR19_IZ | 0.0493 | 6.2395 | 0.0702 | -0.3217 | 1.0324 | -0.9536 | 1.5548 |
| 1 | Nea18_IZ | 0.0498 | 6.0594 | 0.0720 | -0.3126 | 1.0316 | -0.9598 | 1.5610 |
| 2 | ZR19_DS | 0.0521 | 5.8598 | 0.0702 | -0.3411 | 1.0268 | -1.1561 | 1.5023 |
| 2 | Nea18_DS | 0.0529 | 5.7001 | 0.0716 | -0.3322 | 1.0261 | -1.1574 | 1.5126 |
| 2 | ZR19_IZ | 0.0498 | 6.4478 | 0.0687 | -0.3390 | 1.0366 | -1.1536 | 1.3749 |
| 2 | Nea18_IZ | 0.0504 | 6.2425 | 0.0714 | -0.3207 | 1.0364 | -1.1525 | 1.3777 |

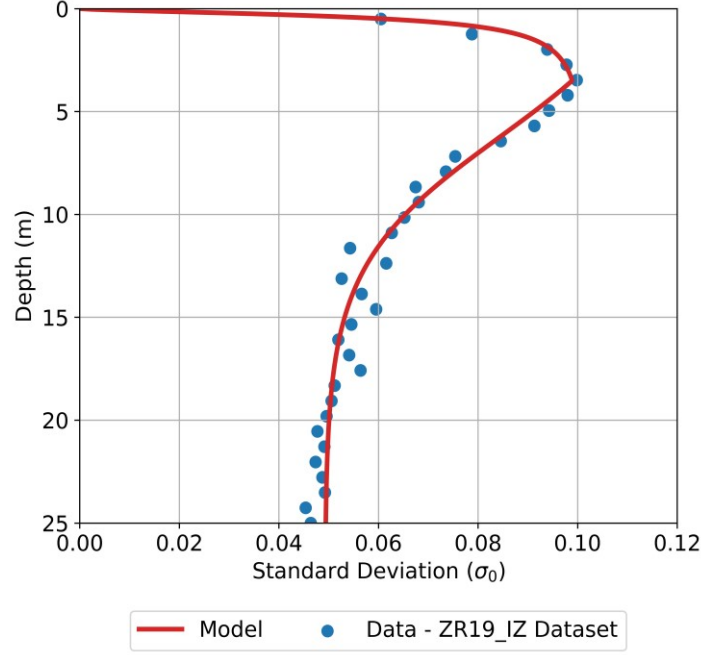


Figure 54. Standard deviation (σ_0) model for r_d Model 1. ZR19_IZ dataset.

Although the random effect terms used in Equation (11) are considered depth-independent, it was still desirable to scale them to zero at the ground surface to ensure $\sigma_{Total_rd} = 0$ and $r_d \leq 1$ at the ground surface. To this end, the logistic scaling term from Equation 19a was applied to τ_{event} and $\tau_{profile}$ at depths less than 3.5 m. The resulting equations for $\tau_{event_rd}(z)$ and $\tau_{profile}(z)$ are

$$\tau_{event_rd}(z) = \frac{\beta_{20}}{\{1 + \exp[-\beta_{22}(\ln(z) - \beta_{21})]\}} \cdot \tau_{event_rd_0}; \text{ for } z \leq 3.5 \text{ m} \quad (20a)$$

$$= \tau_{event_rd_0}; \text{ for } z > 3.5 \text{ m} \quad (20b)$$

and

$$\tau_{profile_rd}(z) = \frac{\beta_{20}}{\{1 + \exp[-\beta_{22}(\ln(z) - \beta_{21})]\}} \cdot \tau_{profile_rd_0}; \text{ for } z \leq 3.5 \text{ m} \quad (21a)$$

$$= \tau_{profile_rd_0}; \text{ for } z > 3.5 \text{ m} \quad (21b)$$

where $\tau_{event_rd_0}$ and $\tau_{profile_rd_0}$ are the depth-independent event and profile random effect standard deviations output during regression (equivalent to τ_{event_rd} and $\tau_{profile_rd}$ in Table 4). Regression coefficients β_{20} through β_{22} from Equations 20 and 21 are the same as from Equation 19. These are listed in Table 5. Total standard deviation as a function of depth is then estimated as:

$$\sigma_{Total_rd}(z) = \sqrt{(\tau_{event_rd}(z))^2 + (\tau_{profile_rd}(z))^2 + (\sigma_{0_rd}(z))^2} \quad (22)$$

Figure 55 shows a comparison of r_d Models 1 and 2 developed for Oklahoma (ZR19_IZ dataset) and the r_d relationships proposed by Lasley et al. (2016) for the CEUS and WUS and by Idriss (1999) for the WUS. Estimates are shown for $M_w = 4.5, 5.0, \text{ and } 5.8$, representative of the general range of overlap for the presented models, and for V_{s12} values 120 m/s and 180 m/s to illustrate the effect of V_{s12} on the predicted r_d . As may be observed from this figure, the r_d estimates for the Oklahoma model tend to be lower than for the Lasley et al. (2016) or Idriss (1999) models for the range of M_w and V_{s12} shown. For $M_w \leq 5$, $V_{s12} = 120$ m/s, and depths greater than approximately 12 m, the difference between the Oklahoma models and Lasley et al. (2016) models is not large. However, for shallower depths, larger M_w , and/or higher V_{s12} , the Lasley et al. (2016) models predict similar r_d values to the Oklahoma models. The Oklahoma models exhibit weaker scaling with both M_w and V_{s12} than the tectonic models. As a result, the difference between r_d estimated by the models becomes significantly more pronounced with increases in either M_w or V_{s12} , particularly for depths between 2 and 10 m.

The Idriss (1999) model leads to larger over-predictions than Lasley et al. (2016) for all values of M_w , a_{max} , and V_{s12} considered. As expected, the Oklahoma models are closer to the Lasley et al. (2016) CEUS model than to either of the WUS models. However, the Lasley et al. (2016) CEUS model still tends to significantly over-predict r_d for $M_w > 5$ and larger V_{s12} values. These trends are consistent with the observations of Novakovic et al. (2018) that induced ground motions are similar to tectonic motions for low M_w but exhibit larger spectral accelerations for higher M_w . The observed trends are also consistent with the observation made by Zalachoris and Rathje (2019) that induced motions with $R_{hyp} < 20$ km have higher spectral accelerations than tectonic motions. Both studies found the differences in spectral accelerations are particularly pronounced at higher frequencies. Greater high frequency content is expected to lead to less rigid response of the soil column and, thus, lower r_d . This is consistent with the lower r_d values estimated by the Oklahoma models. Model 1 for Oklahoma, which includes V_{s12} , exhibits a trend of increasing r_d with increasing V_{s12} . This is consistent with expectations that stiffer soil profiles will exhibit more rigid soil response and larger values of r_d . However, the scaling of r_d with V_{s12} is not as pronounced for the Oklahoma models as for either of the Lasley et al. (2016) models.

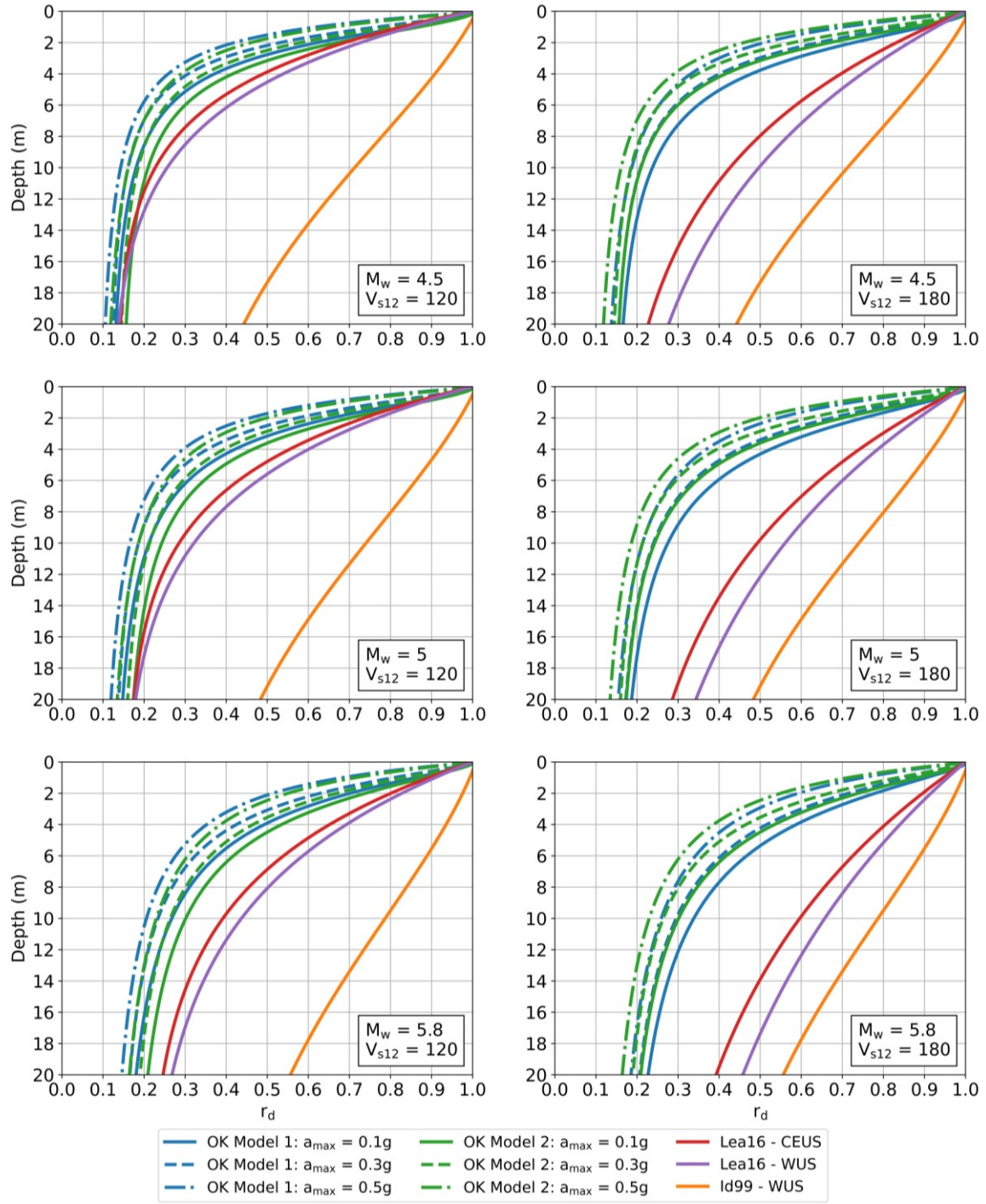


Figure 55. Comparison of r_d models 1 and 2 from the current study (ZR19_IZ dataset) to relationships proposed by Lasley et al. (2016) [Lea16] for the CEUS and WUS and by Idriss (1999) [I99] primarily for the WUS for $M_w = 4.5, 5.0, \text{ and } 5.8$ and $V_{s12} = 120 \text{ m/s}$ and 180 m/s . Estimates for the Oklahoma models are presented for $a_{max} = 0.1g, 0.3g, \text{ and } 0.5g$.

Figure 56 shows a comparison of r_d Model 1 for the ZR19_IZ, ZR19_DS, Nea18_IZ, and Nea18_DS datasets. Curves are shown for $M_w = 4.5, 5.0, \text{ and } 5.8$; $a_{\max} = 0.1g \text{ and } 0.5g$; and $V_{s12} = 120 \text{ m/s and } 180 \text{ m/s}$. Overall trends with depth are similar for the four models, particularly relative to the Lasley et al. (2016) and Idriss (1999) models. However, predicted r_d for the ZR19 datasets tends to be higher than for the Nea18 datasets. The ZR19 estimates for the M_w , a_{\max} , and V_{s12} range values shown are approximately 0-12% higher than the Nea18 estimates. The differences in estimated r_d tend to increase with M_w and depth, decrease with increasing a_{\max} , and remain constant with changes in V_{s12} . Differences are also noted when comparing r_d estimates for the IZ and DS MRD datasets. For $a_{\max} = 0.5g$, estimated r_d for the DS datasets tend to be 10-15% larger than the IZ datasets for depths less than approximately 6 m but approximately 5% smaller for depths greater than 6 m. For $a_{\max} = 0.1g$, predictions are similar for DS and IZ at shallow depths, but estimates for the IZ datasets are 2-10% higher for depths greater than 6 m. The observed differences tend to increase with increases in M_w and decrease with increases in V_{s12} . While the impact of MRD and GMPE selection on r_d tends to be small, the additional uncertainty resulting from MRD and GMPE selection should be considered in forward analyses.

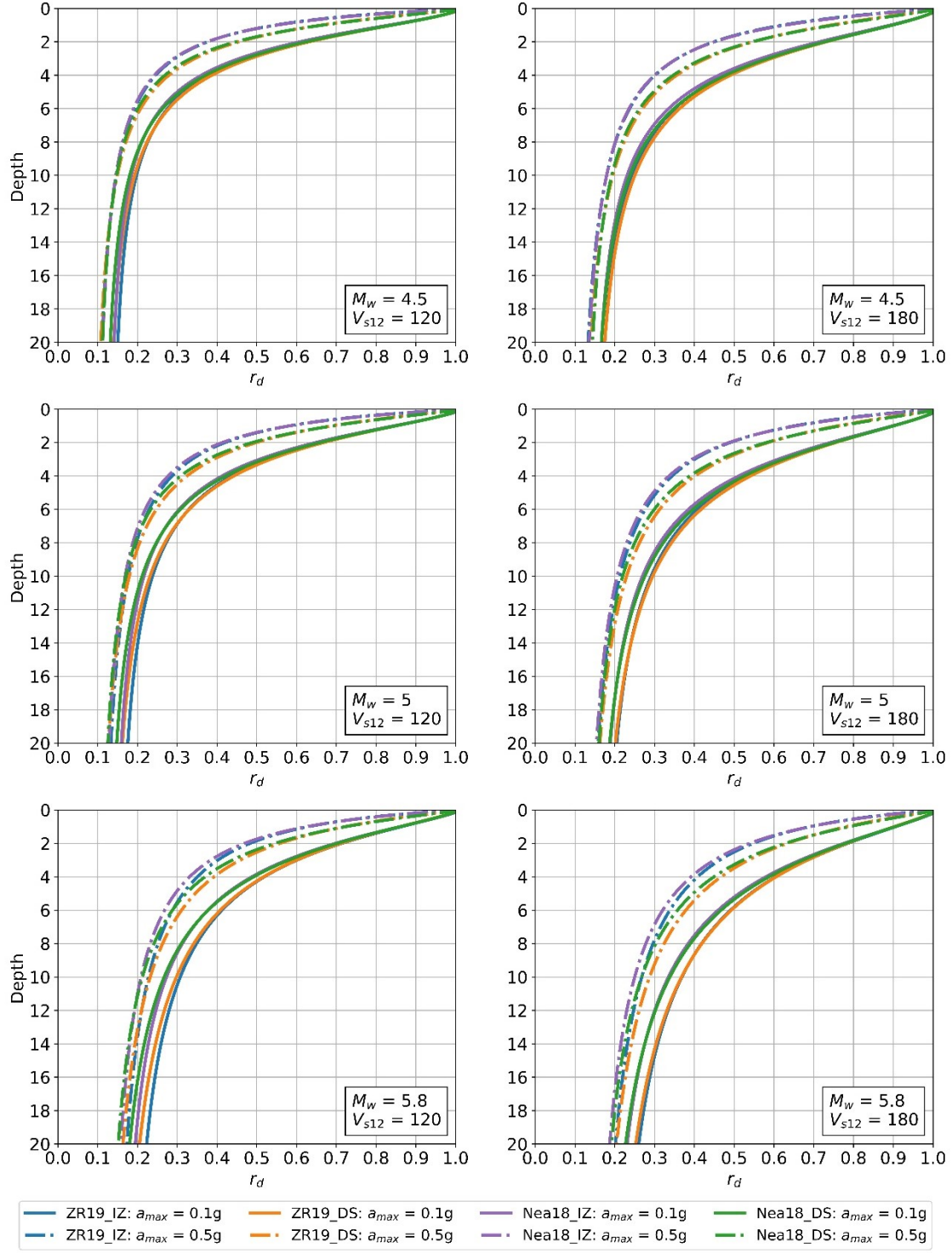


Figure 56. Comparison of r_d Model 1 for the ZR19_IZ, ZR19_DS, Nea18_IZ, and Nea18_DS Datasets. Curves are shown for $M_w = 4.5, 5.0$, and 5.8 ; $a_{max} = 0.1g$ and $0.5g$; and $V_{s12} = 120$ m/s and 180 m/s.

4.5 Proposed n_{eq} and MSF Relationships

Figure 57 and Figure 58 present n_{eq} as a function of several potential predictor variables used in previous n_{eq} models including M_w , $\ln(a_{max})$, R_{hyp} , and V_{s12} . Plots of n_{eq} versus V_{sbed} and depth are also shown. The n_{eq} results shown are for the ZR19_IZ dataset, but the general trends for this dataset are consistent across all four datasets. The most significant predictor variables for n_{eq} are $\ln(a_{max})$ and R_{hyp} , with $\ln(a_{max})$ being negatively correlated to n_{eq} and R_{hyp} being positively correlated to n_{eq} . No significant correlation is observed between n_{eq} and either M_w or V_{s12} , and only very weak positive correlation is observed between n_{eq} and V_{sbed} . Weak correlation is observed between depth and n_{eq} . However, no trend is observed for depths greater than 2 m. The weak trend observed appears to be the result of artificially high n_{eq} values near the ground surface resulting from very small strains. The lack of depth-dependency for n_{eq} is consistent with previous studies.

The negative correlation between a_{max} and n_{eq} is consistent with trends observed by both Lasley et al. (2017) and Green et al. (2020). The positive correlation between R_{hyp} and n_{eq} is consistent with the expectation that the ground motion duration increases with R_{hyp} (e.g., Boore and Thompson 2015). Similar trends were observed by Lee (2009) and Liu et al. (2001) who developed n_{eq} models that included site-to-source distance (R) as a predictor variable. Lasley et al. (2017) also developed a model in terms of M_w and R and found a positive correlation between R and n_{eq} . The shape of the observed n_{eq} - R_{hyp} curve (Figure 58) is similar to the path duration-point source distance model for the CEUS developed by Boore and Thompson (2015) and shown in Figure 4. The Boore and Thompson (2015) model shows path duration increasing rapidly with distance up to a point-source distance of ~ 45 km, at which distance path duration plateaus out to a distance of 125 km. Similarly, n_{eq} for this study, as shown in Figure 57, increases rapidly with R_{hyp} up to $R_{hyp} \approx 35$ km at which distance n_{eq} does not increase significantly with further increases in R_{hyp} .

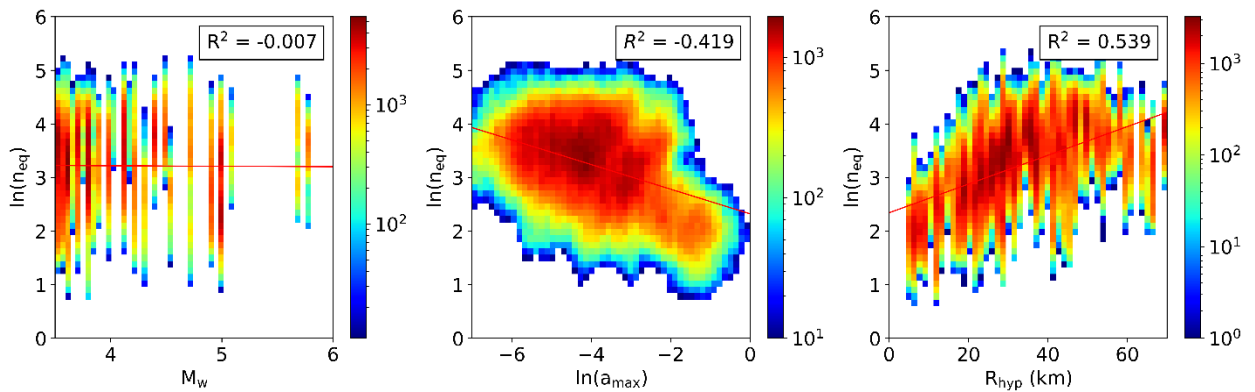


Figure 57. Heat map of $\ln(n_{eq})$ versus M_w , $\ln(a_{max})$, and R_{hyp} . Values shown are for the ZR19_IZ dataset.

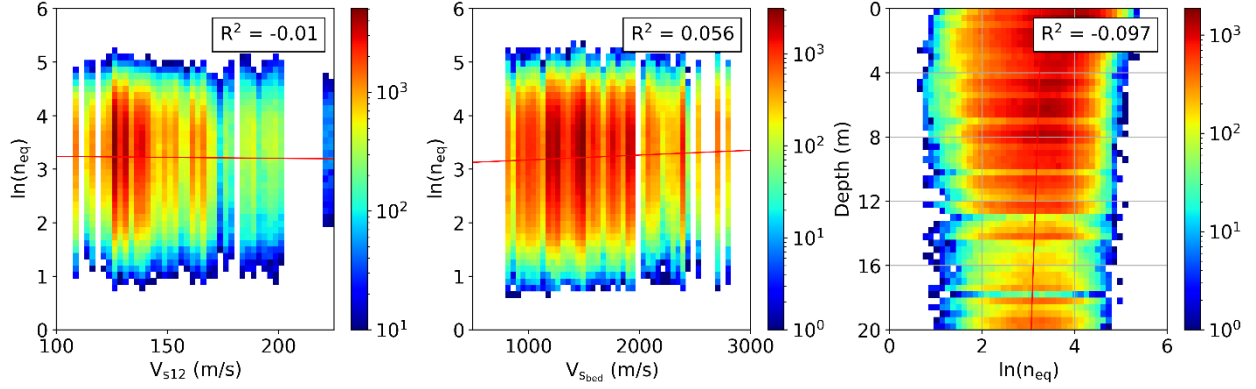


Figure 58. Heat map of $\ln(n_{eq})$ versus R_{hyp} , V_{sbed} , and depth. Values shown are for the ZR19_IZ dataset.

The lack of a strong correlation with M_w was surprising given the tendency for ground motion duration to increase with increasing earthquake magnitude (e.g., Green et al. 2020; Lasley et al. 2017). The relationship between n_{eq} and M_w was investigated further by partitioning the n_{eq} results by a_{max} and then plotting the partitioned n_{eq} values against M_w (Figure 59). As shown in this figure, there is a strong positive correlation between the partitioned n_{eq} values and M_w , consistent with previous studies. This suggests that, while a_{max} is a much stronger predictor of n_{eq} than M_w , M_w is still a significant predictor of n_{eq} when used in conjunction with a_{max} . No significant correlation was observed between n_{eq} and V_{s12} , even after partitioning the data by a_{max} or R_{hyp} . The correlation between n_{eq} and V_{sbed} increased slightly ($R^2 \approx 0.10$) when n_{eq} was partitioned by a_{max} , but this correlation was still considered too weak to include V_{sbed} in the n_{eq} model. Based on the observed trends in the data, it was determined that the n_{eq} model would be regressed using M_w , a_{max} , and R_{hyp} as predictors. The regressions were performed using n_{eq} computed from individual horizontal components of motion similar to the approach used by Green et al. (2020) and Approach 1 from Lasley et al. (2017). This approach was used to accommodate the single-component spectrally matched ground motions included in ground motion database. Accordingly, the proposed n_{eq} relationship should be used in conjunction with Equation (10) when estimating MSF.

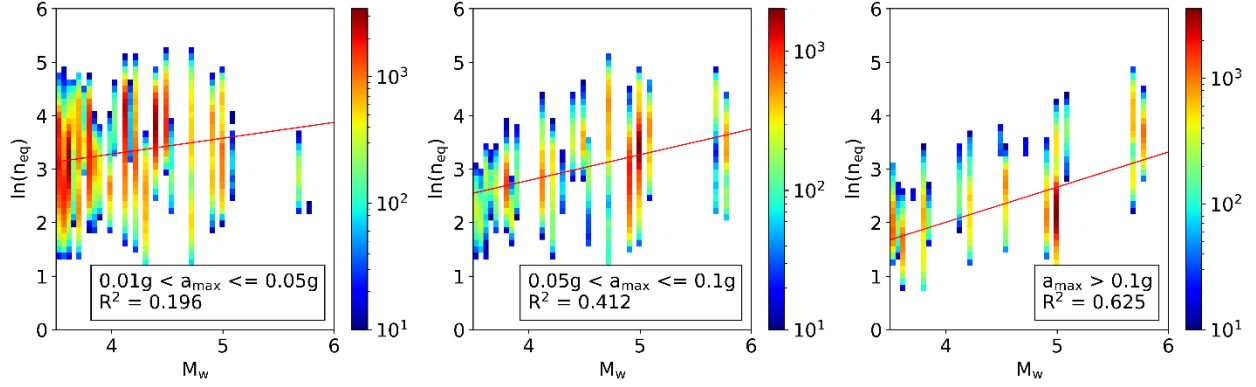


Figure 59. $\ln(n_{eq})$ versus M_w for $0.01g < a_{max} \leq 0.05g$, $0.05g < a_{max} \leq 0.1g$, and $a_{max} > 0.1g$. Values shown are for the ZR19_IZ dataset.

The proposed functional forms for the n_{eq} relationship are based on the n_{eq} models developed by Green et al. (2020) and Lasley et al. (2017). Two models were proposed, one that includes M_w and a_{max} as predictors and a second that includes M_w , a_{max} , and R_{hyp} . Both models include a break in scaling for $a_{max} \geq 0.25g$, similar to the scaling break used for the r_d model. The scaling break observed in Figure 57 for $R_{hyp} \geq 35$ km is also included in the second model. The functional forms for n_{eq} Model 1 (with R_{hyp}) and n_{eq} Model 2 (without R_{hyp}) are:

Model 1:

$$\ln[n_{eq-OK}(M_w, a_{max}, R_{hyp})] = \alpha_1 + \alpha_2 \cdot M_w + \alpha_3 \cdot \ln(a_{max}) + \alpha_5 \cdot R_{hyp} + \delta_{event_neq} + \delta_{profile_neq} + \delta_{0_neq}; \text{ for } a_{max} \leq 0.25g, R_{hyp} \leq 35 \text{ km} \quad (23a)$$

$$= \alpha_1 + \alpha_2 \cdot M_w + \alpha_3 \cdot \ln(a_{max}) + \alpha_4 \cdot \ln\left(\frac{a_{max}}{0.25}\right) + \alpha_5 \cdot R_{hyp} + \delta_{event_neq} + \delta_{profile_neq} + \delta_{0_neq}; \text{ for } a_{max} > 0.25g, R_{hyp} \leq 35 \text{ km} \quad (23b)$$

$$= \alpha_1 + \alpha_2 \cdot M_w + \alpha_3 \cdot \ln(a_{max}) + \alpha_5 \cdot R_{hyp} + \alpha_6 \cdot (R_{hyp} - 35 \text{ km}) + \delta_{event_neq} + \delta_{profile_neq} + \delta_{0_neq}; \text{ for } a_{max} \leq 0.25g, R_{hyp} > 35 \text{ km} \quad (23c)$$

$$= \alpha_1 + \alpha_2 \cdot M_w + \alpha_3 \cdot \ln(a_{max}) + \alpha_4 \cdot \ln\left(\frac{a_{max}}{0.25}\right) + \alpha_5 \cdot R_{hyp} + \alpha_6 \cdot (R_{hyp} - 35 \text{ km}) + \delta_{event_neq} + \delta_{profile_neq} + \delta_{0_neq}; \text{ for } a_{max} > 0.25g, R_{hyp} > 35 \text{ km} \quad (23d)$$

and Model 2:

$$\ln[n_{eq-OK}(M_w, a_{max})] = \alpha_1 + \alpha_2 \cdot M_w + \alpha_3 \cdot \ln(a_{max}) + \delta_{event_neq} + \delta_{profile_neq} + \delta_{0_neq}; \quad (24a)$$

$\text{for } a_{max} \leq 0.25g$

$$= \alpha_1 + \alpha_2 \cdot M_w + \alpha_3 \cdot \ln(a_{max}) + \alpha_4 \cdot \ln\left(\frac{a_{max}}{0.25}\right) + \delta_{event_neq} + \delta_{profile_neq} + \delta_{0_neq}; \text{ for } a_{max} > 0.25g \quad (24b)$$

The mean values and standard deviations of the regression coefficients for the n_{eq} models are presented in Table 6. The low values of standard deviation relative to mean values for the regressed parameters indicate that they are well-constrained by the data.

Table 6. Regression coefficients for the n_{eq} models.

| | Model 1: $n_{eq} = f(M_w, a_{max}, R_{hyp})$ | | | | Model 2: $n_{eq} = f(M_w, a_{max})$ | | | |
|---------------------|--|-----------------|----------------|-----------------|---|-----------------|----------------|-----------------|
| Dataset: | ZR19_DS | Nea18_DS | ZR19_IZ | Nea18_IZ | ZR19_DS | Nea18_DS | ZR19_IZ | Nea18_IZ |
| α_1 | -1.0483 | -0.7663 | -1.1128 | -0.8634 | -2.1040 | -1.9571 | -2.1180 | -2.0142 |
| $\sigma_{\alpha 1}$ | 0.0430 | 0.0465 | 0.0431 | 0.0458 | 0.03901 | 0.04135 | 0.03892 | 0.04077 |
| α_2 | 0.4905 | 0.4207 | 0.5209 | 0.4590 | 0.7658 | 0.7330 | 0.7895 | 0.7672 |
| $\sigma_{\alpha 2}$ | 0.00793 | 0.00882 | 0.00813 | 0.00890 | 0.00616 | 0.00675 | 0.00623 | 0.00676 |
| α_3 | -0.3044 | -0.2995 | -0.3065 | -0.3021 | -0.511 | -0.509 | -0.5003 | -0.4991 |
| $\sigma_{\alpha 3}$ | 0.00517 | 0.00523 | 0.00516 | 0.00508 | 0.00352 | 0.00354 | 0.00346 | 0.00342 |
| α_4 | 0.3504 | 0.4023 | 0.2467 | 0.3019 | 0.4642 | 0.5327 | 0.3059 | 0.3771 |
| $\sigma_{\alpha 4}$ | 0.0307 | 0.0269 | 0.0236 | 0.0204 | 0.03037 | 0.02712 | 0.02273 | 0.02020 |
| α_5 | 0.03094 | 0.03146 | 0.02952 | 0.03009 | - | - | - | - |
| $\sigma_{\alpha 5}$ | 0.000578 | 0.000574 | 0.000584 | 0.000574 | - | - | - | - |
| α_6 | -0.0217 | -0.0222 | -0.0203 | -0.0209 | - | - | - | - |
| $\sigma_{\alpha 6}$ | 0.000754 | 0.000749 | 0.000752 | 0.000742 | - | - | - | - |

Figure 60 and Figure 61 are plots of model residuals versus predictor variables for n_{eq} Models 1 and 2, respectively. This includes M_w , a_{max} , and R_{hyp} . Plots of residuals versus depth are also shown. Both loess and linear fits to the residuals are presented to show the overall trends in the residuals. Error bars showing σ_{0_neq} of the binned residuals are also presented. The binned residuals for both models are generally mean-zero and normally distributed, suggesting the models are suitable fits of the n_{eq} data for the range of M_w , a_{max} , R_{hyp} , and depth considered. Although both models fit the data well, the inclusion of R_{hyp} in Model 1 significantly reduced τ_{event_neq} , $\tau_{profile_neq}$, and σ_{0_neq} , indicating a significantly improved fit of the data. Both models exhibited a tendency to slightly over-predict $\ln(n_{eq})$ for very small a_{max} values ($a_{max} \lesssim 0.003g$). However, a_{max} values in this range do not pose a threat of liquefaction. Plots are shown for the ZR19_IZ dataset but similar trends are observed for the other datasets.

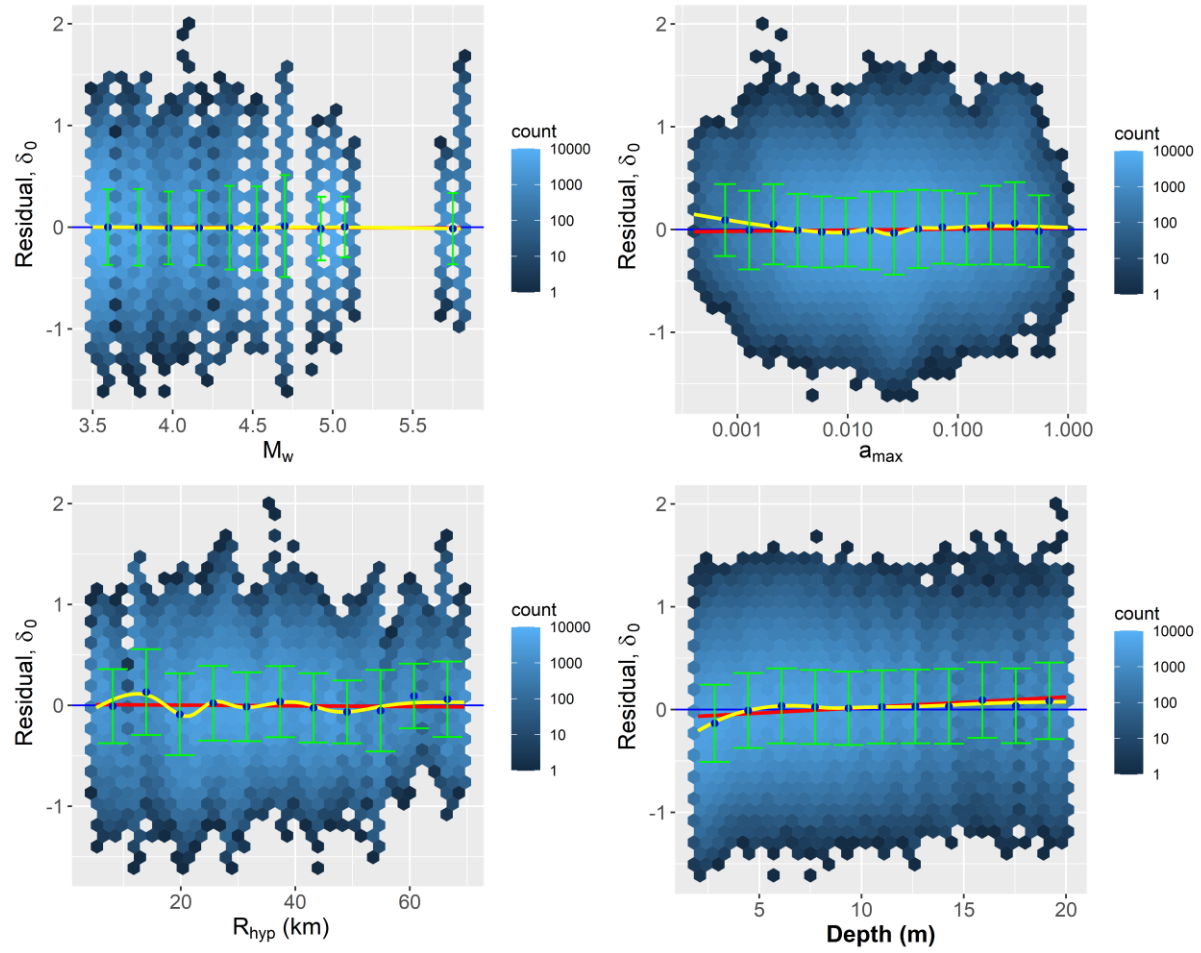


Figure 60. Heat map of n_{eq} Model 1 residuals versus predictor variables (Equation23). Residuals versus depth are also shown. Yellow lines show loess fits to the residuals, red lines show linear trends fitted to the residuals, and the green error bars show the means and standard deviations of the binned residuals. Results shown for ZR19_IZ dataset.

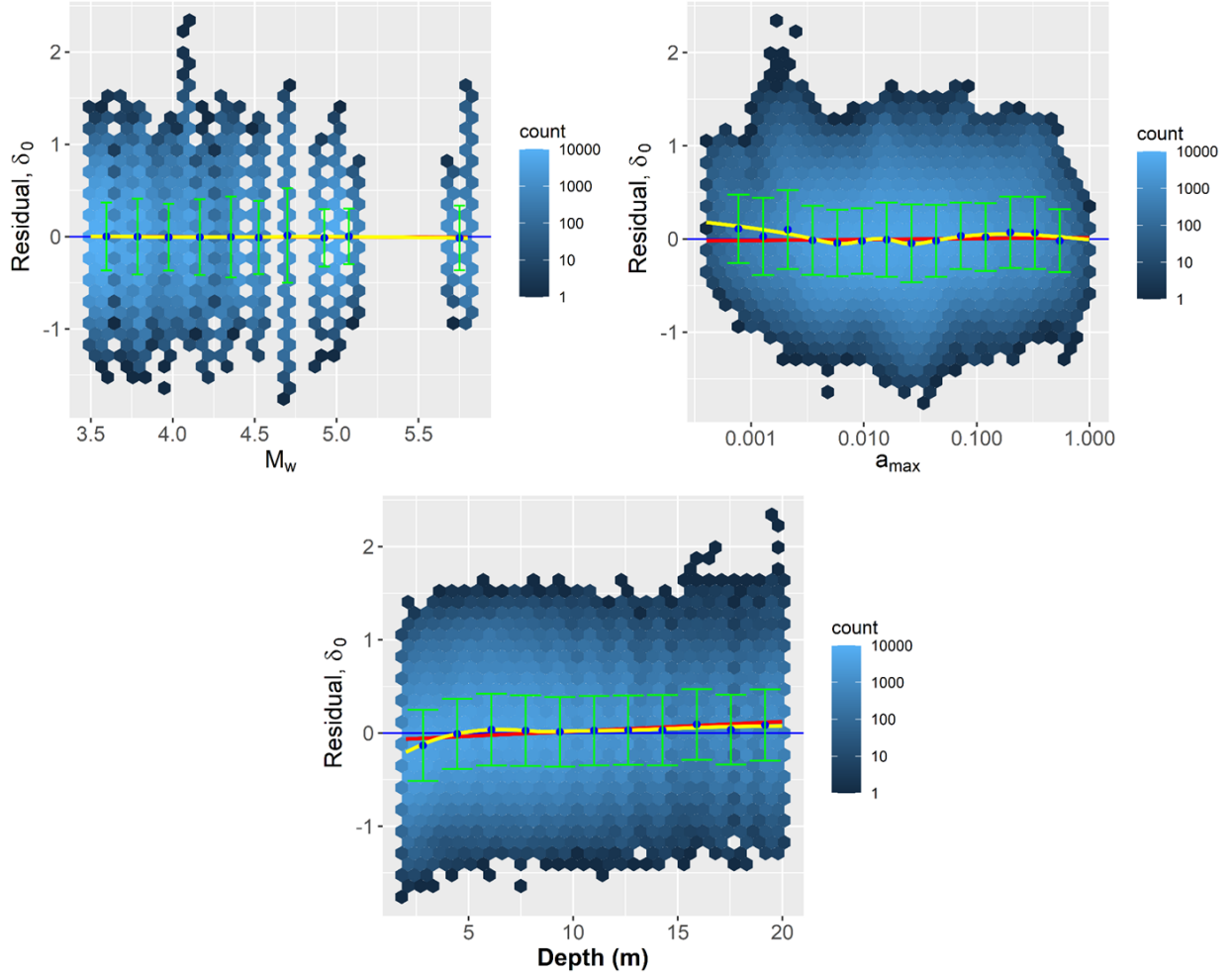


Figure 61. Heat map of n_{eq} Model 2 residuals versus predictor variables (Equation (24)). Residuals versus depth are also shown. Yellow lines show loess fits to the residuals, red lines show linear trends fitted to the residuals, and the green error bars show the means and standard deviations of the binned residuals. Results shown for ZR19_IZ dataset.

Similar to the observations made by Green et al. (2020), there is no compelling evidence of a depth-dependency in σ_{0_neq} for the Oklahoma dataset. Accordingly, a depth-independent model was used for $\sigma_{\ln(n_{eq}-OK)}$ given by:

$$\sigma_{\ln(n_{eq}-OK)} = \sqrt{\tau_{event_neq}^2 + \tau_{profile_neq}^2 + \sigma_{0_neq}^2} \quad (25)$$

where τ_{event_neq} , $\tau_{profile_neq}$, and σ_{0_neq} are the random effect terms and residual standard deviation from the model regression. These values, as well as the estimates for $\sigma_{\ln(n_{eq}-OK)}$, are presented in Table 7.

Table 7. Uncertainty parameters for the n_{eq} models.

| | Model 1: $n_{eq} = f(M_w, a_{max}, R_{hyp})$ | | | | Model 2: $n_{eq} = f(M_w, a_{max})$ | | | |
|-----------------------|--|----------|---------|----------|-------------------------------------|----------|---------|----------|
| Dataset: | ZR19_DS | Nea18_DS | ZR19_IZ | Nea18_IZ | ZR19_DS | Nea18_DS | ZR19_IZ | Nea18_IZ |
| τ_{event_neq} | 0.5404 | 0.5238 | 0.543 | 0.5243 | 0.5789 | 0.5715 | 0.5781 | 0.5669 |
| $\tau_{profile_neq}$ | 0.1048 | 0.1025 | 0.1087 | 0.1066 | 0.1389 | 0.1368 | 0.1384 | 0.1364 |
| σ_{0_neq} | 0.3717 | 0.3725 | 0.3682 | 0.3691 | 0.3865 | 0.3877 | 0.3819 | 0.3832 |
| $\sigma_{ln(neq-OK)}$ | 0.6642 | 0.6508 | 0.665 | 0.65 | 0.7098 | 0.704 | 0.7065 | 0.6978 |

As noted previously, the Oklahoma n_{eq} models were developed using individual horizontal components of ground motion. As a result, MSF for the new model (MSF_{OK}) is computed using $n_{eq M7.5} = 7.25$, similar to the MSF relationship from Green et al. (2020). Accordingly, the Oklahoma-specific MSF relationships for n_{eq} Models 1 and 2 are:

$$MSF_{OK}(M_w, a_{max}, R_{hyp}) = \left(\frac{7.25}{n_{eqM-OK}(M_w, a_{max}, R_{hyp})} \right)^{0.34} \leq 2.04 \quad (26)$$

and

$$MSF_{OK}(M_w, a_{max}) = \left(\frac{7.25}{n_{eqM-OK}(M_w, a_{max})} \right)^{0.34} \leq 2.04 \quad (27)$$

The standard deviation of these models, $\sigma_{ln(MSF_{OK})}$, can be estimated as:

$$\sigma_{ln(MSF_{OK})} = 0.34 \cdot \sigma_{ln(n_{eq-OK})} \leq 2.04 \quad (28)$$

where $\sigma_{ln(n_{eq-OK})}$ is the standard deviation of the n_{eq} model being used.

Figure 62 provides a comparison of MSF model developed herein and MSF models proposed by Green et al. (2017) and Boulanger and Idriss (2014) for the valid M_w range of each model. As may be observed from this figure, MSF for Oklahoma tend to be lower than MSF from either the Green et al. (2017) and Boulanger and Idriss (2014) models for $\sim M_w$ 4.5 to 6 where the models overlap. These differences are more pronounced for larger R_{hyp} . For $R_{hyp} = 10$ km and $a_{max} = 0.1g$, MSF from Oklahoma Model 1 is actually higher than the Green et al. (2017) CEUS model for $M_w < 5.4$ but is lower for $M_w > 5.4$. In general, the Oklahoma MSF tend to be lower than the other MSF models for all values of a_{max} , R_{hyp} , and M_w . Additionally, the Oklahoma models exhibited weaker scaling with a_{max} than the Green et al. (2017) models,

particularly for $a_{\max} \geq 0.3g$. MSF for the current study tend to be higher for Model 1 than Model 2 at small R_{hyp} ($R_{\text{hyp}} \lesssim 15$ km), but this trend is reversed for larger R_{hyp} ($R_{\text{hyp}} \gtrsim 25$ km).

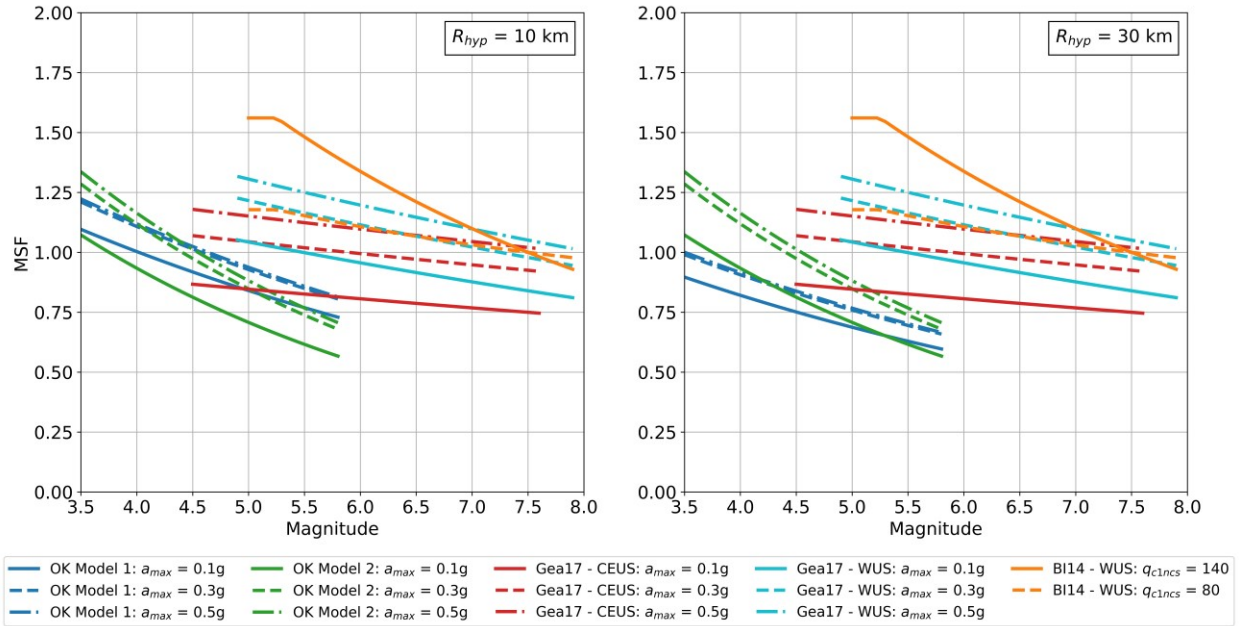


Figure 62. Comparison of MSF Models 1 and 2 developed herein (Model 1 for $R_{\text{hyp}} = 10$ km and 30 km) and models proposed by Green et al. (2017) for the CEUS (Gea17 – CEUS) and WUS (Gea17 – WUS) and by Boulanger and Idriss (2014) primarily for the WUS (BI14 – WUS). Oklahoma and Gea17 MSF estimates are shown for $a_{\max} = 0.1g, 0.3g$, and $0.5g$. The BI14 model is shown for $q_{c1ncs} = 80$ and 140 atm.

The significant differences observed between MSF for induced ground motions in Oklahoma and MSF for the WUS are consistent with the observations about path duration made by Boore and Thompson (2015): the ground motion durations in the CEUS increase much faster with R_{hyp} than they do in the WUS. The Oklahoma MSF are closer to the Green et al. (2017) CEUS MSF but are still significantly lower than CEUS MSF for $M_w \gtrsim 5$. The ground motions used to develop the Green et al. (2017) CEUS model were scaled from WUS ground motions using state-of-the-art methods (McGuire et al. 2001). However, the scaling procedures used were likely focused on scaling for spectral amplitude as opposed to duration. This may explain why the durations of the Green et al. (2017) CEUS ground motions are more in line with those of the Green et al. (2017) WUS model than the Oklahoma models.

Although the MSF curves shown in Figure 62 are for the ZR19_IZ dataset, observed trends are similar for the other datasets. Figure 63 shows a comparison of the regressed MSF models for each of the four datasets

used in this study. Curves are shown for $R_{hyp} = 10$ km and 30 km and for $a_{max} = 0.1$ g and 0.5g. As shown in this figure, the four datasets result in very similar regressed MSF models. For MSF Model 1, the ZR19 dataset and IZ MRD curves tend to result in slightly lower MSF for $M_w \lesssim 4.5$ and slightly higher values for $M_w \gtrsim 4.5$. The maximum observed difference between the models (i.e., comparing ZR19_IZ to Nea18_DS) is approximately 7%. For Model 2, the Nea18 dataset and DS MRD result in slightly higher MSF for $a_{max} = 0.5$ g and $M_w \lesssim 5$, with a maximum observed difference of approximately 5%. For $a_{max} = 0.5$ g and $M_w > 5$, as well as for $a_{max} = 0.1$ g, predictions for all four datasets are within 1-2%. The effect of MRD and GMPE selection on MSF is smaller than for r_d . However, it should still be taken into account in performing forward analyses with these MSF relationships.

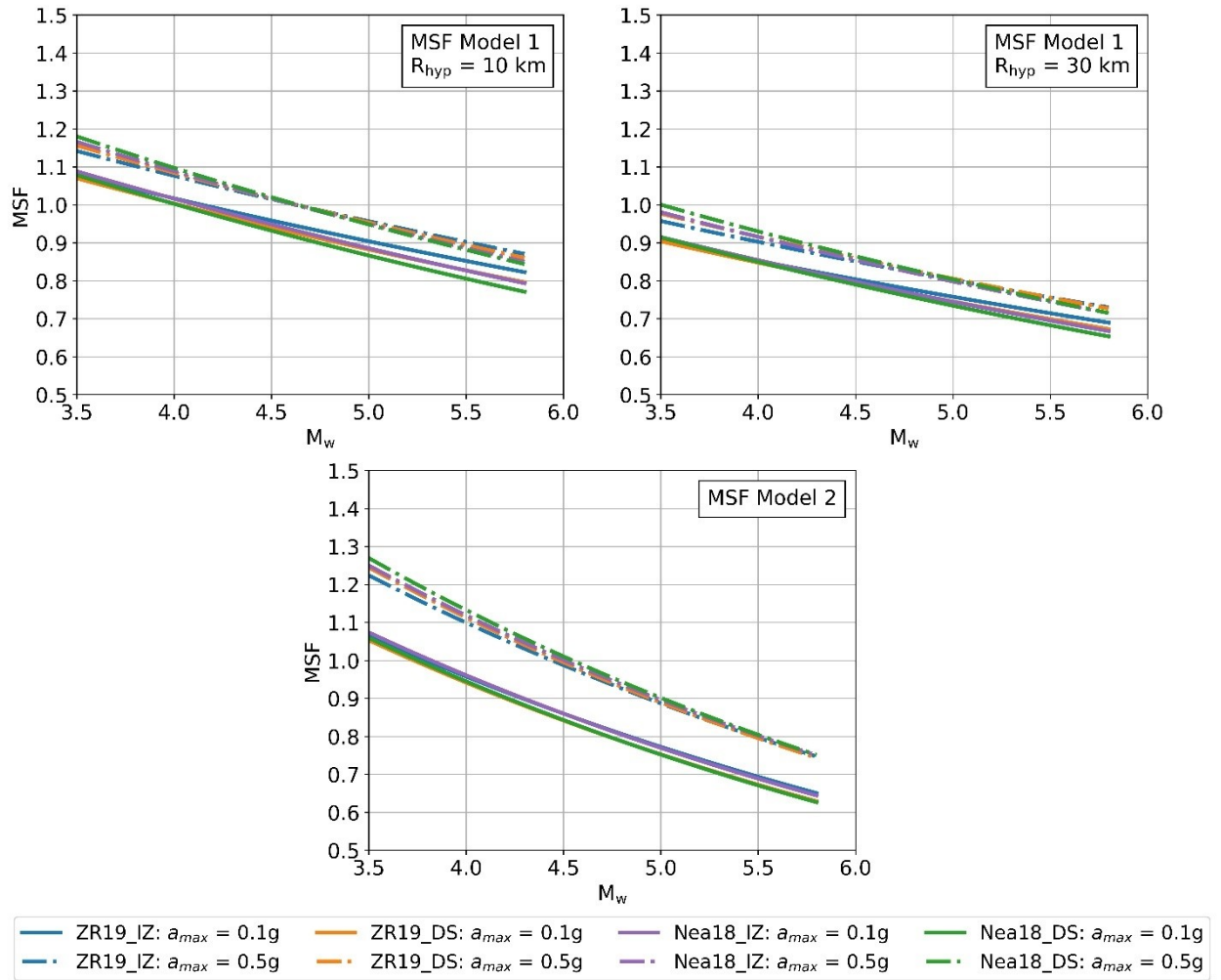


Figure 63. Comparison of MSF models for the ZR19_IZ, ZR19_DS, Nea18_IZ, and Nea18_DS Datasets. Curves for Model 1 are shown for $R_{hyp} = 10$ km and 30 km. Curves for both models are shown for $a_{max} = 0.1$ g and 0.5g.

4.6 Correlation of r_d across Depth and Correlation between Oklahoma r_d and $\ln(n_{eq})$ Relationships

It was found that r_{d-OK} values are correlated across depth. The correlation coefficient of r_{d-OK} between depths z_i and z_j is given by

$$\rho[\epsilon_{r_d}(z_i), \epsilon_{r_d}(z_j)] = 1 + \alpha_{r_d} \cdot |z_i - z_j| \quad (29)$$

where $\epsilon_{r_d}(z_i)$ and $\epsilon_{r_d}(z_j)$ are the residuals of r_d at depths z_i and z_j normalized by $\sigma_0(z_i)$ and $\sigma_0(z_j)$, respectively, and α_{r_d} is a regression coefficient. It was also found that $\ln(n_{eq-OK})$ and r_{d-OK} are negatively correlated at a given depth. Regressed values of α_{r_d} , as well as correlation coefficients between $\ln(n_{eq-OK})$ and r_{d-OK} (i.e., $\rho_{\ln(n_{eq-OK}), r_{d-OK}}$), are presented in Table 8. The observed correlations are similar to correlations observed between $\ln(n_{eq-Gron})$ and r_{d-Gron} and correlations of r_{d-Gron} across depths observed by Green et al. (2020), except the cross-depth correlation was somewhat stronger for the Oklahoma r_d model.

Table 8. Correlation coefficients for r_{d-OK} and $\ln(n_{eq-OK})$ models.

| Dataset | r_d Model | n_{eq} Model | α_{rd} | $\rho_{\ln(n_{eq}), rd}$ |
|----------|-------------|----------------|---------------|--------------------------|
| ZR19_DS | 1 | 1 | -0.05778 | -0.33605 |
| Nea18_DS | 1 | 1 | -0.05702 | -0.33676 |
| ZR19_IZ | 1 | 1 | -0.05842 | -0.33520 |
| Nea18_IZ | 1 | 1 | -0.05724 | -0.33605 |
| ZR19_DS | 1 | 2 | -0.05778 | -0.33103 |
| Nea18_DS | 1 | 2 | -0.05702 | -0.33290 |
| ZR19_IZ | 1 | 2 | -0.05842 | -0.32849 |
| Nea18_IZ | 1 | 2 | -0.05724 | -0.33084 |
| ZR19_DS | 2 | 1 | -0.05662 | -0.33110 |
| Nea18_DS | 2 | 1 | -0.05751 | -0.33146 |
| ZR19_IZ | 2 | 1 | -0.05538 | -0.33125 |
| Nea18_IZ | 2 | 1 | -0.05509 | -0.33227 |
| ZR19_DS | 2 | 2 | -0.05662 | -0.32634 |
| Nea18_DS | 2 | 2 | -0.05751 | -0.32792 |
| ZR19_IZ | 2 | 2 | -0.05538 | -0.32465 |
| Nea18_IZ | 2 | 2 | -0.05509 | -0.32666 |

4.7 MSF and r_d Summary and Comparison with Relationships from Prior Studies

As shown in the previous sections, r_d and MSF relationships for induced earthquakes in Oklahoma, Texas, and Kansas differ from those for tectonic earthquakes in the CEUS and WUS. This section provides a summary of major findings related to r_d and MSF for induced earthquakes in Oklahoma and provides a comparison of the Oklahoma r_d and MSF relationships and relationships for tectonic earthquakes from prior studies.

Major findings from this study related to r_d include:

- Depth, M_w , $\ln(a_{\max})$, and V_{s12} are significant predictors of r_d for induced earthquakes in Oklahoma, Kansas, and Texas.
- r_d increases with increasing M_w and V_{s12} , and decreases with increasing $\ln(a_{\max})$.
- r_d follows a sigmoidal relationship with depth. r_d decreases from 1.0 at the ground surface to a value at depth as a function of M_w , a_{\max} , and V_{s12} .
- r_d for induced earthquakes in Oklahoma exhibits a scaling break for relatively large values of a_{\max} ($> 0.25g$).
- For depths greater than 1-1.5 m, r_d for Oklahoma are lower than for the Lasley et al. (2016) and Idriss (1999) r_d models. r_d is similar for all models at shallower depths.
- r_d for Oklahoma exhibits weaker scaling with M_w than the Lasley et al. (2016) and Idriss (1999) r_d models.
- r_d for Oklahoma exhibits weaker scaling with V_{s12} than the Lasley et al. (2016) r_d models.
- Consequently, the difference between r_d for Oklahoma and r_d for tectonic events increases with increasing M_w and V_{s12} .
- All else being equal, the smaller r_d for Oklahoma result in smaller calculated CSR^* and higher FS_{liq} .

Some of the differences between r_d for the new induced seismicity-specific r_d relationship and existing r_d relationships for tectonic earthquakes are illustrated in Figure 64. Figure 64 provides a comparison of r_d Model 1 for Oklahoma and the r_d relationships proposed by Lasley et al. (2016) and Idriss (1999) for the WUS and CEUS for $M_w = 5$, $a_{\max} = 0.3g$, and $V_{s12} = 135$ m/s. The Oklahoma model shown is for the ZR19_IZ dataset. Mean and mean plus/minus one standard deviation curves are shown for the Oklahoma and Lasley et al. (2016) models. A comparison of r_d for additional M_w , a_{\max} , and V_{s12} values is provided in Section 4.4. As shown in Figure 64, r_d for Oklahoma is lower than for the Lasley et al. (2016) models for all depths deeper than ~ 1 m; the r_d for Oklahoma and Lasley et al. (2016) models are similar above this depth. The Idriss (1999) model predicts higher r_d values than the other models at all

depths. The standard deviation of the Oklahoma r_d relationship is smaller than standard deviations of the Lasley et al. (2016) models, but the standard deviations approach zero at the ground surface for both the Oklahoma and Lasley et al. (2016) models. As noted, all else being equal, the lower r_d for the Oklahoma model results in lower estimated CSR* and higher estimates of FS_{liq} than would be predicted by the other models.

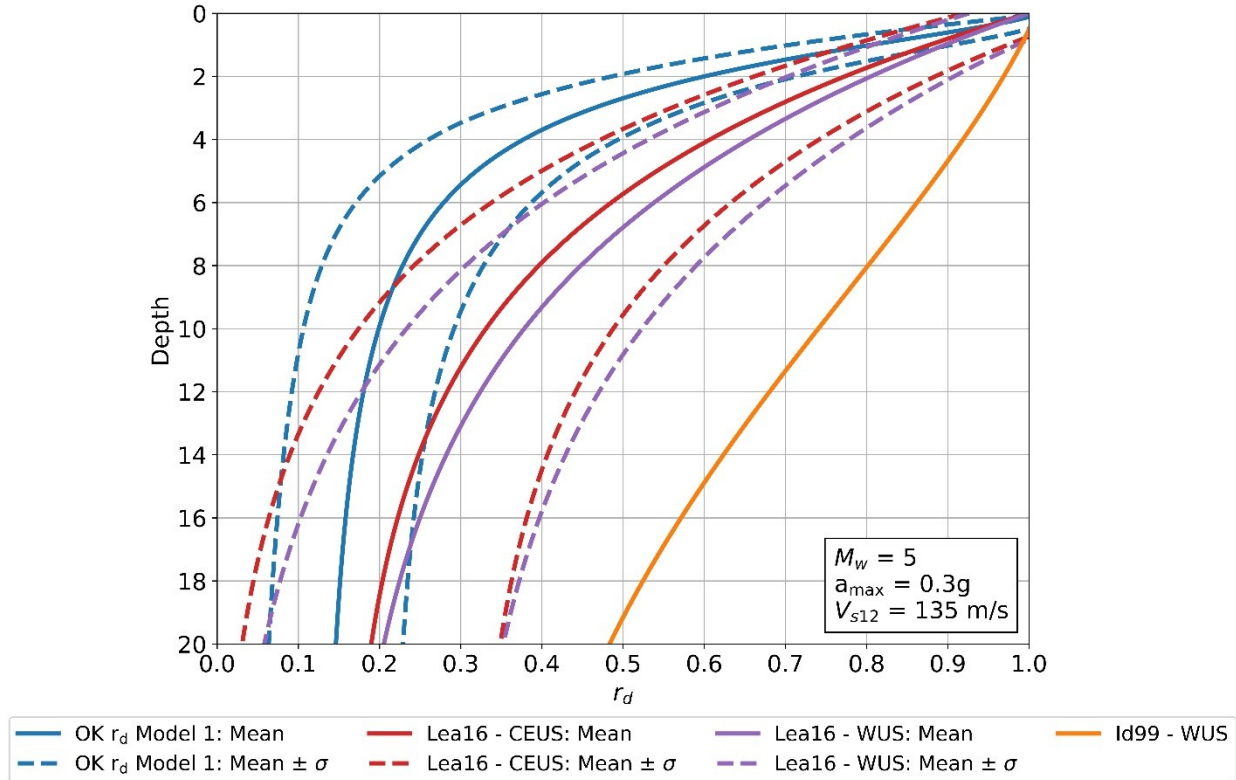


Figure 64. Comparison of Oklahoma r_d Model 1 from the current study and the r_d relationships proposed by Lasley et al. (2016) [Lea16] for the CEUS and WUS and by Idriss (1999) [I99] for the WUS. Estimates are shown for $M_w = 5.0$, $a_{max} = 0.3g$, and $V_{s12} = 135$ m/s. Mean and mean plus/minus one standard deviation curves are shown for the OK and Lea16 models. Oklahoma model estimates are based on the ZR19_IZ dataset.

Major findings from this study related to n_{eq} and MSF include:

- M_w , $\ln(a_{max})$, and R_{hyp} are significant predictors of n_{eq} and MSF for induced earthquakes in Oklahoma, Texas, and Kansas.
- MSF decreases with increases in R_{hyp} and M_w .
- MSF increases with increases in $\ln(a_{max})$.
- MSF exhibits scaling breaks for relatively large values of a_{max} ($> 0.25g$) and for relatively large values of R_{hyp} (> 35 km).
- MSF for Oklahoma tend to be lower than MSF per the Green et al. (2017) and Boulanger and Idriss (2014) models within the range of $\sim M_w 4.5$ to 6 where the models overlap.
- The Oklahoma MSF models exhibit weaker scaling with a_{max} than the Green et al. (2017) MSF models, particularly for $a_{max} \geq 0.3g$.
- The Oklahoma MSF models exhibit stronger scaling with M_w than the Green et al. (2017) MSF models.
- The difference between MSF predicted by the Oklahoma model and MSF predicted by the Green et al. (2017) and Boulanger and Idriss (2014) models increases with increasing R_{hyp} , M_w , and a_{max} .
- All else being equal, the smaller Oklahoma MSF estimates result in larger calculated CSR* and lower estimates of FS_{liq} than for the Green et al. (2017) and Boulanger and Idriss (2014) MSF models.

Figure 65 shows a comparison of MSF for Oklahoma MSF Model 1, the Green et al. (2017) models for the WUS and CEUS for $a_{max} = 0.1g$ and $0.3g$ and $R_{hyp} = 10$ km, and the Boulanger and Idriss (2014) model for $q_{c1Ncs} = 80$ and 140 atm. The Oklahoma models shown are for the ZR19_IZ dataset. Mean and mean plus/minus one standard deviation curves are shown for the Oklahoma and Green et al. (2017) models. The depth-independent Green et al. (2017) standard deviation model was used. As shown in this figure, for $R_{hyp} = 10$ km, MSF estimates for the Oklahoma model tend to be lower than MSF for either the Green et al. (2017) or Boulanger and Idriss (2014) models. For $M_w < 4.8$ and $a_{max} = 0.1g$, the Green et al. (2017) model predicts slightly lower MSF values than the Oklahoma model. However, for $R_{hyp} > 10$ km, MSF for the Oklahoma model is lower for $a_{max} > 0.1g$. The standard deviation of the Oklahoma MSF model is similar to the depth-independent standard deviation for the Green et al. (2017) MSF models. As noted, all else being equal, the lower MSF estimates for the Oklahoma model result in higher estimated CSR* and lower estimates of FS_{liq} than would be predicted by the Green et al. (2017) and Boulanger and Idriss (2014) models.

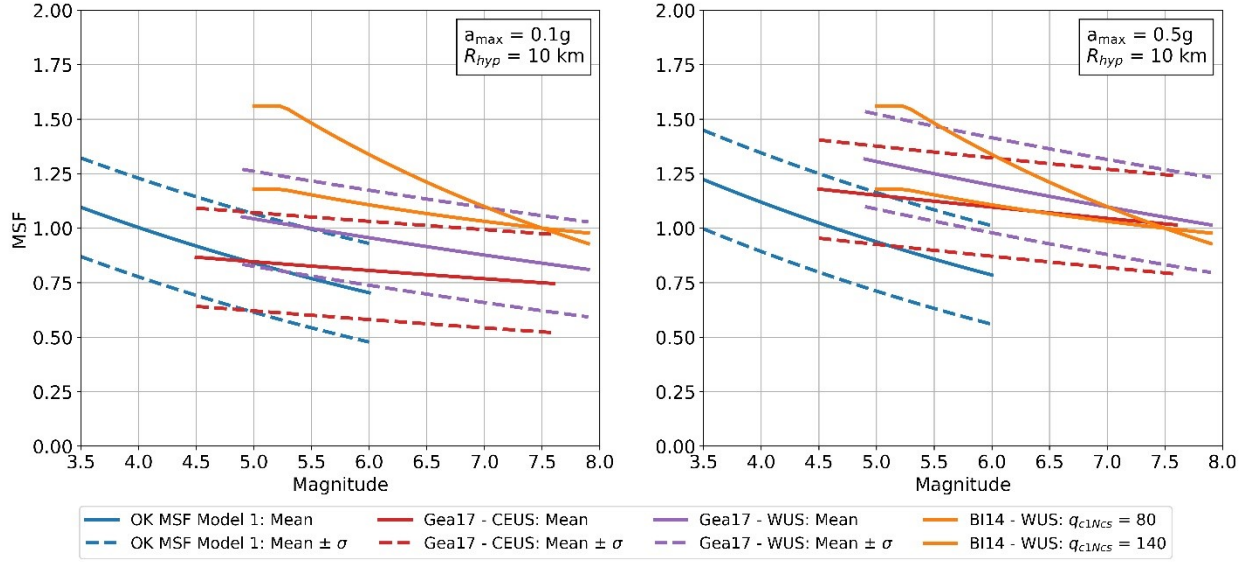


Figure 65. Comparison of Oklahoma MSF Model 1 from the current study and the MSF relationships proposed by Green et al. (2017) [Gea17] for the CEUS and WUS and by Boulanger and Idriss (2014) [BI14] for the WUS. Estimates are shown for $a_{max} = 0.1g$ and $0.3g$, and for $R_{hyp} = 10$ km. Mean and mean plus/minus one standard deviation curves are shown for the OK and Gea17 models. Curves for the BI14 model are shown for $q_{c1Ncs} = 80$ and 140 atm. Oklahoma model estimates are based on the ZR19_IZ dataset.

4.8 Implementation of r_{d-OK} and MSF_{OK} for Assessing Liquefaction Hazard for Induced Ground Motions in Oklahoma, Texas, and Kansas

As noted previously, the r_d and MSF relationships developed herein can be used in conjunction with the Green et al. (2019) $CRR_{M7.5}$ curve to assess liquefaction hazard for induced ground motions in Oklahoma, Kansas, and Texas. Applying this approach and using the r_d and MSF relationships developed herein, CSR^* values for induced events can be calculated as:

$$CSR^* = 0.65 \frac{a_{max}}{g} \frac{\sigma_v}{\sigma'_{v0}} r_{dOK} \frac{1}{MSF_{OK} \cdot K_\sigma \cdot K_\alpha} \quad (30)$$

where r_{d-OK} and MSF_{OK} are the induced seismicity-specific r_d and MSF relationships developed herein, K_σ is a correction factor for initial vertical effective overburden stress using a reference initial effective overburden stress of 1 atm, and K_α is a correction factor for initial horizontal static shear stress using a reference initial static shear stress of zero (e.g., level ground conditions). The computed CSR^* is then compared to the $CRR_{M7.5}$ curves presented by Green et al. (2019) to compute FS_{liq} .

The Green et al. (2019) $CRR_{M7.5}$ curve was developed by reanalyzing the CPT liquefaction case history database compiled by Boulanger and Idriss (2014) using MSF relationships based on Lasley et al. (2017) and the r_d relationship developed by Lasley et al. (2016) while using other parameters and relationships as specified by Boulanger and Idriss (2014). The case histories were then used to regress an “unbiased” deterministic liquefaction curve (i.e., $CRR_{M7.5}$) given by:

$$CRR_{M7.5} = \exp \left[\frac{q_{c1Ncs}}{113} + \left(\frac{q_{c1Ncs}}{1000} \right)^2 - \left(\frac{q_{c1Ncs}}{140} \right)^3 + \left(\frac{q_{c1Ncs}}{137} \right)^4 - 2.8119 \right] \leq 0.6 \quad (31)$$

where q_{c1Ncs} is computed using the procedure outlined by Boulanger and Idriss (2014). This curve corresponds to a probability of liquefaction (P_{liq}) of approximately 35% based on total uncertainty and approximately corresponds to $P_{liq} = 15\%$ for the Boulanger and Idriss (2014) $CRR_{M7.5}$ curve, which considers only model uncertainty. FS_{liq} for a given CSR^* and $CRR_{M7.5}$ can then be computed as:

$$FS_{liq} = \frac{CRR_{M7.5}}{CSR^*} \quad (32)$$

In general, r_d and MSF relationships developed from one study should not be used in conjunction with $CRR_{M7.5}$ relationships developed from other studies (NRC 2016). However, the r_d and MSF relationships used to develop the Green et al. (2019) $CRR_{M7.5}$ and those developed herein were developed using identical approaches. As a result, it is reasonable to assume that the r_d and MSF relationships developed herein for induced earthquakes can be used in conjunction with the Green et al. (2019) $CRR_{M7.5}$ curves as presented in Equations (31 and **Error! Reference source not found.** to evaluate liquefaction potential at sites subjected to induced ground motions. This methodology was applied during model validation as described in the following section.

5 Validation of the Induced Seismicity Liquefaction Triggering Model

To validate the efficacy of the induced seismicity-specific liquefaction triggering model developed herein, liquefaction potential was evaluated at several sites that experienced intense shaking during the 3 September 2016, M_w 5.8 Pawnee, OK, earthquake using the new model as well as existing tectonic models (Boulanger and Idriss 2014; Green et al. 2017). Liquefaction potential was assessed based on ground motions from the Pawnee earthquake and site profiles from the site characterization campaign discussed in Section 3. The predicted liquefaction response was compared to field observations following the Pawnee event to assess the accuracy of these models for evaluating liquefaction triggering potential during induced earthquakes in Oklahoma. The following sections discuss the inputs for the liquefaction assessment including ground motion parameters and site characteristics, introduce the metrics used to assess liquefaction potential at the

selected sites, present the results of the liquefaction hazard evaluation, and discuss the results of the model validation.

5.1 Ground Motion Characteristics and Other Inputs for Liquefaction Hazard Assessment

For the liquefaction assessment, required ground motion parameters included M_w , a_{max} , and R_{hyp} for each site evaluated. Values for a_{max} at each site during the Pawnee event were estimated using the USGS ShakeMap (USGS 2016). While the ShakeMap provides the a_{max} at each location, the geometric mean a_{max} is needed for liquefaction evaluation. Geometric mean a_{max} was computed by dividing peak a_{max} from the ShakeMap by a factor of 1.117 (Boore and Kishida 2017). A map of geometric mean a_{max} for the Pawnee earthquake is shown in Figure 66.

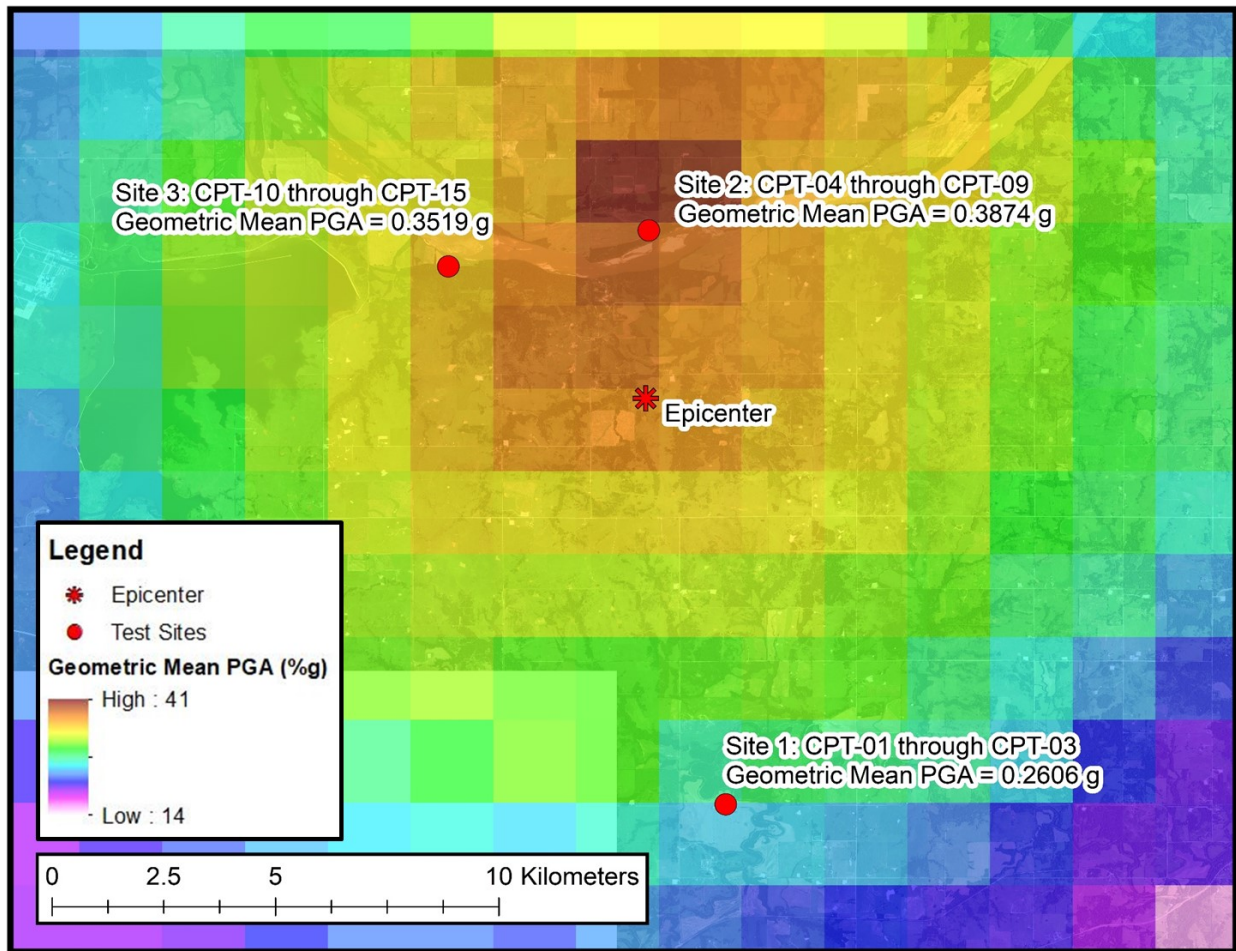


Figure 66. Geometric Mean a_{max} for 3 Sep 2016, Pawnee, OK earthquake based on USGS ShakeMap. (USGS 2016)

For comparison, a_{\max} was also estimated using the Zalachoris and Rathje (2019) GMPE. Estimated a_{\max} from the Zalachoris and Rathje (2019) GMPE are similar to geometric mean values from the ShakeMap (USGS 2016), particularly at Site 1, which is slightly farther from the epicenter. The Zalachoris and Rathje (2019) GMPE predicts a_{\max} values at Sites 2 and 3 that are approximately 13% higher than a_{\max} estimates from the USGS ShakeMap. Estimates of a_{\max} from the ShakeMap are used for assessing liquefaction hazard and model validation.

Site and soil profile information for liquefaction analysis was derived from the site investigation discussed in Section 3. Groundwater depths during the 2016 Pawnee event were estimated by comparing river gage heights during the earthquake with gage heights recorded during CPT testing (U.S. Geologic Survey 2016b,c). The differential in gage height was used to adjust the groundwater depth observed during CPT testing either up or down to provide an estimate of groundwater depth during the Pawnee earthquake. Gage data for Black Bear Creek at Pawnee, OK were used for Site 1, and gage data for the Arkansas River at Ralston, OK were used for Sites 2 and 3 (U.S. Geologic Survey 2016b,c). Figure 67 through Figure 69 show gage heights during CPT testing and the Pawnee earthquake for Sites 1 through 3, respectively.

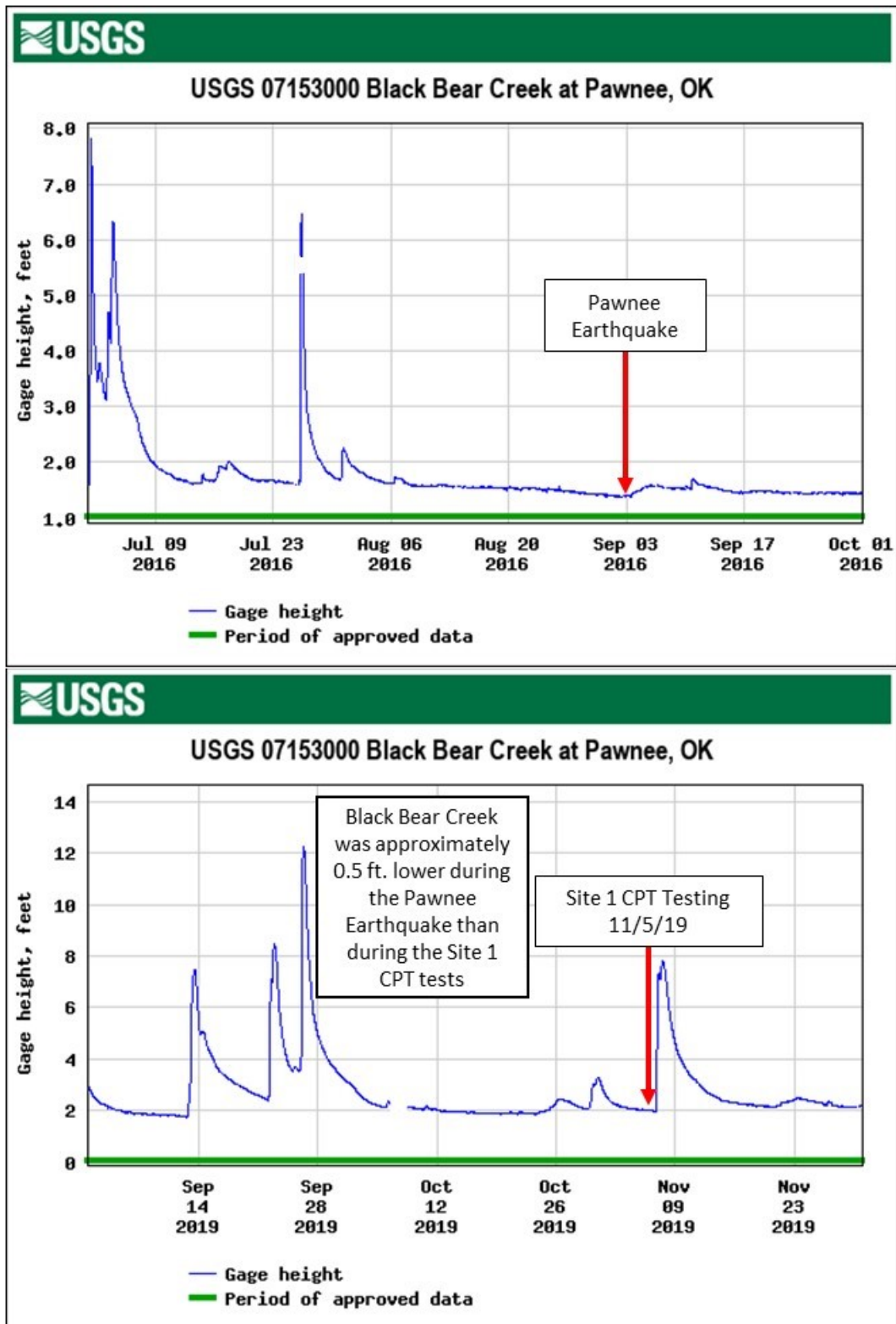


Figure 67. Gage data for Black Bear Creek at Pawnee, OK during the 3 Sep 2016 Pawnee Earthquake and 5 Nov 2019 CPT testing at Site 1. (after U.S. Geologic Survey 2016b,c)

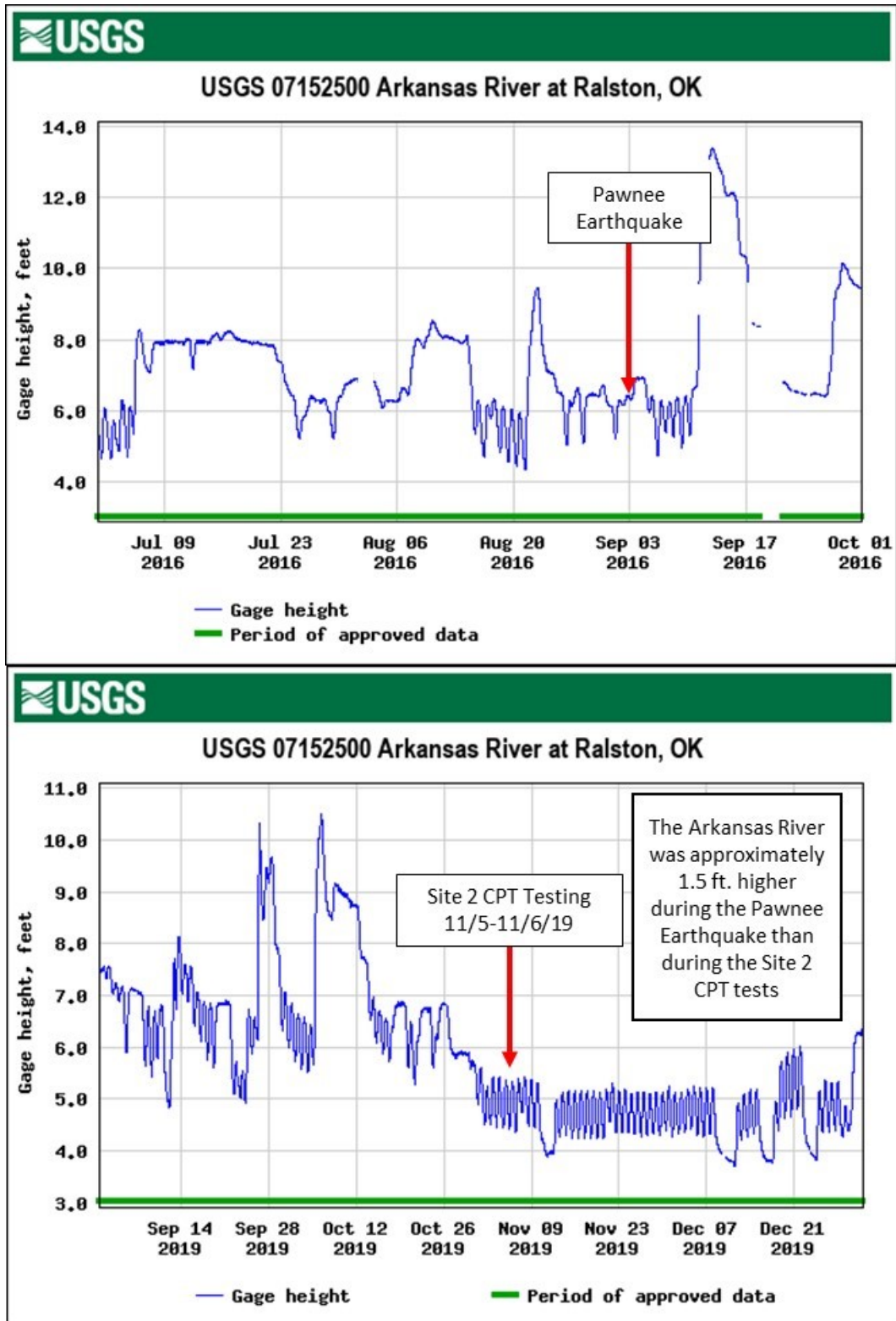


Figure 68. Gage data for Arkansas River at Ralston, OK during the 3 Sep 2016 Pawnee Earthquake and 5-6 Nov 2019 CPT testing at Site 2. (after U.S. Geologic Survey 2016b,c)

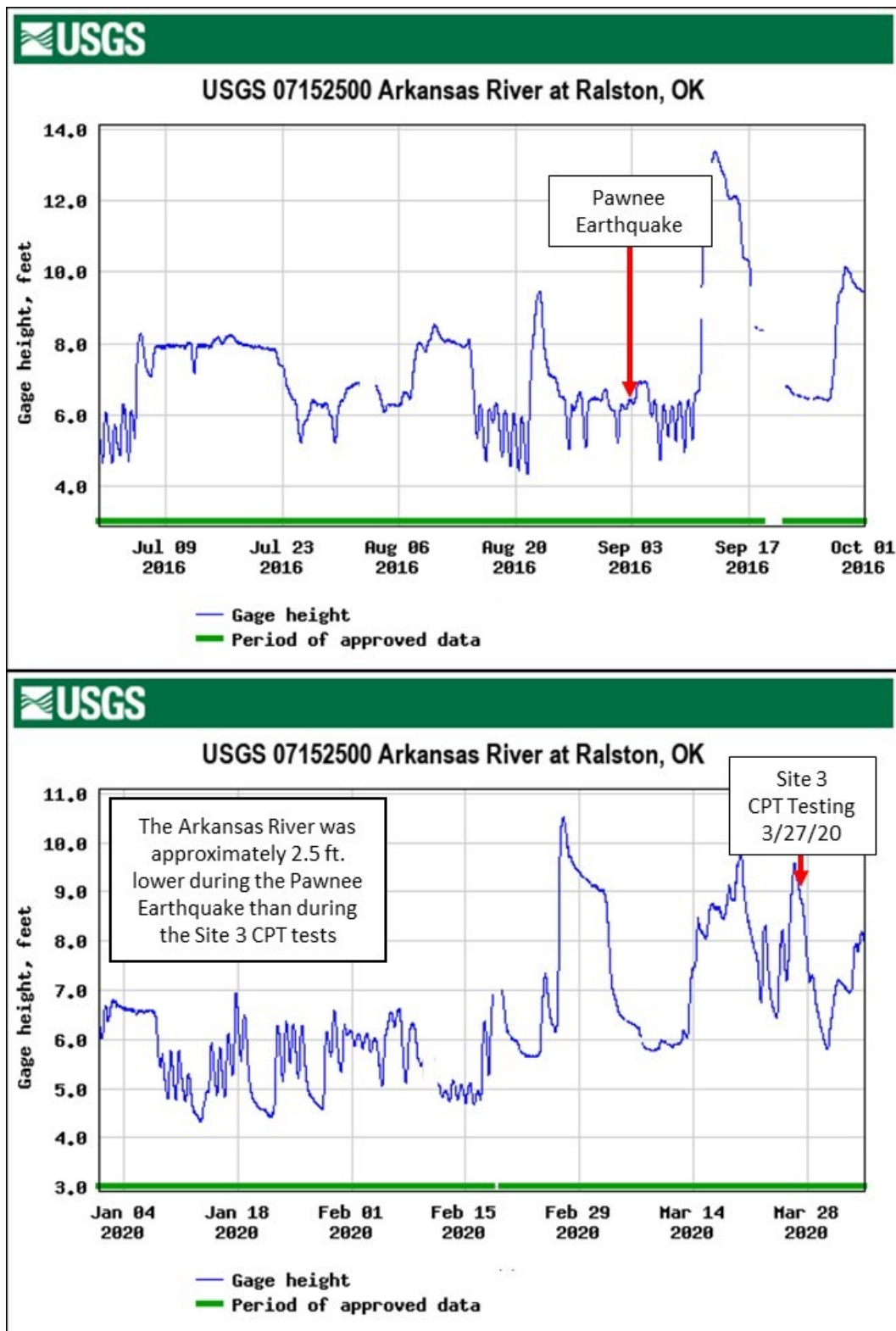


Figure 69. Gage data for Arkansas River at Ralston, OK during the 3 Sep 2016 Pawnee Earthquake and 27 Mar 2020 CPT testing at Site 3. (after U.S. Geologic Survey 2016b,c)

The use of gage height comparisons from gages 15-30 km downstream of the test sites provides only a rough estimate of differences in water level (and water table depth) at the test sites themselves. However, this data provided the best available estimate of water table depths for use during the liquefaction hazard analysis performed as part of model validation. A summary of the ground motion parameters, site characteristics, and groundwater table depths used for the liquefaction hazard analysis is shown in Table 9.

Table 9. Ground motion and site characteristics for liquefaction hazard analysis at the Pawnee Earthquake test sites.

| Sounding | Site | ShakeMap Geometric Mean PGA (g) | ShakeMap Standard Deviation of ln(PGA) (log units) | PGA from ZR19 GMPE (g) | Epicentral Distance (km) | Hypocentral Distance (km) | Estimated Groundwater Depth (m) | V _{s12} (m/s) | V _{s30} (m/s) |
|----------|------|---------------------------------|--|------------------------|--------------------------|---------------------------|---------------------------------|------------------------|------------------------|
| CPT-01 | 1 | 0.2606 | 0.4938 | 0.2543 | 8.64 | 10.30 | 2.29 | 162.65 | 270.16 |
| CPT-02 | 1 | 0.2606 | 0.4938 | 0.2546 | 8.63 | 10.29 | 2.90 | 176.29 | 270.16 |
| CPT-03 | 1 | 0.2606 | 0.4938 | 0.2571 | 8.55 | 10.22 | 3.51 | 176.29 | 270.16 |
| CPT-04 | 2 | 0.3874 | 0.5865 | 0.4337 | 4.36 | 7.10 | 3.05 | 170.20 | 273.56 |
| CPT-05 | 2 | 0.3874 | 0.5865 | 0.4337 | 4.36 | 7.10 | 3.05 | 172.04 | 273.56 |
| CPT-06 | 2 | 0.3874 | 0.5865 | 0.4328 | 4.38 | 7.11 | 2.74 | 140.19 | 273.56 |
| CPT-07 | 2 | 0.3874 | 0.5865 | 0.4354 | 4.34 | 7.08 | 2.59 | 140.98 | 273.56 |
| CPT-08 | 2 | 0.3874 | 0.5865 | 0.4381 | 4.29 | 7.05 | 2.59 | 158.96 | 273.56 |
| CPT-09 | 2 | 0.3874 | 0.5865 | 0.4381 | 4.28 | 7.05 | 2.90 | 173.28 | 273.56 |
| CPT-10 | 3 | 0.3519 | 0.5890 | 0.4003 | 5.18 | 7.63 | 3.36 | 148.28 | 285.66 |
| CPT-11 | 3 | 0.3519 | 0.5890 | 0.4026 | 5.14 | 7.60 | 1.51 | 142.91 | 285.66 |
| CPT-12 | 3 | 0.3519 | 0.5890 | 0.4011 | 5.17 | 7.62 | 2.16 | 150.18 | 285.66 |
| CPT-13 | 3 | 0.3519 | 0.5890 | 0.4003 | 5.18 | 7.63 | 1.36 | 156.54 | 285.66 |
| CPT-14 | 3 | 0.3519 | 0.5890 | 0.3973 | 5.24 | 7.67 | 2.96 | 156.89 | 285.66 |
| CPT-15 | 3 | 0.3519 | 0.5890 | 0.3944 | 5.3 | 7.71 | 4.76 | 174.91 | 285.66 |

5.2 Assessment of Liquefaction Potential at the Pawnee Earthquake Test Sites

To assess the validity of the new liquefaction triggering model developed herein, liquefaction potential at the selected test sites was evaluated using both the new induced seismicity-specific model and a selection of existing liquefaction triggering models developed for tectonic earthquakes (i.e., Boulanger and Idriss (2014) and Green et al. (2017) triggering model for the WUS and CEUS). The Boulanger and Idriss (2014) model was developed for earthquakes in active shallow-crustal tectonic regions but is commonly used in other areas, while the Green et al. (2017) CEUS is an updated model specific to the CEUS region. The Green et al. (2017) WUS model was included as an example of an updated model for active tectonic regimes. These models, particularly the Boulanger and Idriss (2014) and Green et al. (2017) CEUS models,

represent the standard of practice for liquefaction evaluation for tectonic earthquakes in Oklahoma. As such, these models are used as benchmarks against which to compare the new induced seismicity-specific liquefaction hazard model developed herein.

The efficacies of the selected models were evaluated using the Ishihara-inspired liquefaction potential index (LPI_{ish}) (Maurer et al. 2015b). LPI_{ish} is a dimensionless index that correlates to surficial liquefaction manifestation severity and represents the cumulative liquefaction response of a soil profile from the ground surface to a depth of 20 m. This response is related to cumulative thickness of the liquefied layers, the depth to these layers, and the degree to which FS_{liq} for these layers is less than 1.0. However, LPI_{ish} also accounts for the effect of the thickness of the non-liquefied crust (H_1) relative to the cumulative thickness of the underlying liquefied materials (H_2) on the severity of liquefaction manifestations. To accomplish this, the LPI_{ish} framework merges the concepts of the Liquefaction Potential Index (LPI) framework developed by Iwasaki et al. (1978) and the H_1 - H_2 chart developed by Ishihara (1985) (Maurer et al. 2015b). To provide background for the LPI_{ish} framework, these concepts will be briefly discussed.

LPI is a dimensionless index used to predict the severity of surficial liquefaction manifestations for a given soil profile and ground motion. LPI is computed as:

$$LPI = \int_0^{20\text{ m}} F_{LPI}(FS_{liq}) \cdot w(z) dz \quad (33)$$

where $F_{LPI} = 1 - FS_{liq}$ for $FS_{liq} < 1.0$, $F_{LPI} = 0$ for $FS_{liq} \geq 1.0$; and $w(z)$ is a depth weighting function given by $w(z) = 10 - 0.5z$, where z is the depth below the ground surface in meters. LPI assumes that each liquefied layer shallower than 20 m contributes to the severity of surficial liquefaction manifestations. The relative contribution of each liquefied layer increases with both layer thickness and proximity to the ground surface. LPI can range from 0 for a site having $FS > 1.0$ for the entire upper 20 m of the site to a maximum of 100 for a site where $FS_{liq} = 0$ for the entire upper 20 m. Based on the findings of Iwasaki et al. (1978), the following severity criteria are commonly used in practice:

$LPI < 5$: No to Minor Surficial Liquefaction Manifestations;

$5 \leq LPI \leq 15$: Moderate Surficial Liquefaction Manifestations;

$LPI > 15$: Severe Surficial Liquefaction Manifestations.

Ishihara (1985) observed that the thickness of the non-liquefiable crust at a given site had a significant influence on the severity of surficial manifestations at the site. Using data from the 1983, $M_w 7.7$ Nihonkai-chubu and the 1976, $M_w 7.8$ Tangshan earthquakes, Ishihara (1985) developed a generalized relationship between H_1 to H_2 and the potential for liquefaction induced damage at the ground surface. The thicker H_1

is relative to H_2 , the less likely liquefaction induced damage will occur at the ground surface. Figure 70 presents the H_1 - H_2 chart developed by Ishihara (1985) and illustrates how H_1 and H_2 are defined for different site stratigraphies.

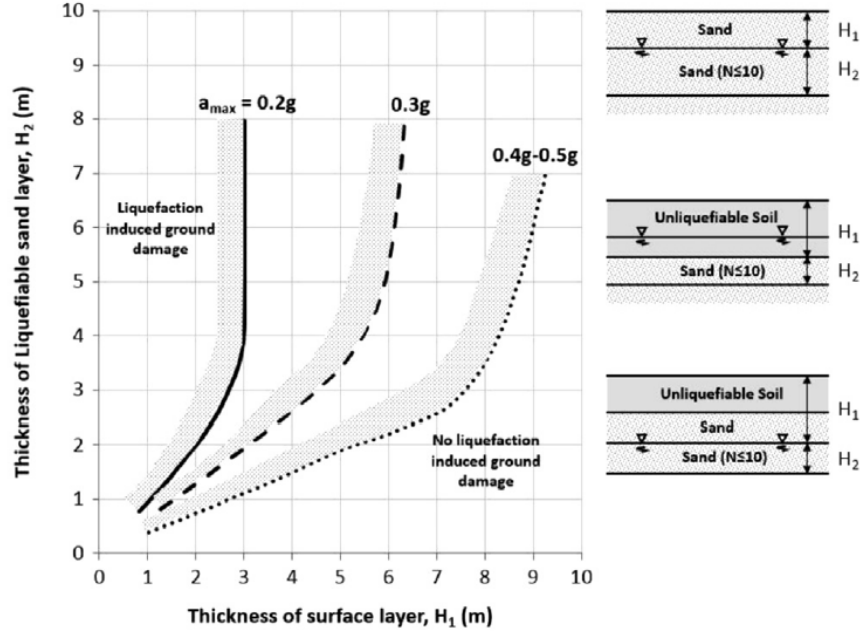


Figure 70. Relationship between the thickness of the non-liquefied surface layer (H_1) and the thickness of the underlying liquefiable sand layer (H_2) for predicting when surficial liquefaction manifestations will and will not occur at level-ground sites (from van Ballegooy et al. 2015; based on Ishihara 1985).

Because LPI_{ish} incorporates the effects of the Ishihara (1985) H_1 - H_2 relationships, it is better able to predict the severity of liquefaction surficial manifestations at sites with varying stratigraphies and non-liquefied crusts than LPI. Also, because LPI_{ish} integrates across depth, similar to LPI, it is able to account for more complex stratigraphies than the Ishihara H_1 - H_2 charts. LPI_{ish} is defined as (Maurer et al. 2015b):

$$LPI_{ish} = \int_{H_1}^{20\text{ m}} F_{LPI_{ish}}(FS_{liq}) \cdot \frac{25.56}{z} dz \quad (34a)$$

$$F_{LPI_{ish}}(FS_{liq}) = 1 - FS_{liq}; \quad \text{if } FS_{liq} \leq 1 \text{ and } H_1 \cdot m(FS) \leq 3 \quad (34b)$$

$$= 0; \quad \text{if } FS_{liq} > 1 \text{ or } H_1 \cdot m(FS) > 3 \quad (34c)$$

$$m(FS_{liq}) = \exp\left\{\frac{5}{25.56 \cdot (1 - FS_{liq})}\right\} - 1; \quad \text{if } FS_{liq} \leq 0.95 \quad (34d)$$

$$= 100; \quad \text{if } FS_{liq} > 0.95 \quad (34e)$$

where H_1 is the shallowest depth where $FS_{liq} < 1$. As noted, unlike LPI, LPI_{ish} explicitly accounts for the influence of the non-liquefied crust on the severity of surficial manifestations (Green et al. 2020). Additionally, van Ballegooy et al. (2014) found that LPI_{ish} more appropriately weights the contribution of shallow layers to surficial manifestations compared to LPI. As a result, LPI_{ish} tends to produce more accurate predictions of surficial manifestation severity than LPI and other similar indices (Maurer et al. 2015b). Maurer et al. (2015a) note that the optimal LPI and LPI_{ish} thresholds corresponding to the different surficial liquefaction manifestation severities will be dependent on the procedure used to estimate FS_{liq} as well as profile characteristics. Because of limited liquefaction case history for induced earthquakes in Oklahoma, the thresholds presented by Maurer et al. (2014) for LPI were adapted for use with LPI_{ish} in this study. Accordingly, the LPI_{ish} thresholds used were:

- $LPI_{ish} < 4$: No Surficial Liquefaction Manifestations;
- $4 \leq LPI_{ish} < 8$: Minor Surficial Liquefaction Manifestations;
- $8 \leq LPI_{ish} < 15$: Moderate Surficial Liquefaction Manifestations;
- $LPI_{ish} \geq 15$: Severe Surficial Liquefaction Manifestations.

To validate the liquefaction triggering models, the LPI_{ish} framework and selected LPI_{ish} thresholds were used to predict the expected severity of liquefaction surficial manifestations at each Pawnee CPT sounding location. Predictions were made based on the estimated ground motions at each site during the Pawnee earthquake. FS_{liq} and the corresponding LPI_{ish} and liquefaction surficial manifestation severity were estimated using each of the selected liquefaction triggering models. The predicted severity was then compared to the severity of liquefaction manifestations observed at each site following the Pawnee earthquake to evaluate the efficacy of these models.

5.3 Liquefaction Hazard Analysis and Model Validation Results – FS_{liq} and LPI_{ish}

As noted, model validation involved determining LPI_{ish} at each sounding location and comparing the predicted liquefaction surficial manifestation severity based on LPI_{ish} to the post-event observed severity. Reported liquefaction manifestation severity at each sounding location was classified as “no liquefaction,” “minor liquefaction,” “moderate liquefaction,” or “severe liquefaction” based on criteria presented by Green et al. (2014), as shown in Table 10. Documented observations of liquefaction at each sounding location and assigned liquefaction severity classifications are shown in Table 11.

Table 10. Liquefaction severity classification criteria. (Green et al. 2014)

| Classification | Criteria |
|-----------------------|---|
| No Liquefaction | No surficial liquefaction manifestation or lateral spread cracking |
| Minor Liquefaction | Small, isolated liquefaction features; streets had traces of ejecta or wet patches less than a vehicle width; < 5% of ground surface covered by ejecta |
| Moderate Liquefaction | Groups of liquefaction features; streets had ejecta patches greater than a vehicle width but were still passable; 5-40% of ground surface covered by ejecta |
| Severe Liquefaction | Large masses of adjoining liquefaction features, streets impassible due to liquefaction, >40% of ground surface covered by ejecta |

Table 11. Liquefaction severity classifications at CPT sounding locations.

| Sounding | Site | Documented Liquefaction Manifestations | Severity Classification (based on Green et al. 2014) |
|-----------------|-------------|---|---|
| CPT-01 | 1 | None | No Liquefaction |
| CPT-02 | 1 | Small cluster of sand boils with small amount of ejecta | Minor |
| CPT-03 | 1 | Small cluster of sand boils with small amount of ejecta | Minor |
| CPT-04 | 2 | Cracks approximately 2 to 5 m long with small amount of ejecta | Minor |
| CPT-05 | 2 | Cracks approximately 2 to 5 m long with small amount of ejecta | Minor |
| CPT-06 | 2 | None | No Liquefaction |
| CPT-07 | 2 | None | No Liquefaction |
| CPT-08 | 2 | None | No Liquefaction |
| CPT-09 | 2 | None | No Liquefaction |
| CPT-10 | 3 | Cracks from 0.5 to 5 cm wide and 4 to 42 m long with small amount of ejecta. | Minor |
| CPT-11 | 3 | Cracks up to 8 cm wide and 4 to 42 m long. Sand blow with ejecta covering a 146 m ² area and associated ground settlement. | Severe |
| CPT-12 | 3 | Cracks from 0.5 to 5 cm wide and 4 to 42 m long with small amount of ejecta. | Minor |
| CPT-13 | 3 | None | No Liquefaction |
| CPT-14 | 3 | None | No Liquefaction |
| CPT-15 | 3 | None | No Liquefaction |

FS_{liq} and LPI_{ish} were determined based on the new induced seismicity-specific liquefaction triggering model developed herein, as well as the Boulanger and Idriss (2014) model for the WUS, and the Green et al. (2017) models for the CEUS and WUS. Plots of q_{c1Ncs} , I_c , FS_{liq} , and FS_{liq} normalized by FS_{liq} for the Green et al. (2017) CEUS model (FS_{Gea17_CEUS}) for each CPT location are shown in Figure 71 through Figure 85. FS_{Gea17_CEUS} was used for FS_{liq} comparisons since it was developed specifically for liquefaction hazard analysis in the CEUS and is thus considered most suitable for evaluating liquefaction potential for tectonic earthquakes in the region. Comparisons of FS_{liq} provide fairly direct comparison of r_d/MSF for each method because the remaining inputs to CSR* are the same for each method. $CRR_{M7.5}$ curves are slightly different for the Boulanger and Idriss (2014) and the Green et al. (2017) models, but the observed differences in FS_{liq} are primarily due to differences in r_d and MSF. Figure headings indicate the severity of observed liquefaction manifestations at each location based on the Green et al. (2014) criteria.

Curves are shown for the Oklahoma model implemented for different combinations of the two r_d and two MSF relationships proposed in Sections 4.4 and 4.5. The preferred implementation would be to use r_d Model 1 and MSF Model 1. However, r_d Model 2 and/or MSF Model 2 may be required if V_{s12} and/or R_{hyp} are not available. As shown in these figures, for the Pawnee sites and earthquake motions, MSF Model 2 results in significantly lower FS_{liq} than Model 1. This is likely due to the short hypocentral distances of these sites ($R_{hyp} \leq 11$ km). The choice of r_d model has less of an impact with r_d Model 1 resulting in slightly lower FS_{liq} at most sites. This difference is more pronounced at locations with larger V_{s12} (e.g., CPT-04, CPT-05, CPT-09, and CPT-15)

Figure 71 through Figure 85 show that $FS_{liq} < 1.0$ over much of the depth of the soil profiles for all the liquefaction triggering models. However, for depths greater than approximately 3 m, the Oklahoma model tends to result in substantially higher estimates of FS_{liq} than the tectonic models. This is reflective of trends in r_d/MSF for the various models. The Oklahoma models result in lower MSF estimates than the Boulanger and Idriss (2014) or Green et al. (2017) models. All else equal, lower MSF results in a decrease FS_{liq} . However, r_d estimates for the Oklahoma model are significantly lower than r_d estimates for the other models, which, all else equal, leads to increases in FS_{liq} . For depths greater than 3 m, the effect of the much lower r_d for Oklahoma outweighs the effect of the lower MSF. As a result, FS_{liq} at these depths tends to be higher for the Oklahoma triggering model. At shallower depths, FS_{liq} for the Oklahoma model is similar to or, in some cases, lower than FS_{liq} for the other models. This is because r_d is fairly similar for all models at shallow depths, but the Oklahoma MSF is lower than for the other models.

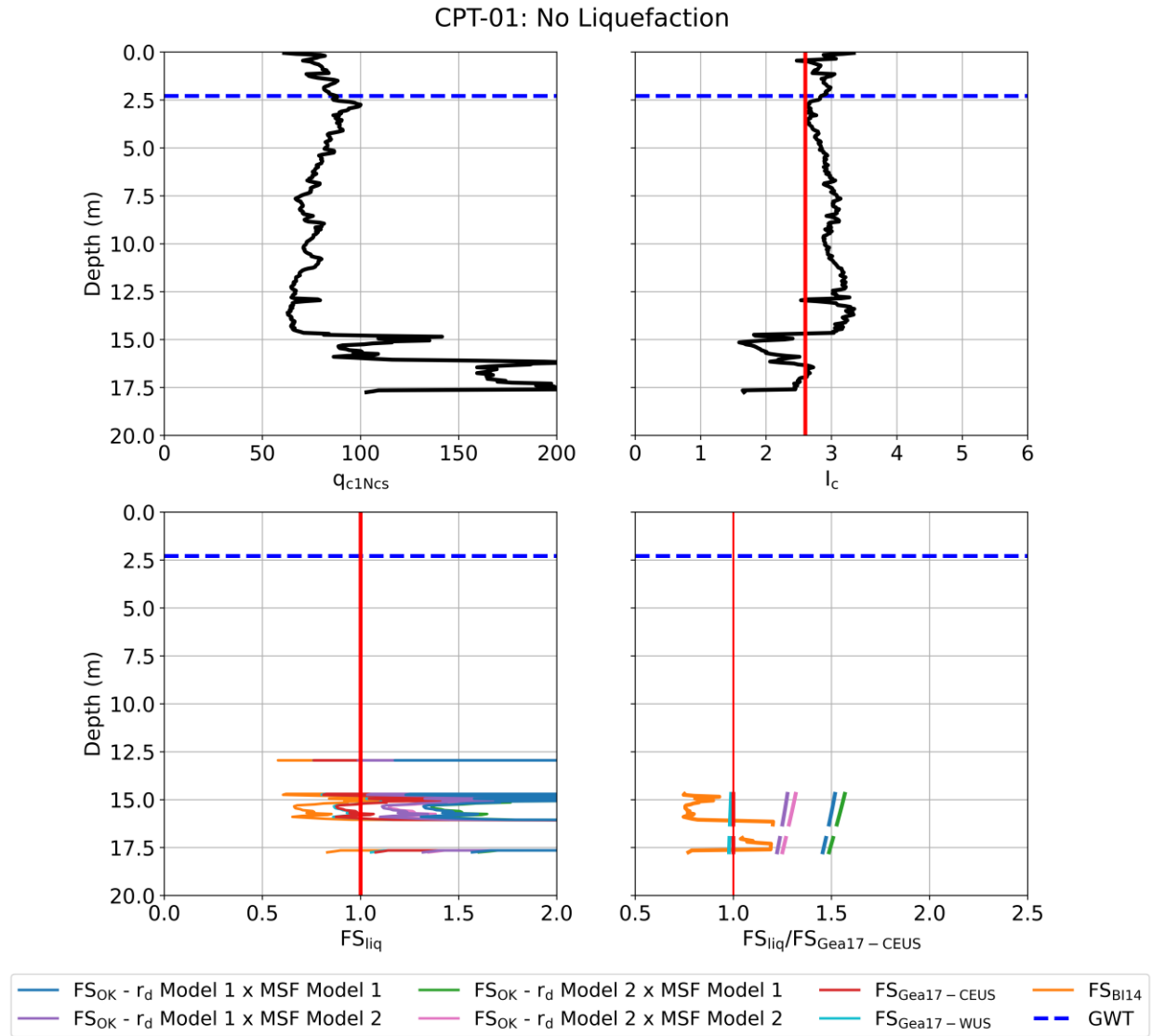


Figure 71. Profiles of q_{c1Ncs} , I_c , FS_{liq} , and FS_{liq} normalized by FS_{liq} for the Green et al. (2017) CEUS model ($FS_{Gea17-CEUS}$) for CPT-01, Site 1 (no post-event liquefaction manifestations observed). FS_{liq} for the current study (FS_{OK}) is shown for the ZR19_IZ database.

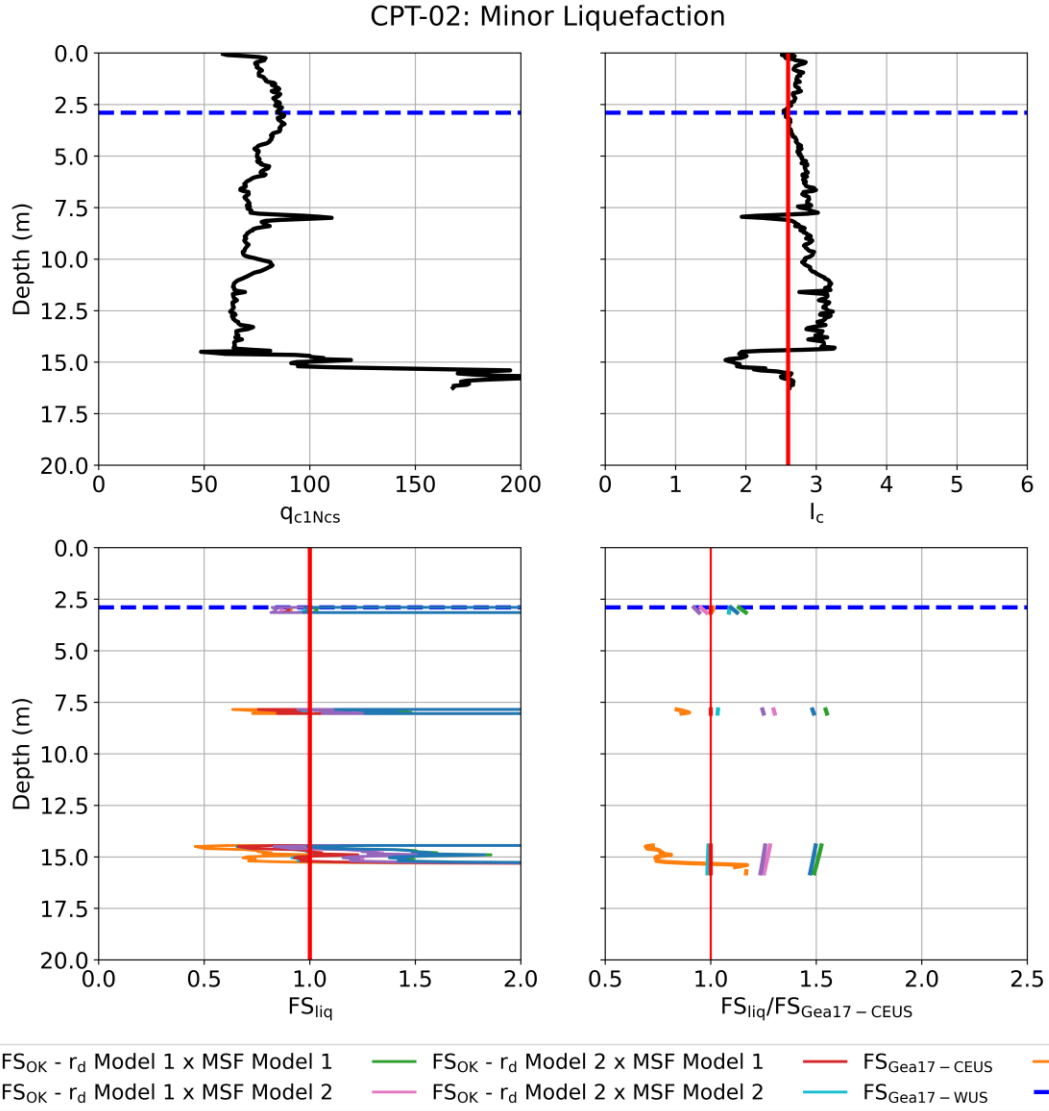


Figure 72. Profiles of q_{c1Ncs} , I_c , FS_{liq} , and FS_{liq} normalized by FS_{liq} for the Green et al. (2017) CEUS model ($FS_{Gea17-CEUS}$) for CPT-02, Site1 (minor post-event liquefaction manifestations observed). FS_{liq} for the current study (FS_{OK}) is shown for the ZR19_IZ database.

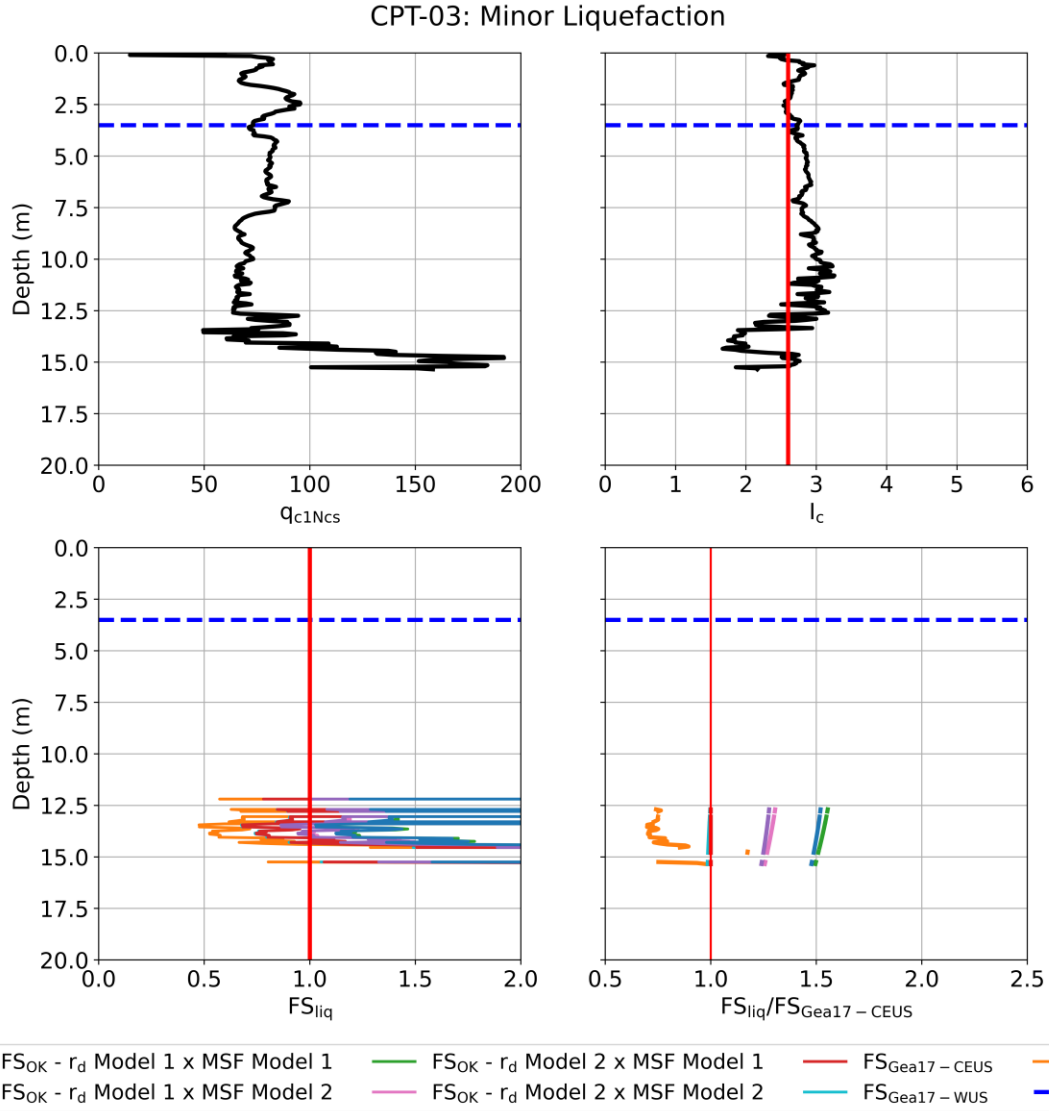


Figure 73. Profiles of q_{c1Ncs} , I_c , FS_{liq} , and FS_{liq} normalized by FS_{liq} for the Green et al. (2017) CEUS model ($FS_{Gea17-CEUS}$) for CPT-03, Site 1 (minor post-event liquefaction manifestations observed).

FS_{liq} for the current study (FS_{OK}) is shown for the ZR19_IZ database.

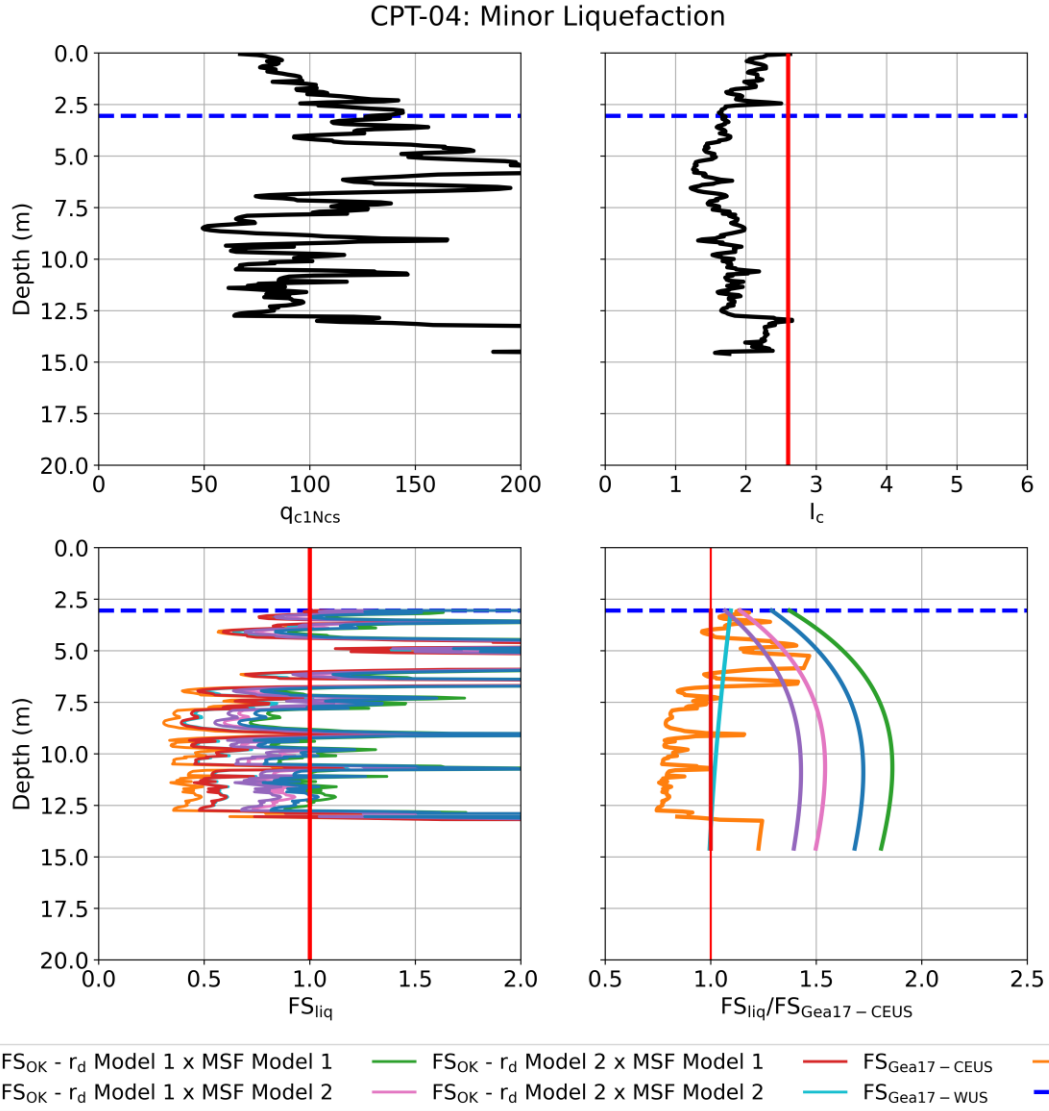


Figure 74. Profiles of q_{c1Ncs} , I_c , FS_{liq} , and FS_{liq} normalized by FS_{liq} for the Green et al. (2017) CEUS model ($FS_{Gea17-CEUS}$) for CPT-04, Site 2 (minor post-event liquefaction manifestations observed).

FS_{liq} for the current study (FS_{OK}) is shown for the ZR19_IZ database.

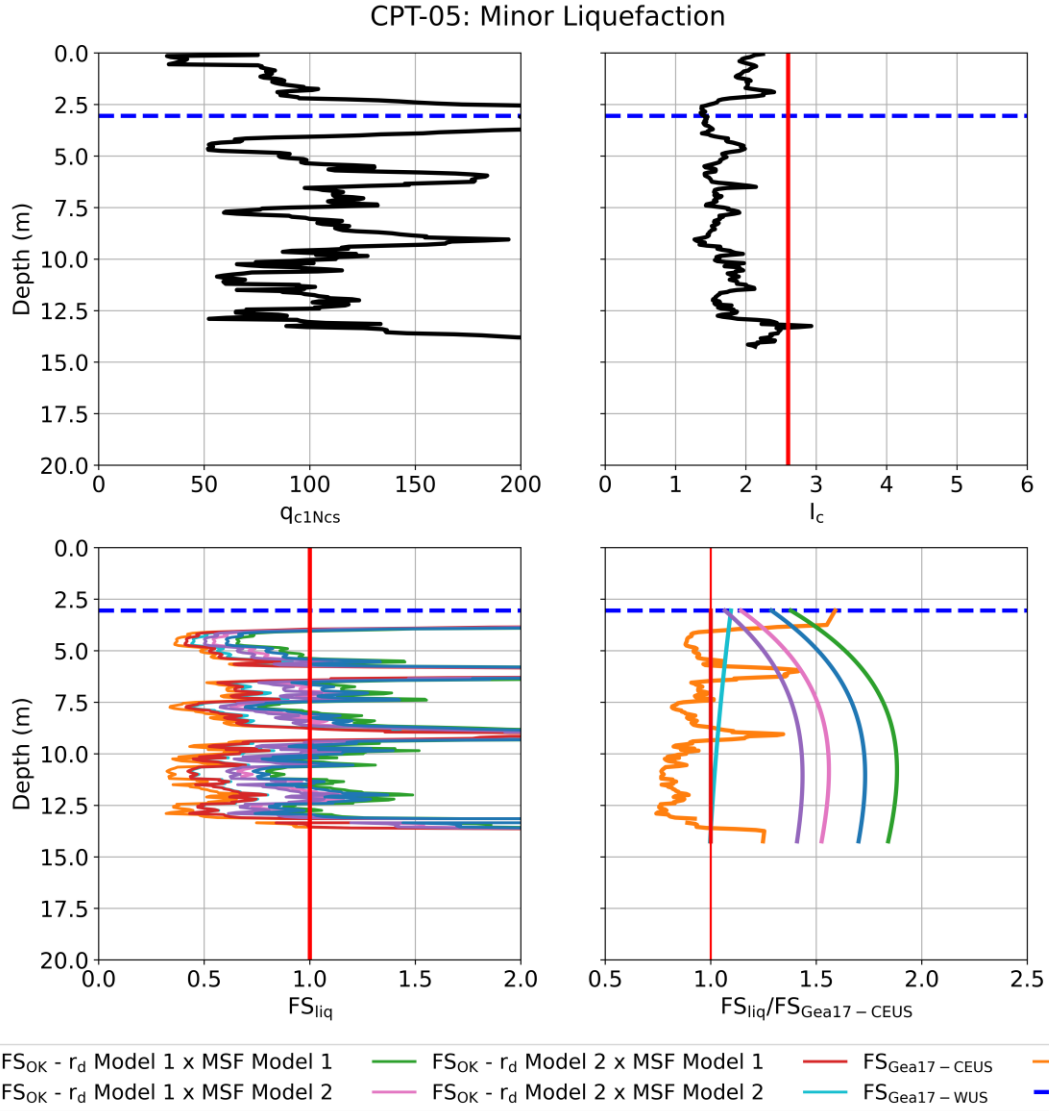


Figure 75. Profiles of q_{c1Ncs} , I_c , FS_{liq} , and FS_{liq} normalized by FS_{liq} for the Green et al. (2017) CEUS model ($FS_{Gea17-CEUS}$) for CPT-05, Site 2 (minor post-event liquefaction manifestations observed).

FS_{liq} for the current study (FS_{OK}) is shown for the ZR19_IZ database.

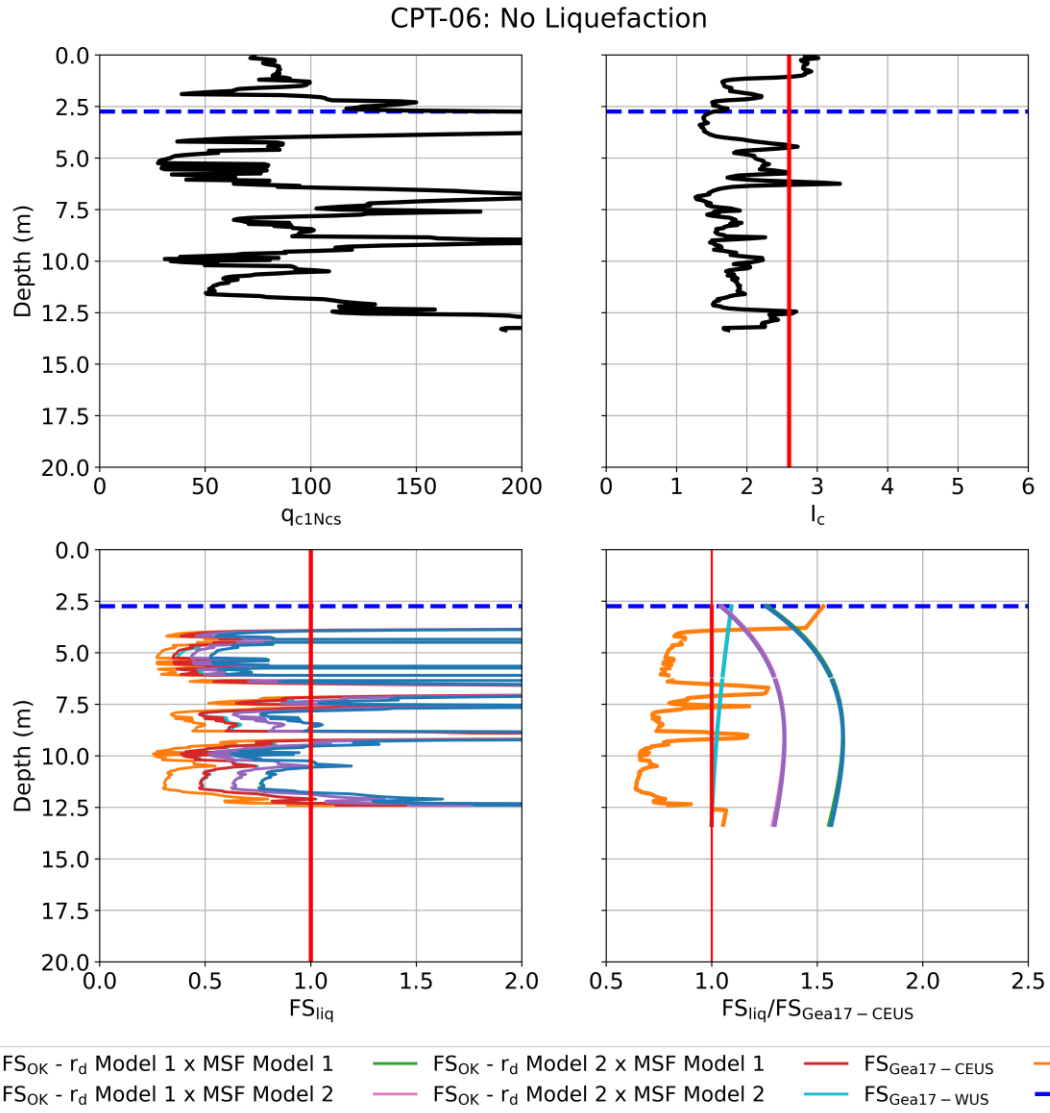


Figure 76. Profiles of q_{c1Ncs} , I_c , FS_{liq} , and FS_{liq} normalized by FS_{liq} for the Green et al. (2017) CEUS model ($FS_{Gea17-CEUS}$) for CPT-06, Site 2 (no post-event liquefaction manifestations observed). FS_{liq} for the current study (FS_{OK}) is shown for the ZR19_IZ database.

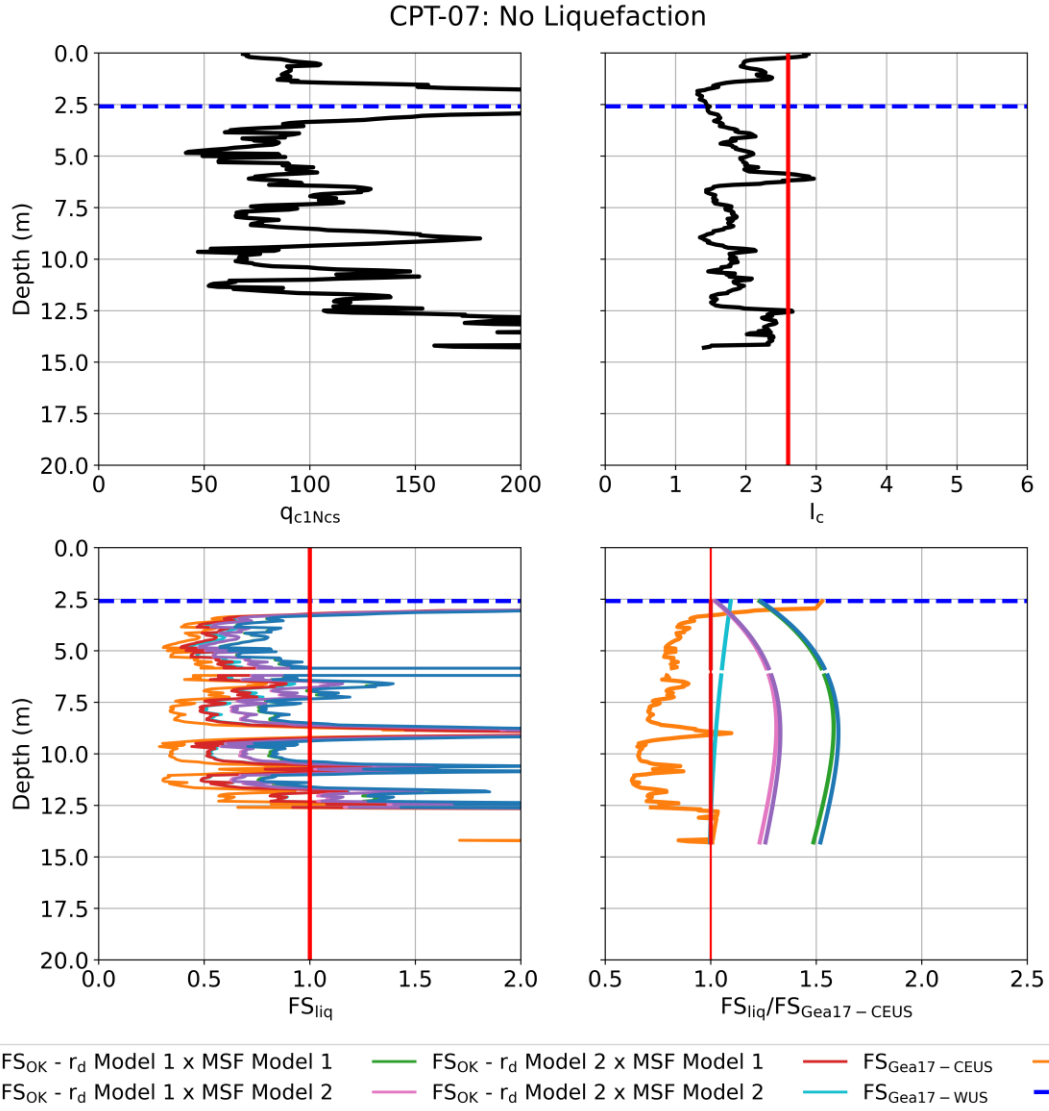


Figure 77. Profiles of q_{c1Ncs} , I_c , FS_{liq} , and FS_{liq} normalized by FS_{liq} for the Green et al. (2017) CEUS model ($FS_{Gea17-CEUS}$) for CPT-07, Site 2 (no post-event liquefaction manifestations observed). FS_{liq} for the current study (FS_{OK}) is shown for the ZR19_IZ database.

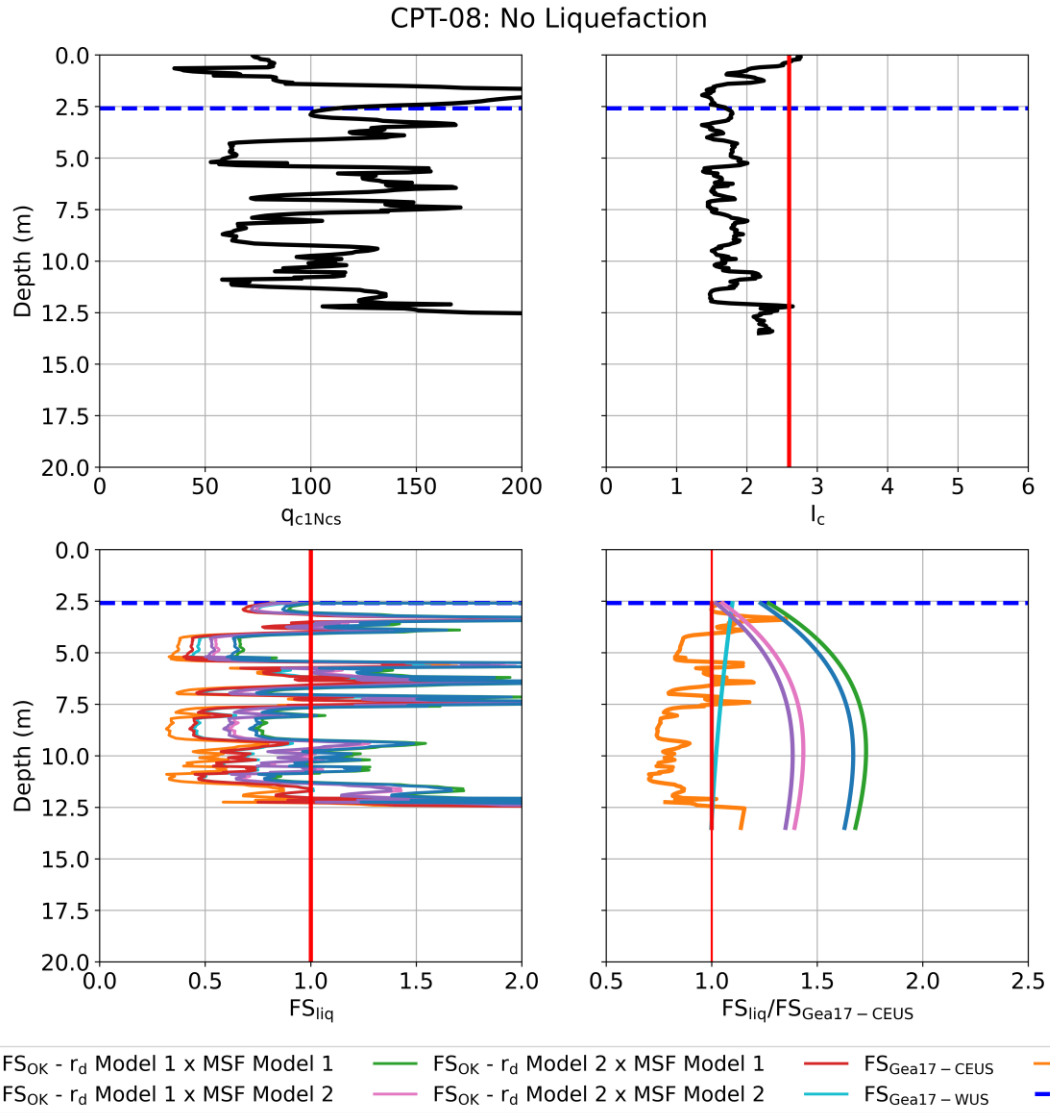


Figure 78. Profiles of q_{c1Ncs} , I_c , FS_{liq} , and FS_{liq} normalized by FS_{liq} for the Green et al. (2017) CEUS model ($FS_{Gea17-CEUS}$) for CPT-08, Site 2 (no post-event liquefaction manifestations observed). FS_{liq} for the current study (FS_{OK}) is shown for the ZR19_IZ database.

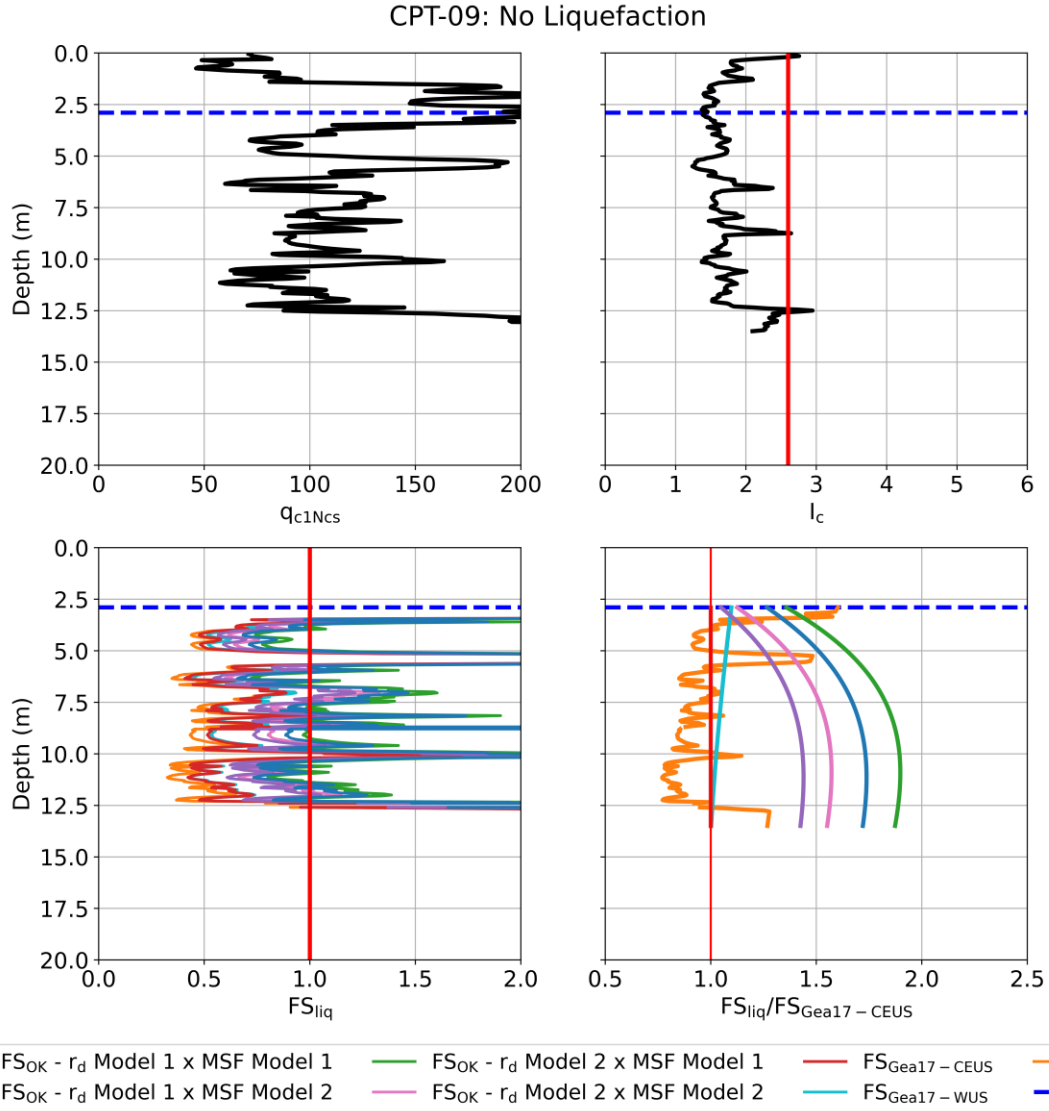


Figure 79. Profiles of q_{c1Ncs} , I_c , FS_{liq} , and FS_{liq} normalized by FS_{liq} for the Green et al. (2017) CEUS model ($FS_{Gea17-CEUS}$) for CPT-09, Site 2 (no post-event liquefaction manifestations observed). FS_{liq} for the current study (FS_{OK}) is shown for the ZR19_IZ database.

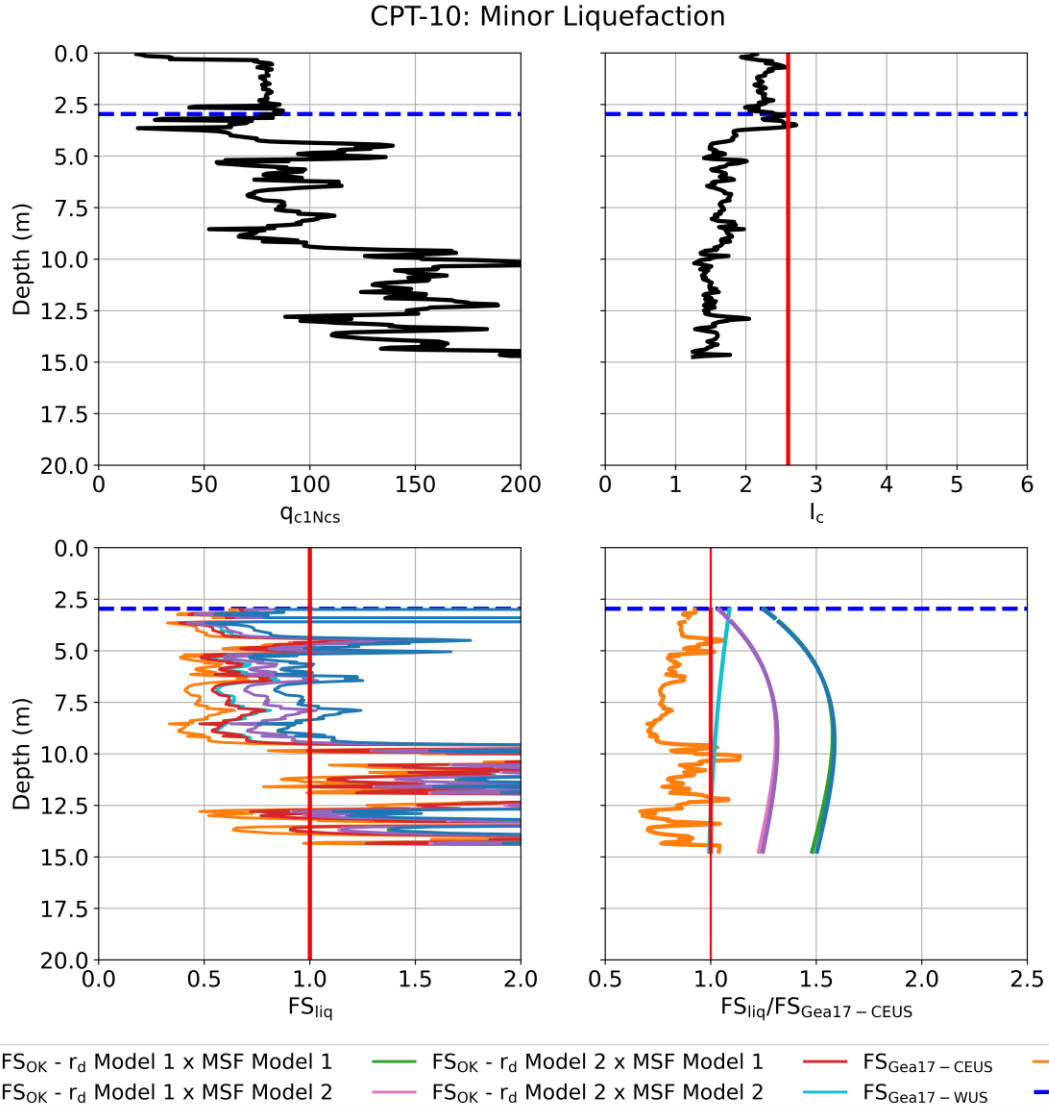


Figure 80. Profiles of q_{c1Ncs} , I_c , FS_{liq} , and FS_{liq} normalized by FS_{liq} for the Green et al. (2017) CEUS model ($FS_{Gea17-CEUS}$) for CPT-10, Site 3 (minor post-event liquefaction manifestations observed).

FS_{liq} for the current study (FS_{OK}) is shown for the ZR19_IZ database.

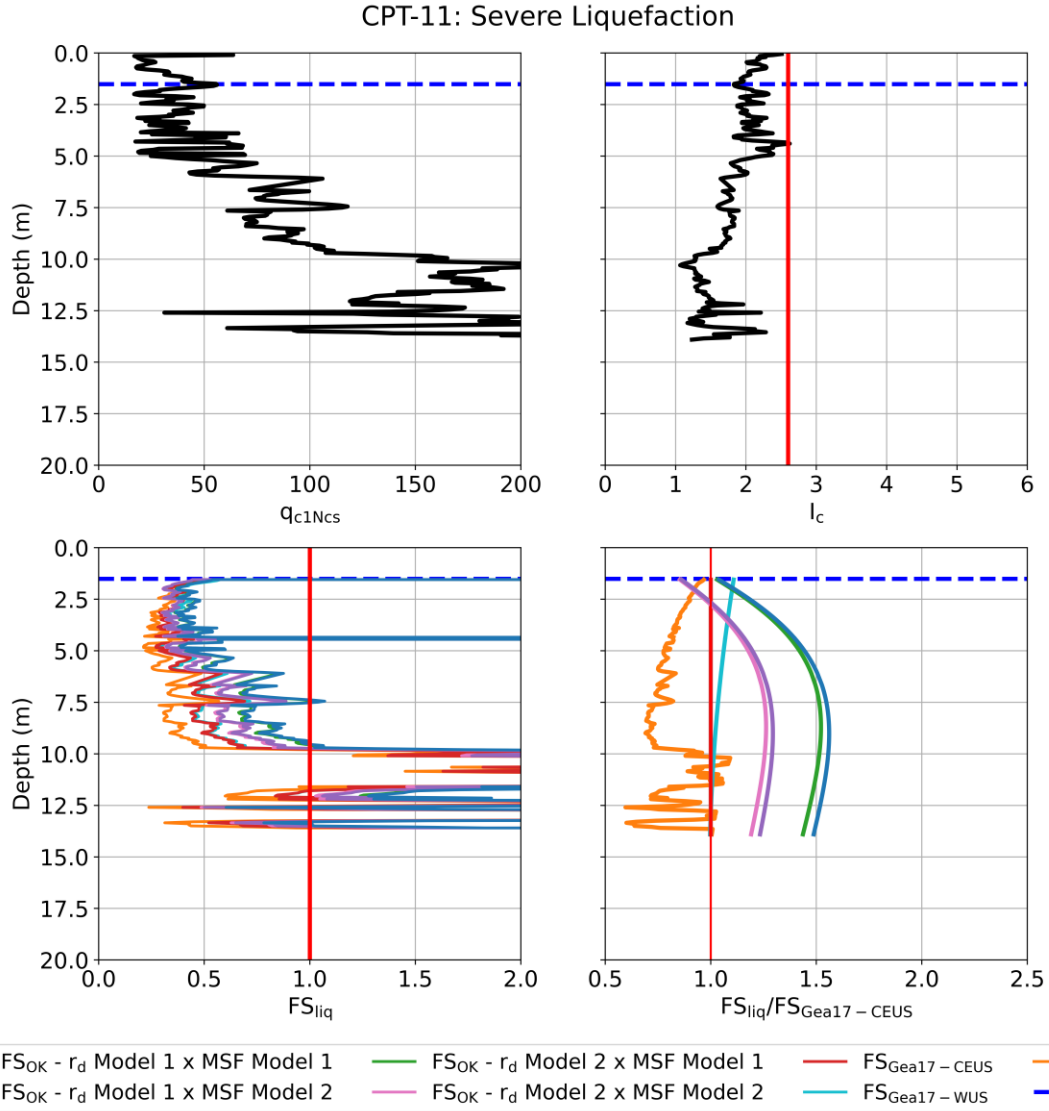


Figure 81. Profiles of q_{c1Ncs} , I_c , FS_{liq} , and FS_{liq} normalized by FS_{liq} for the Green et al. (2017) CEUS model ($FS_{Gea17-CEUS}$) for CPT-11, Site 3 (severe post-event liquefaction manifestations observed).

FS_{liq} for the current study (FS_{OK}) is shown for the ZR19_IZ database.

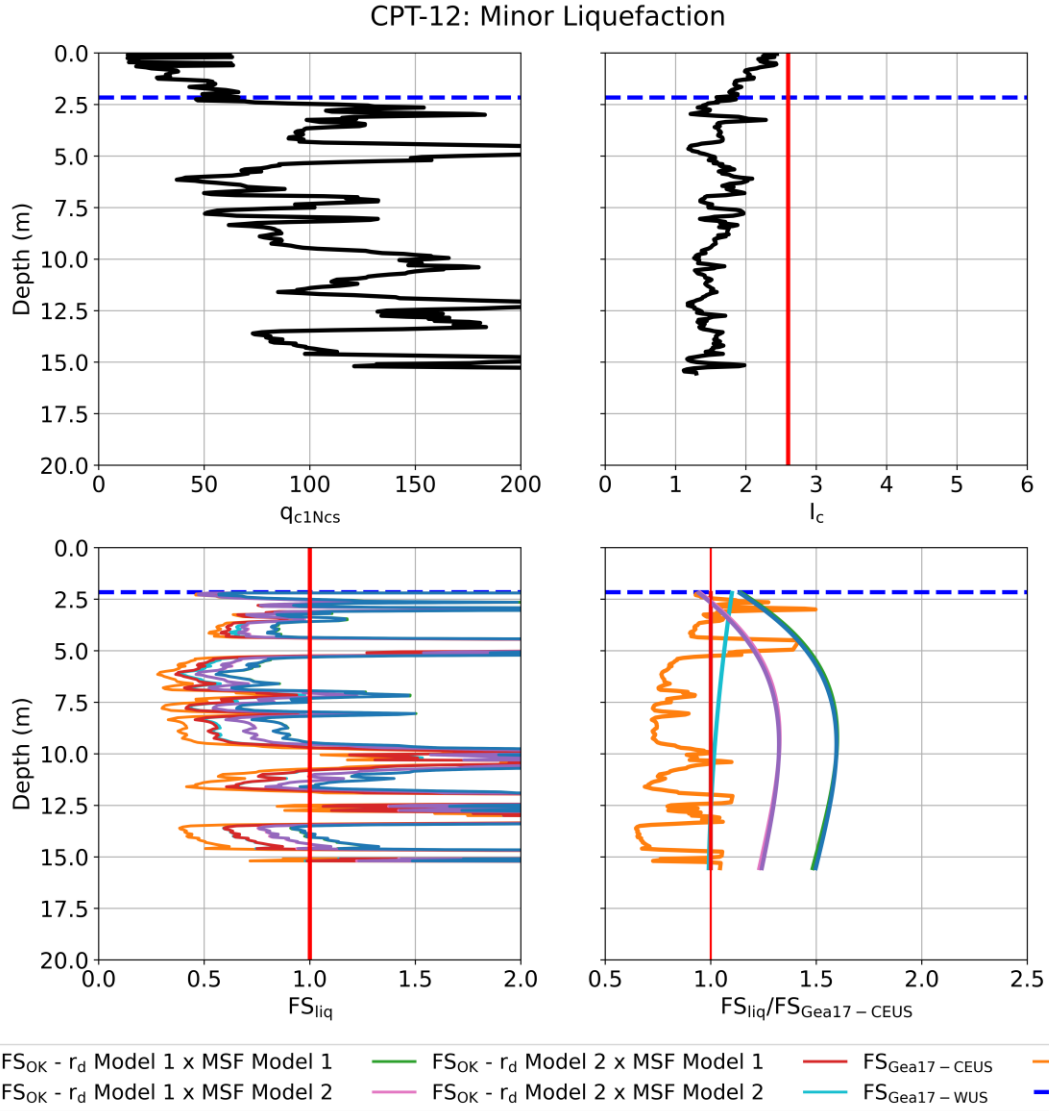


Figure 82. Profiles of q_{c1Ncs} , I_c , FS_{liq} , and FS_{liq} normalized by FS_{liq} for the Green et al. (2017) CEUS model ($FS_{Gea17-CEUS}$) for CPT-12, Site 3 (minor post-event liquefaction manifestations observed).

FS_{liq} for the current study (FS_{OK}) is shown for the ZR19_IZ database.

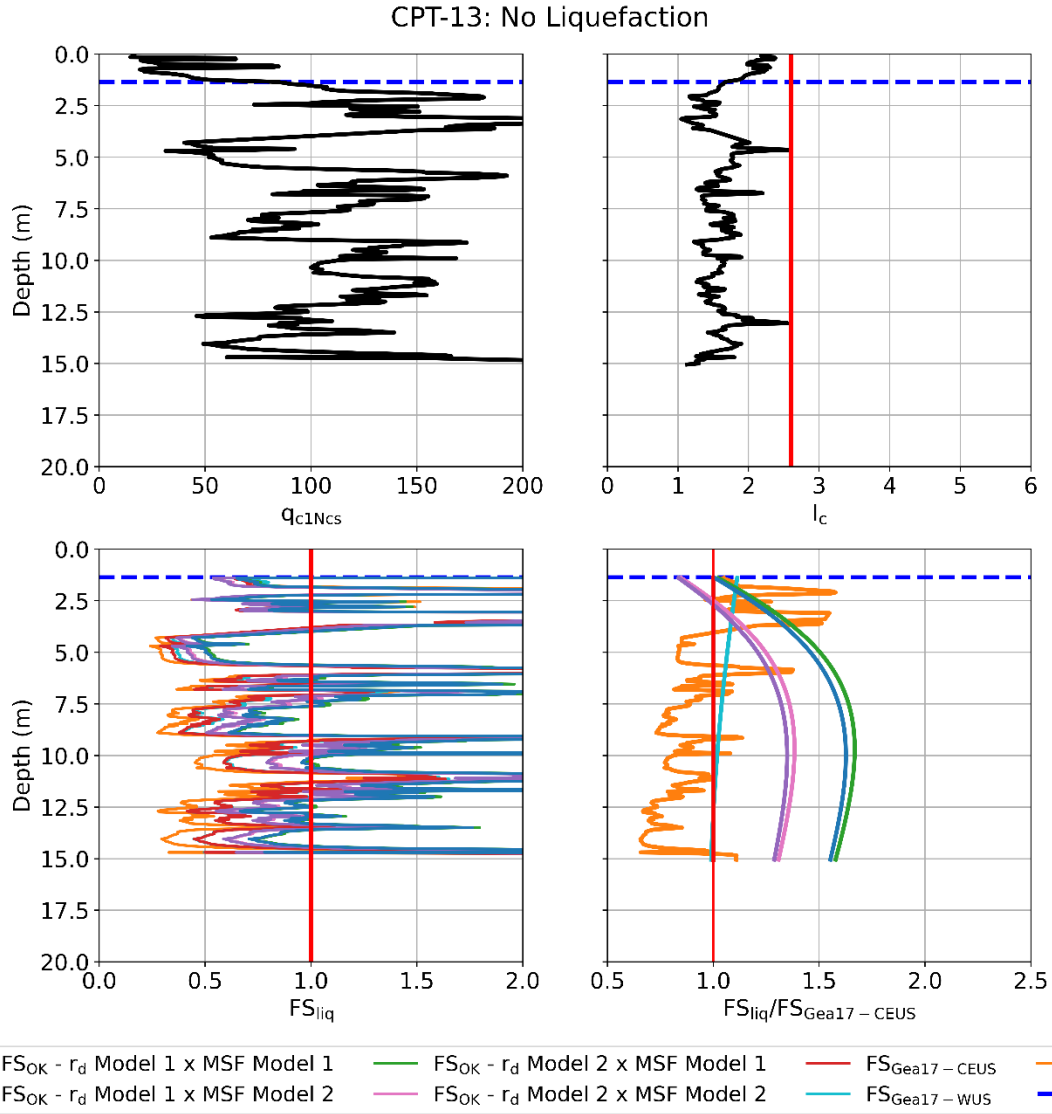


Figure 83. Profiles of q_{c1Ncs} , I_c , FS_{liq} , and FS_{liq} normalized by FS_{liq} for the Green et al. (2017) CEUS model ($FS_{Gea17-CEUS}$) for CPT-13, Site 3 (no post-event liquefaction manifestations observed). FS_{liq} for the current study (FS_{OK}) is shown for the ZR19_IZ database.

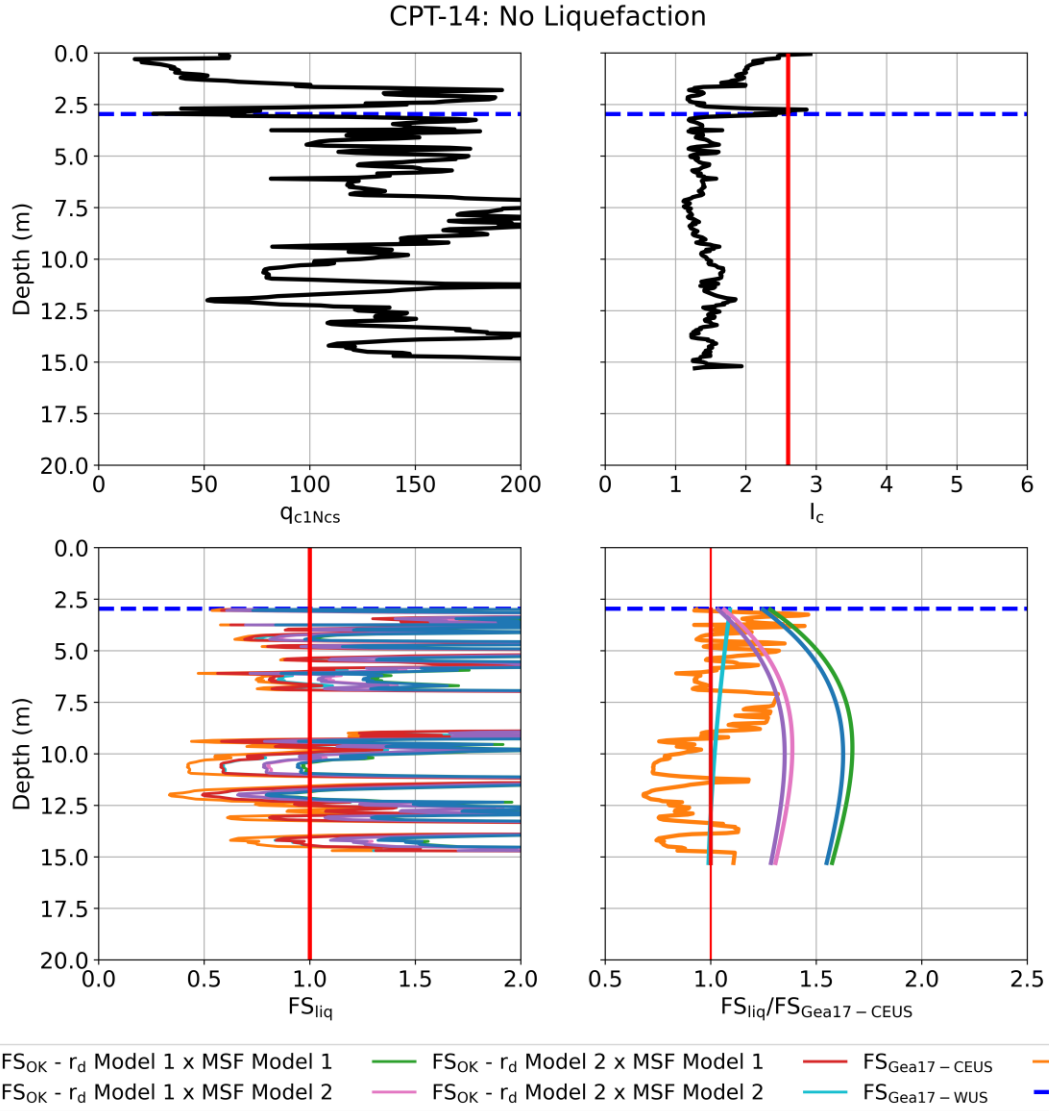


Figure 84. Profiles of q_{c1Ncs} , I_c , FS_{liq} , and FS_{liq} normalized by FS_{liq} for the Green et al. (2017) CEUS model ($FS_{Gea17-CEUS}$) for CPT-14, Site 3 (no post-event liquefaction manifestations observed). FS_{liq} for the current study (FS_{OK}) is shown for the ZR19_IZ database.

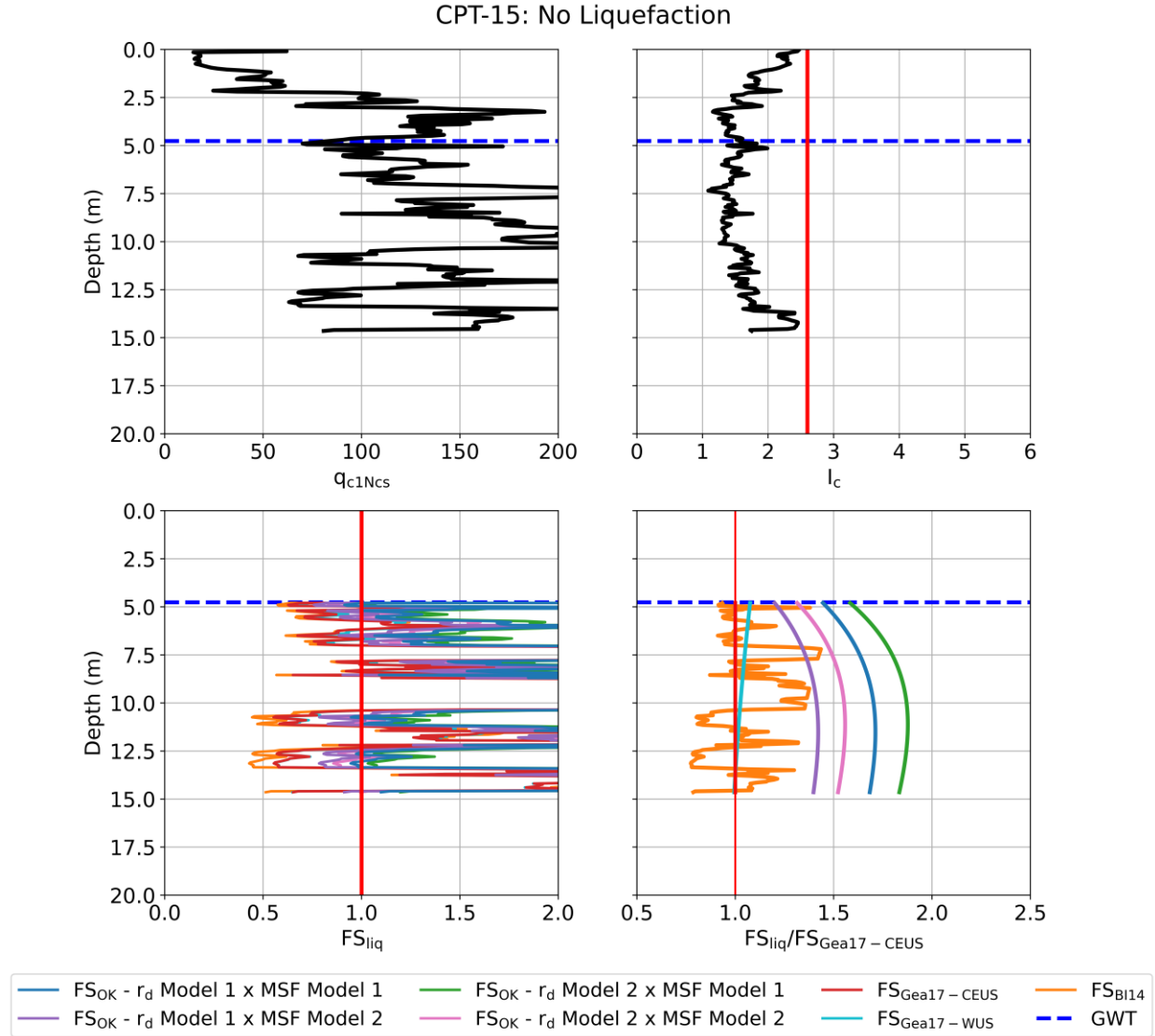


Figure 85. Profiles of q_{c1Ncs} , I_c , FS_{liq} , and FS_{liq} normalized by FS_{liq} for the Green et al. (2017) CEUS model ($FS_{Gea17-CEUS}$) for CPT-15, Site 3 (no post-event liquefaction manifestations observed). FS_{liq} for the current study (FS_{OK}) is shown for the ZR19_IZ database.

LPI_{ish} profiles for each sounding location are shown in Figure 86 through Figure 100. Thresholds for “No,” “Minor,” “Moderate,” and “Severe” liquefaction, as discussed in Section 5.2, are also indicated. Figure titles indicate the observed severity of liquefaction at each sounding location. The FS_{liq} profiles presented in the previous set of figures (Figure 71 and Figure 85) are reproduced in Figure 86 through Figure 100 for reference. FS_{liq} for the Oklahoma triggering model is shown for the ZR19_IZ dataset and for r_d Model 1 and MSF Model 1. As noted previously, the predicted FS_{liq} is less than 1.0 over much of the depth of the

soil profiles for all the liquefaction triggering models. However, the predicted FS_{liq} for the Oklahoma triggering model is consistently higher than for the tectonic models. As a result, LPI_{ish} and the predicted liquefaction surficial manifestation severity tends to be lowest for the Oklahoma liquefaction triggering model. In contrast, FS_{liq} tended to be lowest for the Boulanger and Idriss (2014) liquefaction triggering model. Consequently, LPI_{ish} and predicted liquefaction severity tended to be highest for the Boulanger and Idriss (2014) liquefaction triggering model. The Green et al. (2017) models generally resulted in similar LPI_{ish} values, with the Green et al. (2017) WUS model predicting slightly lower LPI_{ish} values than Green et al. (2017) CEUS.

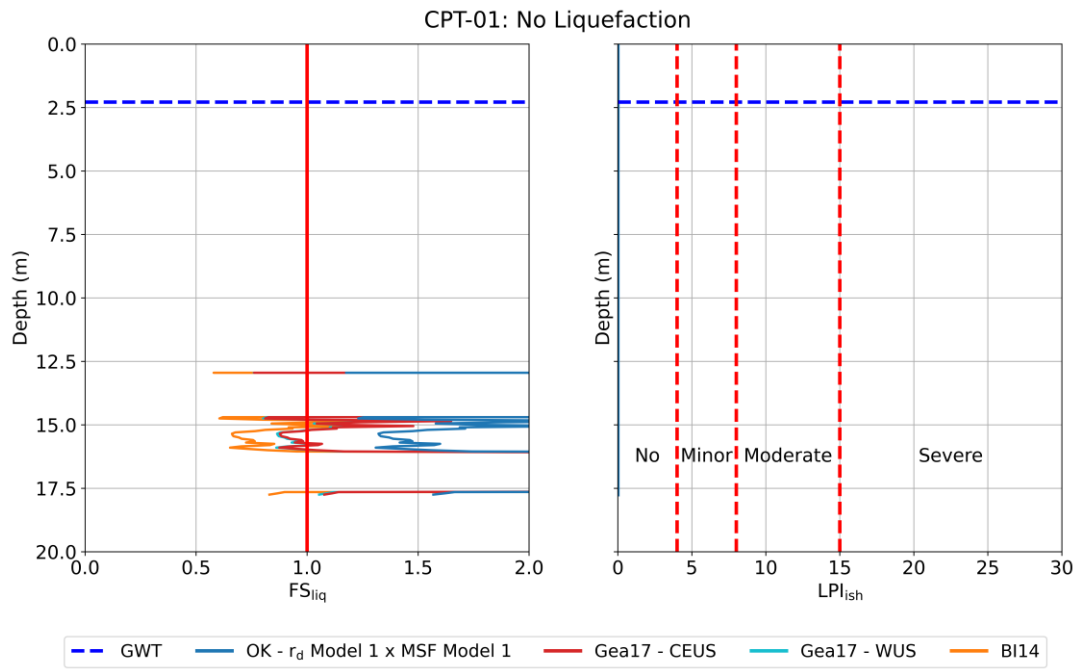


Figure 86. FS_{liq} and LPI_{ish} profiles for CPT-01, Site 1. Results for the current study are shown for the ZR19_IZ database, r_d Model 1, and MSF Model 1. LPI_{ish} liquefaction surficial manifestation severity thresholds are also indicated.

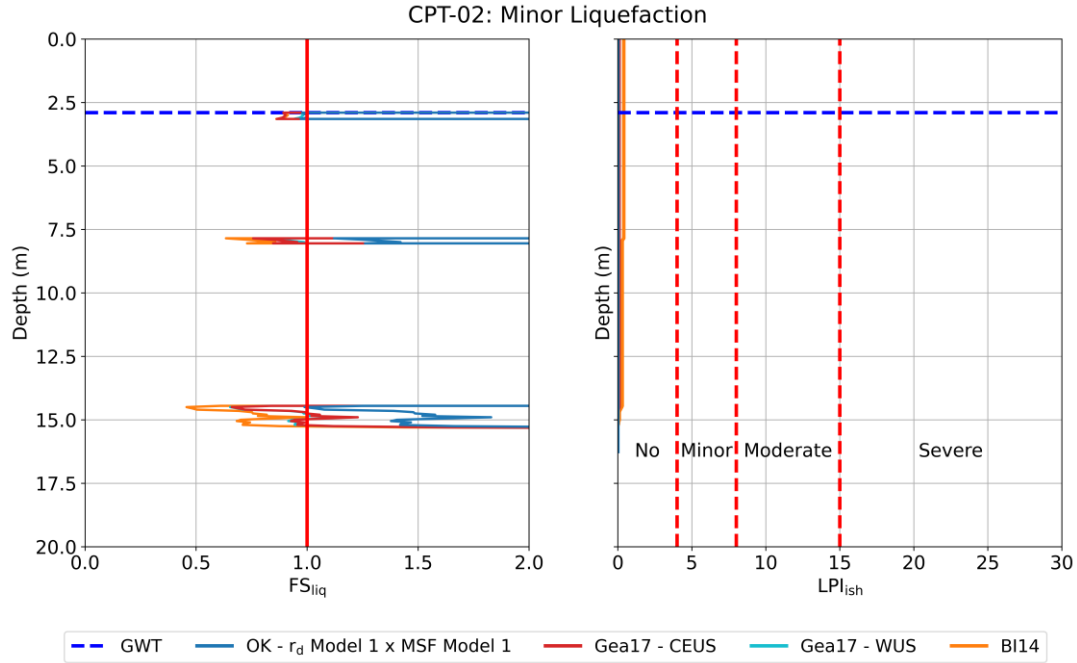


Figure 87. FS_{liq} and LPI_{ish} profiles for CPT-02, Site 1. Results for the current study are shown for the ZR19_IZ database, rd model 1, and MSF model 1. LPI_{ish} liquefaction surficial manifestation severity thresholds are also indicated.

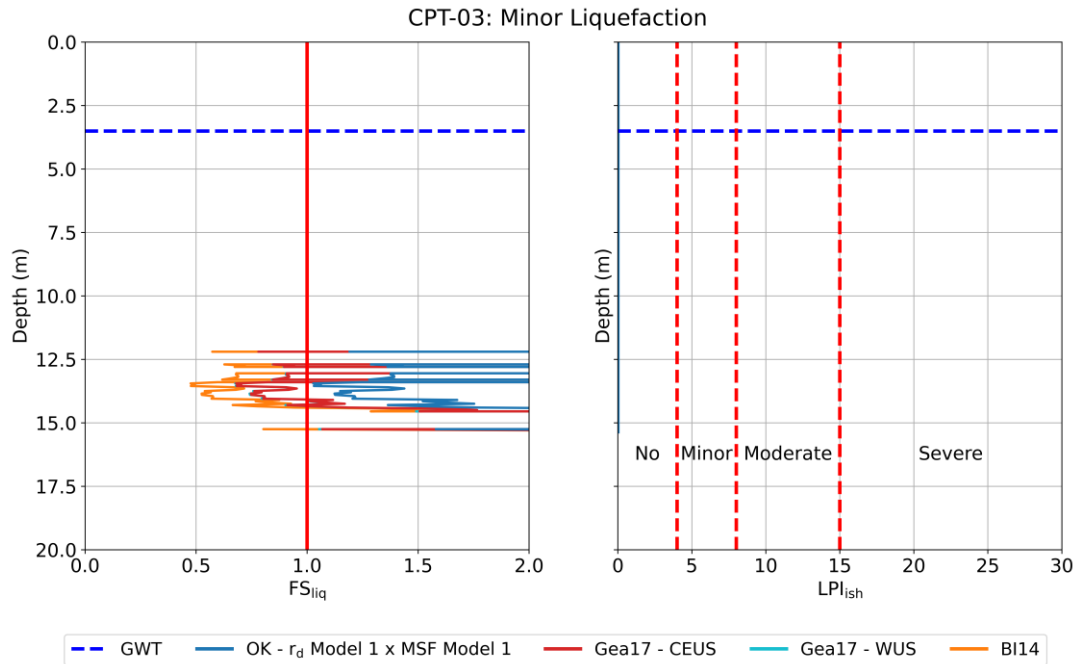


Figure 88. FS_{liq} and LPI_{ish} profiles for CPT-03, Site 1. Results for the current study are shown for the ZR19_IZ database, r_d Model 1, and MSF Model 1. LPI_{ish} liquefaction surficial manifestation severity thresholds are also indicated.

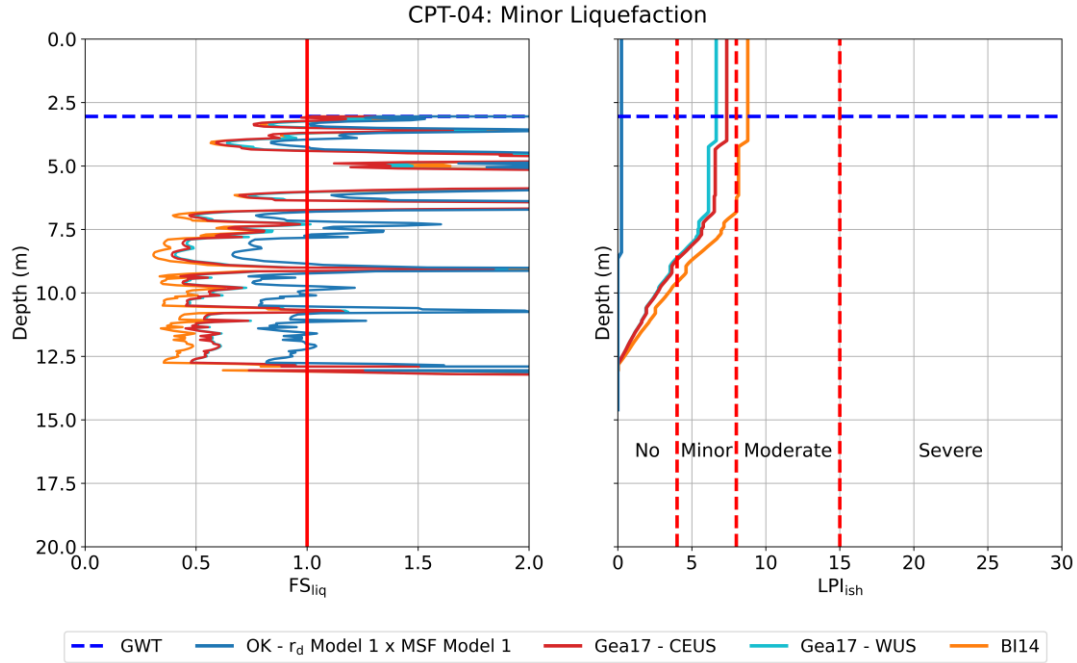


Figure 89. FS_{liq} and LPI_{ish} profiles for CPT-04, Site 2. Results for the current study are shown for the ZR19_IZ database, r_d Model 1, and MSF Model 1. LPI_{ish} liquefaction surficial manifestation severity thresholds are also indicated.

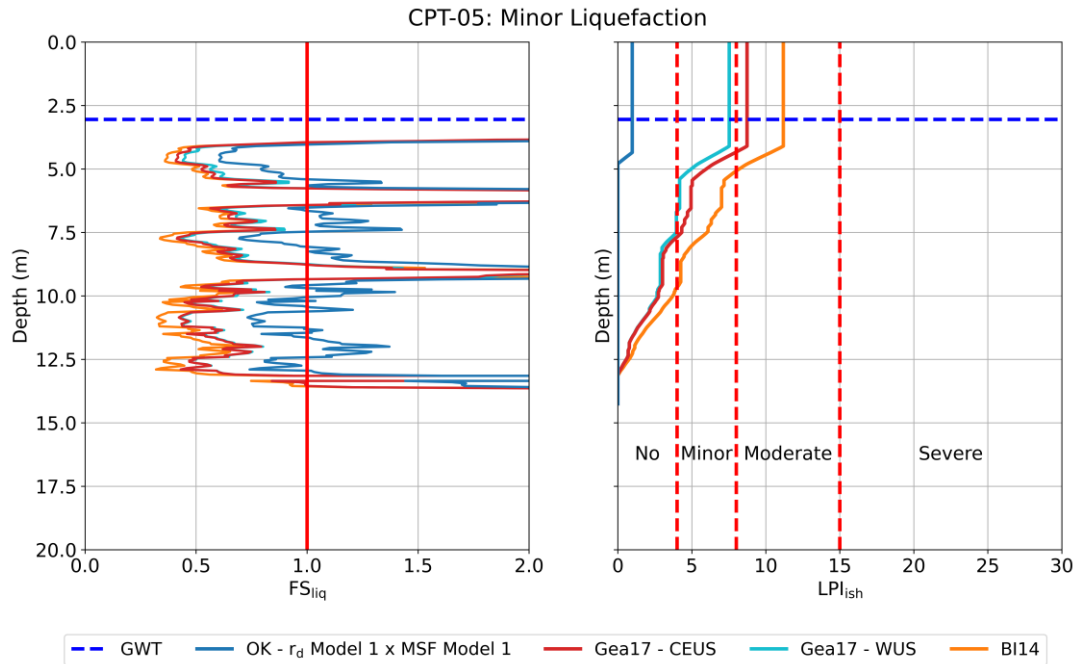


Figure 90. FS_{liq} and LPI_{ish} profiles for CPT-05, Site 2. Results for the current study are shown for the ZR19_IZ database, r_d Model 1, and MSF Model 1. LPI_{ish} liquefaction surficial manifestation severity thresholds are also indicated.

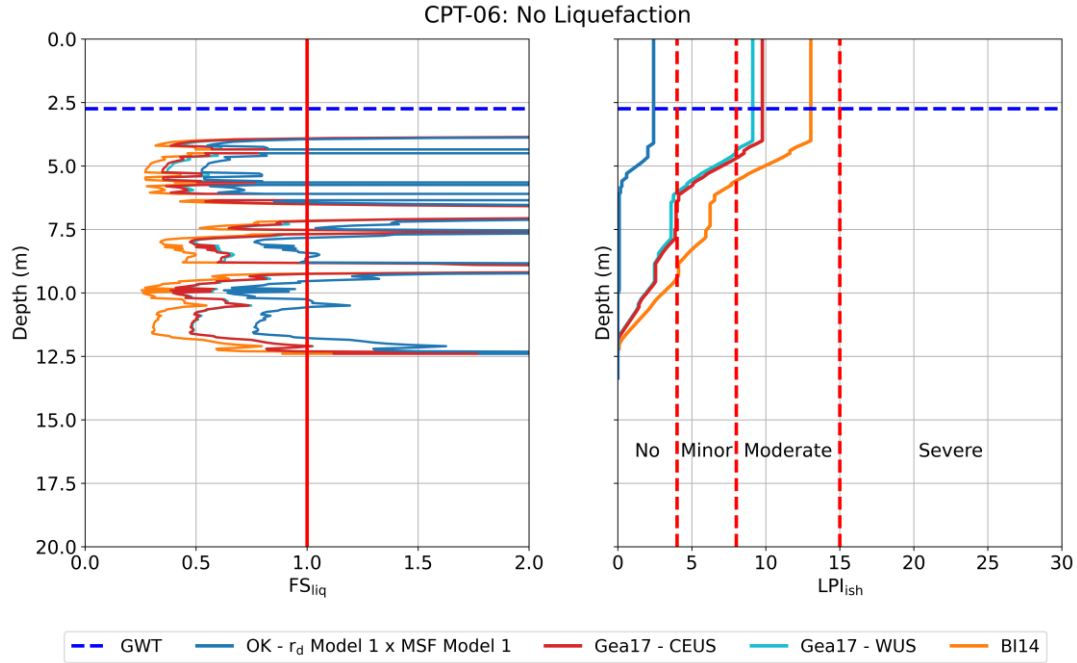


Figure 91. FS_{liq} and LPI_{ish} profiles for CPT-06, Site 2. Results for the current study are shown for the ZR19_IZ database, r_d Model 1, and MSF Model 1. LPI_{ish} liquefaction surficial manifestation severity thresholds are also indicated.

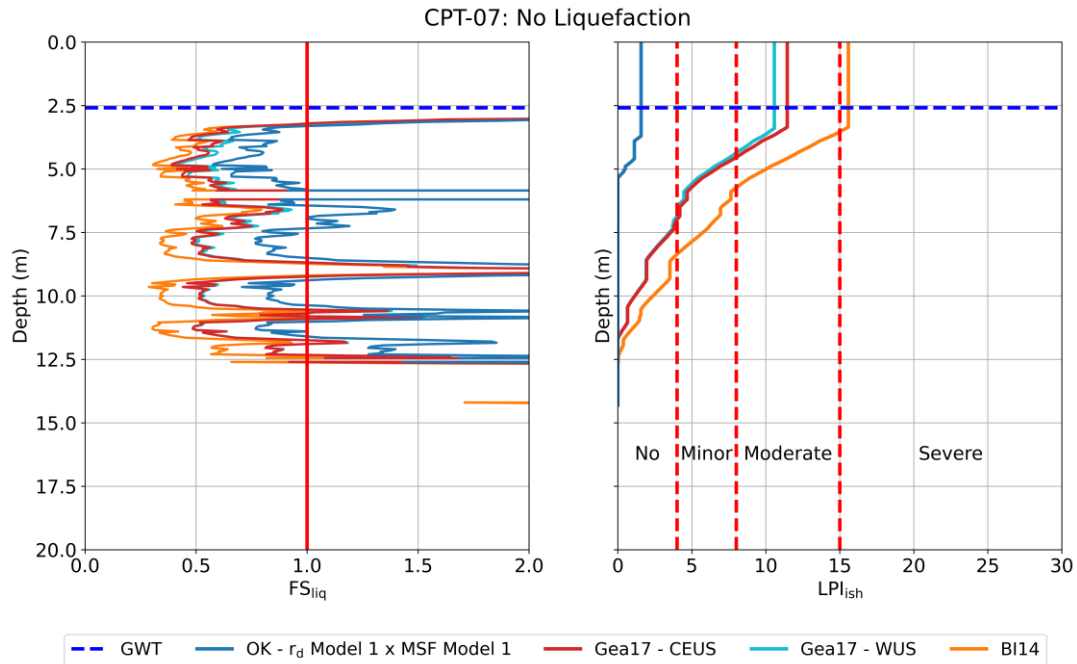


Figure 92. FS_{liq} and LPI_{ish} profiles for CPT-07, Site 2. Results for the current study are shown for the ZR19_IZ database, r_d Model 1, and MSF Model 1. LPI_{ish} liquefaction surficial manifestation severity thresholds are also indicated.

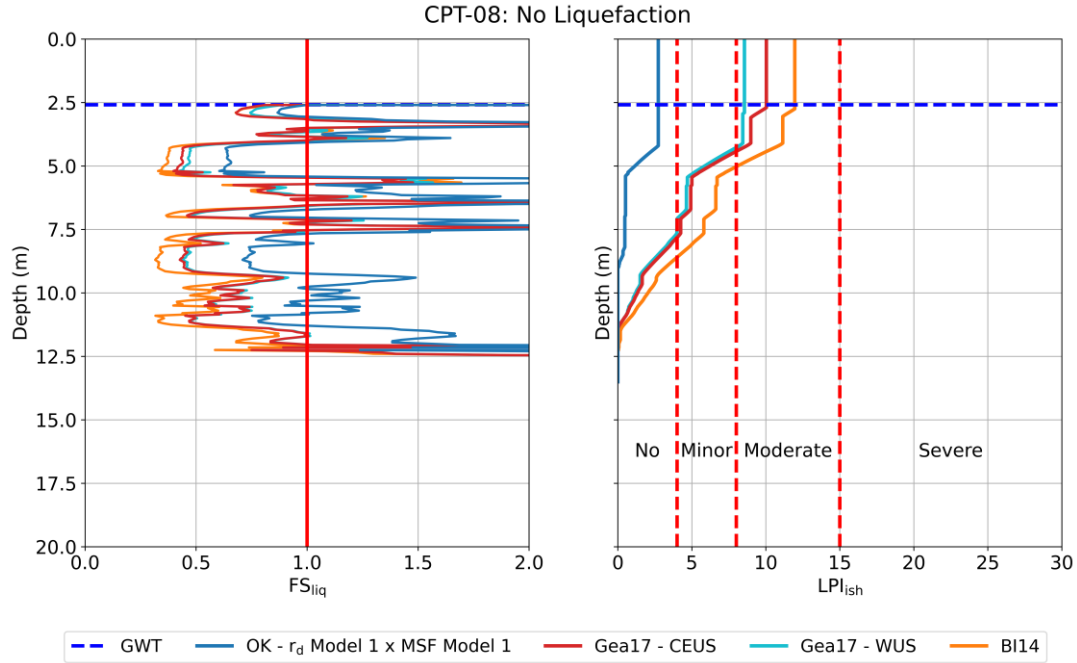


Figure 93. FS_{liq} and LPI_{ish} profiles for CPT-08, Site 2. Results for the current study are shown for the ZR19_IZ database, r_d Model 1, and MSF Model 1. LPI_{ish} liquefaction surficial manifestation severity thresholds are also indicated.

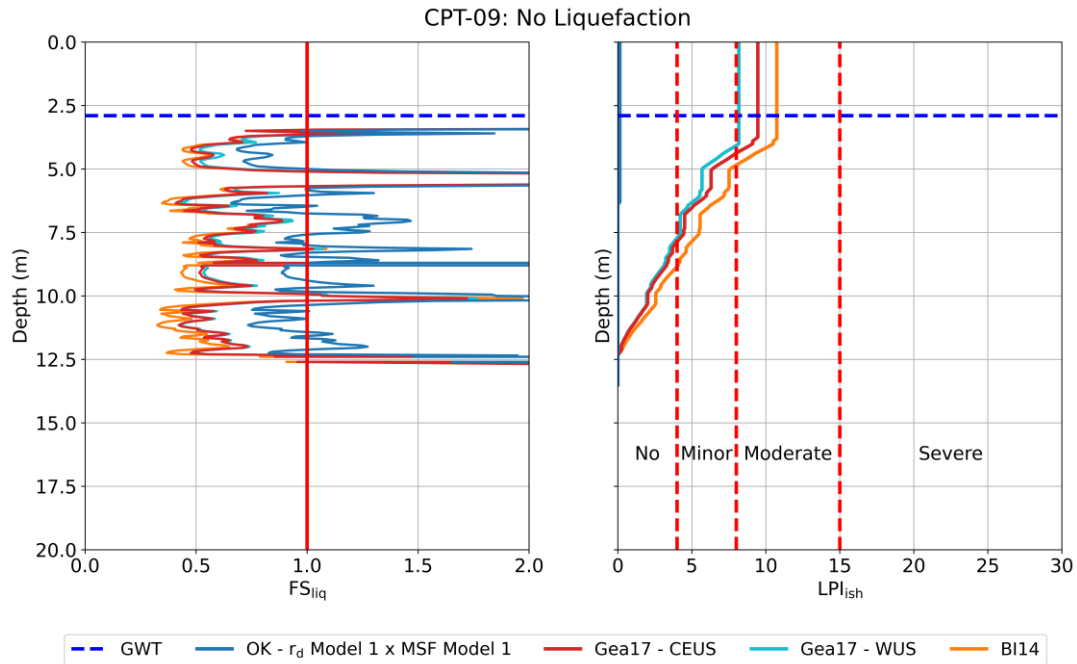


Figure 94. FS_{liq} and LPI_{ish} profiles for CPT-09, Site 2. Results for the current study are shown for the ZR19_IZ database, r_d Model 1, and MSF Model 1. LPI_{ish} liquefaction surficial manifestation severity thresholds are also indicated.

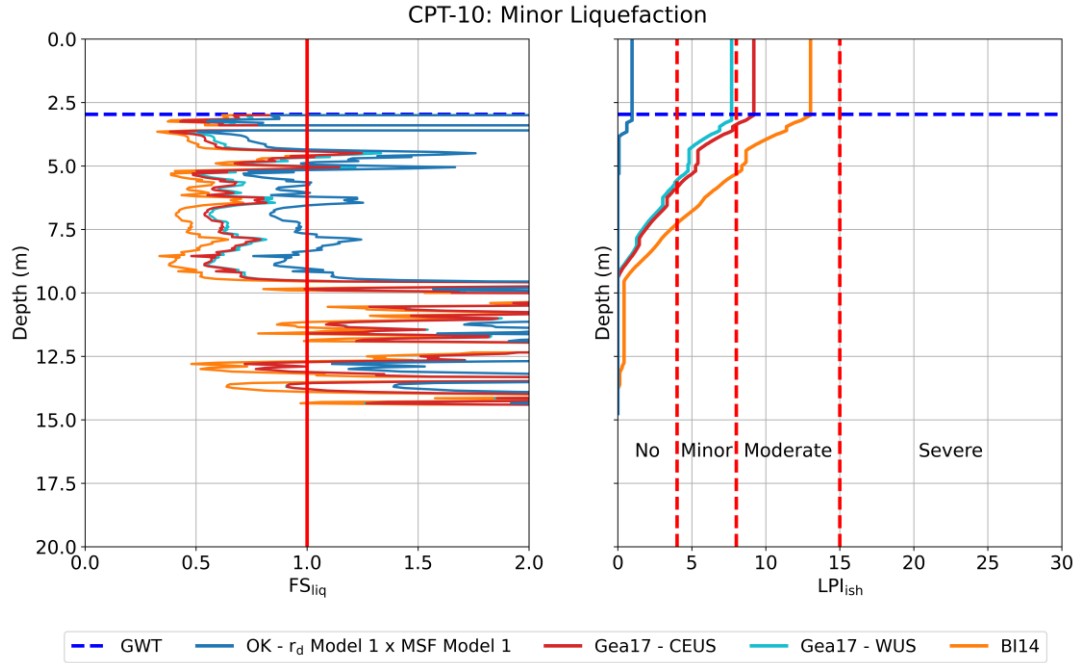


Figure 95. FS_{liq} and LPI_{ish} profiles for CPT-10, Site 3. Results for the current study are shown for the ZR19_IZ database, r_d Model 1, and MSF Model 1. LPI_{ish} liquefaction surficial manifestation severity thresholds are also indicated.

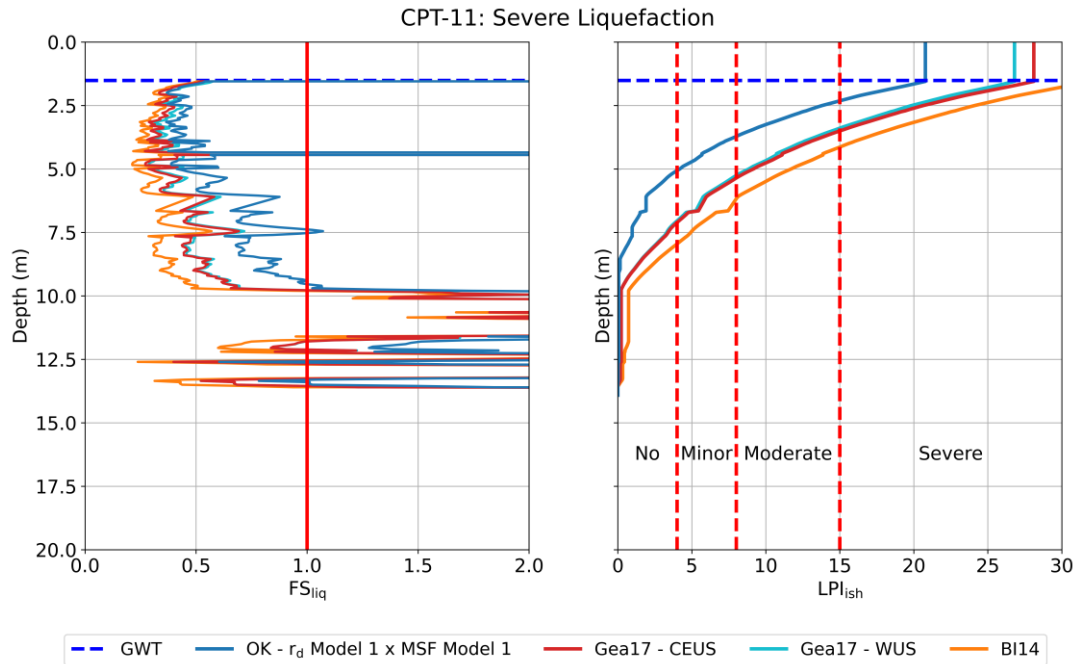


Figure 96. FS_{liq} and LPI_{ish} profiles for CPT-11, Site 3. Results for the current study are shown for the ZR19_IZ database, r_d Model 1, and MSF Model 1. LPI_{ish} liquefaction surficial manifestation severity thresholds are also indicated.

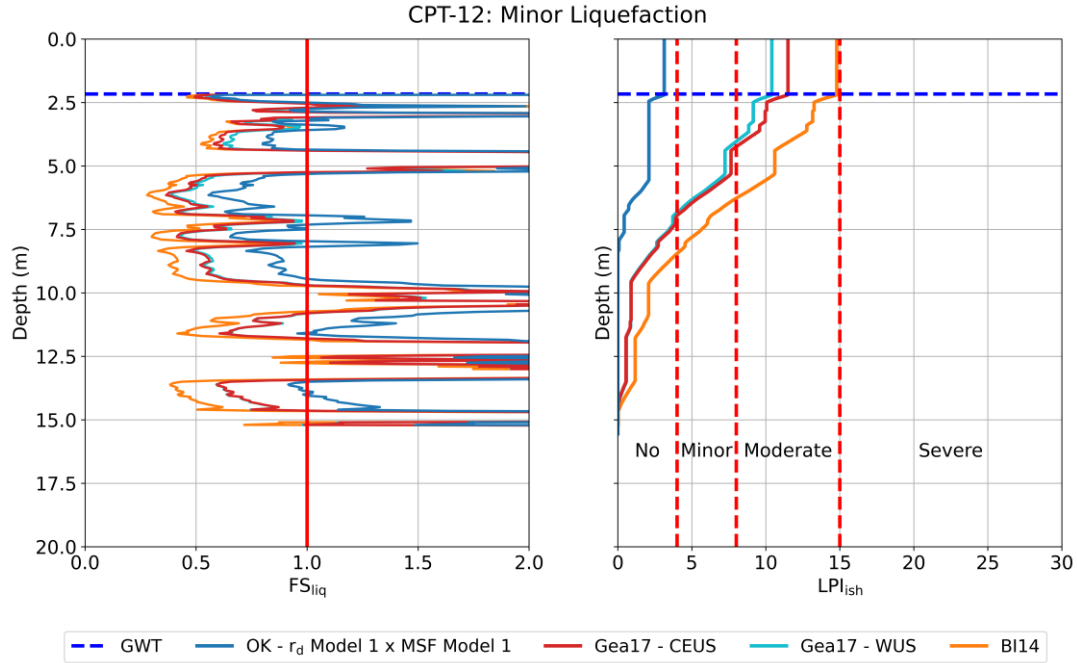


Figure 97. FS_{liq} and LPI_{ish} profiles for CPT-12, Site 3. Results for the current study are shown for the ZR19_IZ database, r_d Model 1, and MSF Model 1. LPI_{ish} liquefaction surficial manifestation severity thresholds are also indicated.

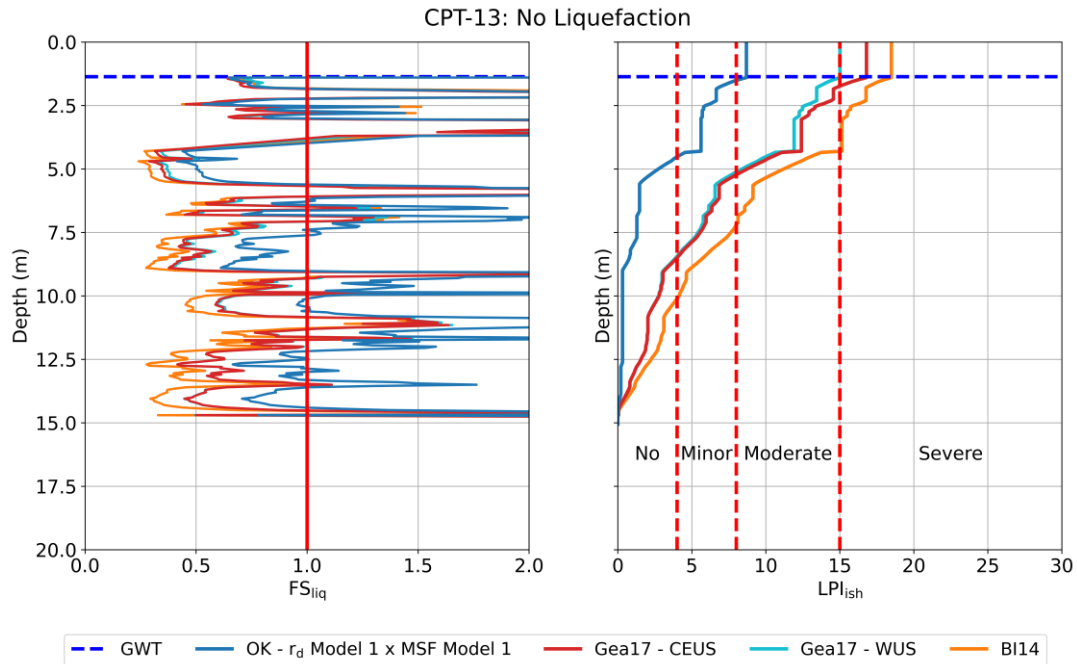


Figure 98. FS_{liq} and LPI_{ish} profiles for CPT-13, Site 3. Results for the current study are shown for the ZR19_IZ database, r_d Model 1, and MSF Model 1. LPI_{ish} liquefaction surficial manifestation severity thresholds are also indicated.

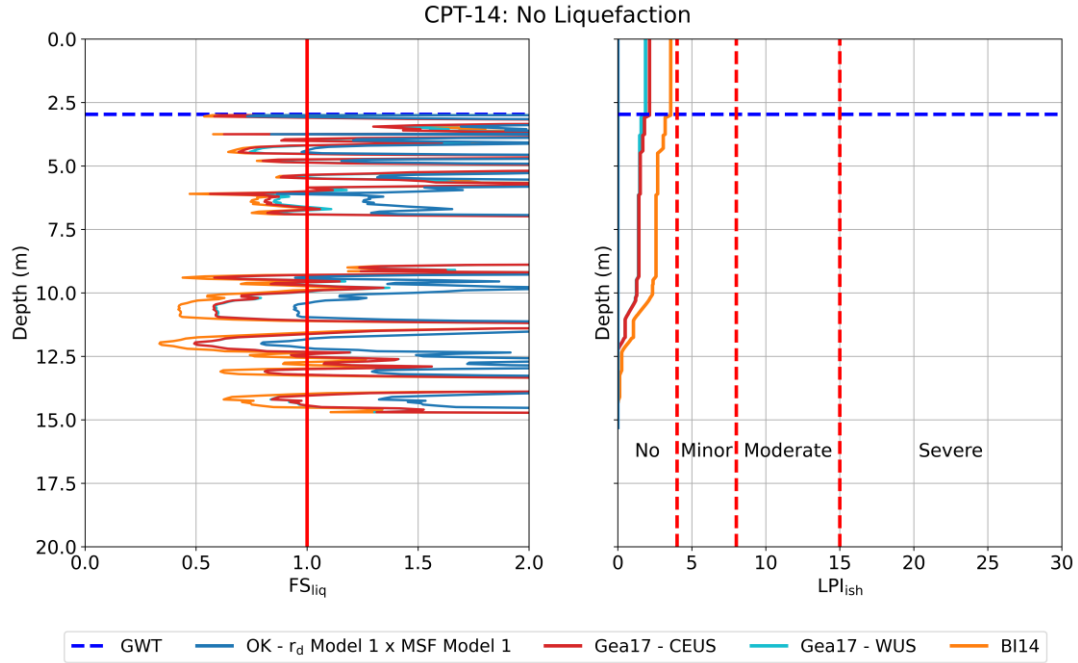


Figure 99. FS_{liq} and LPI_{ish} profiles for CPT-14, Site 3. Results for the current study are shown for the ZR19_IZ database, r_d Model 1, and MSF Model 1. LPI_{ish} liquefaction surficial manifestation severity thresholds are also indicated.

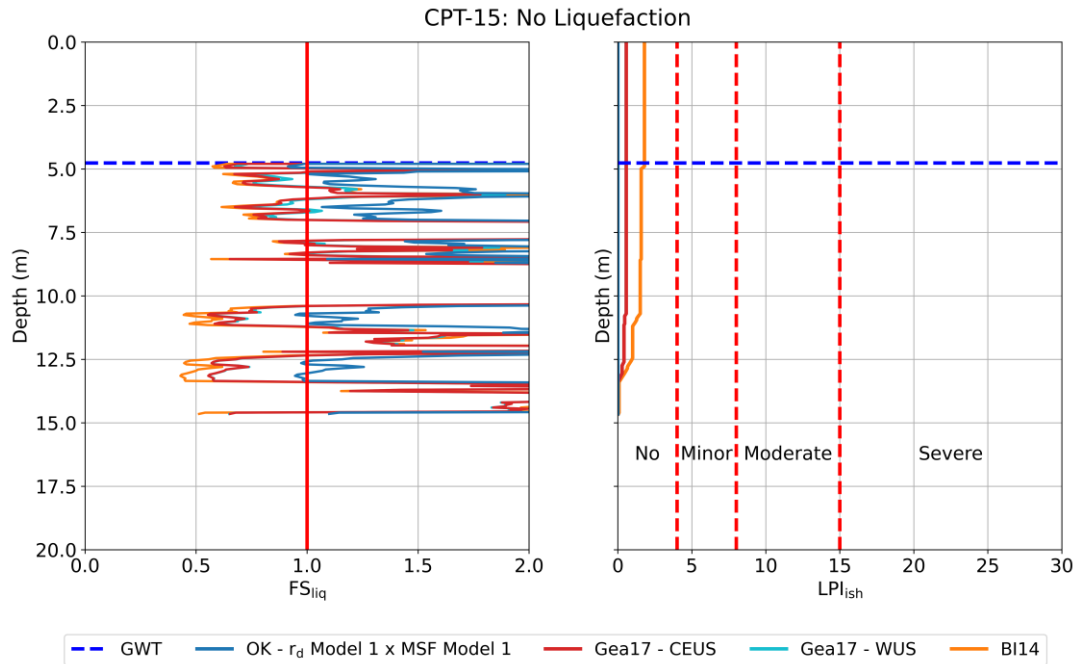


Figure 100. FS_{liq} and LPI_{ish} profiles for CPT-15, Site 3. Results for the current study are shown for the ZR19_IZ database, r_d Model 1, and MSF Model 1. LPI_{ish} liquefaction surficial manifestation severity thresholds are also indicated.

Table 12 presents computed LPI_{ish} values and corresponding liquefaction surficial manifestation severity categories at each CPT sounding location based on the new induced seismicity-specific liquefaction triggering model, the Green et al. (2017) CEUS and WUS triggering models, and the Boulanger and Idriss (2014) triggering model. Documented liquefaction severity at each test location is also presented. As noted previously, the Oklahoma triggering model tends to result in lower LPI_{ish} than the Green et al. (2017) and the Boulanger and Idriss (2014) models. Based on initial comparisons, the lower LPI_{ish} values for the Oklahoma model tend to more accurately predict the severity of liquefaction observed following the Pawnee event. While this comparison provides a quick assessment of model accuracy, a more detailed assessment of model accuracy was performed based on methods used by Maurer et al. (2014) for evaluating LPI model accuracy.

Table 12. LPI_{ish} and predicted liquefaction surficial manifestation category for the Pawnee test sites. Results are shown for the Oklahoma induced seismicity-specific [OK], Green et al. (2017) [Gea17] CEUS and WUS, and Boulanger and Idriss (2014) [BI14] liquefaction triggering models. OK model results are shown based on the ZR19_IZ dataset, r_d Model 1, and MSF Model 1.

| Sounding | Site | Observed Liquefaction Severity | OK (ZR19_IZ Dataset) | | Gea17 CEUS | | Gea17 WUS | | BI14 | |
|----------|------|--------------------------------|----------------------|--------------------|-------------|--------------------|-------------|--------------------|-------------|--------------------|
| | | | LPI_{ish} | Predicted Severity | LPI_{ish} | Predicted Severity | LPI_{ish} | Predicted Severity | LPI_{ish} | Predicted Severity |
| CPT-01 | 1 | None | 0.0 | None | 0.0 | None | 0.0 | None | 0.0 | None |
| CPT-02 | 1 | Minor | 0.0 | None | 0.1 | None | 0.1 | None | 0.4 | None |
| CPT-03 | 1 | Minor | 0.0 | None | 0.0 | None | 0.0 | None | 0.0 | None |
| CPT-04 | 2 | Minor | 0.2 | None | 7.4 | Minor | 6.7 | Minor | 8.8 | Moderate |
| CPT-05 | 2 | Minor | 1.0 | None | 8.7 | Moderate | 7.5 | Minor | 11.2 | Moderate |
| CPT-06 | 2 | None | 2.4 | None | 9.8 | Moderate | 9.1 | Moderate | 13.0 | Moderate |
| CPT-07 | 2 | None | 1.6 | None | 11.5 | Moderate | 10.6 | Moderate | 15.6 | Severe |
| CPT-08 | 2 | None | 2.7 | None | 10.0 | Moderate | 8.6 | Moderate | 12.0 | Moderate |
| CPT-09 | 2 | None | 0.1 | None | 9.5 | Moderate | 8.2 | Moderate | 10.7 | Moderate |
| CPT-10 | 3 | Minor | 1.0 | None | 9.2 | Moderate | 7.7 | Minor | 13.0 | Moderate |
| CPT-11 | 3 | Severe | 20.5 | Severe | 27.1 | Severe | 25.9 | Severe | 30.7 | Severe |
| CPT-12 | 3 | Minor | 3.1 | None | 11.5 | Moderate | 10.4 | Moderate | 14.8 | Moderate |
| CPT-13 | 3 | None | 7.8 | Minor | 15.7 | Severe | 14.0 | Moderate | 17.3 | Severe |
| CPT-14 | 3 | None | 0.0 | None | 2.1 | None | 1.8 | None | 3.5 | None |
| CPT-15 | 3 | None | 0.0 | None | 0.6 | None | 0.6 | None | 1.8 | None |

Following this approach, model prediction error (E) for each sounding was computed based on the expected LPI_{ish} ranges corresponding to the Green et al. (2014) damage classifications. As noted previously, the LPI_{ish} ranges adapted from Maurer et al. (2014) were used in this study. The resulting LPI_{ish} ranges and expected damage classifications used in calculating E are shown in Table 13. Model error was computed as $E = LPI_{ish} - (\text{min or max } LPI_{ish})$ of the relevant range. For example, if LPI_{ish} at a site is computed as 12 for a site with minor liquefaction, $E = 12 - 8 = 4$ (where 8 is the maximum LPI_{ish} for the minor liquefaction range). In contrast, if LPI_{ish} is computed as 5 for a site with moderate liquefaction, $E = 5 - 8 = -3$ (where 8 is the minimum LPI_{ish} for the moderate liquefaction range). Accordingly, positive values of E indicate over-prediction of liquefaction severity while negative values of E indicate under-prediction of liquefaction severity. Based on magnitude of the error, errors were assigned one of nine classifications as shown in Table 14 (Maurer et al. 2014).

Table 13. LPI_{ish} values used to assess prediction accuracy. (after Maurer et al. 2014)

| Damage Classification | Expected LPI_{ish} Range |
|-----------------------|----------------------------|
| No Liquefaction | $LPI_{ish} \leq 4$ |
| Minor Liquefaction | $4 \leq LPI_{ish} < 8$ |
| Moderate Liquefaction | $8 \leq LPI_{ish} < 15$ |
| Severe Liquefaction | $LPI_{ish} \geq 15$ |

Table 14. LPI_{ish} prediction error classifications. (after Maurer et al. 2014)

| Error (E) classification | E (LPI units) |
|--------------------------------------|--------------------|
| Excessive under-prediction | $E < -15$ |
| Severe to excessive under-prediction | $-15 \leq E < -10$ |
| Moderate to severe under-prediction | $-10 \leq E < -5$ |
| Slight to moderate under-prediction | $-5 \leq E < -1$ |
| Accurate prediction | $-1 \leq E \leq 1$ |
| Slight to moderate over-prediction | $1 < E \leq 5$ |
| Moderate to severe over-prediction | $5 < E \leq 10$ |
| Severe to excessive over-prediction | $10 < E \leq 15$ |
| Excessive over-prediction | $E > 15$ |

The computed prediction errors for each of the four liquefaction triggering models are shown in Figure 101 for each CPT sounding location. Results presented for the Oklahoma liquefaction triggering model are shown for the ZR19_IZ database with r_d Model 1 and MSF Model 1. As shown in this figure, the Oklahoma

liquefaction triggering model resulted in accurate predictions ($-1 \leq E \leq 1$) at 9 of the 15 sounding locations, while it resulted in slight under-prediction at 5 locations and slight over-prediction at one location. The slight under-predictions occurred at sites where “minor” liquefaction occurred (e.g., CPT-04, CPT-05, and CPT-10), but estimated LPI_{ish} was between 0 and 4. In contrast, the Green et al. (2017) and Boulanger and Idriss (2014) triggering models tended to over-predict the severity of liquefaction, predicting liquefaction at no-liquefaction locations. These models slightly to excessively over-predict the severity at 7 locations (E as high as 13) and slightly under-predict severity at 2 locations. However, they accurately predict the severity at 6 locations including the minor liquefaction at CPT-04, which is slightly under-predicted by the Oklahoma model. Discussions of model predictions for each site, based on the damage classifications and corresponding LPI_{ish} ranges presented in Table 13, are provided in the following paragraphs.

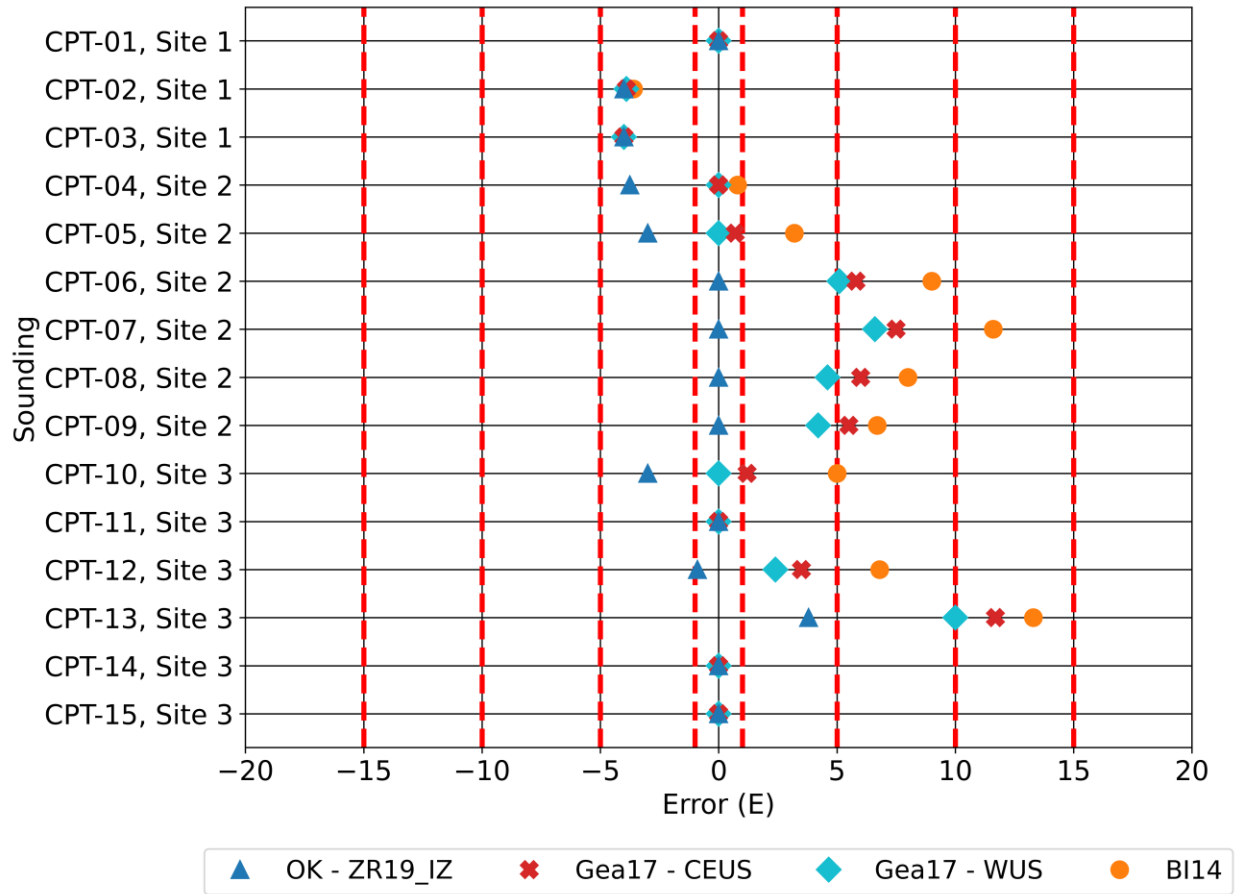


Figure 101. LPI_{ish} prediction error (E) for the Pawnee test sites. Results are shown for the Oklahoma induced seismicity-specific model using the ZR19_IZ dataset with r_d Model 1 and MSF Model 1 [OK – ZR19_IZ], the Green et al. (2017) CEUS [Gea17 – CEUS] and WUS [Gea17 – WUS] triggering models, and Boulanger and Idriss (2014) triggering model [BI14]. Error classification thresholds are also indicated based categories provided in Table 15.

There were two locations at Site 1 (CPT-02 and CPT-03) where minor liquefaction features were reported but all models resulted in $LPI_{ish} \approx 0$. Both the CPT-02 and CPT-03 profiles include a thin, liquefiable sand layer at a depth of approximately 7.5 m. While this layer was thin enough at CPT-02 and CPT-03 that surficial manifestations were not predicted at those locations, this layer may be thicker in nearby areas. This could account for the isolated clusters of sand boils observed in this area while the models predict no liquefaction would occur at the sounding locations themselves. Observed sand boil locations were estimated using GPS-tagged photos, which provide only approximate location information. Additionally, the sounding locations had to be adjusted slightly due to ponding at the site during CPT testing. For these reasons, it is possible that the CPT sounding locations were not located at the exact locations where liquefaction manifested. This could explain why LPI_{ish} were lower than expected at these locations. In general, the predicted LPI_{ish} for the induced seismicity and tectonic seismicity models were very similar at this site being at or near zero for both CPT-02 and CPT-03. All models correctly predict no surficial liquefaction manifestations would occur at CPT-01.

At Site 2, liquefaction was documented at CPT-04 and CPT-05 but was not documented at CPT-06 through CPT-09. Documented liquefaction at CPT-04 and CPT-05 included minor liquefaction consisting of cracks 2 to 5 m long with small amounts of sand ejecta. The observed liquefaction severity at these locations was slightly under-predicted by the Oklahoma models ($LPI_{ish} = 0.3$ and 1.0). The Green et al. (2017) WUS model predictions ($LPI_{ish} = 6.7$ and 7.5) fell within the range of minor liquefaction while the Green et al. (2017) CEUS model ($LPI_{ish} = 7.4$ and 8.7) and Boulanger and Idriss (2014) model ($LPI_{ish} = 8.8$ and 11.2) slightly over-predict liquefaction severity at these locations, particularly CPT-05. As with Site 1, locations of surficial liquefaction manifestations were roughly estimated using GPS-tagged photos. As a result, locations may not coincide exactly with observed liquefaction locations. This may have led to the under-prediction of liquefaction by the Oklahoma triggering model.

No liquefaction was documented at CPT-06 through CPT-09 at Site 2. This is consistent with LPI_{ish} predictions for the Oklahoma triggering model ($LPI_{ish} = 0.1$ to 2.7), which fell within the no liquefaction range. However, the other models ($LPI_{ish} = 8.2$ and 15.6) predict moderate to severe liquefaction at these locations. This is classified as a moderate to excessive over-prediction. The property owner indicated that, as far as he could remember, the cracking and ejecta at Site 2 were limited to the area around CPT-04 and CPT-05. However, given that the property is a large, plowed field, it is possible that liquefaction did occur at the other sounding locations but was not observed or photographed. However, it is unlikely that the moderate to severe liquefaction predicted by these models would go unnoticed or undocumented. As a result, the Oklahoma models appear to more accurately reflect liquefaction manifestation severity at these locations.

At Site 3, liquefaction manifestations were documented at CPT-10, CPT-11, and CPT-12. Detailed mapping of fractures and ejecta was performed across most of the site by Kolawole et al. (2017). As a result, the areal extent of liquefaction was better known at Site 3 than at Sites 1 and 2. Manifestations at CPT-10 and CPT-12 consisted of cracks 0.5 to 5 cm wide with trace amounts of ejecta. These locations were classified as minor liquefaction due to the limited extent of ejecta. The Oklahoma model ($LPI_{ish} = 1.0$) slightly under-predicts liquefaction severity at CPT-10 while the Green et al. (2017) WUS model ($LPI_{ish} = 7.7$) fell within the minor liquefaction range. The Green et al. (2017) CEUS and Boulanger and Idriss (2014) models ($LPI_{ish} = 9.2$ and 13.0) slightly over-predict liquefaction at this location. The Oklahoma model ($LPI_{ish} = 3.1$) accurately predicts minor liquefaction severity at CPT-11, while the other models ($LPI_{ish} = 10.4$ and 14.8) predict more severe liquefaction would occur.

More severe manifestations were observed at Site 3 near CPT-11 where the post-earthquake survey found cracks up to 8 cm wide and sand blows with ejecta covering an approximately 145 m^2 area. As a result, CPT-11 was classified as severe liquefaction. Both the Oklahoma model ($LPI_{ish} = 20.5$) and the tectonic models ($LPI_{ish} = 25.9$ to 30.7) accurately predict severe liquefaction manifestations at this location.

No surficial liquefaction manifestations were observed at CPT-13, CPT-14, or CPT-15. The Oklahoma model predicts $LPI_{ish} = 0$ at both CPT-14 and CPT-15, which accurately predicts the lack of observed liquefaction. The other models result in LPI_{ish} values ranging from 1.8 to 3.5 for CPT-14 and 0.6 to 1.8 for CPT-15. While $LPI_{ish} > 0$ for these models, estimates still lie within the “no liquefaction range.” Calculated LPI_{ish} values for all of the models at CPT-13 were not in accord with field observations. Although no liquefaction was documented at CPT-13, the Oklahoma model ($LPI_{ish} = 7.8$) fell within the minor liquefaction range, the Green et al. (2017) WUS model ($LPI_{ish} = 14.0$) fell within the moderate liquefaction range, and the Green et al. (2017) CEUS and Boulanger and Idriss (2014) models ($LPI_{ish} = 15.7$ and 17.3) fell within the severe liquefaction range. Given the low FS_{liq} and high LPI_{ish} estimated at this location, it is likely that soils at CPT-13 did liquefy during the Pawnee earthquake. The location of CPT-13 was adjusted due to ponding at the site during CPT testing and was moved just outside the Kolawole et al. (2017) detailed survey area. As a result, liquefaction manifestations may have occurred at CPT-13 during the Pawnee earthquake but may not have been observed during the Kolawole et al. (2017) survey. As with the apparent false-positives at Site 2, it seems more likely that the minor liquefaction predicted by the Oklahoma model would not be observed than that moderate to severe manifestations predicted by the tectonic models would not be observed.

Comparisons of observed and predicted surficial liquefaction manifestation severity at Sites 1, 2, and 3 indicate that the triggering model developed herein for induced events did a better job predicting liquefaction manifestation severity for the Pawnee earthquake. Although the induced and tectonic models

yield similar LPI_{ish} values at some locations (e.g., Site 1, CPT-11), the Green et al. (2017) and Boulanger and Idriss (2014) models tended to over-predict the liquefaction potential and manifestation severity relative to observed liquefaction severity. The induced seismicity-specific triggering model resulted in slight under-predictions of liquefaction at some locations but accurately predicts liquefaction severity at most locations. Overall, the model validation results suggest that the new induced seismicity-specific liquefaction triggering model developed herein provides a more accurate assessment of the liquefaction hazard due to induced earthquakes in Oklahoma, Texas, and Kansas than existing models developed for tectonic earthquakes.

The results for the Oklahoma liquefaction triggering model presented in this section were for the ZR19_IZ dataset. Computed LPI_{ish} values for this dataset and the other three datasets are shown in Table 16. As shown in this table, there is some minor variation in LPI_{ish} estimates for the different datasets. In general, the computed LPI_{ish} values tend to be higher for the datasets developed using the Ishibashi and Zhang (1993) MRD curves (i.e., ZR19_IZ, Nea18_IZ) than for datasets developed using the Darendeli and Stokoe (2001) MRD curves (i.e., ZR19_DS, Nea18_DS). Additionally, datasets developed with ground motions scaled to the Novakovic et al. (2018) GMPE (i.e., Nea18_IZ, Nea18_DS) tend to result in higher computed LPI_{ish} values than datasets developed using ground motions scaled to the Zalachoris and Rathje (2019) GMPE (i.e., ZR19_IZ, ZR19_DS). As a result, the Nea18_IZ dataset results in higher computed LPI_{ish} values while the ZR19_DS dataset results in the lowest LPI_{ish} values. The maximum observed difference between LPI_{ish} for the ZR19_DS dataset and the Nea18_IZ dataset is 3.2 (CPT-11). The difference at most locations is smaller. The choice of dataset does not impact the predicted severity category for any of the CPT sounding locations.

Table 16. Computed LPI_{ish} value and prediction error for the Oklahoma liquefaction triggering model for all datasets.

| Sounding | Site | Dataset | | | | | | | |
|----------|------|-------------|------------------|-------------|------------------|-------------|------------------|-------------|------------------|
| | | ZR19_IZ | | ZR19_DS | | Nea18_IZ | | Nea18_DS | |
| | | LPI_{ish} | Prediction Error | LPI_{ish} | Prediction Error | LPI_{ish} | Prediction Error | LPI_{ish} | Prediction Error |
| CPT-01 | 1 | 0.0 | 0.0 | 0.0 | 0.0 | 0.0 | 0.0 | 0.0 | 0.0 |
| CPT-02 | 1 | 0.0 | -4.0 | 0.0 | -4.0 | 0.0 | -4.0 | 0.0 | -4.0 |
| CPT-03 | 1 | 0.0 | -4.0 | 0.0 | -4.0 | 0.0 | -4.0 | 0.0 | -4.0 |
| CPT-04 | 2 | 0.2 | -3.8 | 0.0 | -4.0 | 0.4 | -3.6 | 0.0 | -4.0 |
| CPT-05 | 2 | 1.0 | -3.0 | 0.0 | -4.0 | 1.0 | -3.0 | 0.0 | -4.0 |
| CPT-06 | 2 | 2.4 | 0.0 | 1.3 | 0.0 | 2.8 | 0.0 | 1.7 | 0.0 |
| CPT-07 | 2 | 1.6 | 0.0 | 0.3 | 0.0 | 1.8 | 0.0 | 0.4 | 0.0 |
| CPT-08 | 2 | 2.7 | 0.0 | 0.8 | 0.0 | 3.4 | 0.0 | 1.4 | 0.0 |
| CPT-09 | 2 | 0.1 | 0.0 | 0.0 | 0.0 | 0.5 | 0.0 | 0.0 | 0.0 |
| CPT-10 | 3 | 1.0 | -3.0 | 0.6 | -3.4 | 1.3 | -2.7 | 0.6 | -3.4 |
| CPT-11 | 3 | 20.5 | 0.0 | 17.9 | 0.0 | 21.1 | 0.0 | 18.3 | 0.0 |
| CPT-12 | 3 | 3.1 | -0.9 | 1.6 | -2.4 | 3.5 | -0.5 | 2.3 | -1.7 |
| CPT-13 | 3 | 7.8 | 3.8 | 5.1 | 1.1 | 8.1 | 4.1 | 5.4 | 1.4 |
| CPT-14 | 3 | 0.0 | 0.0 | 0.0 | 0.0 | 0.0 | 0.0 | 0.0 | 0.0 |
| CPT-15 | 3 | 0.0 | 0.0 | 0.0 | 0.0 | 0.0 | 0.0 | 0.0 | 0.0 |

Table 17 provides a comparison for the computed LPI_{ish} values for the Oklahoma liquefaction triggering model based on different combinations of r_d Models 1 and 2 and MSF Models 1 and 2. Results are shown for the ZR19_IZ dataset. As discussed previously, the choice of MSF model had a more significant impact on FS_{liq} than the choice of r_d model. Consequently, the choice of MSF model has a more significant impact on the computed LPI_{ish} . MSF Model 2 results in lower MSF values due to the small R_{hyp} of the Pawnee sites. This results in a lower computed FS_{liq} and higher computed LPI_{ish} for MSF Model 2. The difference in the computed LPI_{ish} between MSF Models 1 and 2 is as high as 4.5, but is generally smaller. The choice of r_d model resulted in much smaller changes in LPI_{ish} with r_d Model 1 leading to computed LPI_{ish} up to 1.2 higher. The maximum difference between the computed LPI_{ish} values for r_d Model 1 with MSF Model 2 and LPI_{ish} values for r_d Model 2 with MSF Model 1 was 5.1. While the difference is smaller at most locations, the choice of r_d and/or MSF model results in differences in predicted liquefaction severity at some locations. This included CPT-07, CPT-08, CPT-12, and CPT-13. At CPT-07, CPT-08, and CPT-13, the use of MSF Model 2 leads to over-prediction of liquefaction severity, while at CPT-12, the larger computed LPI_{ish} values from MSF Model 2 actually match better with observed liquefaction severity. Overall, the use of r_d Model 1 and MSF Model 1 appears to provide more accurate predictions of liquefaction severity.

Table 17. Computed LPI_{ish} values and prediction error for the Oklahoma liquefaction triggering model based on the ZR19_IZ dataset and both r_d and MSF models.

| Sounding | Site | ra Model | | | | | | | |
|----------|------|--------------------|------------------|--------------------|------------------|--------------------|------------------|--------------------|------------------|
| | | 1 | | 1 | | 2 | | 2 | |
| | | MSF Model | | | | | | | |
| | | 1 | | 2 | | 1 | | 2 | |
| | | LPI _{ish} | Prediction Error | LPI _{ish} | Prediction Error | LPI _{ish} | Prediction Error | LPI _{ish} | Prediction Error |
| CPT-01 | 1 | 0.0 | 0.0 | 0.0 | 0.0 | 0.0 | 0.0 | 0.0 | 0.0 |
| CPT-02 | 1 | 0.0 | -4.0 | 0.0 | -4.0 | 0.0 | -4.0 | 0.0 | -4.0 |
| CPT-03 | 1 | 0.0 | -4.0 | 0.0 | -4.0 | 0.0 | -4.0 | 0.0 | -4.0 |
| CPT-04 | 2 | 0.2 | -3.8 | 2.3 | -1.7 | 0.0 | -4.0 | 1.1 | -2.9 |
| CPT-05 | 2 | 1.0 | -3.0 | 2.7 | -1.3 | 0.0 | -4.0 | 1.8 | -2.2 |
| CPT-06 | 2 | 2.4 | 0.0 | 4.9 | 0.9 | 2.3 | 0.0 | 4.7 | 0.7 |
| CPT-07 | 2 | 1.6 | 0.0 | 5.8 | 1.8 | 1.7 | 0.0 | 6.2 | 2.2 |
| CPT-08 | 2 | 2.7 | 0.0 | 5.9 | 1.9 | 2.1 | 0.0 | 5.0 | 1.0 |
| CPT-09 | 2 | 0.1 | 0.0 | 2.8 | 0.0 | 0.0 | 0.0 | 1.9 | 0.0 |
| CPT-10 | 3 | 1.0 | -3.0 | 4.1 | 0.0 | 0.9 | -3.1 | 4.1 | 0.0 |
| CPT-11 | 3 | 20.5 | 0.0 | 24.8 | 0.0 | 20.9 | 0.0 | 25.2 | 0.0 |
| CPT-12 | 3 | 3.1 | -0.9 | 7.8 | 0.0 | 3.1 | -0.9 | 7.7 | 0.0 |
| CPT-13 | 3 | 7.8 | 3.8 | 12.3 | 8.3 | 7.2 | 3.2 | 11.6 | 7.6 |
| CPT-14 | 3 | 0.0 | 0.0 | 0.6 | 0.0 | 0.0 | 0.0 | 0.5 | 0.0 |
| CPT-15 | 3 | 0.0 | 0.0 | 0.0 | 0.0 | 0.0 | 0.0 | 0.0 | 0.0 |

6 Summary and Conclusion

Although several models are commonly used in practice for assessing liquefaction potential due to tectonic earthquakes, these models are semi-empirical, with the empirical aspects being derived from data primarily taken from moderate-sized tectonic earthquakes in active shallow-crustal tectonic regimes. As a result, the suitability of these models for evaluating liquefaction triggering for induced earthquakes in Oklahoma, Texas, and Kansas is uncertain, due to differences in ground motion characteristics and regional geologies. To address this, a new liquefaction triggering model was developed for assessing the liquefaction hazard due to earthquakes resulting from deep wastewater injection in Oklahoma, Texas, and Kansas. This liquefaction triggering model was developed based on the approach used in Green et al. (2017) and Green et al. (2020) to develop analogous models for evaluating liquefaction triggering in the central and eastern United States (CEUS) and the Groningen region of the Netherlands. This approach involved regressing new stress reduction factor (r_d) and Magnitude Scaling Factor (MSF) relationships based on numerical site response analyses performed using a catalog of induced ground motions and representative soil profiles

from the region. The new r_d and MSF relationships can be used to compute normalized cyclic stress ratio (CSR^*) which can be used in conjunction with the normalized cyclic resistance ratio ($CRR_{M7.5}$) curves from Green et al. (2019) to estimate liquefaction potential for induced earthquakes in Oklahoma, Texas, and Kansas.

The new r_d relationship for induced seismicity predicts lower values of r_d than the models developed for tectonic earthquakes at all depths. This is consistent with observations by Novakovic et al. (2018) and Zalachoris and Rathje (2019) that induced earthquake ground motions tend to have higher amplitude high-frequency content than tectonic earthquakes. These high frequency motions lead to less rigid soil column response and, hence, lower r_d . Time-weighted average small-strain shear wave velocity of the upper 12 m (V_{s12}) is shown to be a significant predictor of r_d . However, r_d for the model developed herein did not scale as strongly with V_{s12} as it did for the Lasley et al. (2016) r_d models for the CEUS and western United States (WUS). This may be a corollary to the observation made by Zalachoris and Rathje (2019) that induced ground motions in Oklahoma do not scale as strongly with V_{s30} . MSF for the model developed herein tend to be significantly lower than MSF for existing models. This is consistent with the observations of Boore and Thompson (2015) that path duration tends to increase much more rapidly with hypocentral distance (R_{hyp}) in the CEUS than in the WUS. The resulting trends in r_d and MSF for the induced seismicity-specific liquefaction triggering model lead to a lower factor of safety against liquefaction (FS_{liq}) at depths shallower than ~ 2.5 m and higher FS_{liq} at depths deeper than 2.5 m than would be predicted by existing models for tectonic earthquakes. As a result, existing models will tend to under-predict liquefaction potential during induced earthquakes in the upper 2.5 m and over-predict liquefaction potential during induced earthquakes for depths greater than 2.5 m.

To assess the efficacy of the new liquefaction triggering model, detailed geotechnical site characterizations were performed at sites that experienced significant shaking during the 3 September 2016, $M_w 5.8$ Pawnee, OK, earthquake. Cone Penetration Tests (CPT), Multichannel Analysis of Surface Waves (MASW) tests, and Horizontal-to-Vertical Spectral Ratio (HVSr) tests were performed at each site. Liquefaction potential was computed at each test location using the model developed herein as well as several existing models for tectonic earthquakes. The severity of surficial liquefaction manifestations at each test location were predicted using the Ishihara-inspired Liquefaction Potential Index (LPI_{ish}) (Maurer et al. 2015b). Computed LPI_{ish} values and the corresponding predicted liquefaction surficial manifestation severity categories were compared to the documented observations of liquefaction manifestations made following the Pawnee event to evaluate the accuracy of the selected models.

At most locations evaluated, predictions from the new liquefaction triggering model were more consistent with field observations than predictions from existing models. The models developed for tectonic

earthquakes tended to over-predict the severity of liquefaction for the Pawnee earthquake. While the new model slightly under-predicts liquefaction severity at some sites, it generally provided accurate predictions of liquefaction severity at the Pawnee test locations. There were several sites where either liquefaction is predicted by all models but was not observed or where liquefaction is not predicted by any of the models used but was observed following the Pawnee event. This may be due to underreporting of liquefaction extent or due to difficulties in matching post-event damage surveys with field test locations. In general, this study showed that the new induced seismicity-specific triggering model provides a more accurate assessment of the liquefaction hazard for the Pawnee event.

Accounting for the observed differences in liquefaction potential for induced and tectonic earthquakes is important when considering seismic design and policy in areas subject to induced seismicity. The findings of this study show that existing methods used to assess the liquefaction potential of tectonic earthquakes tend to over-predict the liquefaction potential for a given induced earthquake. As a result, use of traditional liquefaction triggering models in design may lead to over-conservatism in design and increased costs.

The current study considers liquefaction potential from induced earthquakes in a single case study area (i.e., Oklahoma, Texas, and Kansas). As confirmed in this study, relationships for r_d and MSF vary by region and seismic source. As a result, research into liquefaction potential from induced earthquakes in other regions is also needed.

It is important to note, that while the findings of this study show that the liquefaction potential from induced earthquakes is less than from tectonic earthquakes, the overall risk of liquefaction in areas currently experiencing liquefaction is still likely higher than historic levels due to the increased rate of induced seismicity in these areas.

7 Acknowledgements

This study is based on work supported in part by USGS grant G18AP00094. The authors gratefully acknowledge this support. However, any opinions, findings, and conclusions expressed in this paper are those of the authors and do not necessarily reflect the views of the USGS. The authors would also like to thank Dan Ripley, Barry Keeler, Gordon Laird, and Martin Williams for allowing their properties to be used for this study and for their assistance throughout the course of this effort. The authors also acknowledge and thank Dr. Clint Wood from the University of Arkansas for the use of his HVSR equipment.

References

- American Society of Civil Engineers. (2010). *Minimum Design Loads for Buildings and Other Structures, ASCE/SEI 7-10*. Reston, VA, 608 pp.
- Al Atik, L., and Abrahamson, N. (2010). “An Improved Method for Nonstationary Spectral Matching.” *Earthquake Spectra*, 26(3), 601–617.
- Atkinson, G. M. (2020). “The Intensity of Ground Motions from Induced Earthquakes with Implications for Damage Potential.” *Bulletin of the Seismological Society of America*, 110(5), 2366–2379.
- Atkinson, G. M., and Assatourians, K. (2017). “Are Ground-Motion Models Derived from Natural Events Applicable to the Estimation of Expected Motions for Induced Earthquakes?” *Seismological Research Letters*, 88(2A), 430–441.
- Bahrampouri, M., Rodriguez-Marek, A., and Green, R. A. (2020). “Ground motion prediction equations for Arias Intensity using the KiK-net database.” *Earthquake Spectra*, December, 1–18.
- Baise, L. G., and Rashidian, V. (2018). “A Geospatial Approach to Liquefaction Assessment for Rapid Response and Loss Estimation.” *Geotechnical Earthquake Engineering and Soil Dynamics V (GEESD V): Seismic Hazard Analysis, Earthquake Ground Motions, and Regional-Scale Assessment*, GSP 291, American Society of Civil Engineers, Reston, VA, 1–10.
- Bates, D., Maechler, M., Bolker, B., and Walker, S. (2015). “Fitting linear mixed-effects models using lme4.” *Journal of Statistical Software*, 67(1), 1–48.
- Bommer, J. J., Dost, B., Edwards, B., Stafford, P. J., van Elk, J., Doornhof, D., and Ntinalexis, M. (2016). “Developing an application-specific ground-motion model for induced seismicity.” *Bulletin of the Seismological Society of America*, 106(1), 158–173.
- Boore, D. M. (2010). “Orientation-Independent, Nongeometric-Mean Measures of Seismic Intensity from Two Horizontal Components of Motion.” *Bulletin of the Seismological Society of America*, 100(4), 1830–1835.
- Boore, D. M., and Kishida, T. (2017). “Relations between Some Horizontal-Component Ground-Motion Intensity Measures Used in Practice.” *Bulletin of the Seismological Society of America*, 107(1), 334–343.
- Boore, D. M., Stewart, J. P., Seyhan, E., and Atkinson, G. M. (2014). “NGA-West2 Equations for Predicting PGA, PGV, and 5% Damped PSA for Shallow Crustal Earthquakes.” *Earthquake Spectra*, 30(3),

1057–1085.

- Boore, D. M., and Thompson, E. M. (2014). “Path durations for use in the stochastic-method simulation of ground motions.” *Bulletin of the Seismological Society of America*, 104(5), 2541–2552.
- Boore, D. M., and Thompson, E. M. (2015). “Revisions to some parameters used in stochastic-method simulations of ground motion.” *Bulletin of the Seismological Society of America*, 105(2), 1029–1041.
- Boulanger, R. W., and Idriss, I. M. (2014). *CPT and SPT based liquefaction triggering procedures*. Report No. UCD/CGM-14/01, University of California at Davis, Davis, CA.
- Boyd, O. S., McNamara, D. E., Hartzell, S., and Choy, G. (2017). “Influence of lithostatic stress on earthquake stress drops in North America.” *Bulletin of the Seismological Society of America*, 107(2), 856–868.
- Bradley, B. A. (2011). “Correlation of Significant Duration with Amplitude and Cumulative Intensity Measures and Its Use in Ground Motion Selection.” *Journal of Earthquake Engineering*, 15(6), 809–832.
- Cetin, K. O. (2000). “Reliability-Based Probabilistic and Deterministic Assessment of Seismic Soil Liquefaction Initiation Hazard.” Ph.D. Dissertation, University of California, Berkeley, CA.
- Choi, J. H., Ko, K., Gihm, Y. S., Cho, C. S., Lee, H., Song, S. G., Bang, E. S., Lee, H. J., Bae, H. K., Kim, S. W., Choi, S. J., Lee, S. S., and Lee, S. R. (2019). “Surface deformations and rupture processes associated with the 2017 Mw 5.4 Pohang, Korea, earthquake.” *Bulletin of the Seismological Society of America*, 109(2), 756–769.
- Clayton, P., Zalachoris, G., Rathje, E., Bheemasetti, T., Caballero, S., Yu, X., and Bennett, S. (2016). *The geotechnical aspects of the September 3, 2016 M5.8 Pawnee, Oklahoma earthquake*. Report GEER-051, Geotechnical Extreme Events Reconnaissance Association.
- Cox, B. R., and Teague, D. P. (2016). “Layering ratios: a systematic approach to the inversion of surface wave data in the absence of a priori information.” *Geophysical Journal International*, 207(1), 422–438.
- Cramer, C. H. (2017). “Brune stress parameter estimates for the 2016 Mw 5.8 pawnee and other Oklahoma earthquakes.” *Seismological Research Letters*, 88(4), 1005–1016.
- Darendeli, M. B., and Stokoe, K. H. (2001). *Development of a new family of normalized modulus reduction and material damping curves*. Geotechnical Engineering Report GD01-1, Univ. of Texas at Austin,

Austin, TX.

Efron, B., and Tibshirani, R. J. (1994). *An Introduction to Bootstrap*. Vol. 57, CRC Press, Chicago, IL.

Ellsworth, W. L. (2013). "Injection-induced earthquakes." *Science*, 341(6142), 1–8.

Foulger, G. R., Wilson, M. P., Gluyas, J. G., Julian, B. R., and Davies, R. J. (2018). "Global review of human-induced earthquakes." *Earth-Science Reviews*, 178, 438–514.

Green, R. A., and Bommer, J. J. (2019). "What is the Smallest Earthquake Magnitude that Needs to be Considered in Assessing Liquefaction Hazard?" *Earthquake Spectra*, 35(3), 1441–1464.

Green, R. A., Bommer, J. J., Rodriguez-Marek, A., Maurer, B. W., Stafford, P. J., Edwards, B., Kruiver, P. P., de Lange, G., and van Elk, J. (2019). "Addressing limitations in existing 'simplified' liquefaction triggering evaluation procedures: application to induced seismicity in the Groningen gas field." *Bulletin of Earthquake Engineering*, Springer Netherlands, 17(8), 4539–4557.

Green, R. A., Bommer, J. J., Stafford, P. J., Maurer, B. W., Kruiver, P. P., Edwards, B., Rodriguez-Marek, A., de Lange, G., Oates, S. J., Storck, T., Omidi, P., Bourne, S. J., and van Elk, J. (2020). "Liquefaction Hazard in the Groningen Region of the Netherlands due to Induced Seismicity." *Journal of Geotechnical and Geoenvironmental Engineering*, 146(8), 04020068.

Green, R. A., Cubrinovski, M., Cox, B., Wood, C., Wotherspoon, L., Bradley, B., and Maurer, B. (2014). "Select Liquefaction Case Histories from the 2010-2011 Canterbury Earthquake Sequence." *Earthquake Spectra*, 30(1), 131–153.

Green, R. A., Lee, J., Cameron, W., and Arenas, A. (2011). "Evaluation of various definitions of characteristic period of earthquake ground motions." *Proceedings of the 5th International Conference on Earthquake Geotechnical Engineering*, Santiago, Chile, 1–12.

Green, R. A., Maurer, B. W., and Haskell, A. (2017). *Development of Probabilistic Magnitude-Bound Curves for the New Madrid Seismic Zone (NMSZ) for Paleoliquefaction Studies*. U.S. Geological Society Technical Report G14AP00046, U.S. Geological Survey, Reston, VA.

Green, R. A., Mitchell, J. K., and Polito, C. P. (2000). "An Energy-Based Excess Pore Pressure Generation Model for Cohesionless Soils." *Proceedings of the John Booker Memorial Symposium – Developments in Theoretical Geomechanics (D.W. Smith and J.P. Carter, eds.)*, A.A. Balkema, Rotterdam, the Neatherlands, 383–390.

Green, R. A., and Terri, G. A. (2005). "Number of Equivalent Cycles Concept for Liquefaction

- Evaluations—Revisited.” *Journal of Geotechnical and Geoenvironmental Engineering*, 131(4), 477–488.
- Green, R. A., and Ziotopoulou, K. (2015). “Overview of screening criteria for liquefaction triggering susceptibility.” *Proceedings of the Ninth Pacific Conference on Earthquake Engineering*, Australian Earthquake Engineering Society, Sydney, Australia.
- Hallal, M. M., and Cox, B. R. (2019). “Theoretical Evaluation of the Interval Method Commonly Used for Downhole Seismic Testing.” *Proceedings of Geo-Congress 2019*, American Society of Civil Engineers, Reston, VA, 376–386.
- Hassani, B., and Atkinson, G. M. (2015). “Referenced Empirical Ground-Motion Model for Eastern North America.” *Seismological Research Letters*, 86(2A), 477–491.
- Hough, S. E. (2014). “Shaking from injection-induced Earthquakes in the central and eastern United States.” *Bulletin of the Seismological Society of America*, 104(5), 2619–2626.
- Huang, Y., Ellsworth, W. L., and Beroza, G. C. (2017). “Stress drops of induced and tectonic earthquakes in the central United States are indistinguishable.” *Science Advances*, 3(8), 1–7.
- Idriss, I. M. (1999). “An update to the Seed-Idriss simplified procedure for evaluating liquefaction potential.” *Proceedings of TRB Workshop on New Approaches to Liquefaction*, Publication No. FHWA-RD-99-165, Federal Highway Administration, Washington, DC.
- Idriss, I. M., and Boulanger, R. W. (2008). *Soil liquefaction during earthquakes*, Monograph MNO-12. Earthquake Engineering Research Institute, Oakland, CA.
- Idriss, I. M., and Sun, J. I. (1992). *User’s manual for SHAKE91: A computer program for conducting equivalent linear seismic response analyses of horizontally layered soil deposits*. Center for Geotechnical Modeling, Dept. of Civil and Environmental Engineering, Univ. of California, Davis, CA.
- Ishibashi, I., and Zhang, X. (1993). “Unified dynamic shear moduli and damping ratios of sand and clay.” *Soils and Foundations*, 33(1), 182–191.
- Ishihara, K. (1985). “Stability of natural deposits during earthquakes.” *Proceedings of 11th Intern. Conf. on Soil Mechanics and Foundation Engineering*, International Society of Soil Mechanics and Geotechnical Engineering, London, UK, 321–376.
- Iwasaki, T., Tatsuoka, F., Tokida, K., and Yasuda, S. (1978). “A practical method for assessing soil

- liquefaction potential based on case studies at various sites in Japan.” *Proceedings of 2nd International Conference on Microzonation*, National Science Foundation, Washington, DC.
- Jeong, S., Stump, B. W., and DeShon, H. R. (2020). “Spectral Characteristics of Ground Motion from Induced Earthquakes in the Fort Worth Basin, Texas, Using the Generalized Inversion Technique.” *Bulletin of the Seismological Society of America*, 110(5), 2058–2076.
- Johann, L., and Shapiro, S. A. (2020). “Understanding Vectorial Migration Patterns of Wastewater-Induced Earthquakes in the United States.” *Bulletin of the Seismological Society of America*, 110(5), 2295–2307.
- Kaski, K. M., and Atkinson, G. M. (2017). “A Comparison of Ground-Motion Characteristics from Induced Seismic Events in Alberta with Those in Oklahoma.” *Seismological Research Letters*, 88(6), 1570–1585.
- Keranen, K. M., Weingarten, M., Abers, G. A., Bekins, B. A., and Ge, S. (2014). “Sharp increase in central Oklahoma seismicity since 2008 induced by massive wastewater injection.” *Science*, 345(6195), 448–451.
- Kolawole, F., Atekwana, E. A., and Ismail, A. (2017). “Near-surface electrical resistivity investigation of coseismic liquefaction-induced ground deformation associated with the 2016 Mw 5.8 Pawnee, Oklahoma, earthquake.” *Seismological Research Letters*, 88(4), 1017–1023.
- Konno, K., and Ohmachi, T. (1998). “Ground-motion characteristics estimated from spectral ratio between horizontal and vertical components of microtremor.” *Bulletin of the Seismological Society of America*, 88(1), 228–241.
- Langenbruch, C., and Zoback, M. D. (2016). “How will induced seismicity in Oklahoma respond to decreased saltwater injection rates?” *Science Advances*, 2(e1601542), 1–9.
- Lasley, S. J., Green, R. A., and Rodriguez-Marek, A. (2014). “Comparison of Equivalent-Linear Site Response Analysis Software.” *Proceedings of 10th National Conference in Earthquake Engineering*, Earthquake Engineering Research Institute, Oakland, CA, 1–11.
- Lasley, S. J., Green, R. A., and Rodriguez-Marek, A. (2016). “New Stress Reduction Coefficient Relationship for Liquefaction Triggering Analyses.” *Journal of Geotechnical and Geoenvironmental Engineering*, 142(11), 06016013.
- Lasley, S. J., Green, R. A., and Rodriguez-Marek, A. (2017). “Number of Equivalent Stress Cycles for Liquefaction Evaluations in Active Tectonic and Stable Continental Regimes.” *Journal of*

- Geotechnical and Geoenvironmental Engineering*, 143(4), 04016116.
- Lee, J. (2009). "Engineering Characterization of Earthquake Ground Motions." Ph.D. Dissertation, University of Michigan, Ann Arbor, MI.
- Liao, S. S. C., and Whitman, R. V. (1986). *Catalogue of liquefaction and non-liquefaction occurrences during earthquakes*. Department of Civil Engineering, Massachusetts Institute of Technology, Cambridge, MA.
- Liu, A. H., Stewart, J. P., Abrahamson, N. A., and Moriawaki, Y. (2001). "Equivalent Number of Uniform Stress Cycles for Soil Liquefaction Analysis." *Journal of Geotechnical and Geoenvironmental Engineering*, 127(12), 1017–1026.
- Maurer, B. W., Green, R. A., Cubrinovski, M., and Bradley, B. A. (2014). "Evaluation of the Liquefaction Potential Index for Assessing Liquefaction Hazard in Christchurch , New Zealand." *Journal of Geotechnical and Geoenvironmental Engineering*, 140(7), 1–11.
- Maurer, B. W., Green, R. A., Cubrinovski, M., and Bradley, B. A. (2015a). "Fines-content effects on liquefaction hazard evaluation for infrastructure in Christchurch, New Zealand." *Soil Dynamics and Earthquake Engineering*, 76, 58–68.
- Maurer, B. W., Green, R. A., and Taylor, O. D. S. (2015b). "Moving towards an improved index for assessing liquefaction hazard: Lessons from historical data." *Soils and Foundations*, 55(4), 778–787.
- McGarr, A., Simpson, D., and Seeber, L. (2002). "Case histories of induced and triggered seismicity." *International Geophysics*, 81A, 647–661.
- McGuire, R. K., Silva, W. J., and Costantino, C. J. (2001). *Technical basis for revision of regulatory guidance on design ground motions: Hazard- and risk-consistent ground motion spectra guidelines*. Division of Engineering Technology, Office of Nuclear Regulatory Research, U.S. Nuclear Regulatory Commission, Washington, DC.
- McNamara, D. E., Hayes, G. P., Benz, H. M., Williams, R. A., McMahon, N. D., Aster, R. C., Holland, A., Sickbert, T., Herrmann, R., Briggs, R., Smoczyk, G., Bergman, E., and Earle, P. (2015). "Reactivated faulting near Cushing, Oklahoma: Increased potential for a triggered earthquake in an area of United States strategic infrastructure." *Geophysical Research Letters*, 42(20), 8328–8332.
- Miner, M. A. (1945). "Cumulative damage in fatigue." *Journal of Applied Mechanics*, 12(3), A159–A164.
- Mitchell, J. K., and Green, R. A. (2017). "Some induced seismicity considerations in geo-energy resource

- development.” *Geomechanics for Energy and the Environment*, 10(June), 3–11.
- NOAA. (2019). “Normals Annual/Seasonal Station Details: PAWNEE, OK US, GHCND:USC00346940.” https://www.ncdc.noaa.gov/cdo-web/datasets/normal_ann/stations/GHCND:USC00346940/detail (Sep. 10, 2019).
- Novakovic, M., Atkinson, G. M., and Assatourians, K. (2018). “Empirically Calibrated Ground-Motion Prediction Equation for Oklahoma.” *Bulletin of the Seismological Society of America*, 108(5A), 2444–2461.
- Novakovic, M., Atkinson, G. M., and Assatourians, K. (2020). “Erratum: Empirically calibrated ground-motion prediction equation for Oklahoma.” *Bulletin of the Seismological Society of America*, 110(4), 1996–1998.
- NRC. (2016). *State of the Art and Practice in the Assessment of Earthquake-Induced Soil Liquefaction and Its Consequences. State of the Art and Practice in the Assessment of Earthquake-Induced Soil Liquefaction and Its Consequences*, National Research Council, The National Academies Press, Washington, DC.
- Palmgren, A. (1924). “Die lebensdauer von kugellagern (Life length of roller bearings).” *Zeitschrift des Vereins Deutscher Ingenieure*, 68(14), 339–341 (in German).
- Peterie, S. L., Miller, R. D., Intfen, J. W., and Gonzales, J. B. (2018). “Earthquakes in Kansas Induced by Extremely Far-Field Pressure Diffusion.” *Geophysical Research Letters*, 45(3), 1395–1401.
- Pollyea, R. M., Chapman, M. C., Jayne, R. S., and Wu, H. (2019). “High density oilfield wastewater disposal causes deeper, stronger, and more persistent earthquakes.” *Nature Communications*, 10(1), 1–10.
- R Core Team. (2018). *R: A language and environment for statistical computing*. R Foundation for Statistical Computing, Vienna, Austria. Available online at <https://www.R-project.org/>.
- Robertson, P. K. (2010). “Soil behaviour type from the CPT: an update.” *Proceedings of 2nd International Symposium on Cone Penetration Testing*, CPT’10, Huntington Beach, CA, USA.
- Robertson, P. K., and Cabal, K. L. (2015). *Guide to Cone Penetration Testing for Geotechnical Engineering*. Gregg Drilling & Testing, Inc., Signal Hill, CA.
- Robertson, P. K., and Wride, C. (1998). “Evaluating cyclic liquefaction potential using the cone penetration test.” *Canadian Geotechnical Journal*, 35(3), 442–459.

- Rubinstein, J. L., and Mahani, A. B. (2015). “Myths and Facts on Wastewater Injection, Hydraulic Fracturing, Enhanced Oil Recovery, and Induced Seismicity.” *Seismological Research Letters*, 86(4), 1060–1067.
- Schnabel, P., Seed, H. B., and Lysmer, J. (1972). “Modification of seismograph records for effects of local soil conditions.” *Bulletin of the Seismological Society of America*, 62(6), 1649–1664.
- Seed, H. B., and Idriss, I. M. (1971). “Simplified procedure for evaluating soil liquefaction potential.” *Journal of Geotechnical Engineering*, 97(9), 1249–1273.
- Seed, H. B., Idriss, I. M., Makdisi, F., and Banerjee, N. (1975). *Representation of irregular stress time histories by equivalent uniform stress series in liquefaction analyses*, EERC 75-29. Berkeley: Earthquake Engineering Research Center, University of California, Berkeley, CA.
- Stephenson, W. J., Odum, J. K., Hartzell, S., Leeds, A., and Williams, R. A. (n.d.). “Shear wave Velocity Site Characterization in Oklahoma from active-source surface seismic measurements: Implications for Central U.S. Ground Motion Prediction.” *Bulletin of the Seismological Society of America*. (In Review)
- Sumy, D. F., Neighbors, C. J., Cochran, E. S., and Keranen, K. M. (2017). “Low stress drops observed for aftershocks of the 2011 Mw5.7 Prague, Oklahoma, earthquake.” *Journal of Geophysical Research: Solid Earth*, 122(5), 3813–3834.
- Thum, T. S., Lasley, S., Green, R. A., and Rodriguez-Marek, A. (2019). *ShakeVT2: A computer program for equivalent linear site response analysis*, CGPR #98. Center for Geotechnical Practice and Research, Virginia Tech, Blacksburg, VA.
- Tiwari, A., and Rathje, E. M. (2018). “Engineering characteristics of earthquake motions from the Pawnee and Cushing Earthquakes in Oklahoma.” *Proceedings of Geotechnical Earthquake Engineering and Soil Dynamics V (GEESD V): Seismic Hazard Analysis, Earthquake Ground Motions, and Regional-Scale Assessment*, GSP 291, American Society of Civil Engineers, Reston, VA, 378–386.
- U.S. Geologic Survey. (2016a). “Shake Map for M5.8 - 14km NW of Pawnee, Oklahoma.” <<https://earthquake.usgs.gov/earthquakes/eventpage/us10006jxs/executive>> (Jun. 19, 2019).
- U.S. Geologic Survey. (2016b). “National Water Information System data available on the World Wide Web (USGS Water Data for the Nation): USGS 07153000 Black Bear Creek at Pawnee, OK.” <https://waterdata.usgs.gov/nwis/uv?site_no=07153000> (Jul. 4, 2019).
- U.S. Geologic Survey. (2016c). “National Water Information System data available on the World Wide

- Web (USGS Water Data for the Nation): USGS 07152500 Arkansas River at Ralston, OK.” <https://waterdata.usgs.gov/ok/nwis/uv/?site_no=07152500&PARAMeter_cd=00065,00060> (Jul. 4, 2019).
- U.S. Geologic Survey. (2019). “Oklahoma Alluvium.” <<https://mrdata.usgs.gov/geology/state/sgmc-unit.php?unit=OKQal%3B0>> (Jul. 2, 2019).
- U.S. Geologic Survey. (2020a). “Oklahoma Has Had a Surge of Earthquakes since 2009. Are They Due to fracking?” <https://www.usgs.gov/faqs/oklahoma-has-had-a-surge-earthquakes-2009-are-they-due-fracking?qt-news_science_products=0#qt-news_science_products> (Nov. 25, 2020).
- U.S. Geologic Survey. (2020b). “Induced Earthquakes.” <https://www.usgs.gov/natural-hazards/earthquake-hazards/induced-earthquakes?qt-science_support_page_related_con=4#qt-science_support_page_related_con> (Jan. 10, 2020).
- Ulmer, K. J., Green, R. A., and Rodriguez-Marek, A. (2020). “A Consistent Correlation between V_s , SPT, and CPT Metrics for Use in Liquefaction Evaluation Procedures.” *Proceedings of Geo-Congress 2020*, American Society of Civil Engineers, Reston, VA, 132–140.
- Ulmer, K. J., Upadhyaya, S., Green, R. A., Rodriguez-Marek, A., Stafford, P. J., Bommer, J. J., and van Elk, J. (2018). “A Critique of b-Values Used for Computing Magnitude Scaling Factors.” *Proceedings of Geotechnical Earthquake Engineering and Soil Dynamics V (GEESD V), Slope Stability and Landslides, Laboratory Testing, and In Situ Testing*, GSP 293, American Society of Civil Engineers, Reston, VA, 112–121.
- Wair, B. R., Dejong, J. T., and Shantz, T. (2012). *Guidelines for Estimation of Shear Wave Velocity Profiles. PEER Report 2012/08*, Pacific Earthquake Engineering Research Center, University of California, Berkeley, CA.
- Whitman, R. V. (1971). “Resistance of Soil to Liquefaction and Settlement.” *Soils and Foundations*, 11(4), 59–68.
- Wu, Q., Chapman, M., and Chen, X. (2018). “Stress-drop variations of induced earthquakes in Oklahoma.” *Bulletin of the Seismological Society of America*, 108(3), 1107–1123.
- van Ballegooy, S., Green, R. A., Lees, J., Wentz, F., and Maurer, B. W. (2015). “Assessment of various CPT based liquefaction severity index frameworks relative to the Ishihara (1985) H1-H2 boundary curves.” *Soil Dynamics and Earthquake Engineering*, 79, 347–364.
- van Ballegooy, S., Malan, P., Lacrosse, V., Jacka, M. E., Cubrinovski, M., Bray, J. D., O’Rourke, T. D.,

- Crawford, S. A., and Cowan, H. (2014). "Assessment of liquefaction-induced land damage for residential Christchurch." *Earthquake Spectra*, 30(1), 31–55.
- Yang, H., Zhou, P., Fang, N., Zhu, G., Xu, W., Su, J., Meng, F., and Chu, R. (2020). "A Shallow Shock: The 25 February 2019 ML 4.9 Earthquake in the Weiyuan Shale Gas Field in Sichuan, China." *Seismological Research Letters*, 91(6), 3182–3194.
- Yenier, E., and Atkinson, G. M. (2015). "Regionally adjustable generic ground-motion prediction equation based on equivalent point-source simulations: Application to central and eastern North America." *Bulletin of the Seismological Society of America*, 105(4), 1989–2009.
- Yenier, E., Atkinson, G. M., and Sumy, D. F. (2017). "Ground motions for induced earthquakes in Oklahoma." *Bulletin of the Seismological Society of America*, 107(1), 198–215.
- Yust, M. B. S., Cox, B. R., and Cheng, T. (2018). "Epistemic Uncertainty in Vs Profiles and Vs30 Values Derived from Joint Consideration of Surface Wave and H/V Data at the FW07 TexNet Station." *Geotechnical Earthquake Engineering and Soil Dynamics V (GEESD V): Seismic Hazard Analysis, Earthquake Ground Motions, and Regional-Scale Assessment*, GSP 291, American Society of Civil Engineers, Reston, VA, 387–399.
- Zalachoris, G., He, J., and Rathje, E. (2020). "Earthquake Time Series from Events in Texas, Oklahoma, and Kansas." DesignSafe-CI. <https://doi.org/10.17603/ds2-v310-qc53>.
- Zalachoris, G., and Rathje, E. M. (2019). "Ground Motion Model for Small-to-Moderate Earthquakes in Texas, Oklahoma, and Kansas." *Earthquake Spectra*, 35(1), 1–20.
- Zalachoris, G., Rathje, E. M., and Paine, J. G. (2017). "VS30 characterization of Texas, Oklahoma, and Kansas using the p-wave seismogram method." *Earthquake Spectra*, 33(3), 943–961.
- Zhang, X., Jeffrey, R. G., Wu, B., and Zhang, G. (2016). "Modeling of Injection Induced Seismic Events." *Proceedings of SPE Asia Pacific Hydraulic Fracturing Conference*, Society of Petroleum Engineers, Richardson, Texas, 1–25.
- Zoback, M. L., and Zoback, M. D. (1980). "State of Stress in the Coterminous United States." *Journal of Geophysical Research*, 85(B11), 6113–6156.